Journal of Nanomaterials

Fabrication and Applications of Electrospun Nanofibers

Guest Editors: Lan Xu, Fujuan Liu, Yuqin Wan, Domiri D. Ganji, and Naeem Faraz

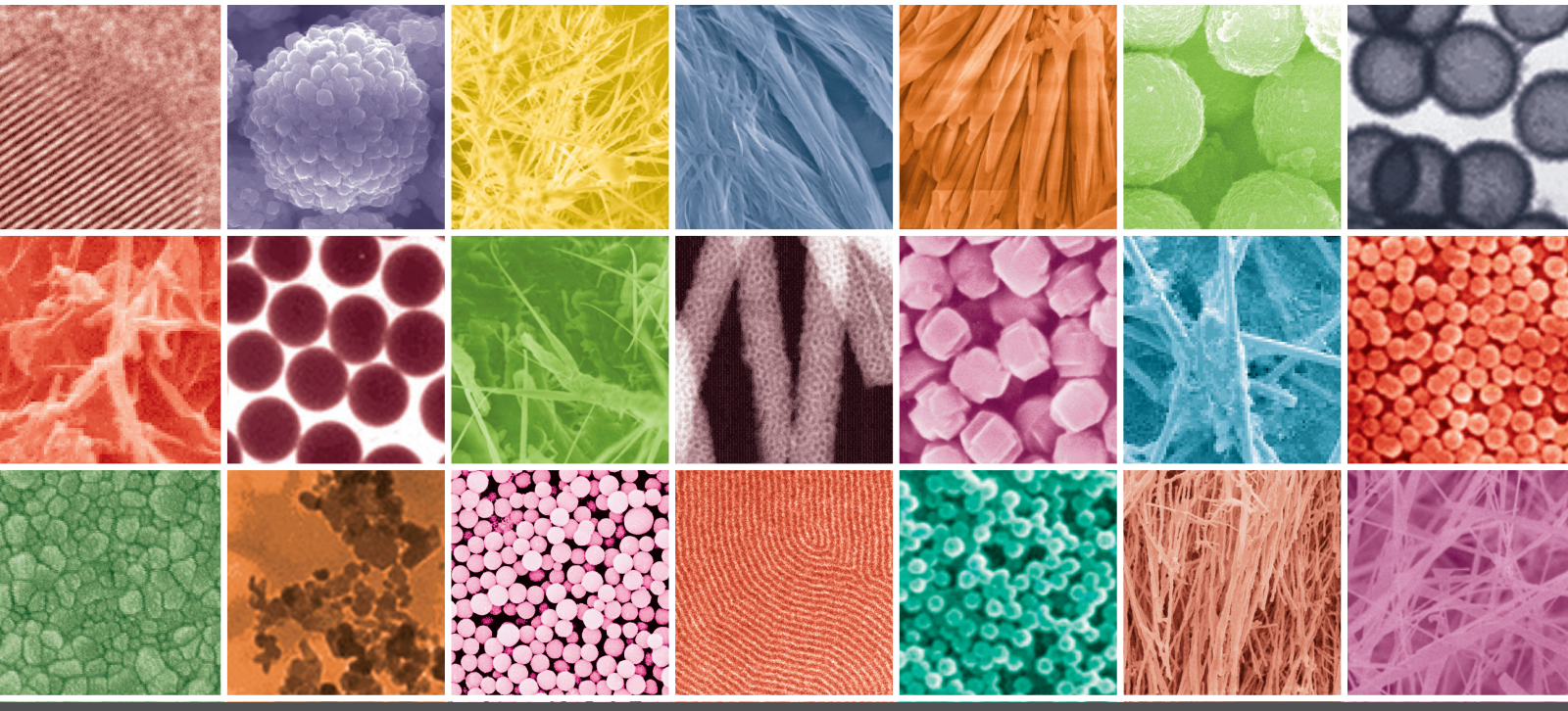

Fabrication and Applications of Electrospun Nanofibers

Journal of Nanomaterials

Fabrication and Applications of Electrospun Nanofibers

Guest Editors: Lan Xu, Fujuan Liu, Yuqin Wan, Domiri D. Ganji, and Naeem Faraz

Editorial Board

Contents

Hindawi Publishing Corporation
Journal of Nanomaterials
Volume 2015, Article ID 697236, 2 pages
http://dx.doi.org/10.1155/2015/697236

Editorial

Fabrication and Applications of Electrospun Nanofibers

Lan Xu,[1] Fujuan Liu,[2] Yuqin Wan,[3] Domiri D. Ganji,[4] and Naeem Faraz[5]

[1]*National Engineering Laboratory for Modern Silk, College of Textile and Clothing Engineering, Soochow University, 199 Ren-Ai Road, Suzhou 215123, China*
[2]*Nantong Textile Institute, Soochow University, 58 Chongchuan Road, Nantong 226018, China*
[3]*Advanced Materials and Process Engineering Laboratory, University of British Columbia, 111-2355 East Mall, Vancouver, BC, Canada V6T 1Z4*
[4]*Department of Mechanical Engineering at Nushirvani Engineering Complex, Mazandaran University, Babolsar 47416-95447, Iran*
[5]*Department of Mathematics, Shanghai University, 99 Shangda Road, Shanghai 200444, China*

Correspondence should be addressed to Lan Xu; lanxu@suda.edu.cn

Received 2 March 2015; Accepted 2 March 2015

Industrialization of nanofibers has been the hottest topic in the whole world because of the various advanced applications of nanofibers in electronic, catalytic, and hydrogen-storage systems, invisibility device (e.g., stealth plane), photonic structures, sensors, medicine, pharmacy and drug delivery, adsorption, separation, filtering, catalysis, fluid storage and transport, electrode materials, radiation protection, medical implants, cell supports, and others [1, 2]. Many highly high-tech enterprises appeared recently in China for mass production of nanofibers, for example, Nantong Bubbfil Nanotechnology Company Limited. Though the remarkable progress in nanotechnology, there are still some open problems to be solved.

(1) What Is the Definition of Nanofibers? There is a confused use of nanofibers in the open literature. What is the correct definition of nanofibers? Li and He [3] define that any materials behaving unlike their mother materials when the size of materials tends to nano/microscales and having obvious nanoeffects [4] are called nanomaterials. Nanofibers are nanomaterials that have a large length-diameter ratio.

(2) Effect of Nanoeffects of Nanofiber on Various Applications. When nanofibers are applied in various fields, many astonishing nanoeffects are predicted, for example, extremely high efficiency in reaction or permeability [4]. Majumder et al. found that liquid flow through a membrane composed of an array of aligned carbon nanotubes is 4 to 5 orders of magnitude faster than would be predicted from conventional fluid-flow theory [5].

(3) Industrialization of Nanofibers. Electrospinning is not valid for mass production of nanofibers due to its very limited throughput. The mechanism for mass production has been studied, but only few can be used in industry. The Bubbfil spinning process by Nantong Bubbfil Nanotechnology Company Limited is the most advanced nanotechnology so far, which uses polymer/melts' bubbles instead of solutions/melts for mass production of nanofibers [6].

According to Chen equation [7], the surface tension of a spherical bubble under electrostatic field can be expressed as

$$\sigma = \frac{1}{4} r \left(\Delta P + 2\varepsilon E\right), \tag{1}$$

where σ is the surface tension, r the radius of the bubble, ΔP the pressure difference, E the electric field intensity, and ε the electric charge per area.

In case the bubble size tends to nano/microscales, the surface tension is remarkably reduced that is very helpful for the electrostatic force to overcome the surface tension of bubbles for mass production of nanofibers.

This special issue addresses focus on electrospinning and nanofiber applications and special attention is paid to nanoeffects of various applications.

Acknowledgments

The work is supported by Priority Academic Program Development of Jiangsu Higher Education Institutions (PAPD), National Natural Science Foundation of China (Grant no. 11372205), Jiangsu Provincial Natural Science Foundation of China (Grant no. BK20131175), Natural Science Foundation of the Jiangsu Higher Education Institutions of China (Grant no. 14KJA130001), Suzhou Science and Technology Project (Grant no. SYG201434), Nantong Science and Technology Project (Grant no. BK2014050), and Science & Technology Pillar Program of Jiangsu Province (Grant no. BE2013072). Hereby Dr. L. Xu should thank the coeditors of this special issue, Dr. F. Liu, Dr. Y. Wan, Dr. D. D. Ganji, and Dr. N. Faraz, for their effective work in this special issue; Dr. L. Xu should also thank all reviewers for their time and effect to improve the special issue. Without their help, the success of this special issue was impossible.

Lan Xu
Fujuan Liu
Yuqin Wan
Domiri D. Ganji
Naeem Faraz

References

[1] J.-H. He, H.-Y. Kong, R.-R. Yang et al., "Review on fiber morphology obtained by bubble electrospinning and blown bubble spinning," *Thermal Science*, vol. 16, no. 5, pp. 1263–1279, 2012.

[2] L. Xu, Y. Wu, and Y. Liu, "Electrospun nanoporous materials: reality, potential and challenges," *Materials Science and Technology*, vol. 26, no. 11, pp. 1304–1308, 2010.

[3] Z. B. Li and J. H. He, "When nanotechnology meets filteration: from nanofiber fabrication to biomimetic design," *Matéria (Rio de Janeiro)*, vol. 19, no. 4, pp. 1–3, 2014.

[4] J.-H. He, Y.-Q. Wan, and L. Xu, "Nano-effects, quantum-like properties in electrospun nanofibers," *Chaos, Solitons & Fractals*, vol. 33, no. 1, pp. 26–37, 2007.

[5] M. Majumder, N. Chopra, R. Andrews, and B. J. Hinds, "Nanoscale hydrodynamics: enhanced flow in carbon nanotubes," *Nature*, vol. 438, no. 7064, p. 44, 2005.

[6] R.-X. Chen, Y. Li, and J.-H. He, "Mini-review on Bubbfil spinning process for mass-production of nanofibers," *Matéria*, vol. 19, no. 4, pp. 325–343, 2014.

[7] R. X. Chen, "On surface tension of a bubble under presence of electrostatic force," *Thermal Science*, vol. 19, no. 1, pp. 353–355, 2015.

Hindawi Publishing Corporation
Journal of Nanomaterials
Volume 2015, Article ID 367964, 9 pages
http://dx.doi.org/10.1155/2015/367964

Research Article

Electrospinning Preparation of Timosaponin B-II-Loaded PLLA Nanofibers and Their Antitumor Recurrence Activities *In Vivo*

Zhonghua Huo,[1] Yan Qiu,[2] Zhuling Chu,[1] Peng Yin,[1] Wenquan Lu,[3] Yijia Yan,[4] Na Wan,[4] and Zhilong Chen[4]

[1] *Department of General Surgery, 454th Hospital of PLA, Najing 210002, China*
[2] *Department of Pharmacy, 454th Hospital of PLA, Najing 210002, China*
[3] *Department of Pharmacy, Shanghai Changzheng Hospital, 415 Fengyang Road, Shanghai 200003, China*
[4] *Department of Pharmaceutical Science & Technology, College of Chemistry and Biology, Donghua University, 2999 North Renmin Road, Shanghai 201620, China*

Correspondence should be addressed to Wenquan Lu; luwenquan@126.com and Zhilong Chen; chenzhilongdhu@gmail.com

Received 30 June 2014; Revised 11 September 2014; Accepted 15 September 2014

Academic Editor: Fujuan Liu

Poly(L-lactic)-acid (PLLA) as a drug carrier and a water-soluble drug timosaponin B-II (TB-II) as a model drug were selected to prepare drug-loaded nanofibers by electrospinning. The average diameters of pure PLLA nanofibers and TB-II-loaded nanofibers were 212.5 ± 68.5, 219.7 ± 57.8, 232.8 ± 66.9, and 232.9 ± 97.7 nm, respectively. DSC and XRD results demonstrated that TB-II was well incorporated into the nanofibers in an amorphous state. FI-TR spectroscopy indicated that TB-II had good compatibility with PLLA. *In vitro* release studies showed that TB-II was rapidly released from the nanofibers within 6 h, followed by a gradual release for long time. *In vivo* biosafety test revealed no noticeable toxicity of these TB-II nanofibers. The TB-II released from the nanofibers had obvious inhibition effect against human hepatocellular carcinoma SMMC 7721 cells both *in vivo* and *in vitro*. It was confirmed that the TB-II-loaded nanofibers were a sustained delivery system which could effectively inhibit the tumor growth and recurrence after surgery.

1. Introduction

Classically, surgery is the first-line treatment for most solid tumors [1]. However, it is difficult to completely remove the tumor through surgery [2]. The residual cancer cells remaining at or near the resection margins or site of initial treatment always initiate a local recurrence of tumors [3, 4]. Thus, chemotherapy has been applied widely as an adjuvant procedure followed by surgery.

In recent years, substances derived from medical plants, such as paclitaxel, camptothecin, and vincristine, have been confirmed to be useful as chemotherapy drugs [5]. *Anemarrhenae rhizoma* (Zhimu in Chinese), the dried rhizome of *A. asphodeloides* Bunge (*A. asphodeloides*, Faro. Liliaceae), is a well-known traditional Chinese medicinal herb which has long been included in Chinese traditional medical recipes for treatment of inflammation, fever, and diabetes [6, 7]. Timosaponin B-II (TB-II) (Figure 1) is a typical furostanol saponin isolated from the rhizome of *A. asphodeloides* [8]. It has been reported that TB-II has remarkable inhibiting effects on superoxide generation, inflammatory reaction, and platelet aggregation potential [9, 10]. Recent research has shown that TB-II will be converted to Timosaponin A-III (TA-III) by glycosidase treatment *in vivo*, which can induce apoptosis in various cancer cell lines [11].

Since chemotherapy drugs exhibit low selectivity, they destroy both tumor cells and normal cells. A locoregional drug administration need to be studied to avoid the systemic toxicity associated with chemotherapy drugs and maintain their therapeutic concentrations in the local region of tumors [8]. Electrospinning has been proven to be a great fabrication method for drug delivery systems due to the large selection of possible synthetic and natural, biodegradable or nondegradable polymers, and large surface-to-volume ratio [12, 13].

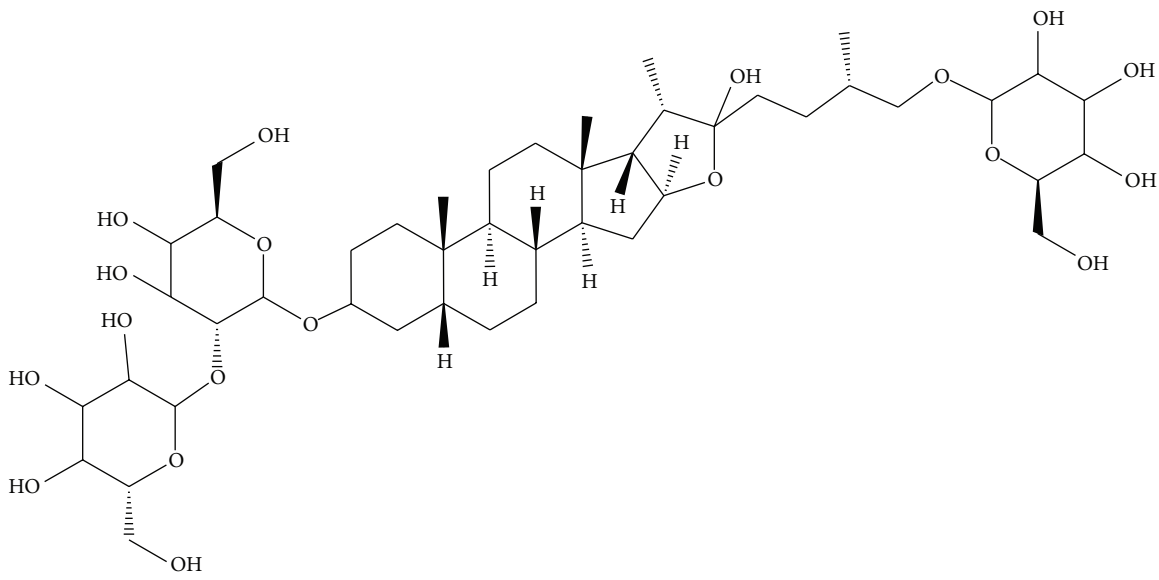

Figure 1: Chemical structures of TB-II.

The drug-loaded fibers prepared by electrospinning can be implanted intratumorally, adjacent to the cancerous tissue or at the surgical resection margins for cancer chemotherapy of solid tumors [14, 15]. For preventing the recurrence of tumor, the drug-loaded fibers can be attached to the surgical site following removal of the tumor. As the drugs were moderately released from the sustained-release carriers, relatively steady effective concentration can be achieved to inhibit tumor growth [4, 14].

In this study, the poly(L-lactic)-acid (PLLA), a promising material with good biocompatibility, biodegradability, and nontoxic property, was selected as a drug carrier. TB-II-loaded PLLA nanofibers were successfully prepared by electrospinning and their antitumor activities were evaluated both *in vitro* and *in vivo*.

2. Materials and Methods

2.1. Materials. TB-II with at least purity 95% was obtained from the Second Military Medical University. Poly(L-lactic) acid (PLLA), with an average molecular weight of 100,000, was purchased from Jinan Daigang Biomaterials company. RPMI 1640 and DMED were purchased from Shanghai Gino biological Ltd. All other chemicals and reagents were of analytical grade and used without any purification.

2.2. Animals. BALB/c-nu rats, 5 weeks, were provided by Hanghai SLAC Laboratory Animal Company. All animals were housed individually with water and food available and quarantined for 7 days prior to initiation of the study. A 12 h light/12 h dark cycle (light was switched at 06:00) was used. Room temperature was ranged from 22°C to 27°C and the humidity was maintained between 30% and 70%. All animal procedures were approved by the University Animal Care and Use Committee.

2.3. Cell Lines and Culture. Human hepatocellular carcinoma cell line SMMC-7721 was purchased from Chinese Academy of Sciences. The cells were cultured in RPMI 1640 medium, supplemented with 10% fetal calf serum, and incubated at 37°C in a humidified atmosphere containing 5% CO_2.

2.4. Preparation of TB-II-Loaded PLLA Nanofibers by Electrospinning

2.4.1. Preparation of Spinning Solutions. The concentration of PLLA in the spinning solution was fixed at 5% (w/v) according to preexperiments about its filament-forming properties. TB-II was mixed with PLLA to achieve a sustained release, and then the mixture was dissolved in chloroform/acetone solution (2/1 in volume ratio) and stirred for at least 3 h at room temperature. The weight ratio of TB-II in spinning solution that ranged from 10 to 15 was studied.

2.4.2. Electrospinning Process. Spinning solution was loaded in a 5 mL syringe to which a stainless-steel blunt needle was attached. The outer diameter of blunt needle was 1.0 mm, and the inner diameter was 0.7 mm. The needle tip was connected to an electrode of the high voltage power supply (DW-P503-1ACDF, Tianjin Dongwen High Voltage Power Supply Co., Ltd. China), and an 18 kV of electrical potential was applied. The flow rate of solutions was controlled at 1.0 mLh^{-1} by the syringe pump (LSP01-1A, Hebei Baoding LongerPump Co., Ltd. China). Randomly nonwoven fibers were collected on a metal collector wrapped with aluminum foil which was kept at a distance of 20–22 cm from the needle tip. Formed fibers were dried initially for over 24 h at 25°C under vacuum to remove residual solvent.

2.5. Characterization. The morphology of the nanofibers was observed with a scanning electron microscopy (SEM, JEOL JSM-5600LV, Japan) at a voltage of 15 kV. The fiber average diameter was determined by measuring 50 fibers selected randomly from each sample using software image. Differential scanning calorimetry (DSC) analyses were performed on a MDSC 2910 differential scanning calorimeter (TA Instruments Co., DE, USA) at a heating rate of 10°C/min. X-ray diffraction (XRD) patterns were obtained using a D/max-2550PC (Geigerflex, Rigaku, Japan) with monochromated CuKa radiation operated at 40 kV and 300 mA. Fourier transformed infrared spectroscopy (FT-IR) was conducted using a Nicolet-Nexus 670 FTIR spectrometer (Nicolet Instrument Corporation, WI, USA) over the scanning range 500–4000 cm^{-1} with a resolution of 2 cm^{-1}.

2.6. Release of TB-II from the Nanofibers In Vitro. To evaluate the *in vitro* release of TB-II, 10 mg of drug-loaded PLLA nanofibers was incubated in 50 mL of phosphate buffer solution (PBS, pH = 7.4) at 37°C. 2 mL of the sample solution was collected and diluted using fresh PBS at each time point. The amount of TB-II was monitored using a UV-vis spectrophotometer (7600CRT, Jinghua Instruments, China) at the wavelength of 280 nm. All the measurements were carried out in triplicate and the average values were shown in this study.

2.7. Biosafety Test In Vivo. The nanofibers were cut to 1 cm × 1 cm pieces and sterilized by exposure to UV light for 24 h before implantation. BALB/c-nu rats (weighing 20 g) were divided randomly into five groups ($n = 3$) as follows:

Groups 1–3: rats implanted with nanofibers containing different concentrations of TB-II;

Group 4: rats implanted with pure PLLA nanofibers;

Group 5: rats with no treatment (control group).

Animals were anesthetized with ethyl ether, and then nanofibers were implanted into subcutaneous sites in the dorsal thoracic region of the rats. Body weight and survival rate of rats were evaluated every day. The weight growth rate was calculated by the use of the following equation:

$$\text{Weight growth rate } (\%) = \frac{(W_d - W_0)}{W_0} \times 100\%, \quad (1)$$

where W_d and W_0 are the average weights of rats at day t and day 0 after implantation, respectively.

2.8. Antitumor Activities In Vitro. *In vitro* antitumor activities of the nanofibers were determined by MTT assay. Briefly, the nanofibers with different concentrations of TB-II were fixed on bottom of the wells of a 48-well plate, and then 5×10^4 SMMC 7721 cells were seeded on the membranes and incubated for 24 h, 48 h, and 72 h, respectively [16]. 40 μL MTT (5 mg/mL) reagent was added to each well and incubated at 37°C for 4 h. At the end of the incubation, the medium was removed and the formazan complex was solubilized with 300 μL DMSO. Absorbance of the complex was measured with a microplate reader (Bio-Rad, California, USA) at a wavelength of 492 nm and cell viability was calculated.

2.9. Antitumor Activities In Vivo. The tumor model was established by subcutaneous injection of 5×10^6 SMMC 7721 cells in the left axilla of female BALB/c-nu rats (weighing 20 g). When tumors reached approximately 1 cm in diameter (between 21 and 28 days after tumor injection), rats were randomized into four groups ($n = 3$) and the antitumor recurrence activity was determined after overlay of TB-II-loaded PLLA nanofibers on tumors:

Group 1: rats had 60% partial tumor resection and were treated with TB-II-loaded PLLA nanofibers;

Group 2: rats had complete tumor resection and were treated with TB-II-loaded PLLA nanofibers;

Group 3: rats had 60% partial tumor resection with no treatment;

Group 4: rats had complete tumor resection with no treatment.

Briefly, rats were anesthetized with ethyl ether and a small incision was made on the skin to expose the tumor. Partial or complete tumor resection was carried out. The TB-II-loaded PLLA nanofibers were laid over the resection site and then the wound was closed using subcutaneous suturing. Animals were cared and observed for tumor recurrence. The tumor volumes of animals were monitored every three days after treatment. The tumor volumes were calculated using the following formula: $V = LW^2/2$, where L is the long diameter and W is the shot diameter. The tumor growth inhibition rate (RTG) was calculated by the use of the following equation: RTG (%) = $(V_d - V_0)/V_0 \times 100\%$, where V_d and V_0 are the average volumes of tumors at day t and day 0 after treatment, respectively.

2.10. Statistical Analysis. Data were presented as mean ± standard deviation (S.D.). Student's t-test was used to measure differences using the Origin 9.0 software package. Statistical significance was taken as $P < 0.05$.

3. Results and Discussion

3.1. Characterization of TB-II-Loaded PLLA Nanofibers. The morphology and diameter distributions of the fibers with various concentrations of TB-II were analyzed using SEM (Figure 2). It could be observed that all of the fibers were randomly oriented and had smooth surfaces, which indicated that TB-II was uniformly distributed in the fibers. The average diameters of the nanofibers with different TB-II concentrations were 219.7 ± 57.8 nm, 232.8 ± 66.9 nm, and 232.9 ± 97.7 nm, respectively, when the diameter of pure PLLA fibers was about 212.5 ± 68.5 nm. The result indicated that the concentration of TB-II affected the diameter of the fibers slightly.

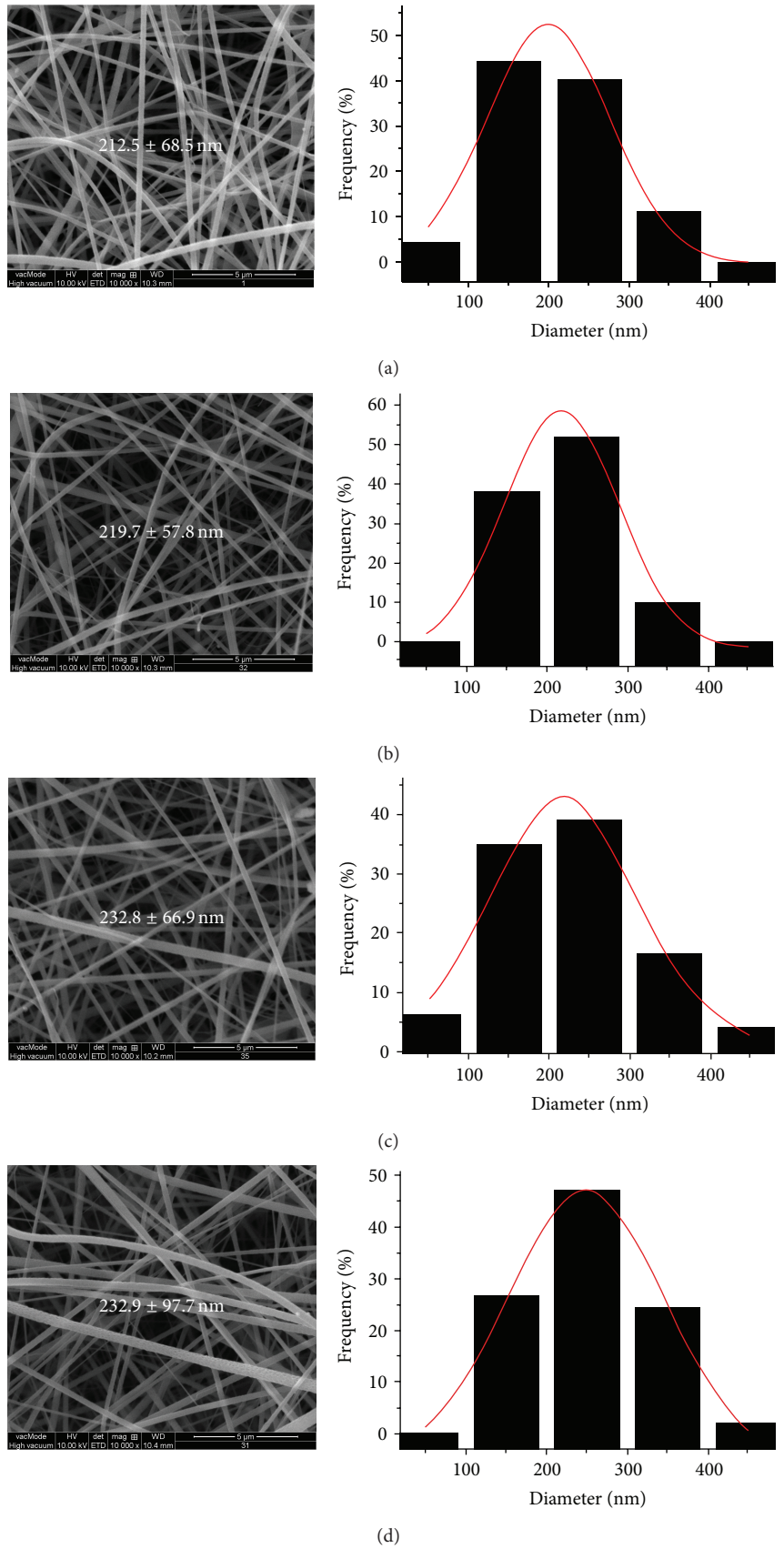

Figure 2: SEM images and diameter distributions of the pure PLLA nanofiber (a) and TB-II-loaded PLLA nanofibers with different drug concentration: (b) 10 wt.%, (c) 12 wt.%, and (d) 15 wt.%. The scale bars are 5 μm.

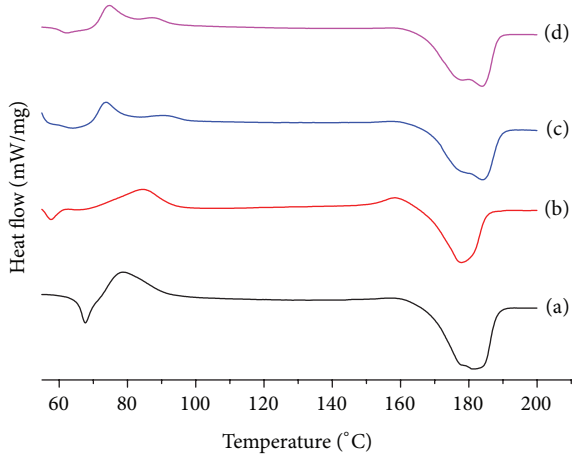

Figure 3: DSC curves of pure PLLA nanofiber (a) and TB-II-loaded nanofibers with different drug concentration: (b) 10 wt.%, (c) 12 wt.%, and (d) 15 wt.%.

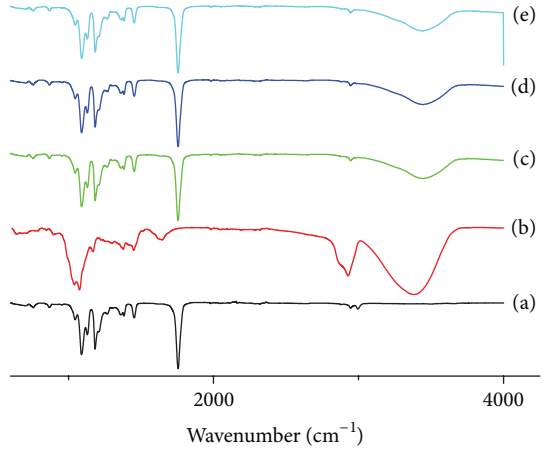

Figure 4: FT-IR spectra of TB-II (a), pure PLLA nanofiber (b), and TB-II-loaded nanofibers with different drug concentration: (c) 10 wt.%, (d) 12 wt.%, and (e) 15 wt.%.

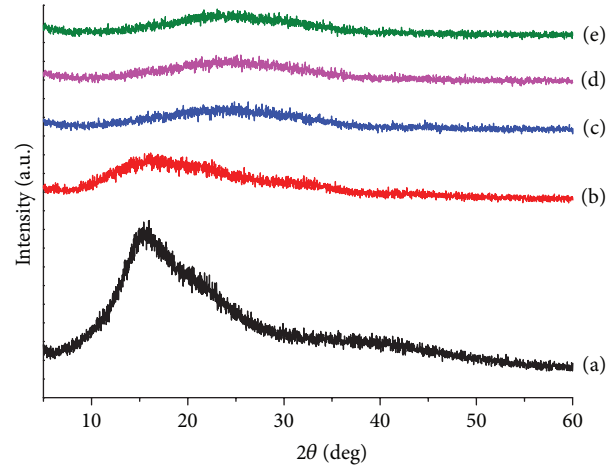

Figure 5: X-ray diffraction patterns of TB-II (a), pure PLLA nanofiber (b), and TB-II-loaded nanofibers with different drug concentration: (c) 10 wt.%, (d) 12 wt.%, and (e) 15 wt.%.

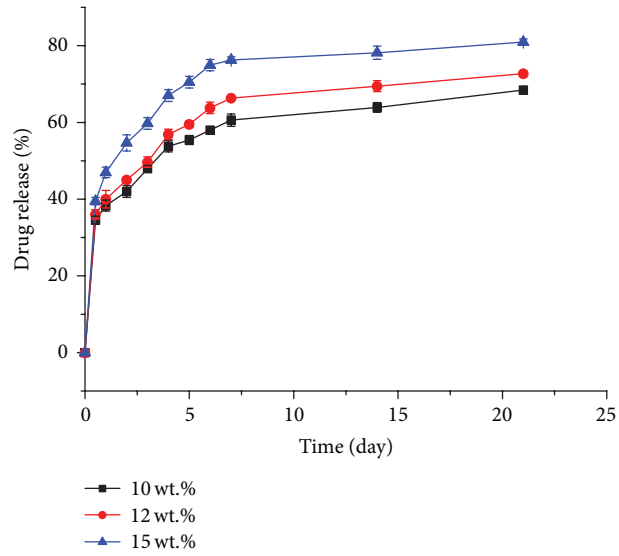

Figure 6: *In vitro* cumulative percentage of TB-II released from the nanofibers at various time points ($n = 3$).

The DSC curves of PLLA nanofibers with and without different concentrations of TB-II were shown in Figure 3. The curve of pure PLLA nanofibers exhibited a single endothermic peak corresponding to melting at 181.2°C. For the TB-II nanofibers, the DSC curves did not show any melting peaks of TB-II, suggesting that TB-II was not present as a crystalline material but had been converted into an amorphous state. The peak temperatures of the TB-II nanofibers were slightly shifted to 177.9, 183.9, and 183.7°C when the concentrations of TB-II increased to 10, 12, and 15 wt.%, respectively. The result indicated that the concentrations of TB-II in the nanofibers had little effect on the thermal behavior.

The FT-IR spectra of pure PLLA nanofiber and TB-II-loaded nanofibers were depicted in Figure 4. The TB-II samples were prepared by KBr pellet technique, and the nanofibers were scanned directly. The FI-TR spectrum of pure PLLA nanofibers showed characteristic peaks at 1756 cm^{-1} (–C=O), 1090 cm^{-1} (–C–O), and 1184 cm^{-1} (–C–O). The spectrum of TB-II showed the dominant absorption peaks at 3379 cm^{-1} (–O–H), 2928 cm^{-1} (–C–H), and 1075 cm^{-1} (–C–O). The typical peaks corresponding to PLLA and TB-II were both observed in the spectra of 10–15 wt.% TB-II-loaded nanofibers, which indicated that TB-II had good compatibility with PLLA and was well incorporated into the nanofibers.

XRD patterns for the nanofibers were displayed in Figure 5. The pure PLLA nanofiber was amorphous material with a diffraction peak at 16.64°, when TB-II was a crystalline material with a strong peak at 15.94°. The XRD of all TB-II nanofibers showed that the characteristic peaks of PLLA and TB-II were both absent, suggesting that these two molecules were fully converted into an amorphous state. The result was further confirmed that TB-II was amorphously distributed in the nanofibers.

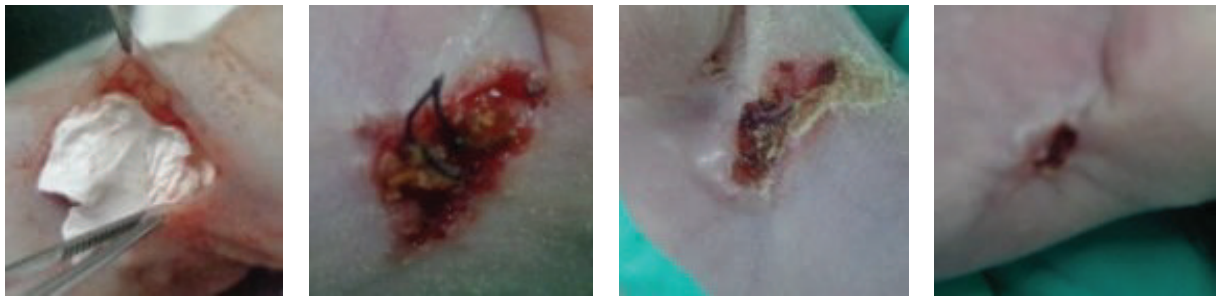

Figure 7: TB-II-loaded nanofibers implanted into subcutaneous sites in the dorsal thoracic region of the rats on days 0, 7, 14, and 21.

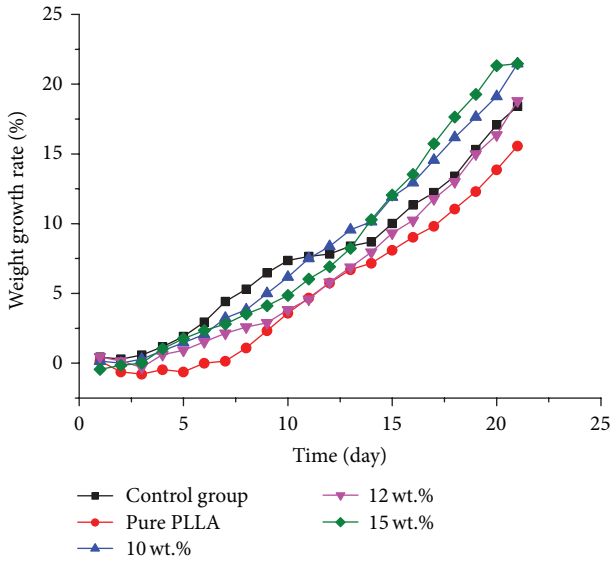

Figure 8: The weight growth rate of the rats after implantation by pure PLLA nanofibers and 10–15 wt.% TB-II-loaded nanofibers ($n = 3$).

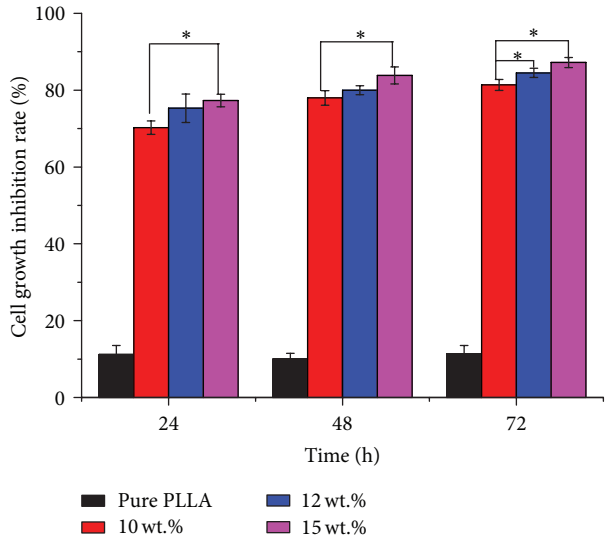

Figure 9: The growth inhibition rate of Human hepatocellular carcinoma SMMC 7721 cells on the pure PLLA nanofibers and 10–15 wt.% TB-II-loaded nanofibers ($n = 3$). $^*P < 0.05$.

3.2. Release of TB-II from Nanofiber In Vitro. PLLA was selected as a drug carrier in this study as it is a relatively hydrophobic polymer because of the methyl group in its structure and therefore it can inherently slower biodegrade [16]. Drug release from the nanofibers with different concentrations of TB-II was shown in Figure 6. In all cases, TB-II was rapidly released, followed by a gradual release. The amount of TB-II release within 6 h was 34.57, 36, and 39.5% corresponding to drug concentrations of 10, 12, and 15 wt.%, respectively. This was probably due to the high concentration of the drug distributed on the electrospun nanofiber surface [17]. It could be observed that the release rate and maximum total amount of TB-II released from the nanofibers increased with the increasing of drug content. After 21 days, around 68.5, 72.7, and 81% of TB-II were released from the nanofibers with drug concentrations of 10, 12, and 15 wt.%, respectively. The result indicated that the release of TB-II from the nanofibers might be continued for long time, suggesting that the TB-II nanofibers could be applied in the following *in vitro* and *in vivo* study.

3.3. Biosafety Test In Vivo. In order to investigate the toxicity of the TB-II nanofibers, the nanofibers were implanted into subcutaneous sites in the dorsal thoracic region of the rats (Figure 7). The body weight and survival rate were monitored every day. As shown in Figure 8, most rats experienced a slight weight loss within 3 days after implantation due to the pain-induced loss of appetite. However, the weight loss recovered in the following days, and there was no significant difference in the weight growth rate among the groups. All the animals survived within 21 days, indicating that there was no noticeable toxicity of the nanofibers with different concentrations of TB-II.

3.4. Antitumor Activities In Vitro. Liver cancer (LC) is the leading cause of cancer-related death worldwide [18]. Because of the high prevalence of the Hepatitis B virus, China has the highest mortality rate for LC [19–21]. Surgery is the only potentially curative treatment for LC [22]. However, tumor recurrence is still common after curative resection. Adjuvant treatment could be helpful in preventing tumor recurrence

Figure 10: Rats had partial tumor resection and then TB-II-loaded nanofibers were laid over the tumor remnant.

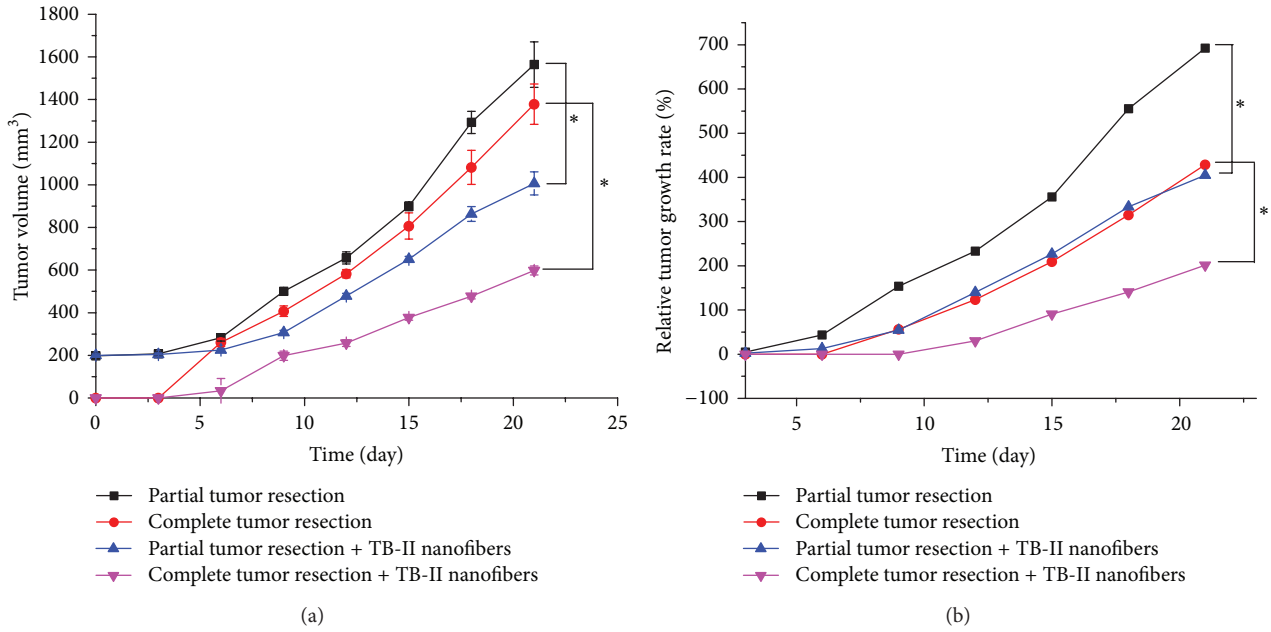

Figure 11: The tumor volume (a) and relative tumor growth rate (b) of rats after treatment with 15 wt.% TB-II-loaded PLLA nanofibers ($n = 3$). $^*P < 0.05$.

after partial surgical resection [23]. In this study, *in vitro* antitumor activities of TB-II-loaded nanofibers against human hepatocellular carcinoma SMMC 7721 cells were determined by MTT assay for 24, 48, and 72 h. The results were shown in Figure 9. Compared to the pure PLLA nanofibers, all TB-II-loaded nanofibers showed very effective antitumor activity. A time-dependent and dose-dependent increase in the rate of cell growth inhibition rate could be observed, which indicated that TB-II could continuously be released in an active form from the nanofibers. Thus, the TB-II-loaded nanofibers were a sustained delivery system.

3.5. Antitumor Recurrence Activities In Vivo. According to the results of characterization and *in vitro* antitumor activities, PLLA nanofibers with 15 wt.% TB-II were applied for the antitumor recurrence efficacy study *in vivo*. Animals had partial or complete tumor resection where the nanofibers were laid over, and then the wound was closed using subcutaneous suturing (Figure 10).

Figure 11 showed the tumor development after implantation of the TB-II-loaded nanofibers. In the cases of complete tumor resection, one of three rats treated with the TB-II-loaded nanofibers presented macroscopic tumor (about 102 mm^3) at day 9 when all three rats with no treatment presented macroscopic tumors (about 260 ± 19 mm^3) at day 6. There was a significant difference both in the tumor volumes and RTG between control and treatment group. After 21 days, the tumor volumes of rats treated with the TB-II-loaded nanofibers reached around 598 ± 20 mm^3, while those of rats with no treatment reached around 1006±53 mm^3. In the cases of partial tumor resection, tumor volumes of rats from the control and treatment group were 197 ± 12 and 199 ± 8 mm^3 at day 0, respectively. As shown in Figure 11, tumor volumes of rats treated with the TB-II-loaded nanofibers increased more slowly compared to those of rats with no treatment from the third day. The tumor volumes of rats treated with the TB-II-loaded nanofibers reached around 1379 ± 94 mm^3 on day 21, which was significantly smaller than those of rats with no treatment (about 1564 ± 106 mm^3).

The above results demonstrated the potential of the TB-II-loaded nanofibers as an implantable drug delivery system for liver cancer after surgery to effectively inhibit

the tumor growth and recurrence. Therefore, the continuous inhibition of tumor growth after treatment with the TB-II-loaded nanofibers confirmed further that TB-II could be continuously released from the nanofibers.

4. Conclusions

In this study, the TB-II-loaded nanofibers were prepared by electrospinning. The average diameter increased with the increase of TB-II content. DSC and XRD results demonstrated that TB-II was well incorporated into the nanofibers in an amorphous state. FI-TR spectroscopy indicated that TB-II had good compatibility with PLLA. *In vivo* biosafety test revealed no noticeable toxicity of these TB-II nanofibers. *In vitro* release studies showed that TB-II was rapidly released from the nanofibers within 6 h, followed by a gradual release for long time. The TB-II released from the nanofibers has obvious inhibition effect against human hepatocellular carcinoma SMMC 7721 cells both *in vivo* and *in vitro*. Thus, it was confirmed that the TB-II-loaded nanofibers were a sustained delivery system which could effectively inhibit the tumor growth and recurrence after surgery.

Conflict of Interests

The authors declare that there is no conflict of interests regarding the publication of this paper.

Acknowledgments

This work was supported by the Chinese National Natural Science Foundation (21372042, 81301878, and 81101298), Foundation of Shanghai government (13431900700, 13430722300, 13ZR1441000, and 13ZR1440900), the Medical Research Foundation of Nanjing Military Command (12mb020), Foundation of Donghua University (11D10501 and 12D10515), and Foundation of Yiwu Science and Technology Bureau (2011-G1-15 and 2013623).

References

[1] D. R. Beil and L. M. Wein, "Sequencing surgery, radiotherapy and chemotherapy: insights from a mathematical analysis," *Breast Cancer Research and Treatment*, vol. 74, no. 3, pp. 279–286, 2002.

[2] B. A. Pockaj and R. J. Gray, "Current surgery for breast cancer," *Future Oncology*, vol. 5, no. 4, pp. 465–479, 2009.

[3] P. Bouchard and J. Efron, "Management of recurrent rectal cancer," *Annals of Surgical Oncology*, vol. 17, no. 5, pp. 1343–1356, 2010.

[4] X. Luo, C. Xie, H. Wang, C. Liu, S. Yan, and X. Li, "Antitumor activities of emulsion electrospun fibers with core loading of hydroxycamptothecin via intratumoral implantation," *International Journal of Pharmaceutics*, vol. 425, no. 1-2, pp. 19–28, 2012.

[5] N. Wang, Y. Feng, M. Zhu, F.-M. Siu, K.-M. Ng, and C.-M. Che, "A novel mechanism of XIAP degradation induced by timosaponin AIII in hepatocellular carcinoma," *Biochimica et Biophysica Acta—Molecular Cell Research*, vol. 1833, no. 12, pp. 2890–2899, 2013.

[6] C. Guo, L. Li, X. Yang et al., "Protective effects of timosaponin B-II on high glucose-induced apoptosis in human umbilical vein endothelial cells," *Environmental Toxicology and Pharmacology*, vol. 37, no. 1, pp. 37–44, 2014.

[7] T.-J. Li, Y. Qiu, P.-Y. Yang, Y.-C. Rui, and W.-S. Chen, "Timosaponin B-II improves memory and learning dysfunction induced by cerebral ischemia in rats," *Neuroscience Letters*, vol. 421, no. 2, pp. 147–151, 2007.

[8] S. Cheng, Y. Du, B. Ma, and D. Tan, "Total synthesis of a furostan saponin, timosaponin BII," *Organic and Biomolecular Chemistry*, vol. 7, no. 15, pp. 3112–3118, 2009.

[9] F. Cai, L. Sun, S. Gao, Y. Yang, Q. Yang, and W. Chen, "A rapid and sensitive liquid chromatography-tandem mass spectrometric method for the determination of timosaponin B-II in blood plasma and a study of the pharmacokinetics of saponin in the rat," *Journal of Pharmaceutical and Biomedical Analysis*, vol. 48, no. 5, pp. 1411–1416, 2008.

[10] Z. Liu, X. Dong, X. Ding et al., "Comparative pharmacokinetics of timosaponin B-II and timosaponin A-III after oral administration of Zhimu-Baihe herb-pair, Zhimu extract, free timosaponin B-II and free timosaponin A-III to rats," *Journal of Chromatography B*, vol. 926, pp. 28–35, 2013.

[11] F. W. King, S. Fong, C. Griffin et al., "Timosaponin AIII is preferentially cytotoxic to tumor cells through inhibition of mTOR and induction of ER stress," *PLoS ONE*, vol. 4, no. 9, Article ID e7283, 2009.

[12] A. Rogina, "Electrospinning process: versatile preparation method for biodegradable and natural polymers and biocomposite systems applied in tissue engineering and drug delivery," *Applied Surface Science*, vol. 296, pp. 221–230, 2014.

[13] T. J. Sill and H. A. von Recum, "Electrospinning: applications in drug delivery and tissue engineering," *Biomaterials*, vol. 29, no. 13, pp. 1989–2006, 2008.

[14] X. Luo, G. Xu, H. Song et al., "Promoted antitumor activities of acid-labile electrospun fibers loaded with hydroxycamptothecin via intratumoral implantation," *European Journal of Pharmaceutics and Biopharmaceutics*, vol. 82, no. 3, pp. 545–553, 2012.

[15] B. D. Weinberg, E. Blanco, and J. Gao, "Polymer implants for intratumoral drug delivery and cancer therapy," *Journal of Pharmaceutical Sciences*, vol. 97, no. 5, pp. 1681–1702, 2008.

[16] P. Chen, Q.-S. Wu, Y.-P. Ding, M. Chu, Z.-M. Huang, and W. Hu, "A controlled release system of titanocene dichloride by electrospun fiber and its antitumor activity in vitro," *European Journal of Pharmaceutics and Biopharmaceutics*, vol. 76, no. 3, pp. 413–420, 2010.

[17] S. Huang, X. Kang, Z. Cheng, P. Ma, Y. Jia, and J. Lin, "Electrospinning preparation and drug delivery properties of Eu^{3+}/Tb^{3+} doped mesoporous bioactive glass nanofibers," *Journal of Colloid and Interface Science*, vol. 387, pp. 285–291, 2012.

[18] Y.-H. Liao, C.-C. Lin, T.-C. Li, and J.-G. Lin, "Utilization pattern of traditional Chinese medicine for liver cancer patients in Taiwan," *BMC Complementary and Alternative Medicine*, vol. 12, article 146, 2012.

[19] A. Jemal, R. Siegel, E. Ward et al., "Cancer statistics, 2006," *CA: A Cancer Journal for Clinicians*, vol. 56, no. 2, pp. 106–130, 2006.

[20] B. H. Yang, J. L. Xia, L. W. Huang et al., "Changes of clinical aspect of PLC in China during the past 30 yearsdcontrol study for 3, 250 cases with PLC," *National Medical Journal of China*, vol. 83, pp. 1053–1057, 2003.

[21] P. Wang, Z. Q. Meng, Z. Chen et al., "Diagnostic value and complications of fine needle aspiration for primary liver cancer

and its influence on the treatment outcome-a study based on 3011 patients in China," *European Journal of Surgical Oncology*, vol. 34, no. 5, pp. 541–546, 2008.

[22] M. A. Canosa, S. P. Fernández, J. Q. Fandiño et al., "Surgical treatment of liver cancer: experience of the A Coruña UHC (Spain)," *Cirugía Española*, vol. 89, no. 4, pp. 223–229, 2011.

[23] B. Aussilhou, Y. Panis, A. Alves, C. Nicco, and D. Klatzmann, "Tumor recurrence after partial hepatectomy for liver metastases in rats: prevention by in vivo injection of irradiated cancer cells expressing GMCSF and IL-12," *Journal of Surgical Research*, vol. 149, no. 2, pp. 184–191, 2008.

Hindawi Publishing Corporation
Journal of Nanomaterials
Volume 2015, Article ID 616879, 6 pages
http://dx.doi.org/10.1155/2015/616879

Research Article

Horseradish Peroxidase-Carrying Electrospun Nonwoven Fabrics for the Treatment of o-Methoxyphenol

Chao Pan,[1] Ran Ding,[1] Li Dong,[2] Jing Wang,[1] and Yucai Hu[1]

[1]*College of Science, Dalian Ocean University, Dalian, Liaoning 116023, China*
[2]*College of Science, Dalian Nationalities University, Dalian 116600, China*

Correspondence should be addressed to Li Dong; dongli@dlnu.edu.cn

Received 3 July 2014; Revised 7 September 2014; Accepted 21 September 2014

Academic Editor: Yuqin Wan

The carboxyl-functionalized polystyrene (poly(styrene-co-methacrylic acid), PSMAA) nanofibers with average diameters of 250 ± 20 nm was prepared by electrospinning. PSMAA nanofibrous membrane were employed for immobilization of horseradish peroxidase (HRP) enzyme on the fibrous surface by a chemical method. The parameters about immobilizing HRP on the PSMAA nanofibers were studied and the influence on the activity of the HRP is discussed. This study showed that soap-free emulsion method is an ideal technology to modify the polystyrene surface and ultimately achieve enzyme immobilization on electrospun PSMAA nanofibers surfaces. Compared with free HRP, the acid-base stability, thermal stability, and storage stability of HRP were increased after the immobilization. The immobilized HRP maintained about 60% of its initial activity during a 20-day storage period. However, the free HRP maintained only 40% of its initial activity. The removal percentages of o-methoxyphenol (OMP) reached 80.2% after 120 min for immobilized HRP. These results suggest that the proposed scheme for immobilization of HRP has potential in industrial applications for the treatment of phenolic wastewater.

1. Introduction

Horseradish peroxidase (HRP) has been shown to be able to remove a variety of phenols and aromatic amines from aqueous solutions [1–3]. However, the main drawback of treating wastewater by free HRP is its instability. To overcome this shortcoming, immobilization of HRP has been developed as an effective method for the applications of HRP, since it offered many advantages, such as increasing the stability of HRP and being repeatedly used easily [4, 5].

Electrospinning, being a simple and economical way to immobilize enzymes *in situ*, has received more and more attention in the last decade [6–10]. The appealing prospects of using electrospun fibrous membranes (EFMs) for enzyme immobilization include their tunable sizes (from micro to nanometer diameters), controllable morphology, high surface-to-volume ratio, and compositional variance. Thus, EFMs are regarded as a suitable support for the immobilization of enzymes. Recently, an application of immobilized HRP by electrospinning for removal of environmental pollutants from contaminated water has been reported. For example, Niu and coworkers [4] fabricated a HRP-immobilized poly(d,l-lactide-co-glycolide) (PLGA) fibers membrane for degradation of pentachlorophenol (PCP), obtaining removal efficiency of 83%.

In preparations for enzyme membranes, it is difficult to get bulk active groups on the membrane surface. The traditional plasma surface physics modification [11, 12] is complex and fussy and it has only a low effect on increasing immobilization of enzymes. The chemical modification of electrospun fibers has been shown to be an effective immobilization method compared with the physics modification. For instance, there has been reported in immobilization procedures using chemical modification, which allows condensation reaction between the carboxyl groups on electrospun fibers and the side chain amino groups of enzyme molecules, leading to covalent bond formations between the fibrous surfaces and enzyme molecules [13]. The chemical binding for enzyme immobilization can be applied for the enzymes which do not adsorb onto the cationic matrix, and thus the matrix is used for immobilizing a wider range of enzyme species.

In this paper, poly(styrene-*co*-methacrylic acid) (PSMAA) random copolymer nanofibers, having carboxyl

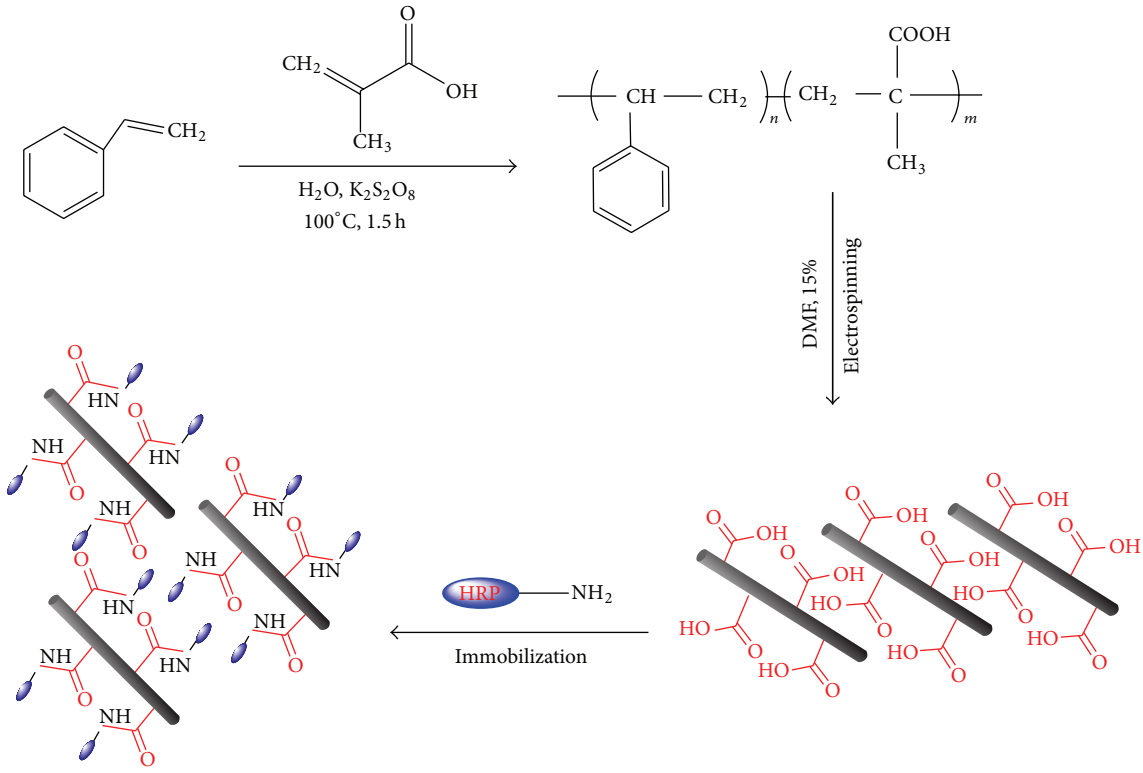

Scheme 1: Chemical route for synthesis of styrene-co-methacrylic acid copolymer and subsequent electrospinning nanofibers attachment of HRP.

groups on the MAA, were prepared by a combination of the soap-free emulsion polymerization method and an electrospinning technique (Scheme 1), which were employed as solid support to HRP enzyme, and immobilized HRP was used to remove OMP from water. The morphology, chemical structure of the PSMAA nanofibers, and the enzymatic properties of the immobilized HRP were investigated. The degradation efficiency of OMP by immobilized HRP was assessed.

2. Experimental

2.1. Materials. The materials were used without further purification. N,N-Dimethylformamide (DMF) and o-methoxyphenol were purchased from the Shanghai Chemical Co. (China). The ingredients of phosphate buffer solution (PBS), such as orthophosphoric acid, dibasic sodium phosphate, and potassium phosphate monobasic, were of analytical grade and used as received. Horseradish peroxidase (HRP), Coomassie Brilliant Blue (G250), bovine serum albumin (BSA, molecular mass: 67,000 Da), phenol, 4-aminoantipyrine, and pyrocatechol (1,2-dihydroxybenzene) were purchased from Sigma-Aldrich co., China. The water used in all experiments was prepared in a three-stage Millipore Milli-Q Plus 185 purification system (Richmond Scientific Ltd. Great Britain) and had a resistivity higher than 18.2 MΩ/cm.

The styrene (Sty) and methacrylic acid (MAA) monomers were purchased from the Lingfeng Chemical Co. (China). These chemicals were distilled under vacuum at 75°C before use.

2.2. Synthesis of Poly(styrene-co-methacrylic Acid). A typical synthesis was as follows: first, both Sty and MAA were distilled under vacuum at 75°C. 25 mL Sty and 1.0 mL MAA were then mixed, and the mixture and 100 mL water were added into a three-mouth flask with condenser and mechanical stirrer. The mixture was stirred at a speed of 300 rpm and heated under a heater cover. After 5 min of boiling, 0.1 g potassium persulfate powder (Sinopharm Chemical Reagent Co., Ltd, China) as initiator was added from the side mouth and the polymerization continued for 1.5 hours. The whole reaction was completed within 1.5 hours, with a conversion in excess of 90% (measured by the method of [14]). The resulting latex was cooled to ambient temperature and filtered through cheesecloth. The coagulum was dried and weighed.

2.3. Fabrication of PSMAA Nanofibers. A 15 wt.% PSMAA solution was prepared by adding 1.5 g PSMAA powder to 8.5 mL DMF at room temperature with magnetic stirring until it finally became a viscous precursor solution. The solution was quickly loaded into a 5 mL syringe equipped with a steel needle with a tip diameter of 0.5 mm, whose tip was filed flat, which was connected to a high-voltage supply

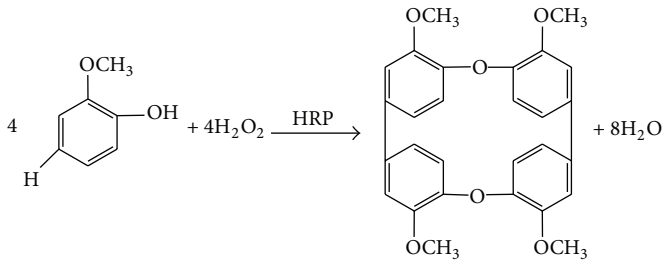

Scheme 2

capable of generating voltage up to 30 kV. A copper wire-framed drum collection screen was placed at a horizontal distance of 15 cm from the tip of the needle. The copper wire drum was connected to a motor with two pulleys and rotated at a speed of 300 rpm. The feeding rate of the precursor solution was controlled at 1 mL/h using an automatic syringe pump so that a small drop was maintained at the capillary tip due to the surface tension of the solution. The solution on the tip of the needle was ejected under a strong electric field of the 20 KV, and the PSMAA fibers thus formed were dried initially for 5 h at 70°C under vacuum.

2.4. Immobilization of HRP. An appropriate amount of electrospun PSMAA nanofibrous membranes were immersed in 50 mL of BSA solution (1% wt) for about 1.5 h at 20°C in shakers while stirring continuously and then thoroughly washed with deionized water to remove the residue BSA. Subsequently, the pretreated membranes were submerged into 20 mL of the HRP solution (1 mg/mL in the PBS, pH 7.0) in a 25 mL beaker and shaken gently in an ice bath for the required time. Finally, the membranes were taken out and washed with the PBS until no protein was detected in the washings.

2.5. Determination of Immobilization Capacity. The concentration of HRP in the solutions was determined by the method of Bradford [15] based on the absorbance of Coumassie Brilliant Blue reagent at 595 nm by UV-Visible spectroscopy (U-4100, Hitachi Co., Ltd, Japan). The amount of the bound enzyme was calculated as

$$Q = \frac{(C_0 - C)V}{m}, \quad (1)$$

where Q is the amount of HRP bound onto unit mass of nanofibrous membranes (mg/g), C_0 and C are the initial and equilibrium HRP concentrations in the solution (mg/mL), V is the volume of the HRP solution, and m is the mass of the nanofibrous membrane.

2.6. Characterization. The PSMAA nanofibers morphology was examined using (S-3000N, Hitachi, Co., Ltd, Japan) scanning electron microscope (SEM). All samples were sputter coated with gold. Fourier transform infrared (FTIR) spectra (BRUKER IFS66/S Perkin-Elmer) were recorded using pressed KBr pellets over the wavenumber range of 4000–500 cm^{-1} at a resolution of 4 cm^{-1} to determine the PS and PSMAA.

2.7. Activity Measurements of HRP. The Worthington protocol was followed to calculate the activity of the HRP enzymes [15]. In this method, hydrogen peroxide (H_2O_2), 4-aminoantipyrene (4-AAP), and phenol were first mixed to form a colorless reagent and the HRP enzyme was immersed in the colorless reagent to catalyze the conversion of H_2O_2 to water, along with the conversion of the colorless dye to a red color (quinoneimine). The rate of color change was recorded by using UV-vis absorbance spectroscopy at 510 nm, and the increase of absorbance was translated into enzyme activity through the specific absorptivity of the chromogen ($\varepsilon = 7100\ M^{-1}\,cm^{-1}$) [16]. The substrates used were 2.46×10^{-3} mol/L 4-AAP with 0.172 mol/L phenol and 1.76×10^{-3} mol/L H_2O_2. All measurements were in a PBS with a pH of 7.0. Each experiment was repeated three times.

2.8. Degradation Experiments. HRP-PSMAA (1 cm × 1 cm, total weight 20 ± 1 mg) membrane pieces were added one each to 10 mL solutions with the concentration of OMP at 8.06×10^{-4} mol/L; the molar ratio of the reaction between OMP and H_2O_2 was about 1 : 1. The reaction scheme was suggested as shown in Scheme 2 [17, 18].

The mixture was incubated at 25 ± 1°C and pH 6.0 under reciprocal agitation at 30 rounds per minute. For the purpose of terminating the HRP catalysis, 0.1 mL of 0.658 mol/L H_3PO_4 was added when sampling. The control experiment for free HRP was carried out in the same reactor using an equivalent amount of HRP. The OMP concentrations in the aqueous phase and on/in the HRP-PSMAA (washed by acetonitrile) were measured by a UV-vis spectrophotometer (U-4100, Hitachi Co., Ltd, Japan) at 470 nm. The amount of OMP degraded by HRP was calculated by

$$P\% = \frac{Q_0 - Q_S}{Q_0} \times 100\%, \quad (2)$$

where Q_0 is the initial amount of OMP in solution and Q_S is the amount of OMP retained in solution. All experiments were carried out at 25 ± 1°C.

3. Results and Discussion

3.1. FTIR Spectra of Copolymer. FTIR spectra of (a) the PS and (b) the PSMAA are shown in Figure 1; comparing these

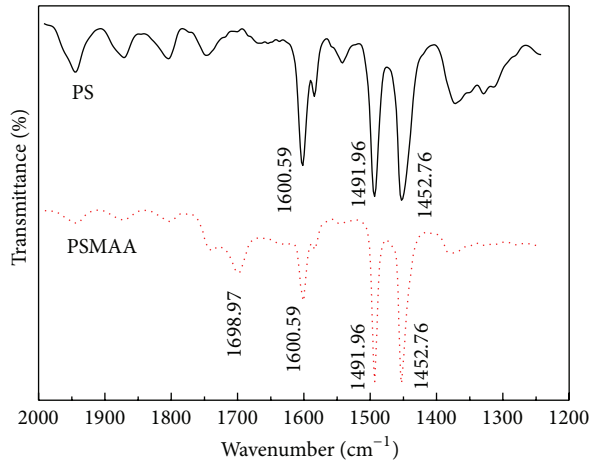

Figure 1: FT-IR spectrum of PS and PSMAA.

two spectra, the spectrum of the PSMAA membrane showed an absorbance band at 1698.97 cm^{-1}, which is a characteristic band for carboxyl groups. It indicates that COOH groups of methacrylic acid have been blocked to styrene successfully.

3.2. The Surface Morphologies of the Nanofibrous Membrane. A SEM image of the original PSMAA nanofibers is displayed in Figure 2(a). The morphology of the nanofiber appears uniform, with the diameter of the nanofibers ranging from 230 to 270 nm. After HRP immobilization, as shown in Figure 2(b), the diameter and the morphology of the nanofibers did not change substantially, although some of adhesion between the fibers compared with that un-immobilized. It might be because the –COOH groups of the PSMAA nanofibrous membranes reacted with amine groups of HRP protein, the bound protein then acted as a seed, and other unbound HRP molecules were adsorbed on the bound protein to form protein aggregation by molecular interactions.

3.3. Effect of Immobilization Time on Enzyme Capacity and Activity of HRP Immobilized on the PSMAA Nanofibers. To determine the optimum adsorption time, the effect of adsorption time on the immobilized amount of protein was studied. As shown in Figure 3, adsorption equilibrium was reached when the experiment running for 4 h and the activity of the immobilized HRP increased with prolonged coupling time, and the highest activity was obtained when immobilization was allowed to proceed for 4 h. However, the activity decreased if the reaction time was longer; this might be because the long time coupling reaction to change unfolding degree of the enzyme molecule, resulting in a enzyme conformation is destroyed, causing inactivation of the enzyme. Therefore, to ensure the maximum adsorption of HRP onto the membranes, the adsorption time was adopted as 4 h in the following experiments.

3.4. Effect of Temperature on the Activity of HRP. The effect of temperature on the activity of free and immobilized HRP at pH 7.0 is shown in Figure 4, the maximum activity of the free HRP appeared at 35°C, but the optimum temperature of the immobilized HRP was slightly higher at 40°C. At temperatures above 35°C, as the temperature increased, the residual activity of the free HRP decreased faster than that of the immobilized HRP; that is, the immobilized HRP exhibited higher heat resistance than the free one. This is suggested to be due to interactions between enzyme and the PSMAA-COOH supports that limited the enzyme movement to reduce the degree of freedom of the spatial structure of enzyme, protecting it from deactivation at high temperatures.

3.5. Storage Stability. The storage stability of immobilized and free enzyme is presented in Figure 5 and the residual activity of immobilized and free HRP was 87.4% and 45.4% after 5 days, respectively. The results indicated that the storage stability of immobilized HRP was better than that of free HRP, which is suggested to be due to the immobilization of the enzyme limiting the freedom of conformational changes, resulting in increasing stability towards denaturalization [19].

3.6. Effect of pH on the Activity of HRP. Figure 6 shows the effect of pH on the activity of the free and immobilized HRP. The optimal pH value was about 6.0 for both free and immobilized enzyme; no significant shift of the optimal pH was observed. But the residual relative activity of the immobilized HRP was higher than that of the free one at all other pH in the range between 2.0 and 9.0. The lower sensitivity of the immobilized enzyme to pH is probably because of a significant alteration of the enzyme microenvironment upon immobilization on the fibers.

3.7. o-Methoxyphenol (OMP) Removal by Free and Immobilized HRP. Figure 7 shows the efficiency of removal of OMP in a batch experiment running for 120 min. The removal process by PSMAA-HRP was fast and reached a removal percentage of about 80.2%. The removal efficiency of PSMAA-HRP was higher than free HRP. This is suggested to be due to the fact that the OMP removal by immobilized enzyme was the result of both PSMAA nanofibers adsorption and enzymatic catalyzation; the OMP molecules diffuse from the bulk solution to the external surfaces of the PMAA nanofibers and adsorb onto the easily accessible hydrophobic sites on the surface. In addition a great amount of OMP was degraded by the HRP which is immobilized on the surface of fibers, and this step is usually assumed to be a fast one.

4. Conclusion

PSMAA nanofibrous membranes with uniform fiber diameters between 230 and 270 nm were prepared by an electrospinning method. HRP enzyme was successfully immobilized on the MAA carboxyl groups of the PSMAA nanofibers. The results of degradation experiments indicated that a removal efficiency of 80.2% was achieved. Immobilized HRP showed a better acid-base stability, thermal stability, and storage stability than free HRP, which is a very attractive aspect for real applications involving a sufficiently wide range of external conditions.

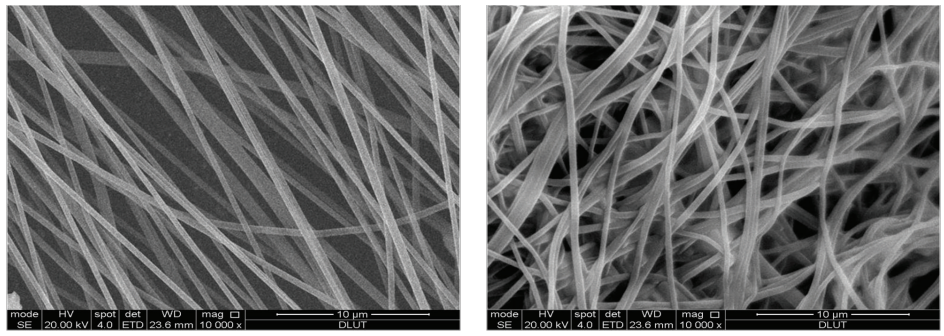

(a) (b)

Figure 2: Morphologies of PSMAA nanofiber. (a) Original PSMAA nanofibers. (b) PSMAA nanofibers with immobilization of HRP.

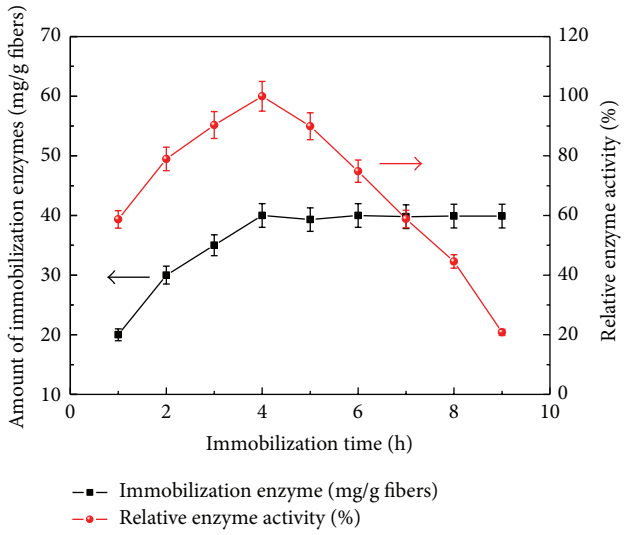

Figure 3: Effect of immobilization time on enzyme loading capacity at pH 7.0 and room temperature.

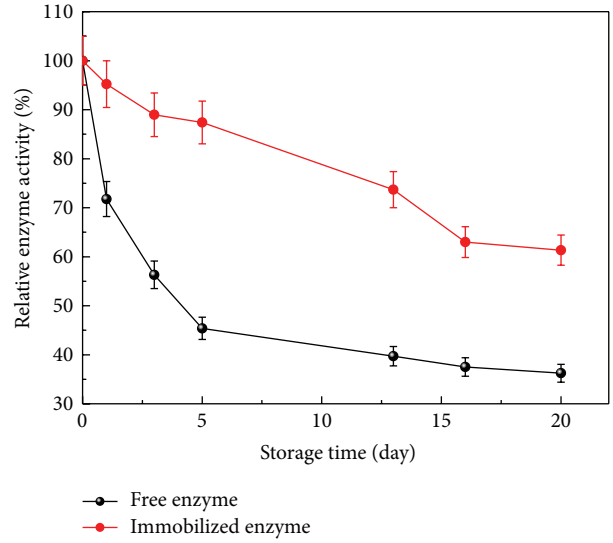

Figure 5: Storage stability of free and immobilized HRP.

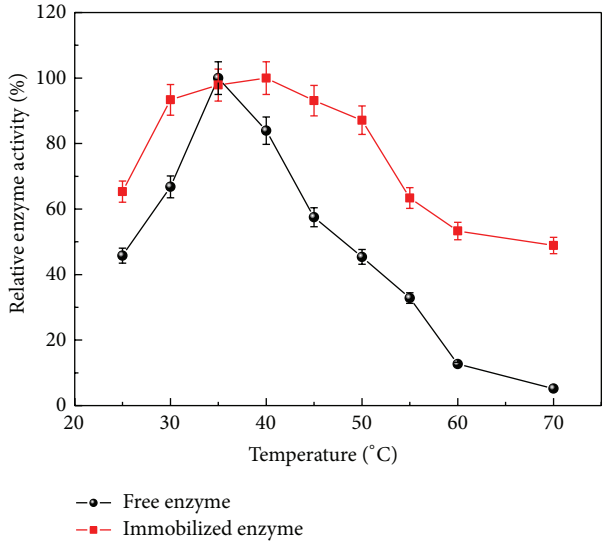

Figure 4: Effect of temperature on the activity of free and immobilized HRP.

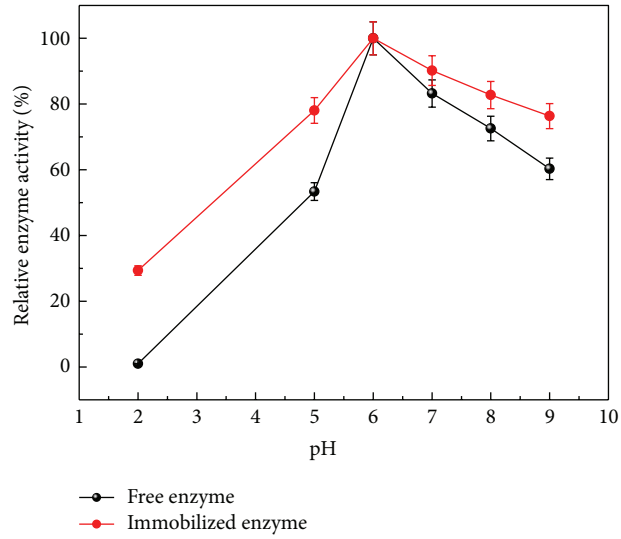

Figure 6: Effect of pH on the activity of HRP.

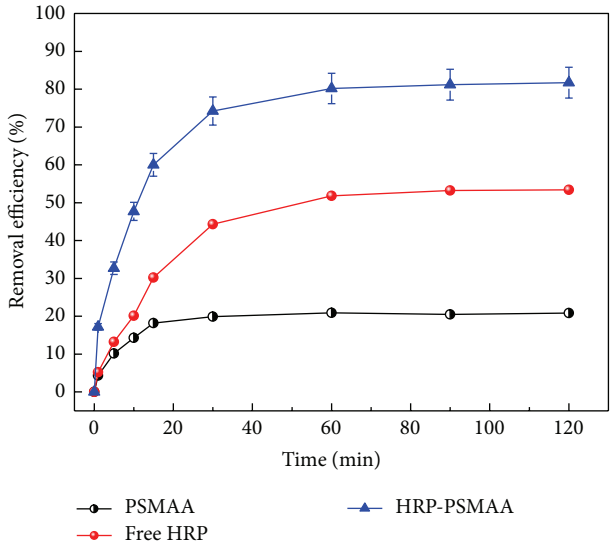

Figure 7: Degradation kinetics of OMP by PSMAA, free HRP, and HRP-PSMAA.

Conflict of Interests

The authors declare that there is no conflict of interests regarding the publication of this paper.

Acknowledgments

The authors acknowledge the financial support of the National Natural Science Foundation (no. 21102033), the Open Research Fund of MOIDAT (no. 201205), the Open Research Fund of State Key Laboratory of Fine Chemicals (no. KF1012), the Open Project Program of Key Laboratory of Ecotextiles, Ministry of Education, Jiangnan University (no. KLET1205), and the Scientific Research Fund of Liaoning Provincial Education Department (no. L2011122).

References

[1] A. M. Klibanov, T. M. Tu, and K. P. Scott, "Peroxidase-catalyzed removal of phenols from coal-conversion waste waters," *Science*, vol. 221, no. 4607, pp. 259–261, 1983.

[2] K. Tatsumi, S. Wada, and H. lchikawa, "Removal of chlorophenols from wastewater by immobilized horseradish peroxidase," *Biotechnology and Bioengineering*, vol. 51, no. 1, pp. 126–130, 1996.

[3] J. Cheng, S. Ming Yu, and P. Zuo, "Horseradish peroxidase immobilized on aluminum-pillared interlayered clay for the catalytic oxidation of phenolic wastewater," *Water Research*, vol. 40, no. 2, pp. 283–290, 2006.

[4] J. Niu, J. Xu, Y. Dai et al., "Immobilization of horseradish peroxidase by electrospun fibrous membranes for adsorption and degradation of pentachlorophenol in water," *Journal of Hazardous Materials*, vol. 246-247, pp. 119–125, 2013.

[5] J. Zhang, P. Ye, S. Chen, and W. Wang, "Removal of pentachlorophenol by immobilized horseradish peroxidase," *International Biodeterioration and Biodegradation*, vol. 59, no. 4, pp. 307–314, 2007.

[6] D. Han, S. Filocamo, R. Kirby, and A. J. Steckl, "Deactivating chemical agents using enzyme-coated nanofibers formed by electrospinning," *ACS Applied Materials and Interfaces*, vol. 3, no. 12, pp. 4633–4639, 2011.

[7] K. Sun and Z. H. Li, "Preparations, properties and applications of chitosan based nanofibers fabricated by electrospinning," *Express Polymer Letters*, vol. 5, no. 4, pp. 342–361, 2011.

[8] D. N. Tran and K. J. Balkus Jr., "Enzyme immobilization via electrospinning," *Topics in Catalysis*, vol. 55, no. 16–18, pp. 1057–1069, 2012.

[9] N. Amini, S. Mazinani, S.-O. Ranaei-Siadat, M. Kalaee, K. Niknam, and V. Adlfar, "Manufacturing polymethyl methacrylate nanofibers as a support for enzyme immobilization," *Fibers and Polymers*, vol. 13, no. 8, pp. 994–998, 2012.

[10] P. Ye, Z.-K. Xu, J. Wu, C. Innocent, and P. Seta, "Nanofibrous poly(acrylonitrile-co-maleic acid) membranes functionalized with gelatin and chitosan for lipase immobilization," *Biomaterials*, vol. 27, no. 22, pp. 4169–4176, 2006.

[11] O. G. Mouritsen, T. L. Andresen, A. Halperin et al., "Activation of interfacial enzymes at membrane surfaces," *Journal of Physics Condensed Matter*, vol. 18, no. 28, Article ID S1293, 2006.

[12] A. Kondyurin, N. J. Nosworthy, M. M. M. Bilek, R. Jones, and P. J. Pigram, "Surface attachment of horseradish peroxidase to nylon modified by plasma-immersion ion implantation," *Journal of Applied Polymer Science*, vol. 120, no. 5, pp. 2891–2903, 2011.

[13] H. Jia, G. Zhu, B. Vugrinovich, W. Kataphinan, D. H. Reneker, and P. Wang, "Enzyme-carrying polymeric nanofibers prepared via electrospinning for use as unique biocatalysts," *Biotechnology Progress*, vol. 18, no. 5, pp. 1027–1032, 2002.

[14] J. W. Goodwin, J. Hearn, C. C. Ho, and R. H. Ottewill, "The preparation and characterisation of polymer latices formed in the absence of surface active agents," *Br Polym J*, vol. 5, no. 5, pp. 347–362, 1973.

[15] M. M. Bradford, "A rapid and sensitive method for the quantitation of microgram quantities of protein utilizing the principle of protein dye binding," *Analytical Biochemistry*, vol. 72, no. 1-2, pp. 248–254, 1976.

[16] I. D. Buchanan and J. A. Nicell, "Model development for horseradish peroxidase catalyzed removal of aqueous phenol," *Biotechnology and Bioengineering*, vol. 54, no. 3, pp. 251–261, 1997.

[17] J. L. Muñoz-Muñoz, F. García-Molina, P. A. García-Ruiz et al., "Enzymatic and chemical oxidation of trihydroxylated phenols," *Food Chemistry*, vol. 113, no. 2, pp. 435–444, 2009.

[18] F. Quintanilla-Guerrero, M. A. Duarte-Vázquez, B. E. García-Almendarez, R. Tinoco, R. Vazquez-Duhalt, and C. Regalado, "Polyethylene glycol improves phenol removal by immobilized turnip peroxidase," *Bioresource Technology*, vol. 99, no. 18, pp. 8605–8611, 2008.

[19] Q. Feng, B. Tang, Q. F. Wei, D. Y. Hou, S. M. Bi, and A. F. Wei, "Preparation of a Cu(II)-PVA/PA6 composite nanofibrous membrane for enzyme immobilization," *International Journal of Molecular Sciences*, vol. 13, no. 10, pp. 12734–12746, 2012.

Hindawi Publishing Corporation
Journal of Nanomaterials
Volume 2015, Article ID 418932, 8 pages
http://dx.doi.org/10.1155/2015/418932

Research Article

Experimental Investigation of the Properties of Electrospun Nanofibers for Potential Medical Application

Anhui Wang,[1] Chao Xu,[2] Chuanwei Zhang,[2] Yunna Gan,[3] and Bin Wang[4]

[1] *Department of Epidemiology, School of Public Health, The Fourth Military Medical University, No. 169, Changle West Road, Xi'an, Shaanxi 710032, China*
[2] *School of Mechanical Engineering, Xi'an University of Science and Technology, No. 58, Yanta Road, Xi'an, Shaanxi 710054, China*
[3] *Clinics of Stomatology, Naval Logistics Branch of Hangzhou Sanatorium, Nanjing Military Area Command, Yuhuangshang Road, No. 76, Hangzhou, China*
[4] *College of Engineering, Design and Physical Sciences, Brunel University, Uxbridge, UK*

Correspondence should be addressed to Yunna Gan; 457183253@qq.com and Bin Wang; bin.wang@brunel.ac.uk

Received 31 October 2014; Revised 8 January 2015; Accepted 23 January 2015

Academic Editor: Davood D. Ganji

Polymer based nanofibers using ethylene-co-vinyl alcohol (EVOH) were fabricated by electrospinning technology. The nanofibers were studied for potential use as dressing materials for skin wounds treatment. Properties closely related to the clinical requirements for wound dressing were investigated, including the fluid uptake ability (FUA), the water vapour transmission rate (WVTR), the bacteria control ability of nanofibers encapsulated with different antibacterial drugs, and Ag of various concentrations. Nanofibre degradation under different environmental conditions was also studied for the prospect of long term usage. The finding confirms the potential of EVOH nanofibers for wound dressing application, including the superior performance compared to cotton gauze and the strong germ killing capacity when Ag particles are present in the nanofibers.

1. Introduction

Skin wounds and their treatment are significant health problems [1–3]. The dressing material plays a key role in treatment and recovery, providing surface protection, tissue and cell restriction, moisture maintaining, air permeability, bacteriostatic controlling activities, drug delivery, and other functions [4, 5]. Electrospinning, also known as electrostatic spinning, is a popular method to fabricate nonwoven fibers with different shapes and sizes [6, 7]. It is currently the only method to prepare fabric of fibers with diameters down to a few nanometers [8]. Fibrous materials of submicron dimensions are potentially better candidates in skin wound treatment than normal dressing materials such as cotton pads and bandages due to a number of advantageous features, including high porosity ratio, high permeability and mechanical strength, and biocompatibility and biodegradability, among others [9–12]. A number of methods have also been developed to add drugs into the electrospinning process so the nanofibers obtained become carriers [13] for the additional function of anti-inflammation [14]. EVOH was selected for this study due to its good biocompatibility and proven usage in nanofibers preparation with electrospinning [15–17].

In a previous study [18], we presented a method to fabricate poly (ethylene-co-vinyl alcohol) (EVOH) nanofibers encapsulated with Ag nanoparticle using electrospinning technique. The fibers were fabricated with controlled diameters (59 nm-3 μm) by regulating three main parameters, that is, EVOH solution concentration, the electric voltage, and the distance between the injection needle tip (high voltage point) and the fiber collector. The study showed the relationship between the electrospinning fabrication parameters and the properties of the fibers produced, such as the diameter of the nanofibers, the regularity of the nanofiber shape, the uniformity of the diameter, and the average length of the uniform fiber. The mechanical strengths of nanofiber mats under monotonic and cyclic tension loading were also discussed [19].

Table 1: Materials.

Materials	Provenience	Dosage in the experiments
Poly (ethylene-co-vinyl alcohol) (EVOH)	Sigma-Aldrich (Batch number: 12822PE)	7.5% (0.75 g EVOH dissolved in 10 mL 80% 2-propanol/water)
$AgNO_3$	Alfa Aesar (Alfa Aesar, 7761-88-8)	0.1 g $AgNO_3$ in 10 mL EVOH solution
Iodine	Tianli (Tianli, AR/250 g)	0.1 g in 10 mL EVOH solution
Gentamicin	Xi'an 1st Hospital	60 k units in 10 mL EVOH solution

In this study, we investigated the nanofibers' properties closely related to the clinical requirements for wound dressing. The fluid uptake ability, the water vapour transmission rates, the bacteria control ability of nanofibers encapsulated with different antibacterial drugs and Ag of various concentrations, and the degradation of EVOH nanofibers under different environmental conditions were investigated. The study was entirely experiment based and is reported in the following order in this paper. First, the materials used were discussed, followed by a brief introduction on the electrospinning process. The tests and results of fluid up taking, water vapour transmission, and bacteria control were then reported, followed by degradation results. Discussion on the findings and conclusions were then provided in view of the potential medical application.

2. Material and Electrospinning Process

2.1. Materials. Poly (ethylene-co-vinyl alcohol) (EVOH) was used to make nanofibers in this study. The material was ordered in granular form from Sigma-Aldrich (Batch number: 12822PE). Solid granules were diluted into solutions of 80% 2-propanol/water, in composition of EVOH from 7.5, 10, and 12% (wt%) for injection use.

For the antibiotics used in the study, $AgNO_3$ was obtained in powder form from Alfa Aesar (Alfa Aesar, 7761-88-8). Iodine was purchased from Tianli (Tianli, AR/250 g) in powder form. And gentamicin of a clinical grade was obtained from Xi'an 1st Hospital in the specification of 60000 units/mL. Dosages of the antibiotics used in the experiments are listed in Table 1 together with the carrier material EVOH. *Staphylococcus aureus*, one of the main pathogenic bacteria found on both animal and human wound surfaces [20, 21], was chosen to test the antibacterial ability of the nanofibers.

2.2. Experimental Procedure for Electrospinning of Nanofibers. The electrospinning system (Figure 1) used for electrospinning is an improved in-house platform developed in the previous study [18, 22]. The system is composed of a high voltage power supply with a low current output (Spellman CZE1000R, 0–30 kV, maximum 0.1 mA), a peristaltic pump with a feeding capacity in the range of 1.0 to 15.0 mL h^{-1} (Masterflex, 77120-52), and a feeding tube fixed with a fine metal needle at the end. All nanofiber samples were prepared from the solution of 7.5% (w/v) EVOH. Three bacterial control agents, $AgNO_3$, iodine, and gentamicin, were added to EVOH solution, respectively. The solutions were then injected at the speed of 2.5 mL h^{-1} in a space field charged

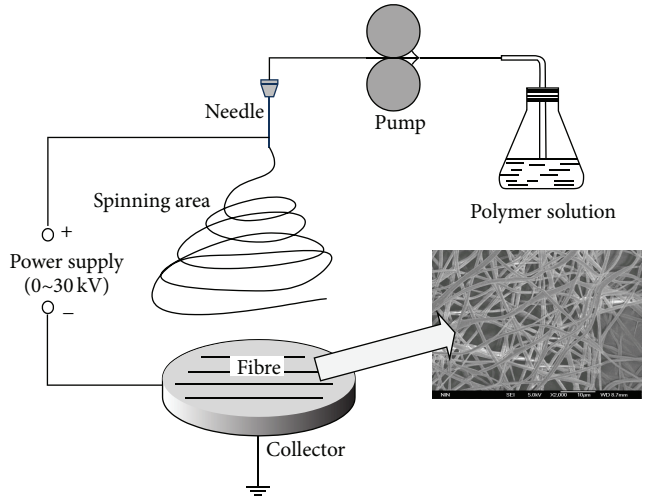

Figure 1: The electrospinning system.

to 25 kV to obtain the nanofibers through the spinning of the jet. Table 1 lists the fabrication parameters of the three fiber groups used in this study.

Fibers obtained in this study were in the diameter range from 400 nanometers to 2.2 micron meters. Scanning electron microscopy (SEM) was performed to characterize the dimension profile of the fibers obtained. Figure 2(a) shows SEM image of the nanofibers obtained. Fibers are smooth and randomly oriented, with an average diameter of 500 nm. Figure 2(b) is a transmission electron microscopy (TEM) image showing a local section of a fiber obtained from EVOH solution containing $AgNO_3$. Shaded dots distributed inside the nanofibers are simple Ag particles according to an EDX analysis [18].

3. Properties Related to Clinical Requirements

In this study, a few important features of the nanofibers were considered for the potential application as a wound dressing material, such as the fluid uptake ability (FUA) and the water vapour transmission rates (WVTRs), which are important characteristics in skin wound treatment. Such properties are also significant in tissue engineering where the nanofibers may also be used as scaffolding for cell growth and controlled drug release.

For wound addressing, the bacteria control ability is another key parameter, and new functionality can be developed for optimized application of antibacterial agents [23–25]. Here, only a preliminary study was carried out using

Table 2: Sample descriptions of EVOH nanofibers.

Sample group	Fabrication parameters	Fibre diameter range
A	7.5% solution, 15 kV, 2.5 mL/hr, 20 cm standing distance	0.4–0.9 μm
B	10% solution, 15 kV, 2.5 mL/hr, 20 cm standing distance	0.8–1.5 μm
C	12% solution, 15 kV, 2.5 mL/hr, 20 cm standing distance	1.3–2.2 μm

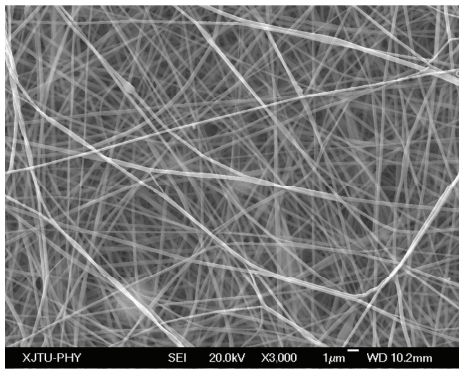

(a)

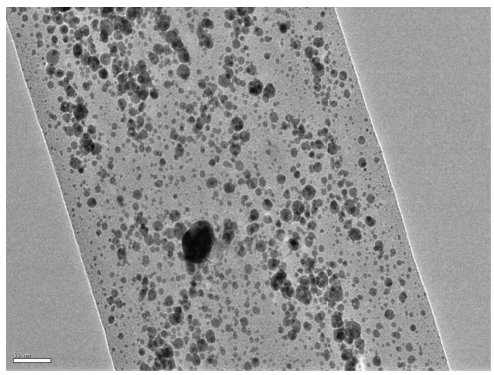

(b)

Figure 2: SEM image and TEM image of nanofibers contain Ag: (a) SEM image, (b) TEM image.

the bacteriostatic loops to demonstrate the possibility of bacteria control.

The degradation of nanofibers under environmental conditions was also considered. Degradation tests in phosphate buffer solution and under ultraviolet light were carried out, providing an indication on the integrity of nanofiber materials in simulated human body conditions and accelerated environment exposures.

3.1. Fluid Uptake Ability (FUA). The fluid uptake ability (FUA) (%) of the nanofibers was calculated as a percentage of water loss per unit weight:

$$\text{FUA (\%)} = \frac{(W_s - W_d) \times 100\%}{W_s}, \quad (1)$$

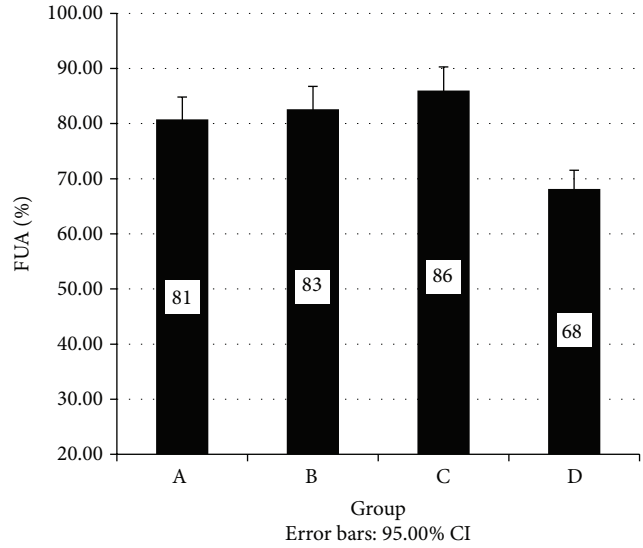

Figure 3: The fluid uptake ability of different nanofibers (A, B, and C) and cotton gauze (D).

where W_s is the wet weight of the nanofiber and W_d is the dry weight of the nanofiber.

A piece of dry nanofiber mat (in room condition) was first measured for its weight. It was then fully submerged into distilled water for 15 seconds. The wet mat piece was picked up and put on a fresh absorbing paper for 30 seconds, and its weight was then measured again.

The FUA experimental data of the sample Groups A, B, and C (categorized in Table 2) are given in Figure 3 compared with those of normal medical cotton gauzes, denoted as Group D (diameters of the cotton fibers are between 0.1 and 0.2 mm). The result shows that all nanofiber groups have a higher FUA (%) than that of cotton gauze. On average, nanofibers can take 22% more water than cotton gauze per unit weight.

Among the nanofiber groups, Group C has the highest FUA at (85.97 ± 0.7) %, while Group A has the lowest (81.66 ± 0.8)%, though the difference is only 5%. Figure 3 appears to suggest that in the diameter range smaller than the micron level, a lager diameter will lead to a higher FUA. But when the fiber diameter is above the micron level, such as in cotton gauze, FUA will drop with increased diameter.

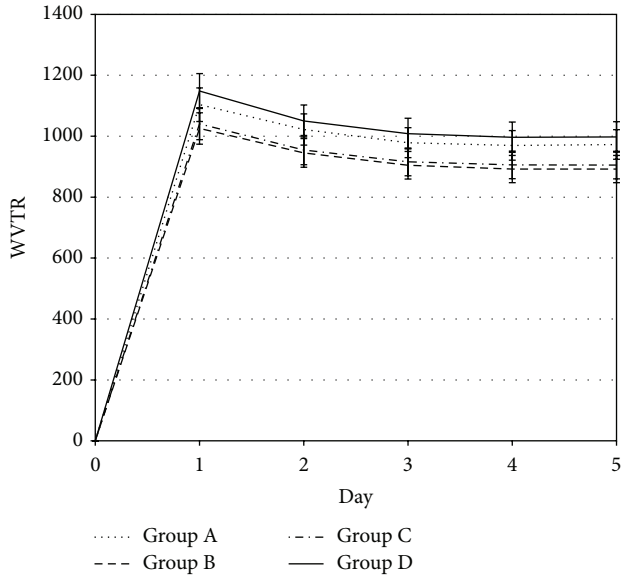

Figure 4: Changes of WVTR of nanofiber groups in terms of time.

3.2. Water Vapour Transmission Rates (WVTRs). The water vapour transmission performance of the nanofibers was measured in the following approach. Beakers filled with 5 mL distilled water were covered with a nanofiber mat of the three sample groups, respectively. The covered beakers were placed in an airtight environment chamber with saturated ammonium sulfate solution. The weight of the beakers was measured once every 24 hours over a period of 120 hours (5 days). The difference of the measured weight was divided by the cross-section area of the beaker. The water vapour transmission rates, WVTRs ($g{\cdot}m^{-2}$ per day), were calculated as the weight loss of water (gram) per evaporation exposure area (m^2) per day [26].

Measured WVTR of the nanofibers s is given in Figure 4, showing that WVTR increases rapidly in Day 1. The 24-hour measurement span means that there is only one data point at the end of Day 1; thus, higher points which could occur within Day 1 may have been missed. However, the tread is captured. WVTR drops slightly from Day 1 and remains virtually constant from Day 2 onwards with the values kept in the range of 900 to 1000 $g{\cdot}m^{-2}$ per day. There is virtually no difference between Groups A, B, and C. Group A has a slightly higher WVTR, close to that of Group D, which shows the highest WVTR constantly, though marginally.

3.3. Antibacterial Tests. To evaluate the clinical related performance of the nanofibers, antibacterial tests were carried out using culture dishes. Clear dishes were first covered with LB culture mixed with *Staphylococcus aureus* (OD600 value: 1.1). One circular pad of 6 mm diameter, cut from each of the nanofiber samples containing Ag, iodine, and gentamicin, respectively, and from pure EVOH nanofibers with no antibacterial agent as the control group, was placed at equal distance in a culture dish. The quantity of the antibiotic agents contained in the nanofibers is, before electrospinning, as follows:

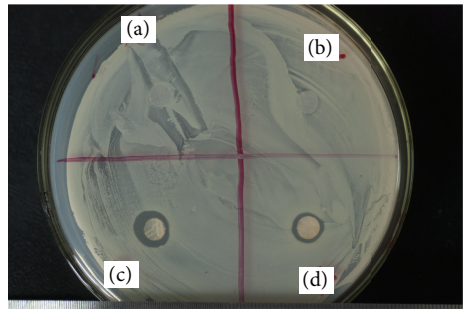

Figure 5: Bacteria test after 6 hours of incubation at 37°C: (a) pure EVOH nanofiber and the rest are nanofibers containing (b) gentamicin (60 k units in 10 mL solution), (c) Ag nanoparticle (0.1 g in 10 mL solution), and (d) iodine (0.1 g in 10 mL solution).

gentamicin, 60 k units in 10 mL solution;

Ag nanoparticle, 0.1 g $AgNO_3$ in 10 mL solution, and iodine, 0.1 g in 10 mL solution.

The culture dishes hosting the nanofiber pads were then placed on a disk in a nursery box which was maintained at 37°C. The disk was rotated continually inside the nursery box at a constant rotational speed of frequency of 1 Hz.

Figure 5 illustrates one of the culture dishes after 6 hours of incubation at 37°C, showing the four pads of samples with pure EVOH fibres containing no antibacterial agent marked as (a), and fibres containing gentamicin (b), Ag nanoparticle (c), and iodine (d). While the disk is covered by cultured *Staphylococcus aureus* seen in a foggy colour, the clear shaded rings surrounding the pads (red circles indicate the original pad size) are bacteriostatic loops where *Staphylococcus aureus* had been eliminated. A bigger outer ring diameter indicates stronger antibacterial effectiveness. It can be clearly seen in Figure 5 that Ag (c) has the biggest bacteriostatic loop while pure EVOH (a) and gentamicin (b) show limited effectiveness.

Figure 6(a) shows the measured outer diameters of the bacteriostatic loops. Nanofibers containing Ag nanoparticles demonstrate the strongest germ killing capacity and the outer diameter of its bacteriostatic loop is 58, 174, and 420%, which is bigger than the one of iodine, gentamicin, and pure EVOH, respectively. Consequently, only the influence of the Ag density was further examined. Nanofibers using solutions dissolved with different weight of $AgNO_3$ were produced and used for antibacterial tests. Figure 6(b) illustrates the outer diameter of the bacteriostatic ring as a function of the weight of Ag content in the nanofibers, measured in grams per milliliter. The test set-up remained the same except the culture time which was increased to 12 hours for this Ag effectiveness study. As seen in Figure 6(b), the bacteriostatic effectiveness shows approximately a power law relation to the Ag density in the nanofibers.

4. Degradation of EVOH Nanofibers

The integrity of nanofibers under environmental elements during production, storage, transportation, and usage is

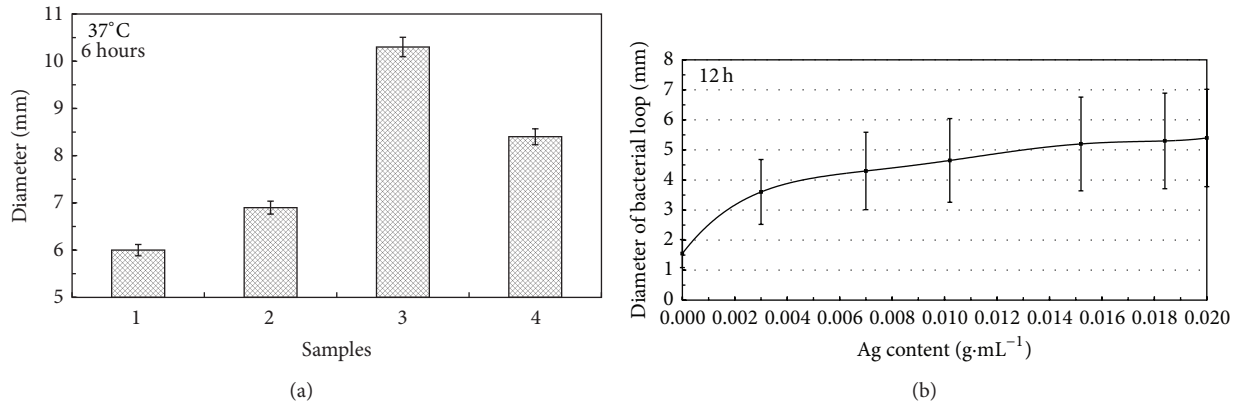

Figure 6: (a) Average diameter of bacterial loop, 6 mm, indicates no antibacterial effect: (1) Pure EVOH nanofiber, (2) nanofiber containing gentamicin, (3) nanofiber containing Ag nanoparticle, and (4) nanofibers containing iodine. (b) Averaged bacteriostatic loop diameter plotted as a function of Ag concentration.

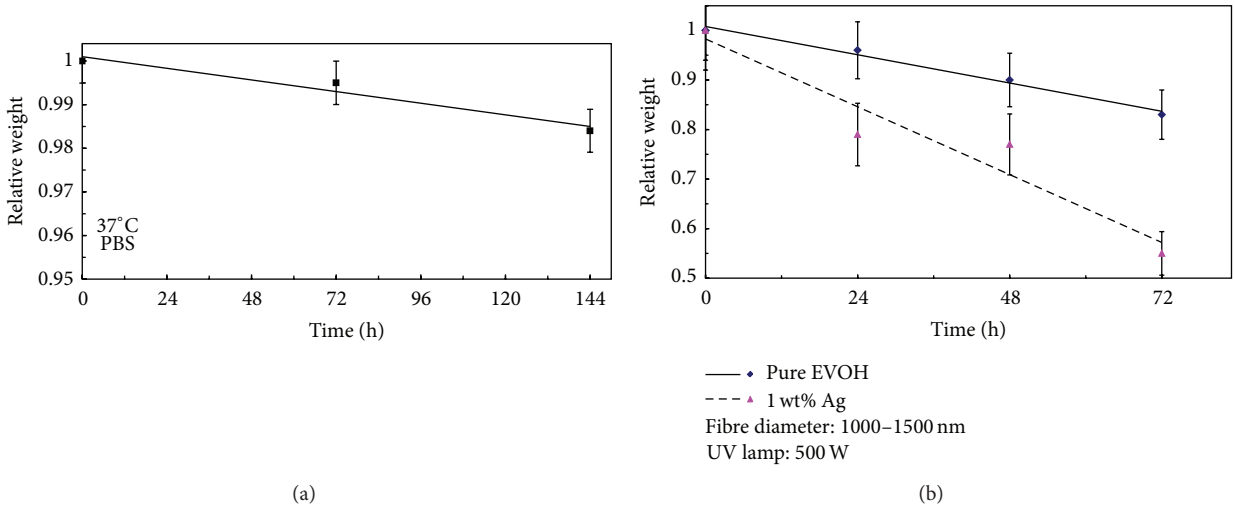

Figure 7: (a) Degradation of EVOH nanofiber in PBS solution. (b) UV degradation of nanofibers.

an important factor for the application. To investigate this, hydrolysis tests and ultraviolet light exposure tests were performed. For the hydrolysis tests, nanofiber samples were submerged in phosphate buffer solution (PBS) of pH value of 7.2 and kept at 37°C. The test was aimed to evaluate time-based stability of the material in simulated *in vivo* conditions. The samples were weighted every 72 hours with a bioelectronic balance after 30 mins of drying at 37°C.

The ultraviolet exposure tests were performed in a photochemical reaction chamber. The irradiation strength of the light at 240–280 nm wavelengths was 3.23×10^3 μW cm^{-2} as measured with a UV radiometer at the point where the samples were placed. The samples were weighted and photographed every 24 hours of exposure.

Hydrolysis *in vitro* shows that the nanofibers hardly decompose in the simulated body environment. As shown in Figure 7(a), only 2% weight change of the samples was recorded after being submerged in PBS solution for 168 hours (7 days). Also, little degradation was observed. These indicate good integrity of the nanofibers for long term use in the human body condition, an importance requirement on dressing materials.

In contrast to the hydrolysis tests, significant weight loss and fiber break-up were observed during the UV exposure tests (see Table 3 for comparable light exposures). Figure 7(b) shows the weight variation of the nanofibers with and without Ag nanoparticles versus the UV exposure hours. It can be seen that the nanofibers degrade approximately linearly in terms of the exposure duration. And those containing Ag nanoparticles degrade faster with more than 40% weight reduction over 72 hours (3 days) of exposure, twice the weight loss in pure EVOH nanofibers.

In the format of the degradation, nanofibers show strong signs of disintegration with shrinkage and break-down into pieces, as shown in Figure 8. Figures 8(a) and 8(b) provide a graphic revelation on nanofibers' texture deterioration under UV exposure. The relatively short duration for almost complete structural destruction just over 72 hours indicates

Table 3: Irradiation strength of different light sources.

Light source	Distance between the light source and the fibres/mm	Wave length/nm	Radiation strength/μW cm^{-1}
UV lamp	50.0	240–280	3.32×10^3
Daylight lamp	2000.0	400–700	0.19
Sunlight	Ground, direct exposure	250–2500	49.9

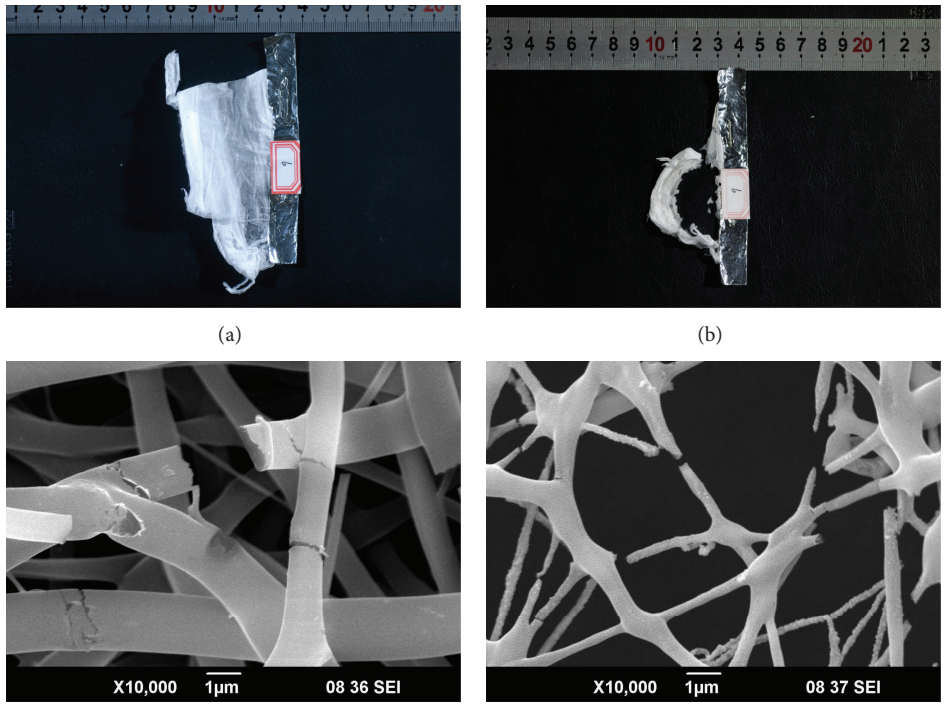

(a) (b) (c) (d)

Figure 8: (a) Original fine fiber sample before exposure to UV light, (b) fiber sample after 72 h continuous exposure to UV light, (c) SEM image of EVOH fiber after 24 h UV exposure, and (d) SEM image of EVOH fiber after 72 h UV exposure.

a high sensitivity to UV lights. SEM images (Figures 8(c) and 8(d)) show nanofibers breaking up and thinning out, resulting in fabric structural destruction.

To further study the light sensitivity of the nanofibers, the effects of exposure to different light sources were compared. The irradiations of an UV lamp, a daylight lamp, and direct sunlight were compared. In Table 2, the irradiation strength of an UV lamp is 66 times stronger than that of the direct sunlight exposure. Results of degradation under UV lamp indicate that the nanofibers show signs of deteriorated structures after 24 hours and are largely destroyed after 72 hours. This is equivalent to about half a year of exposure to direct sunlight.

The high sensitivity in EVOH nanofibers degradation under UV exposure leads to two interesting features. Firstly, the UV light may be used as a mechanism to speed up the release of Ag nanoparticles and possibly other drugs, through the material break-up of the nanofibers when they are used as a carrier. Secondly, the rapid texture deterioration under UV lighting also means there would be implications in using the EVOH nanofibers as wound dressing or bandage for a prolonged period, where some UV shielding might be required.

5. Conclusions

The EVOH nanofibers were obtained in this study from an electrospinning process. Experimental studies carried out in the lab on some of the performance related to clinical applications have led to the following conclusions.

(1) The electrospinning process does not inactivate the antibacterial ability of encapsulated agents.

(2) Nanofibers show a good fluid uptake ability (FUA), taking 22% more water than cotton gauze per unit weight.

(3) Nanofibers' water vapour transmission rates (WVTRs) are comparable to those of cotton gauze.

(4) Nanofibers containing silver particles demonstrate a superior antibacterial capacity than those containing gentamicin and iodine.

(5) The rapid degradation of nanofibers indicates that shielding of UV exposure might be needed for prolonged usage, but the feature may be used for controlled drug release.

(6) Nanofibers are found to be stable *in vitro* condition, thus potentially a good candidate for wound dressing applications.

Based on the outcome of the study, we can draw the conclusion that EVOH nanofibers are potentially a promising candidate for skin wound dressing. In particular, the drug carrying and slow release functions can be further explored for optimal usage. As the study was based on a small quantity of samples, results may be affected by random factors, though care was taken to eliminate noticeable uncertainties. However, more tests are needed on a large quantity and in a broader scope and wider range of parameters. These will be addressed in the continuity of this research programme.

Nomenclature

EVOH: Poly (ethylene-co-vinyl alcohol)
FUA: Fluid uptake ability
PBS: Phosphate buffer solution
SEM: Scanning electron microscopy
TEM: Transmission electron microscopy
UV: Ultraviolet
WVTR: Water vapour transmission rates (WVTRs)
W_s: Wet weight of the nanofiber
W_d: The dry weight of the nanofiber.

Conflict of Interests

The authors declare that there is no conflict of interests regarding the publication of this paper.

Authors' Contribution

Anhui Wang and Chao Xu contributed equally to this paper.

Acknowledgments

This work was supported by the following Grants: The General Research Program of Medical Health in Zhejiang Province (2013KYB230), Established Project of Nanjing Military Region (12MA113), Hangzhou Health Research Projects (20130633B01), and Xi'an University of Science and Technology Ph.D. Starting and Cultivating Funding.

References

[1] F. Xu, P. F. Wang, M. Lin, T. J. Lu, and E. Y. K. Ng, "Quantification and the underlying mechanism of skin thermal damage: a review," *Journal of Mechanics in Medicine and Biology*, vol. 10, no. 3, pp. 373–400, 2010.

[2] L. Zhou, Y. Hu, and M. Zhang, "Investigation on the psychological conditions of face or body burned patients," *Journal of North China Coal Medical College*, vol. 10, no. 4, pp. 503–504, 2008 (Chinese).

[3] M. Choinière, R. Melzack, N. Girard, J. Rondeau, and M.-J. Paquin, "Comparisons between patients' and nurses' assessment of pain and medication efficacy in severe burn injuries," *Pain*, vol. 40, no. 2, pp. 143–152, 1990.

[4] Y. Zhou, H. Yang, X. Liu, J. Mao, S. Gu, and W. Xu, "Electrospinning of carboxyethyl chitosan/poly(vinyl alcohol)/silk fibroin nanoparticles for wound dressings," *International Journal of Biological Macromolecules*, vol. 53, pp. 88–92, 2013.

[5] A. R. Unnithan, G. Gnanasekaran, Y. Sathishkumar, Y. S. Lee, and C. S. Kim, "Electrospun antibacterial polyurethane—cellulose acetate-zein composite mats for wound dressing," *Carbohydrate Polymers*, vol. 102, no. 1, pp. 884–892, 2014.

[6] J.-H. He, Y.-Q. Wan, and J.-Y. Yu, "Application of vibration technology to polymer electrospinning," *International Journal of Nonlinear Sciences and Numerical Simulation*, vol. 5, no. 3, pp. 253–262, 2004.

[7] D. I. Braghirolli, D. Steffens, and P. Pranke, "Electrospinning for regenerative medicine: a review of the main topics," *Drug Discovery Today*, vol. 19, pp. 743–753, 2014.

[8] A. Greiner and J. H. Wendorff, "Electrospinning: a fascinating method for the preparation of ultrathin fibers," *Angewandte Chemie—International Edition*, vol. 46, no. 30, pp. 5670–5703, 2007.

[9] C. R. Carlisle, C. Coulais, M. Namboothiry, D. L. Carroll, R. R. Hantgan, and M. Guthold, "The mechanical properties of individual, electrospun fibrinogen fibers," *Biomaterials*, vol. 30, no. 6, pp. 1205–1213, 2009.

[10] F. Xu, T. J. Lu, K. A. Seffen, and E. Y. K. Ng, "Mathematical modeling of skin bioheat transfer," *Applied Mechanics Reviews*, vol. 62, no. 5, Article ID 050801, 2009.

[11] F. Xu and T. J. Lu, "Skin biothermomechanics: modeling and experimental characterization," *Advances in Applied Mechanics*, vol. 43, pp. 147–248, 2009.

[12] I. Armentano, M. Dottori, E. Fortunati, S. Mattioli, and J. M. Kenny, "Biodegradable polymer matrix nanocomposites for tissue engineering: a review," *Polymer Degradation and Stability*, vol. 95, no. 11, pp. 2126–2146, 2010.

[13] T. J. Sill and H. A. von Recum, "Electrospinning: applications in drug delivery and tissue engineering," *Biomaterials*, vol. 29, no. 13, pp. 1989–2006, 2008.

[14] S. Shahverdi, M. Hajimiri, M. A. Esfandiari et al., "Fabrication and structure analysis of poly(lactide-co-glycolic acid)/silk fibroin hybrid scaffold for wound dressing applications," *International Journal of Pharmaceutics*, vol. 473, no. 1-2, pp. 345–355, 2014.

[15] E.-R. Kenawy, J. M. Layman, J. R. Watkins et al., "Electrospinning of poly(ethylene-co-vinyl alcohol) fibers," *Biomaterials*, vol. 24, no. 6, pp. 907–913, 2003.

[16] E. Bugnicourt, M. Schmid, O. M. Nerney et al., "Processing and validation of whey-protein-coated films and laminates at semi-industrial scale as novel recyclable food packaging materials with excellent barrier properties," *Advances in Materials Science and Engineering*, vol. 2013, Article ID 496207, 10 pages, 2013.

[17] M. Schmid, K. Dallmann, E. Bugnicourt et al., "Properties of whey-protein-coated films and laminates as novel recyclable food packaging materials with excellent barrier properties," *International Journal of Polymer Science*, vol. 2012, Article ID 562381, 7 pages, 2012.

[18] C. Xu, F. Xu, B. Wang, and T. J. Lu, "Electrospinning of poly(ethylene-co-vinyl alcohol) nanofibres encapsulated with Ag nanoparticles for skin wound healing," *Journal of Nanomaterials*, vol. 2011, Article ID 201834, 7 pages, 2011.

[19] B. Wang, X. Chao, Y. Li, and S. R. Reid, "Tensile strength of electrospun Poly(ethylene-co-vinyl alcohol) nanofibre sheets," *Key Engineering Materials*, vol. 535-536, pp. 215–218, 2013.

[20] A. S. Colsky, R. S. Kirsner, and F. A. Kerdel, "Analysis of antibiotic susceptibilities of skin wound flora in hospitalized dermatology patients: the crisis of antibiotic resistance has come to the surface," *Archives of Dermatology*, vol. 134, no. 8, pp. 1006–1009, 1998.

[21] S. Ravindra, Y. Murali Mohan, N. Narayana Reddy, and K. Mohana Raju, "Fabrication of antibacterial cotton fibres loaded with silver nanoparticles via 'Green Approach'," *Colloids and Surfaces A. Physicochemical and Engineering Aspects*, vol. 367, no. 1–3, pp. 31–40, 2010.

[22] A. Tamayol, M. Akbari, N. Annabi, A. Paul, A. Khademhosseini, and D. Juncker, "Fiber-based tissue engineering: progress, challenges, and opportunities," *Biotechnology Advances*, vol. 31, no. 5, pp. 669–687, 2013.

[23] S. Ravindra, Y. Murali Mohan, N. Narayana Reddy, and K. Mohana Raju, "Fabrication of antibacterial cotton fibres loaded with silver nanoparticles via 'Green Approach'," *Colloids and Surfaces A: Physicochemical and Engineering Aspects*, vol. 367, no. 1–3, pp. 31–40, 2010.

[24] S. Çalamak, C. Erdoğdu, M. Özalp, and K. Ulubayram, "Silk fibroin based antibacterial bionanotextiles as wound dressing materials," *Materials Science and Engineering: C*, vol. 43, pp. 11–20, 2014.

[25] D. Campoccia, L. Montanaro, and C. R. Arciola, "A review of the biomaterials technologies for infection-resistant surfaces," *Biomaterials*, vol. 34, no. 34, pp. 8533–8554, 2013.

[26] L. Ruiz-Cardona, Y. D. Sanzgiri, L. M. Benedetti, V. J. Stella, and E. M. Topp, "Application of benzyl hyaluronate membranes as potential wound dressings: evaluation of water vapour and gas permeabilities," *Biomaterials*, vol. 17, no. 16, pp. 1639–1643, 1996.

Hindawi Publishing Corporation
Journal of Nanomaterials
Volume 2015, Article ID 247471, 9 pages
http://dx.doi.org/10.1155/2015/247471

Research Article

Electrospun Carbon Nanofiber Membranes for Filtration of Nanoparticles from Water

Mirko Faccini, Guadalupe Borja, Marcel Boerrigter, Diego Morillo Martín, Sandra Martìnez Crespiera, Socorro Vázquez-Campos, Laurent Aubouy, and David Amantia

LEITAT Technological Center, C/de la Innovació 2, 08225 Terrassa, Spain

Correspondence should be addressed to Mirko Faccini; mfaccini@leitat.org

Received 13 October 2014; Accepted 12 December 2014

Academic Editor: Fujuan Liu

Nowadays, hundreds of consumer products contain metal and metal oxide nanoparticles (NP); this increases the probability of such particles to be released to natural waters generating a potential risk to human health and the environment. This paper presents the development of efficient carboneous nanofibrous membranes for NP filtration from aqueous solutions. Free-standing carbon nanofiber (CNF) mats with different fiber size distribution ranging from 126 to 554 nm in diameter were produced by electrospinning of polyacrylonitrile (PAN) precursor solution followed by thermal treatment. Moreover, tetraethoxyorthosilicate was added to provide flexibility and increase the specific surface area of the CNF. The resulting membranes are bendable and mechanically strong enough to withstand filtration under pressure or vacuum. The experimental results of filtration revealed that the fabricated membranes could efficiently reject nanoparticles of different types (Au, Ag, and TiO_2) and size (from 10 to 100 nm in diameter) from aqueous solutions. It is worth mentioning that the removal of Ag NP with diameters as small as 10 nm was close to 100% with an extremely high flux of 47620 L m^{-2} h^{-1} bar^{-1}.

1. Introduction

Nanotechnology is having a large impact in manufactured products in most major industry sectors, including electronic, cosmetic, automotive, and healthcare sectors. According to a recent survey [1] over 1,300 nanotechnology-related products are currently on the market. Free nanoparticles (NP) are likely to enter the aquatic environment in all stages of nanomaterials life cycle (production, processing, use, recycling, and disposal). These particles can persist in natural bodies and are not fully removed by drinking water treatment systems, thereby posing a potential public health concern [2, 3]. Therefore, the development of new barrier materials is needed to reduce the potential risks related to human and environmental exposure to nanomaterials [4]. Nanofiber webs, due to their very large specific area, very small pore size, and high porosity, have been shown to improve the efficiency of conventional materials used for the filtration and separation of particulate materials [5, 6].

Electrospinning is a well-established and versatile process that has been used to produce ultrafine fibers including microfibers (>1 μm) or nanofibers (<1000 nm) [7, 8]. The main advantage of electrospinning process among other techniques is the relative quick, simple, and economical way to fabricate a variety of materials into nanofibrous structures [9].

Particularly, electrospun carbon nanofibers (CNF) have attracted considerable attention in the field of water filtration as they exhibit a number of unique features [10]. While the development of free-standing ceramic nanofibrous mats is still a technological challenge due to the intrinsic brittleness of the material, large area CNF sheets with high mechanical strength can be easily fabricated. In addition, their higher chemical resistance, compared to polymeric filters, makes them suitable for filtration [11, 12].

In this study, the development of efficient nanofiber membranes for the removal of nanoparticles from aqueous solutions is presented. Free-standing carbon nanofibrous

membranes were fabricated by electrospinning of a polyacrylonitrile (PAN) precursor solution followed by a thermal treatment of the electrospun fibers. Moreover, tetraethoxyorthosilicate (TEOS) was added to provide flexibility and to increase the specific surface area of the CNF [13, 14].

To the best of our knowledge, CNF derived from PAN/TEOS have not been used for such filtration purposes. Unlike carbonized PAN mats, which were too brittle to tolerate high vacuum filtration process, the PAN/TEOS derived CNF mats were bendable and showed sufficient mechanical strength to withstand filtration under pressure or vacuum. The experimental results demonstrate that the membranes could efficiently reject various NP (Au, Ag, and TiO_2) of different sizes and natures from the aqueous solution.

2. Experimental Part

2.1. Materials and Methods. PAN (Mw = 150,000 g/mol) powder, *N-N* dimethylformamide (DMF), and TEOS (98%) were purchased from Sigma-Aldrich. CNF precursor solutions were prepared by dissolving PAN at concentrations ranging from 4 to 12 wt.% in DMF at 60°C. PAN/TEOS precursor solutions were prepared by the addition of TEOS to the PAN solutions in DMF to achieve the proper PAN/TEOS weight ratios, as shown in Table 2. All polymer solutions were mixed by a magnetic stirrer for a sufficiently long time until they became homogeneous. The viscosity and electrical conductivity of polymer solutions were measured by a digital viscometer (DV-E, Brookfield Co.) and an electric conductivity meter (CRISON EC-meter BASIC) at 25°C. To produce nanofibers the solutions were electrospun onto an aluminum foil by using commercially available electrospinning equipment (MECC Co. LTD., model NF-103). Plastic syringes fitted with metal needles were used as electrospinning nozzles. Typical operating conditions were the following: flow rates of 1-2 mL/h, applied voltages between 25 and 30 kV, and working distance of 9–16 cm. For carbonization, the as-spun polymer fibers were first placed in a chamber furnace and stabilized in air for 5 hours at 280°C and then carbonized for 1 hour in nitrogen at 800–1000°C; in both cases the ramp rate was 1°C/min [15].

2.2. Preparation of the NP Solutions. The filtration performance of carbonized PAN/TEOS nanofibers was evaluated with different types of NP, including metallic NP, such as Ag and Au, and metal oxide NP, such as TiO_2. TiO_2 dispersions were prepared by the sonication of proper amounts of NP in milliQ water for 10 min at 50% of the total power (750 W). Au and Ag aqueous nanoparticle solutions were kindly provided by ICN (Catalonia Institute of Nanotechnology). The concentrations of the NP solutions were adjusted to have a high ultraviolet-visible (UV-vis) absorbance without signal saturation.

2.3. Characterization. The surface morphology of the nanofiber mats was examined using scanning electron microscopy (SEM, Zeiss Evo MA-10) after coating with carbon to minimize the charging effect. Images taken by the SEM were analyzed to obtain the fiber diameter by the ImageJ software. At least four pictures were used to calculate the mean values of the diameter of the fibers.

The clean water permeance (CWP) of CNF membranes was determined using a bench-scale dead-end filtration setup. The system consists of a reservoir tank containing ultrapure water (Type 1) connected to a 200 mL Amicon stirred ultrafiltration cell (Merck Millipore). The stirred cell houses a 63.5 mm diameter flat CNF sheet with an effective area of 28.7 cm^2. Pressure in the feed tank was provided by compressed air. The applied pressure measured during the CWP experiments was 3 kPa (0.43 psi).

The pore size of the CNF membranes was determined using a simple particle removal method. Solutions containing 20 mg/L of polystyrene latex beads (from Magsphere Corp.) with diameter between 0.1 μm and 3 μm were passed through the membrane at the pressure of about 0.1 bar. The absorbance of the feed and filtrate latex solutions was measured using UV-vis spectrometer and the removal rate was calculated by the following formula, where A_{feed} and A_{filtrate} are the absorbance at 250 nm of feed and filtrate solutions, respectively:

$$\text{Removal rate}\,\% = \left[1 - \left[\frac{A_{\text{feed}}}{A_{\text{filtrate}}}\right]\right] * 100. \quad (1)$$

A latex removal curve was drawn by plotting the removal rates against the beads diameter size (Figure 7). The nominal pore size is defined as the diameter where 90% of latex beads are removed.

For filtration experiments, disc filter was cut out of the nanofibrous mats by using a hollow punch and placed on the metallic support of the filtration setup. A solution of nanoparticles was passed through it and UV-vis spectrometer was used to measure the absorbance of the feed and filtrate solutions. The filtration efficiency was calculated using the following formula, where A_{feed} and A_{filtrate} are the absorbance at $\lambda_{\max}$ of feed and filtrate solutions, respectively:

$$\text{Filtration efficiency}\,\% = \left[\frac{\left[A_{\text{feed}} - A_{\text{filtrate}}\right]}{A_{\text{feed}}}\right] * 100. \quad (2)$$

3. Result and Discussion

3.1. CNF Membranes. It is known that the morphology of electrospun fibers depends on various processing parameters, solution properties, and environmental conditions. Through control of the spinning conditions, the resulting fibers can range from about 20 nm to a few micrometers. To gain control over the properties of the obtained nanofibers, the viscosity and conductivity were measured as a function of the PAN concentration. Figure 1 shows an overlay plot of the viscosity and conductivity as function of the PAN weight percentage in DMF. By increasing the PAN concentration from 4 to 12 wt.% the viscosity rises exponentially from 31 to 2053 cP, as a result of the higher molecular entanglement. In fact, at higher precursor concentration the polymer chains are more tangled, which leads to the production of broader fibers. The electric conductivity also increases from 48 to 86 μs/cm by

Table 1: Process parameters used for the electrospinning of solutions C-1 to C-5 and the average diameters of the PAN nanofibers and CNF mats.

Solution code	PAN (wt.%)	Feed rate (mL/h)	Voltage (kV)	Distance (cm)	Applied electric field (kV/cm)	PAN nanofibers diameter (nm)	Carbon nanofibers diameter (nm)
C-1	4	2	30	7	4.2	96 ± 24	—
C-2	6	2	30	10	3.0	189 ± 47	126 ± 19
C-3	8	2	29	13	2.2	282 ± 51	184 ± 31
C-4	10	2	29	15	1.9	351 ± 78	249 ± 24
C-5	12	2	27	16	1.7	620 ± 39	554 ± 107

Table 2: Characterization of the PAN/TEOS solutions C-Si-1 to C-Si-3 and the average diameters of the PAN/TEOS nanofibers and CNF/Si mats.

Solution code	PAN (wt.%)	PAN/TEOS (w/w)	Viscosity (cP)	Conductivity (μs/cm)	PAN/TEOS nanofibers diameter (nm)	CNF/Si diameter (nm)
C-Si-1	6	7/3	132	96	244 ± 31	158 ± 38
C-Si-2	8	7/3	285	93	300 ± 33	193 ± 36
C-Si-3	10	7/3	647	102	487 ± 65	387 ± 33

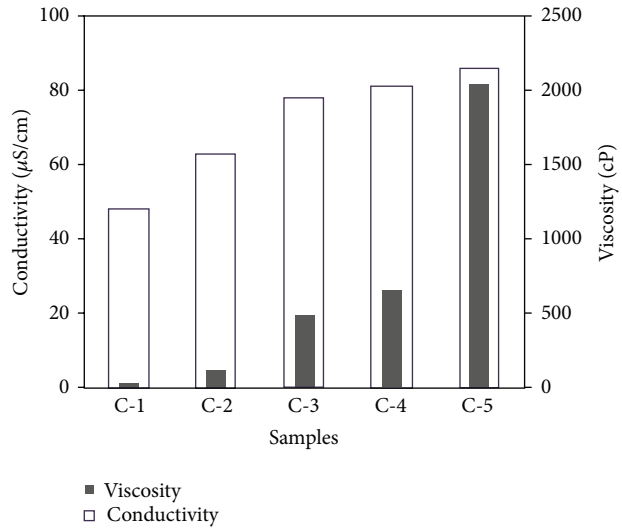

Figure 1: Solution viscosity and electrical conductivity as function of the polymer solution concentration.

increasing the concentration from 4 to 12 wt.%. As shown in Table 1, for each solution, different operating conditions were set to produce nanofibers in a continuous and stable electrospinning process. When the electrical conductivity of the solution was higher, a lower electrical field (voltage/distance) was needed for the formation of nanofibers. For example, for solution C-1, having the lowest viscosity of 31 cP, the electrospinning process was not sufficiently stable, and a high voltage had to be applied to form fibers. In fact, the fibers were formed by the application of the highest electrical field, and this led to the formation of beads and defects. Moreover, solution C-5, with a polymer concentration of 12 wt.%, although it possessed the highest viscosity of 2053 cP, could be electrospun by the application of the lowest electrical field. This means that the most critical parameter to be controlled for a continuous and stable process is the solution conductivity. For instance, at low conductivities, the addition of salts is commonly used to improve process stability [16]. The SEM micrographs and diameter distribution of PAN nanofibers as function of polymer concentration are shown in Figure 2. The average fiber diameter increases gradually with polymer concentration going from 189 nm at 6 wt.% to 620 nm at 12 wt.%. This indicates that the morphology of the nanofibers depends on polymer concentration which effects viscosity. At higher viscosity there are more chain entanglements and less chain mobility, resulting in less extension during spinning, therefore producing thicker fibers.

The pyrolysis process of PAN based nanofibers generally consists of stabilization process in air followed by carbonization at higher temperatures in inert atmosphere. The optimal stabilization temperature for PAN has been reported to be around 280°C; at this temperature several reactions, that is, cyclization, dehydrogenation, aromatization, and oxidation, take place, which generates the formation of conjugated ladder-type structures [15]. These structures are thermally stable and might be able to withstand high temperature to prevent melting of the polymer and loss of nanofiber morphology during carbonization. Moreover, stabilization changes the color of PAN nanofibrous mats from white to brown. The trend of color change from light to dark results from the increment of carbon content and formation of dense structure of polymer in thermal cyclization and dehydrogenation. Large area CNF mats could be obtained after the thermal treatment process. These sheets, however, were quite rigid and could be easily broken by manipulation or bending.

Figure 3 shows the SEM micrographs and diameter distribution of the CNF after the thermal treatment of the as-spun nanofibers at different concentrations. As expected, remarkable weight loss and shrinkage occurred during the carbonization of the PAN fibers. However, the heat-treated fibers were still long and retained their cylindrical and uniform shape. In fact, at high temperatures, some small molecules may have broken down into highly volatile gases

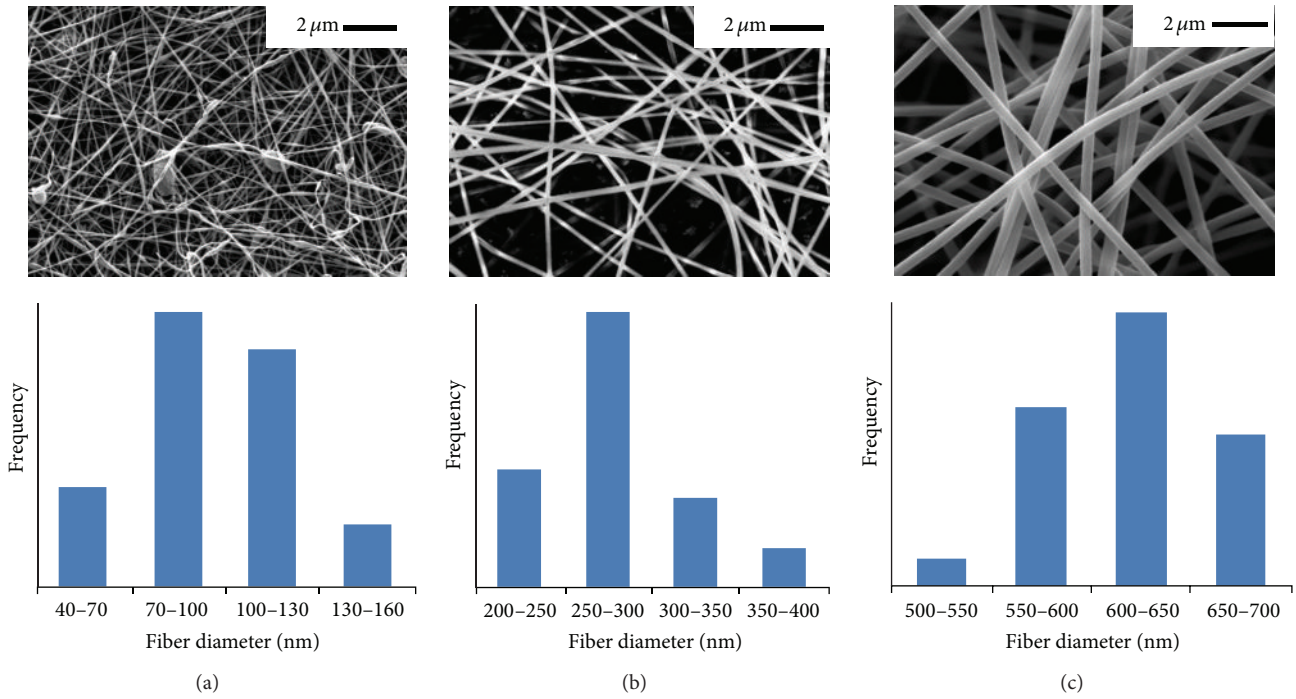

FIGURE 2: SEM images and diameter distribution of nanofibers obtained by electrospinning PAN solutions C-1 (a), C-3 (b), and C-5 (c).

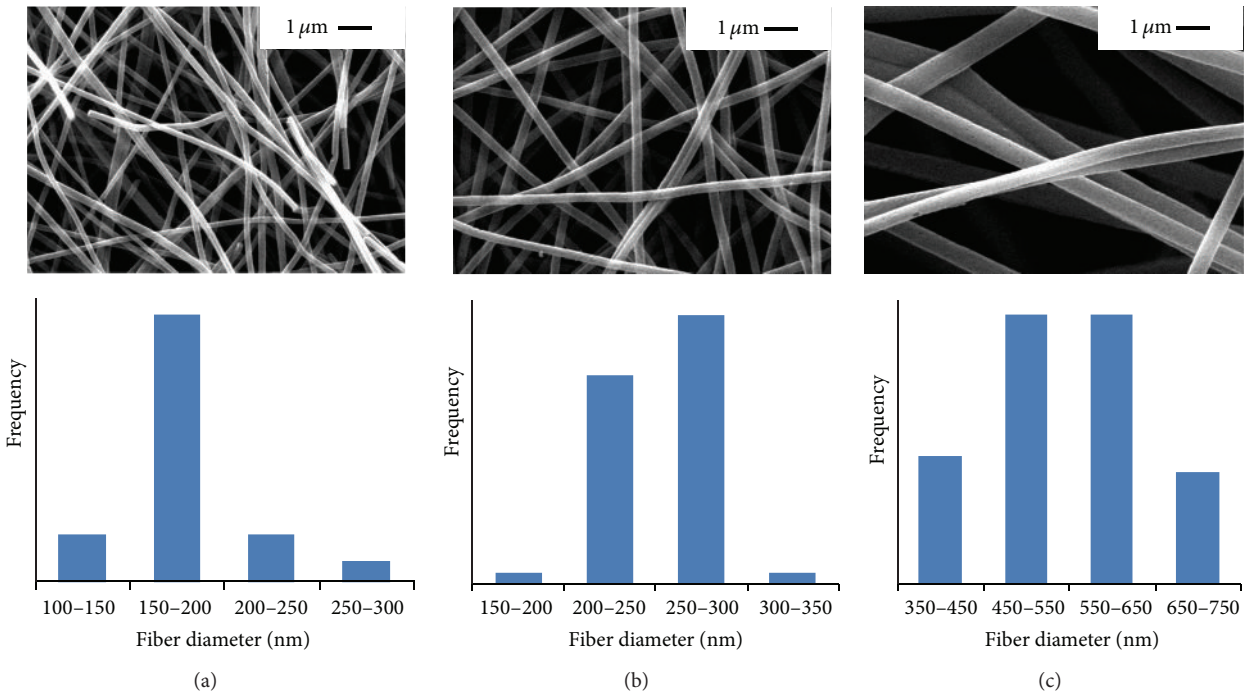

FIGURE 3: SEM images and diameter distribution of the CNF obtained by the thermal treatment of the as-spun nanofibers of the PAN solutions: (a) C-3, (b) C-4, and (c) C-5.

or carbon char. In addition, during the carbonization, the disruption of the molecules occurred with the loss of carbon oxides and the formation of a structure with a higher carbon assay, which resulted in significant weight loss and shrinkage. In other words, when the PAN nanofibrous mats are subjected to the stabilization temperature, the dense ladder-polymer structures react with oxygen and prevent melting during carbonization. The carbonization process of stabilized PAN mats involves thermal treatment to remove noncarbon elements. Then, denitrogenation takes place and thus results in the formation of a network structure [17].

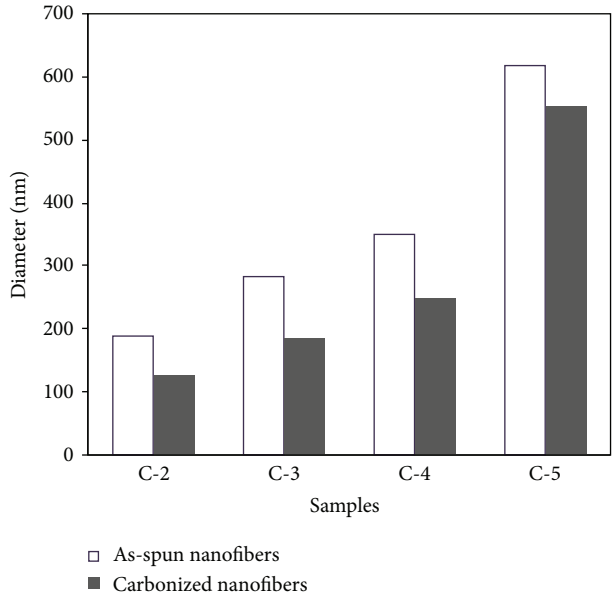

Figure 4: Average fiber diameter of as-spun and carbonized nanofibers.

A comparison between the average fiber diameters of the as-spun and carbonized nanofibers is presented in Figure 4. The as-spun nanofibers thermally treated at 800°C shrink in diameter and lose approximately 25–30% of their weight. In this step, the CNF mats with fiber diameters ranging from 126 to 554 nm were successfully obtained. However, because of the rigidity of the CNF, a more flexible material was needed to reduce any potential accidental damage of the membrane that might occur during filtration generating preferential pathways for contaminants and consequently loss of retention capacity.

3.2. CNF/Si Membrane. Recently, Kim et al. [13] reported the fabrication of flexible CNF mats by the incorporation of TEOS into PAN via electrospinning for supercapacitor electrodes. They also concluded that the new mats had high capacitance and energy/power density values because of the formation of ultramicropores and the introduction of heteroatoms. We hypothesized that the same approach could be successfully applied to produce flexible CNF mats with high surface areas for NP filtration from aqueous solutions. For this purpose, different solutions were prepared by varying of the concentration of PAN in DMF (C-Si-1, C-Si-2, and C-Si-3), as shown in Table 2. For the PAN/TEOS solutions presented in this table, the optimum concentrations of PAN (obtained from Table 1) were chosen to produce the CNF/Si mats. TEOS was added to the PAN solutions on the basis of a specific ratio of 3 : 7, respectively. According to data reported in the literature [14], through the application of this specific ratio of PAN/TEOS, the highest mesoporous structures could be formed, and this could enhance the filtration efficiency of the fibers. As described in the previous section for the CNF, the average fiber diameter grew gradually with the polymer concentration.

In fact, at a constant PAN/TEOS weight ratio, the fiber diameter went from 244 nm at 6 wt.% PAN (for the solution of C-Si-1) to 487 nm when the concentration was 10 wt.% (for the solution of C-Si-3). The PAN/TEOS mats were thermally treated with the stabilization-calcination procedure previously described. The diameter of the carbonized PAN/TEOS nanofibers (CNF/Si) after carbonization at 800°C reduced roughly to 35% of its initial diameter regardless of the PAN concentration in DMF (see Table 2) [18].

To investigate the effect of higher carbonization temperatures on the fiber morphology, the PAN/TEOS nanofibers were also carbonized at 1000°C. It is notable that stabilization is critical in obtaining morphological stability. These kinds of oxidative stabilizations include complex chemical reactions and time-consuming steps. It was reported previously that the stabilization processes of TEOS-incorporated nanofibers were kinetically higher than those of pure polymeric electrospun nanofibers because of the catalytic ability of TEOS [14]. The trapped TEOS in the nanofibers could be transformed into hydrated forms. During the stabilization process, silanol $[Si(OH)_x]$ groups tended to be produced by sequence hydrolysis reactions. Further condensation of Si–OH led to the formation of SiO_x and to gas formation (e.g., CO, CO_2, H_2, CH_4, and H_2O). Figure 5 shows the SEM micrographs and diameter distribution diagrams of CNF/Si after the thermal treatment of the as-spun nanofibers produced by the solution C-Si-3 at 800 and 1000°C. As shown, all of the resulting samples were smooth and exhibited cylindrical morphologies. The average diameter of the nanofibers decreased from 487 to 387 nm and then to 289 nm as the carbonization temperature increased from 800 to 1000°C. Moreover, when the nanofibers were thermally treated at temperatures greater than 800°C, a color change from brownish black to black was observed due to a higher percentage of graphite [19].

The resulting CNF/Si mats showed good robustness and were more flexible than the CNF mats obtained by the thermal treatment of PAN. In addition, no broken fibers were visible; this indicated that the mats were exceptionally strong with long nanofibers having diameters ranging from 158 to 387 nm (see Table 2). The observations indicated that the CNF/Si membranes are mechanically strong enough and they can be bent completely without breaking (Figure 6). The robustness of the CNF/Si membranes and the ability to be produced in an easy and cost-efficient way by electrospinning make these carbonaceous nanofibers potential candidates for the filtration of NP from aqueous solutions.

3.3. Pore Size and Water Flux. Nanofiber membranes have been shown to provide dramatic increases in filtration efficiency at relatively small reduction in permeability [20]. Moreover, in many laboratory tests and actual operating environments, nanofiber filter media have also enabled new levels of filtration performance and more capacity to retain pollution compared to traditional fibers thanks to their open porous structure. Several methods have been used for pore size measurement of nanofibrous membranes [21]. Each of them has different measuring theory and it is often seen that

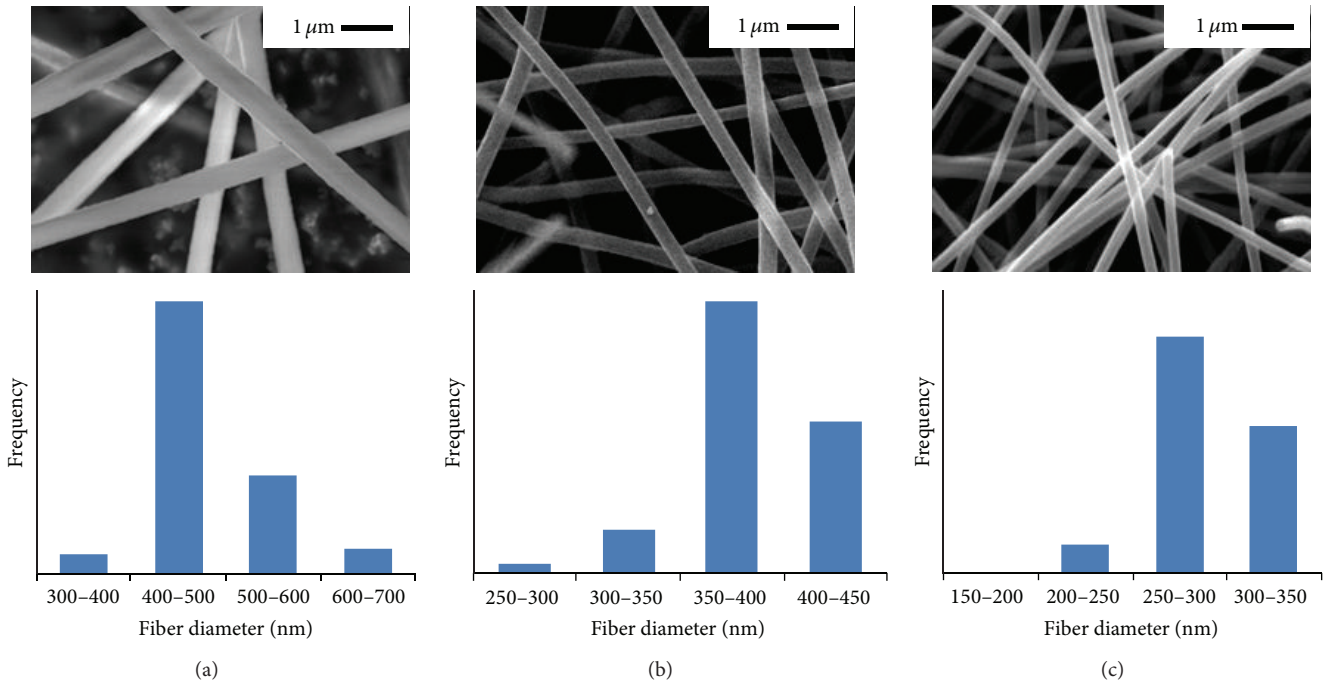

Figure 5: SEM images and diameter distribution of the (a) PAN/TEOS nanofiber mats and CNF/Si obtained by the thermal treatment of the as-spun PAN/TEOS nanofibers of solution C-Si-3 at (b) 800°C and (c) 1000°C.

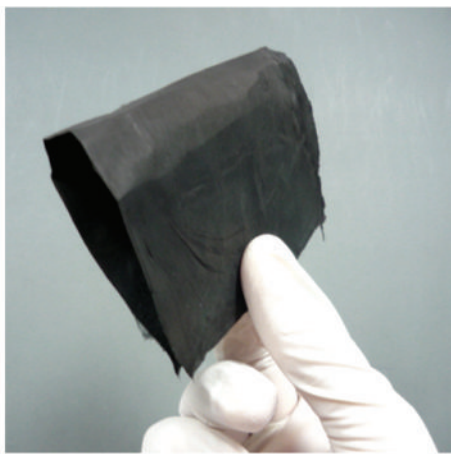

Figure 6: Digital picture showing the flexibility of the CNF/Si mats.

different results are obtained by measurement of the same membrane using different methods.

In this study, the nominal pore size of CNF/Si membrane is determined using a simple method based on the filtration of latex beads of well-established size. The graph in Figure 7 shows that the CNF/Si membrane was able to retain almost completely particles of approximately 1 μm or larger, resulting in an extrapolated nominal pore size of 0.8 μm. Polystyrene beads of different sizes trapped on the surface of the nanofiber filter are clearly visible in the SEM image of Figure 7. Although most of the 1 μm beads and larger are trapped onto the membrane top surface, smaller beads are visible not only onto the membrane surface but also throughout the whole membrane section.

As consequence of the large porosity and the hydrophilicity, the CNF/Si membrane possesses an extremely large water flux of 47620 L m^{-2} h^{-1} bar^{-1}. This is almost 4 times higher than the carbonaceous nanofiber membranes recently reported by Liang et al., which were 12250 L m^{-2} h^{-1} bar^{-1} and 80 times higher than commercially available membranes with cut-off of 0.05 μm being 757 L m^{-2} h^{-1} bar^{-1} [22]. This difference is due to the low porosity of the commercially available membranes and the low porosity of vertical cylindrical channels which can easily get blocked by particles [22, 23].

3.4. Filtration of Aqueous NP Dispersions. Recently, Lin et al. [24] reported the preparation of a mechanically robust and thermally tolerant nanofibrous membrane via electrospinning of Nomex solution. They concluded that the preparation of membranes in the form of nanofibers dramatically enhanced the specific surface area of the membranes compared to the commercial Nomex fibers. In addition, their nanofibrous membranes demonstrated a highly efficient rejection of SiO_2 NP from aqueous solution. This observation significantly proved the high potential of polymeric nanofibers for filtration due to their larger surface area. Here, the membranes produced by the carbonization at 1000°C of electrospun nanofibers from solution C-Si-3 were initially used to assess the filtration ability of CNF/Si mats. The filtration performance of the CNF/Si membrane was evaluated with different types of NP, including metal NP, such as Au and Ag, and metal oxide NP, such as TiO_2.

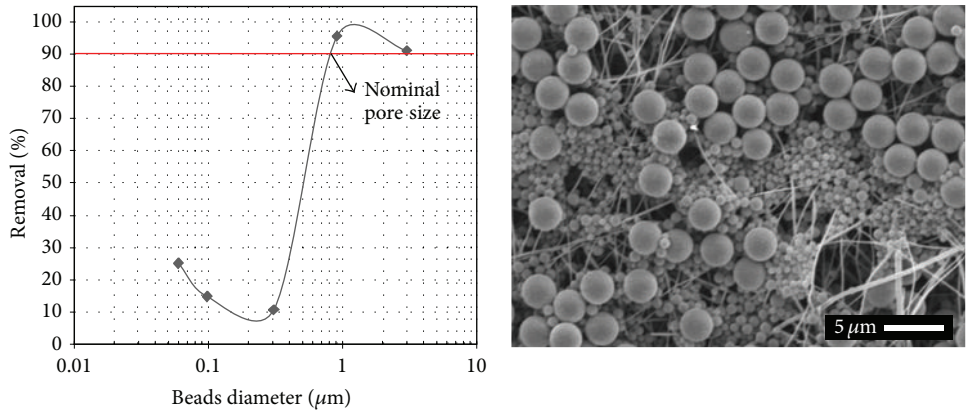

FIGURE 7: Latex beads removal percentage curve as function of beads diameter for CNF/Si membrane (a) and SEM image of the CNF/Si membrane top surface after filtration with beads with diameter going from 0.1 μm to 3 μm (b).

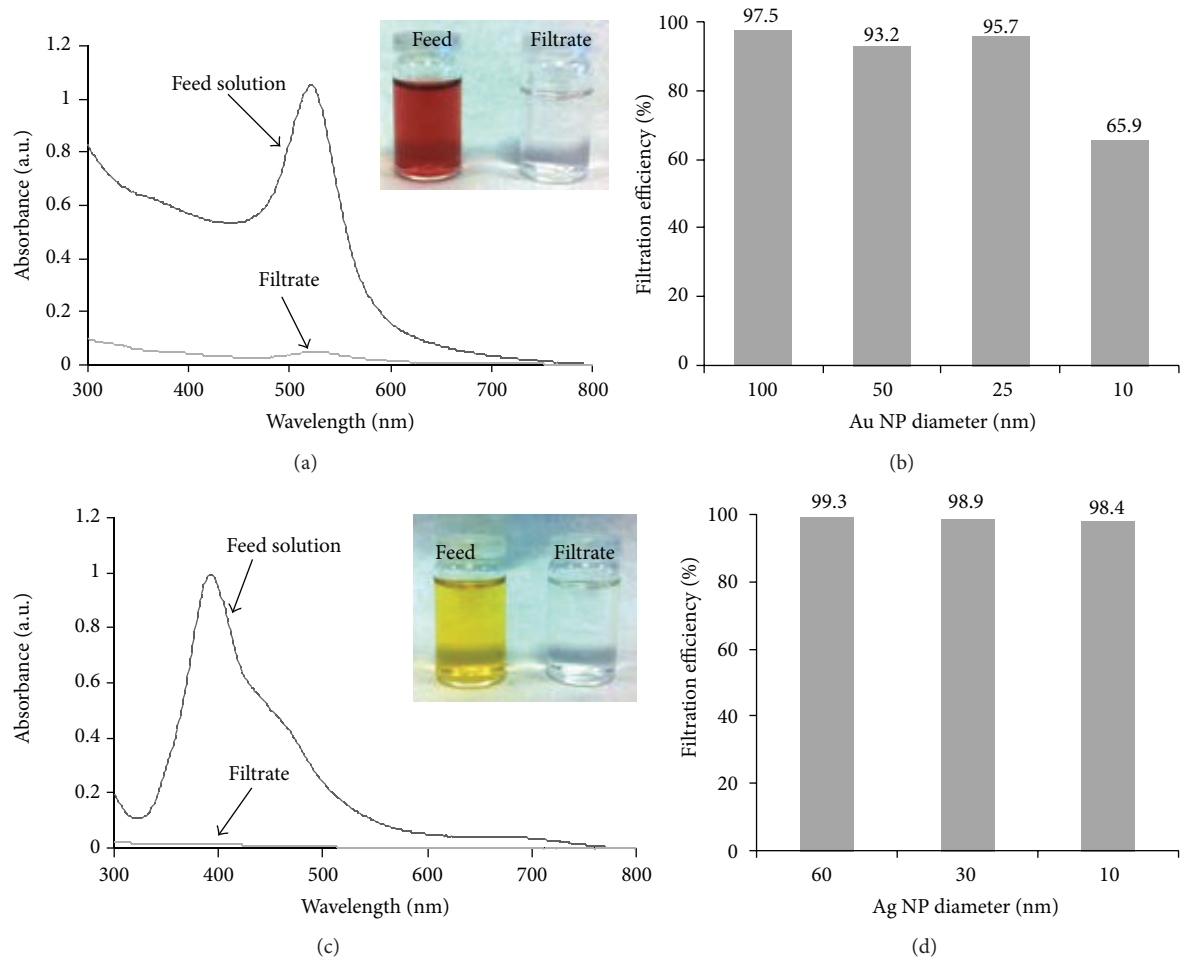

FIGURE 8: UV-vis spectra of feed solution and filtrate showing the filtration of Au NP (a) and Ag NP (c) and the filtration efficiency as function of particle size for Au NP (b) and Ag NP (d).

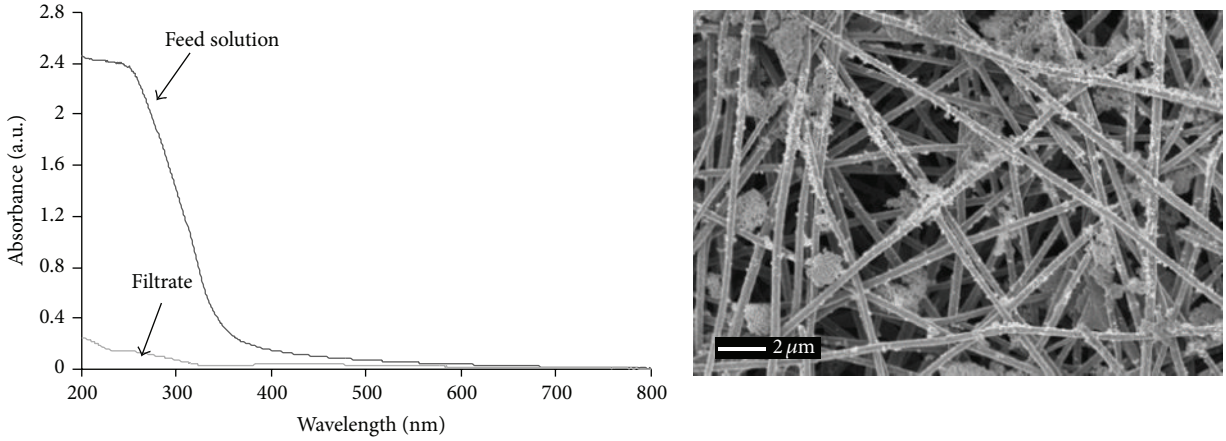

(a) (b)

Figure 9: UV-vis spectra of feed solution and filtrate showing the filtration of TiO_2 NP (a) and SEM image of top surface of the CNF/Si membrane after filtration with TiO_2 NP (b).

Metal NP visualization of the filtration can easily be achieved by following the characteristic intense color that is yellow for Au NP and red for Ag NP dispersions. In the case of the Au NP solutions, the filtration efficiency was determined by measurement of the absorption at λ_{max} in the range 520–540 nm of the feed and filtrate solutions using NP with diameter of 100, 50, 25, and 10 nm. As an example, a typical UV-vis spectrum is shown in Figure 8, as well as the retention as function of NP size. The nanostructured CNF/Si filters were able to retain about 95% of the Au NP of 100, 50, and 25 nm. However, when smaller NP were used, the filtration efficiency dropped to about 66% for the 10 nm NP.

For the Ag NP dispersions, the UV-vis absorption at λ_{max} values around 400–420 nm was used, and solutions with NP of average diameters of 60, 30, and 10 nm were used. As shown in Figure 8, the nanofibrous membranes could almost completely remove the Ag NP regardless of their particle sizes. In fact, for all three NP sizes, the retention was around 99%. Interestingly, in contrast to what was observed for the Au NP, in this case, the filtration efficiency did not decrease when smaller NP (e.g., 10 nm) were used.

The demand of TiO_2 NP is significantly increasing due to its wide range of applications such as environmental technologies, paints, cosmetics, paper, and solar cells [25]. The world production of TiO_2 NP is an order of magnitude greater than the next most widely produced nanomaterial, ZnO. TiO_2 may reach high concentrations in surface waters and pose a significant threat to aquatic ecosystems [26]. Therefore, here, the filtration efficiency of CNF/Si membranes against dispersions of TiO_2NP with average diameter of 10–15 nm in water is examined. The UV-vis spectra of the feed solution and filtrate are shown in Figure 9. The filtration efficiency for the TiO_2 NP was very high, being 94.1%. Figure 9(b) shows the typical SEM micrograph of the top surface of the CNF/Si membrane after filtration of the TiO_2 NP solution.

Small and large NP aggregates are clearly visible on the surface of single nanofibers. The SEM image evidencing that the pore size of the nanofiber filter is too large to retain NP based on sieving model. Therefore, the high NP retention capacity of the membrane might be attributed to strong electrostatic interaction of metal and metal oxide NP with the CNF/Si membranes resulting in a good retention capacity of the filters.

4. Conclusion

CNF membranes were fabricated by the electrospinning of PAN precursor solutions followed by the thermal treatment of the electrospun fibers. TEOS was added to the polymer solution to increase the specific surface area of the CNF and to provide flexibility and mechanical strength needed to withstand filtration under pressure or vacuum. These developed filters were capable of efficiently rejecting NP of different sizes and natures (e.g., Au, Ag, and TiO_2) from aqueous solution. The results described herein demonstrate the great potential of these membranes for the filtration of NP from water, mainly because of their tunable pore size, very high permeability, and ability to produce nanofibers in an easy and cost-efficient way by electrospinning. Moreover, they can be proposed for the promising system recovery of valuable nanomaterials from complex matrices.

Conflict of Interests

The authors declare that there is no conflict of interests regarding the publication of this paper.

Acknowledgment

The financial support of this work was provided by European Community's Seventh Framework Programme (FP7/2007–2013) under Grant Agreement no. 247899 of the project named NANOPOLYTOX.

References

[1] "Project on Emerging Nanotechnologies," http://www.nanotechproject.org/inventories/consumer/.

[2] R. Brayner, "The toxicological impact of nanoparticles," *Nano Today*, vol. 3, no. 1-2, pp. 48–55, 2008.

[3] V. L. Colvin, "The potential environmental impact of engineered nanomaterials," *Nature Biotechnology*, vol. 21, no. 10, pp. 1166–1170, 2003.

[4] P. I. Dolez, N. Bodila, J. Lara, and G. Truchon, "Personal protective equipment against nanoparticles," *International Journal of Nanotechnology*, vol. 7, no. 1, pp. 99–117, 2010.

[5] R. S. Barhate and S. Ramakrishna, "Nanofibrous filtering media: filtration problems and solutions from tiny materials," *Journal of Membrane Science*, vol. 296, no. 1-2, pp. 1–8, 2007.

[6] D. Aussawasathien, C. Teerawattananon, and A. Vongachariya, "Separation of micron to sub-micron particles from water: electrospun nylon-6 nanofibrous membranes as pre-filters," *Journal of Membrane Science*, vol. 315, no. 1-2, pp. 11–19, 2008.

[7] A. Greiner and J. H. Wendorff, "Electrospinning: a fascinating method for the preparation of ultrathin fibers," *Angewandte Chemie*, vol. 46, no. 30, pp. 5670–5703, 2007.

[8] D. Li and Y. Xia, "Electrospinning of nanofibers: reinventing the wheel?" *Advanced Materials*, vol. 16, no. 14, pp. 1151–1170, 2004.

[9] C. J. Luo, S. D. Stoyanov, E. Stride, E. Pelan, and M. Edirisinghe, "Electrospinning versus fibre production methods: from specifics to technological convergence," *Chemical Society Reviews*, vol. 41, no. 13, pp. 4708–4735, 2012.

[10] M. Inagaki, Y. Yang, and F. Kang, "Carbon nanofibers prepared via electrospinning," *Advanced Materials*, vol. 24, no. 19, pp. 2547–2566, 2012.

[11] S. N. Arshad, M. Naraghi, and I. Chasiotis, "Strong carbon nanofibers from electrospun polyacrylonitrile," *Carbon*, vol. 49, no. 5, pp. 1710–1719, 2011.

[12] J. Sutasinpromprae, S. Jitjaicham, M. Nithitanakul, C. Meechaisue, and P. Supaphol, "Preparation and characterization of ultrafine electrospun polyacrylonitrile fibers and their subsequent pyrolysis to carbon fibers," *Polymer International*, vol. 55, no. 8, pp. 825–833, 2006.

[13] B.-H. Kim, K. S. Yang, Y. H. Bang, and S. R. Kim, "Thermally induced porous carbon nanofibers for electrochemical capacitor electrodes from phenylsilane and polyacrylonitrile blend solutions," *Materials Letters*, vol. 65, no. 23-24, pp. 3479–3481, 2011.

[14] B.-H. Kim, K. S. Yang, and H.-G. Woo, "Thin, bendable electrodes consisting of porous carbon nanofibers via the electrospinning of polyacrylonitrile containing tetraethoxy orthosilicate for supercapacitor," *Electrochemistry Communications*, vol. 13, no. 10, pp. 1042–1046, 2011.

[15] M. Wu, Q. Wang, K. Li, Y. Wu, and H. Liu, "Optimization of stabilization conditions for electrospun polyacrylonitrile nanofibers," *Polymer Degradation and Stability*, vol. 97, no. 8, pp. 1511–1519, 2012.

[16] F. Cengiz and O. Jirsak, "The effect of salt on the roller electrospinning of polyurethane nanofibers," *Fibers and Polymers*, vol. 10, no. 2, pp. 177–184, 2009.

[17] S. K. Nataraj, K. S. Yang, and T. M. Aminabhavi, "Polyacrylonitrile-based nanofibers—a state-of-the-art review," *Progress in Polymer Science*, vol. 37, no. 3, pp. 487–513, 2012.

[18] N. T. Hieu, J. Suk, D. W. Kim, O. H. Chung, J. S. Park, and Y. Kang, "Kang Silicon nanoparticle and carbon nanotube loaded carbon nanofibers for use in lithium-ion battery anodes," *Synthetic Metals*, vol. 198, pp. 36–40, 2014.

[19] A. Ramos, I. Cameán, and A. B. García, "Graphitization thermal treatment of carbon nanofibers," *Carbon*, vol. 59, pp. 2–32, 2013.

[20] K. Yoon, B. S. Hsiao, and B. Chu, "Functional nanofibers for environmental applications," *Journal of Materials Chemistry*, vol. 18, no. 44, pp. 5326–5334, 2008.

[21] A. Jena and K. Gupta, "Pore volume of nanofiber nonwovens," *International Nonwovens Journal*, vol. 14, pp. 25–30, 2005.

[22] H. W. Liang, L. Wang, P. Y. Chen et al., "Carbonaceous nanofiber membranes for selective filtration and separation of nanoparticles," *Advanced Materials*, vol. 22, no. 42, pp. 4691–4695, 2010.

[23] X. B. Ke, H. Y. Zhu, X. P. Gao, J. W. Liu, and Z. F. Zheng, "High-performance ceramic membranes with a separation layer of metal oxide nanofibers," *Advanced Materials*, vol. 19, no. 6, pp. 785–790, 2007.

[24] J. Lin, B. Ding, J. Yang, J. Yu, and S. S. Al-Deyab, "Mechanical robust and thermal tolerant nanofibrous membrane for nanoparticles removal from aqueous solution," *Materials Letters*, vol. 69, pp. 82–85, 2012.

[25] X. Chen and S. S. Mao, "Titanium dioxide nanomaterials: synthesis, properties, modifications and applications," *Chemical Reviews*, vol. 107, no. 7, pp. 2891–2959, 2007.

[26] F. Gottschalk, T. Sonderer, R. W. Scholz, and B. Nowack, "Modeled environmental concentrations of engineered nanomaterials (TiO_2, ZnO, Ag, CNT, fullerenes) for different regions," *Environmental Science and Technology*, vol. 43, no. 24, pp. 9216–9222, 2009.

Hindawi Publishing Corporation
Journal of Nanomaterials
Volume 2015, Article ID 803937, 7 pages
http://dx.doi.org/10.1155/2015/803937

Research Article

Fabrication and Properties of High-Content Keratin/Poly (Ethylene Oxide) Blend Nanofibers Using Two-Step Cross-Linking Process

Yong Liu,[1] Xia Yu,[1] Jia Li,[1] Jie Fan,[1,2] Meng Wang,[3] Tong-Da Lei,[1] Jian Liu,[4] and Dongwei Huang[5]

[1]*Key Laboratory of Advanced Textile Composites, Ministry of Education, School of Textiles, Tianjin Polytechnic University, 399 West Binshui Road, Tianjin 300387, China*
[2]*National Engineering Laboratory for Modern Silk, College of Textile and Clothing Engineering, Soochow University, Suzhou 215123, China*
[3]*Tianjin Medical University Cancer Institute and Hospital, Huanhuxi Road, Hexi District, Tianjin 300060, China*
[4]*Department of Textiles, Zhejiang Fashion Institute of Technology, 495 Fenghua Road, Ningbo, Zhejiang Province 31521, China*
[5]*School of Science, Tianjin Polytechnic University, 399 West Binshui Road, Tianjin 300387, China*

Correspondence should be addressed to Jie Fan; fanjie@tjpu.edu.cn and Meng Wang; wm@medmail.com.cn

Received 26 October 2014; Revised 6 January 2015; Accepted 6 January 2015

Academic Editor: Yuqin Wan

High-content keratin/poly (ethylene oxide) (PEO) (90/10) blend nanofibers were prepared by electrospinning combined with a two-step cross-linking process. The keratin/PEO aqueous solution was firstly mixed with ethylene glycol diglycidyl ether (EGDE) as cross-linker and then electrospun into nanofibers. The resulting nanofibrous mats were cross-linked with EGDE vapor to decrease the solubility of nanofibers in water. The morphologies and properties of electrospun fibers were investigated by SEM, FTIR, TG, XRD, and contact angle testing, respectively. The results showed that the morphologies of nanofibers were uniform at the fiber average diameter of 300 nm with negligible bead defects by adding EGDE to keratin/PEO solutions. The cross-linking results showed that EGDE vapor could improve the hydrophobic property of blended nanofibers. The crystallinity of the keratin/PEO blend nanofiber mat increased from 13.14% for the uncross-linked sample to 21.54% and 35.15% for the first cross-linked and second cross-linked samples, respectively. Free defect nanofiber mats with high keratin content producing from this two-step cross-linking process are particularly promising for tissue engineering and cell-seeded scaffold.

1. Introduction

Keratin, as the major protein component of hair, wool, feathers, nails, and horns, belongs to a family of fibrous structural proteins and can be used in a variety of biomedical applications due to its biocompatibility and biodegradability [1–7]. Among these sources, human hair keratin emerges as an attractive protein because it can be easily obtained from the unlimited supply of human hair, making it abundant and readily available [8]. Electrospun nanofiber mats have many potential biomedical applications for their attractive features such as high surface-to volume ratio and very high porosity [9–11]. In addition, the structure and fiber distribution of the mats can be controlled to provide them with necessary mechanical property and induction during the cell culture process [12]. Due to their excellent properties, a handful of research groups have tried to create keratin fibrous matrices through electrospinning technology [13–16]. However, because of the low molecular weight and low viscosity of extracted keratin, most researchers have to resort to fabricate nanofibrous mats using keratin in combination with other natural or synthetic polymers [17].

Poly (ethylene oxide) (PEO) is a water-soluble polymer with good biocompatibility, low toxicity, and excellent spinnability. It has been proved that the fiber-forming property of keratin solution can be greatly improved by proper

addition of PEO [13, 18]. When PEO is blended with keratin in ratio of 30/70, the viscosity of spinning solutions increased and could be electrospun into continuous nanofibers with few defects. However, when the keratin content is further increased, the bead-like defects would appear on the fiber. How to prepare keratin/PEO nanofiber mat with high keratin content is the urgent problem to be solved for medical applications such as tissue engineering. Xin et al. [19] proposed a method to prepare keratin/PEO nanofiber mat with high keratin content. In their method, keratin was chemically modified by reacting sulfide side group with iodoacetic acid to enhance its solubility in organic solvent. Then, the modified keratin was blended with PEO in weight ratio of 90/10 and dissolved in 2, 2, 2,-trifluoroethanol (TFE) for preparation of nanofibers. Although organic solvent can increase keratin content in the resulting samples, the residual solvent in the nanofibers may cause an unexpected risk such as allergy. In addition, comparing with water as spinning solvent, organic reagent as solvent is not environmental friendly and not economic. Another problem to be solved for making biomedical keratin/PEO blend nanofiber mat is that the blend nanofiber mats are easily to be dissolved in water because of the water solubility of keratin and PEO. Xin et al. [19] also suggested that the water tolerance of the keratin/PEO blend nanofiber mat should be improved by cross-link treatment.

Ethylene glycol diglycidyl ether (EGDE) is a diepoxy cross-linker with two epoxide groups on either end. The epoxide group is reactive cyclic ether composed of three ring atoms, which make EGDE easily react with amino group on the amino acid at the end or in the middle of the keratin molecules in neutral condition; see Figure 1. In this condition, the keratin molecules can be extended by EGDE. Therefore, the spinnability of keratin and its content in the keratin/PEO blend nanofiber mat might be improved. Furthermore, EGDE might also provide an appropriate choice for improving the waterproof performance of the blend nanofiber mat.

In this work, a high keratin content keratin/PEO (90/10) blend nanofiber mat was fabricated by electrospinning using aqueous solution after cross-linking treatment with ethylene glycol diglycidyl ether (EGDE). In order to improve the water resistance of the nanofiber mat, the obtained blend nanofiber mat was further treated with EGDE vapor. The properties of nanofibers were investigated by SEM, FTIR, TG, and a video optics contact angle apparatus.

2. Experimental

2.1. Extraction of Human Hair Keratin. Human hair was obtained randomly from a local hair salon, washed extensively, rinsed with petroleum ether, and then dried at room temperature for 24 h and cut into 5 mm length. The extraction of keratin from human hair was performed according to the previously reported method [20]. The human hair (6 g) was shaken in 200 mL of aqueous solution containing 7 M urea, 2 wt% SDS, and 5 wt% $Na_2S_2O_5$ at 95°C for 4 h. The resulting mixture was filtered through a stainless-steel mesh, and subsequently dialyzed against 3 L of distilled water in cellulose tubing (molecular weight cut off = 8000–14000 Da) for 36 h with three changes of H_2O. Finally, the keratin solution was then lyophilized to obtain keratin powder.

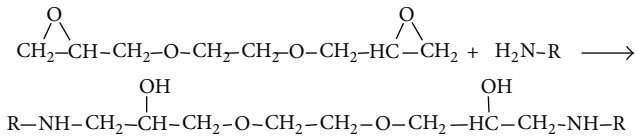

Figure 1: The schematic reaction of keratin with EGDE in neutral condition.

2.2. First Cross-Linking in Keratin/PEO Solutions. PEO (molecular weight = 400000 Da) power (10.5 g) was stirred in 150 mL of distilled water at 45°C for about 4 h. Keratin powder (0.126 g) was first dissolved in 7 wt% PEO solution (0.2 mL) and then distilled water was added into the mixture. The final mixture solution was 2 mL. Subsequently, EGDE (0.125 mL) was mixed into the keratin/PEO solution for electrospinning. The mixtures were stirred for 30 min at 60°C to ensure complete dissolution.

2.3. Fabrication of Electrospun Keratin/PEO Nanofibrous Mats. After dispensing the keratin/PEO solution after cross-linking by EGDE, electrospinning was performed at a constant feed rate of 0.5 mL/h, an accelerating voltage of 16 kv and the distance of 15 cm from the syringe tip to collector for ensuring complete evaporation of solvent. The nanofibrous mats were produced with a deposition time of 30 min.

2.4. Second Cross-Linking of Keratin/PEO Nanofibrous Mats. In order to increase the water resistance of nanofibers for their biomedical applications, keratin/PEO nanofiber mat was further cross-linked with EGDE vapor (99.5%) at 80°C for 5 h.

2.5. Characterization. The morphologies of the samples were analyzed using a scanning electron microscope (SEM, TM-1000, Hitachi, Japan). A Fourier transform infrared spectroscopy (FTIR, TENSOR37, Bruker, Germany) was employed to determine the chemical composition of the untreated keratin/PEO nanofibers, first cross-linking keratin/PEO nanofibers and second cross-linking keratin/PEO nanofibers. Infrared absorbance spectra of the samples were recorded at wavelengths 400–4000 cm^{-1}.

A video optics contact angle apparatus (JY-80, Chende Dingsheng Test machine equipment Co., Ltd., China) was used to assess the hydrophilicity of keratin/PEO nanofibers obtained in these experiments.

3. Results and Discussion

3.1. Morphologies of Nanofiber Mat. Figure 2 shows the SEM micrographs of the nanofiber mats produced from spinning solution containing 90 wt% keratin. As shown in Figure 2(a), there were bead defects in nanofibers when the spinning solution had not recieved EGDE cross-linking pretreatment. The

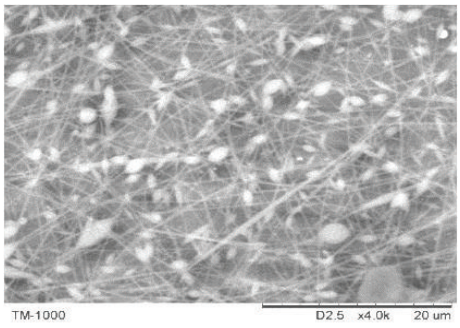

(a) Untreated keratin/PEO nanofibers mat

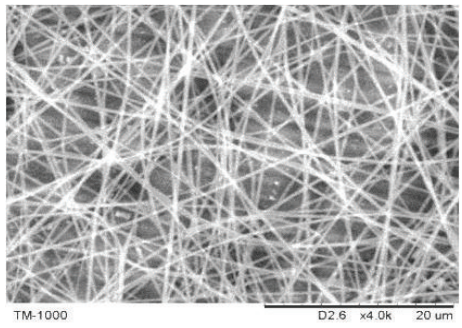

(b) First cross-linking keratin/PEO nanofibrous mat

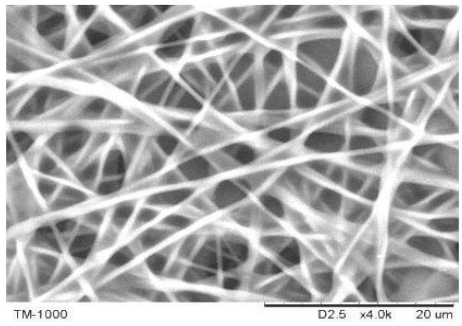

(c) Secondary cross-linking keratin/PEO nanofibrous mat

Figure 2: Scanning electron micrographs of nanofiber mats (a) uncross-linked keratin/PEO nanofibres mat; (b) first cross-linked keratin/PEO mat; (c) second cross-linked keratin/PEO mat.

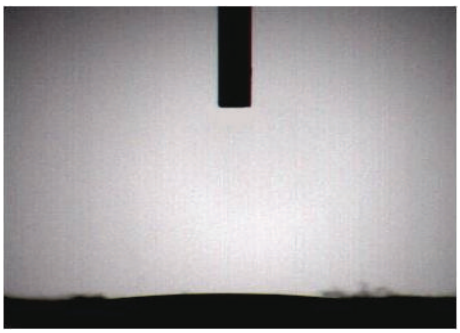

(a) First cross-linking keratin/PEO nanofibrous mat

(b) Secondary cross-linking keratin/PEO nanofibrous mat

Figure 3: Contact angle images of (a) First cross-linked keratin/PEO nanofibers mat; (b) second cross-linked with EGDE vapor (99.5%) keratin/PEO nanofibers mat.

reason might be that the low viscosity of spinning solution caused rise to break of jet [13]. Electrospun nanofibers with negligible bead defects were produced using the cross-linked spinning solution by EGDE (see Figure 2(b)), suggesting that EGDE could improve the spinnability of high content keratin solution. The improvement of fiber morphology is due to the cross-linking reaction between keratin molecules, which extends the keratin molecular length.

Figure 2(c) showed the morphology of the second cross-linked keratin/PEO nanofiber mat. Obviously, the morphologies of keratin/PEO nanofiber mat deteriorated slightly after the crosslinking. That may be due to the high temperature of the cross-link reaction with EGDE vapor.

3.2. Hydrophobicity of Nanofibers Mats. The water resistances of first cross-linked keratin/PEO nanofibers and secondary cross-linked keratin/PEO nanofibers were evaluated using a contact angle test apparatus. Contact angle images from the cross-linked keratin/PEO nanofibers are shown in Figure 3. For the first cross-linked keratin/PEO nanofibers, the angle was almost 0 (Figure 2(a)), suggesting that the first cross-linked keratin/PEO nanofibers are hydrophilic.

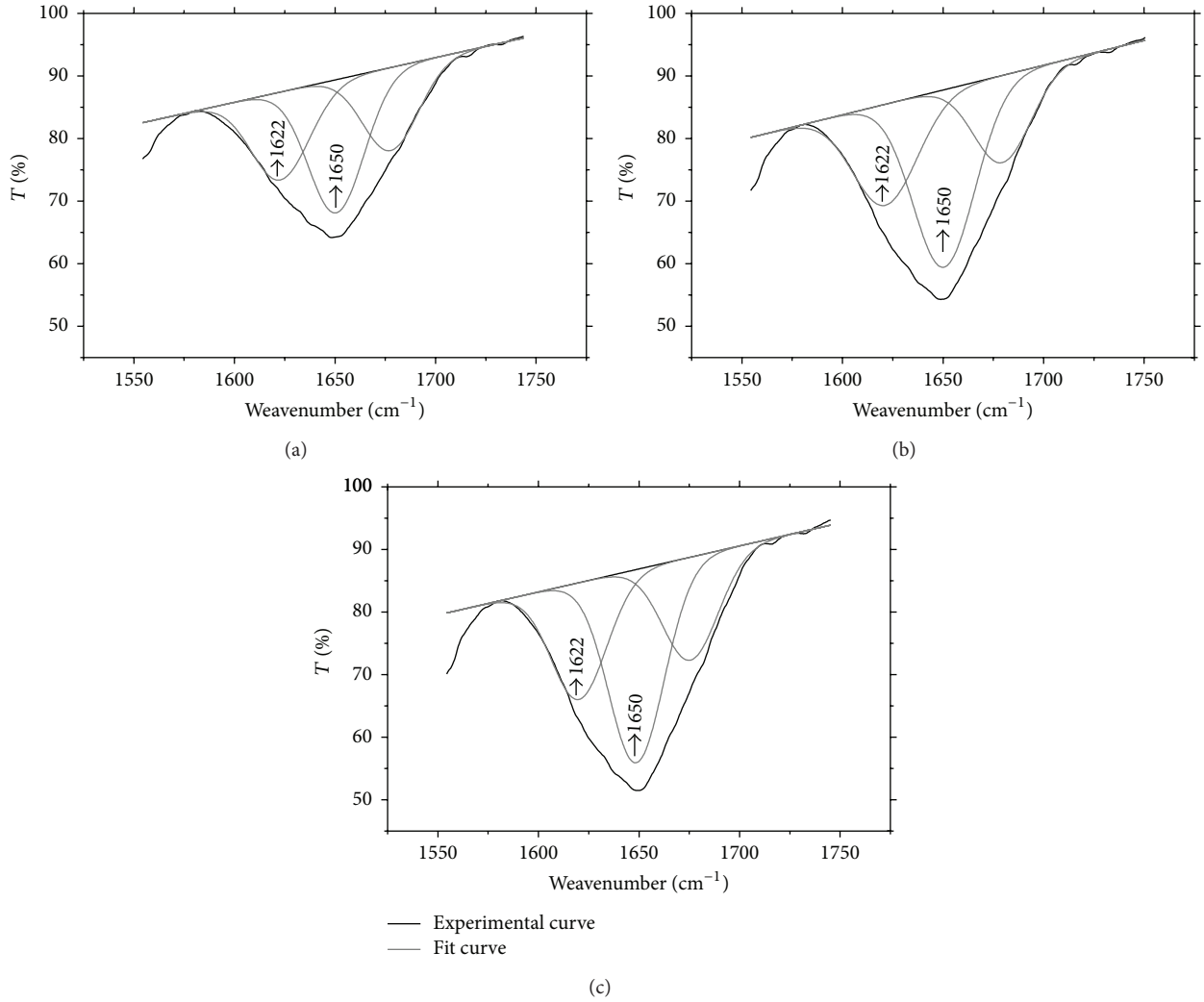

Figure 4: Curve-fitted amide I region of the keratin/PEO blend nanofiber mats.

The contribution of the first cross-linking reaction to the hydrophobicity of the fiber mat was negligible.

After secondary cross-linking with EGDE vapor, the contact angle of nanofiber mat increased to about 36.5°. The results showed that the secondary cross-linked method had a significant effect on the water resistances of keratin/PEO nanofibers.

3.3. FTIR Spectra Analysis. Infrared spectroscopy has been applied to investigate the molecular conformation of keratin/PEO nanofiber. The keratin component of the fiber gives the characteristic absorption bands in the regions named the amide A (2800–3286 cm^{-1}), amide I (1600–1700 cm^{-1}), amide II (1480–1580 cm^{-1}), and amide III (1220–1300 cm^{-1}) peaks, among which the amide I band corresponding to the C=O stretching vibration is especially sensitive to the secondary structure of the proteins. And the amide I transmission band is not disturbed by the transmission peak generated by PEO and EGDE. As a result, the amide I band is appropriate to characterize the structural conformation of keratin in the blend nanofibers [13].

The secondary structure of keratin in the different nanofibers was compared by curve fitting of the amide I band. Firstly, the transmitted spectra were normalized at 3284 cm^{-1}, at which the band corresponds to N-H stretching vibration of amide A. Since this transmission band was rarely affected by chemical treatment, it could be chosen as the band for spectrum normalization. Then, the amide I band was resolved in Gaussian-shaped bands at about 1622 cm^{-1} and 1650 cm^{-1} corresponding to the β-sheet structure and α-helix structure of keratin, shown in Figure 4. The maximum peak height and content of the peak's corresponding structure were calculated from peak area, as listed in Table 1.

It can be seen from Figure 4 that the shapes of peaks at 1625 cm^{-1} and 1622 cm^{-1} are almost the same for the three nanofiber mats. Table 1 suggests that the β-sheet structure and α-helix structure content of keratin almost do not change by the cross-link reaction by EGDE. The intensities of the two characteristic transmission peaks are gradually increased

Table 1: Amide I absorption bands of keratin/PEO blend nanofiber mats.

Wavenumber (cm^{-1})	Uncross-linked nanofiber mat		First cross-linked nanofiber mat		Second cross-linked nanofiber mat	
	Max height	Content	Max height	Content	Max height	Content
1622	14.0	29.7	16.1	28.9	18.7	28.2
1625	21.3	43.4	28.3	49.0	30.9	46.8

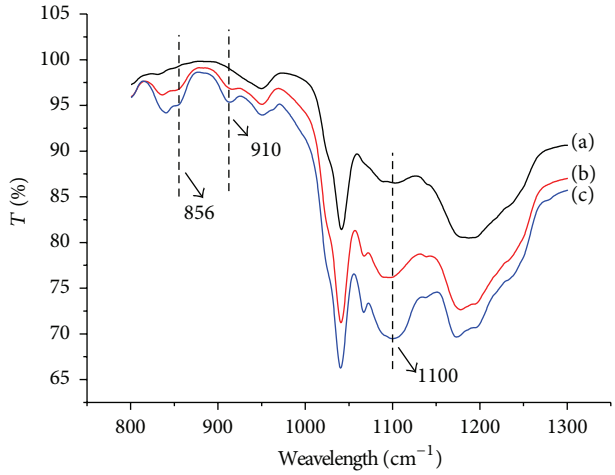

Figure 5: FTIR spectrum of keratin/PEO blend nanofiber mats (a) Untreated keratin/PEO nanofibers mat; (b) first cross-linking keratin/PEO nanofibrous mat; (c) secondary cross-linking keratin/PEO nanofibrous mat.

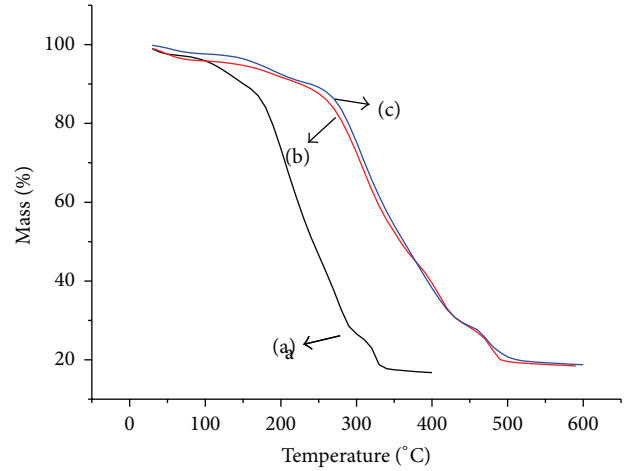

Figure 6: The TG curves of samples (a) untreated keratin/PEO nanofibers mat; (b) first cross-linking keratin/PEO nanofibrous mat; (c) secondary cross-linking keratin/PEO nanofibrous mat.

accompanying with the step-by-step cross-linking reaction (see Figure 4 and Table 1), meaning that the cross-linking reaction strengthened the absorption capability of keratin on its characteristic bands.

Previous research work showed that the characteristic transmission peak of PEO attributed to the C-O-C stretching vibration presents at 1094 cm^{-1} [21]. In addition, the peak value corresponding to the C-O-C stretching vibration would move to larger wave number at about 1102 cm^{-1} as the keratin content increased to 60% in the keratin/PEO blend materials. As a result, the weak peak at 1100 cm^{-1} of the uncross-linked nanofiber mat (line (a) in Figure 5) is due to the C-O-C stretching vibration of PEO for the three blend nanofiber mats with high keratin content [22]. The transmission spectrums of first and second cross-linked nanofiber mats in Figure 5 show that the C-O-C stretching vibration absorption are intensified by further cross-linking reaction with EGDE. That should be attributed to the epoxide groups in cross-linker EGDE.

The other two characteristic transmissions of EGDE located at the band 910 cm^{-1} and 859 cm^{-1} arise from the stretching vibrations of the epoxide groups in EGDE [23]. Figure 5 suggests that there are two weak transmission peaks at 910 cm^{-1} and 859 cm^{-1}, which indicates that there are small amount of EGDE residual in the first and second cross-linked nanofiber mats.

3.4. Thermal Analysis. TG analysis was conducted to evaluate the effect of cross-linking treatment on keratin/PEO nanofiber mats. Figure 6 illustrates that the uncross-linked nanofiber mat presents lower thermal stability comparing with the first and second cross-linked nanofiber mats.

There are four weight loss stages of evident mass losses in thermogravimetric graphs (Table 2). The smallest percentage of weight loss in the first stage that occurred bellow 100°C is ascribed to the vaporization of the free water, physical adsorption of water, and the water of crystallization [24]. The second weight loss stage ranging from 127°C to 230°C in the TG curve of the first and second cross-linked fiber mats can be attributed to the melting of a-keratin [25]. The corresponding weight loss stage of the uncross-linked sample appeared in the range from 111°C to 154°C [26].

The third weight loss stage of the first and second cross-linked fiber mats emerge from 211°C to 384°C with the maximum decomposition rate at 307°C, which corresponding to the decomposition of keratin [25]. The corresponding broad endothermic region of the uncross-linked sample emerges from 154°C to 258°C with the maximum decomposition rate at 209°C [22]. The last phase of mass loss is connected with the decomposition of keratin/PEO nanofibers. Weight loss analysis of nanofiber mats suggests that the lower temperature of denaturation/melting of a-keratin crystallites structure was shifted to the higher temperature after cross-linking treatment, suggesting that EGDE cross-link treatment can improve the thermal property of the keratin/PEO blend nanofiber mat.

3.5. X-Ray Diffraction Analysis. X-ray diffraction graphs were shown in Figure 7. It can be found that the typical

Table 2: The weight loss and range of temperatures with different stages in the TG curves of different samples.

	Untreated nanofiber mat		First cross-linking nanofiber mat		Second cross-linking nanofiber mat	
	Temperature (°C)	Weight loss (%)	Temperature (°C)	Weight loss (%)	Temperature (°C)	Weight loss (%)
Phase I	20–111	8.05	22–127	3.98	36–127	1.96
Phase II	111–154	21.01	127–211	5.35	127–229	7.15
Phase III	154–258	36.66	211–384	36.77	229–384	49.6
Phase IV	258–346	12.18	384–445	12.41	384–447	12.30

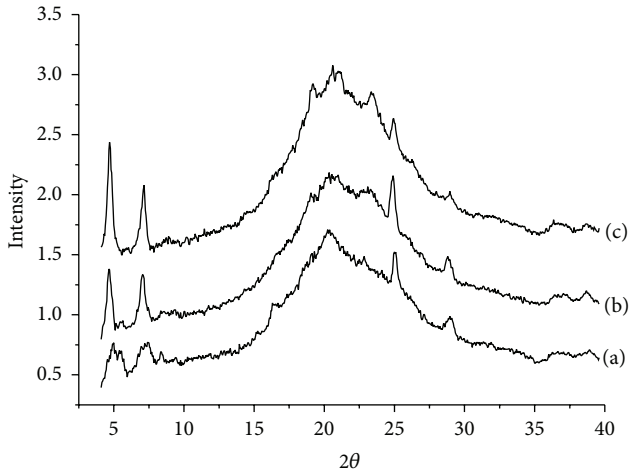

Figure 7: X-ray diffraction curves of the samples (a) untreated keratin/PEO nanofibers mat; (b) first cross-linking keratin/PEO nanofibrous mat; (c) secondary cross-linking keratin/PEO nanofibrous mat.

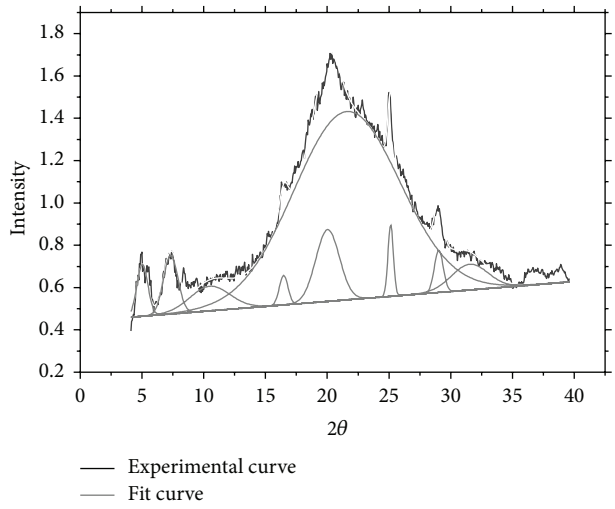

Figure 8: Curve decomposition of the uncross-linked keratin/PEO blend nanofiber mats.

diffraction pattern of keratin located at $2\theta = 10^{\circ}$ almost disappeared in the keratin/PEO blend nanofiber mats [26, 27]. Meanwhile, two diffraction peaks at $2\theta = 4.7^{\circ}$ and 7.0° emerge in the diffraction curve of the uncross-linked keratin/PEO blend nanofiber mats, and the intensity of the two peaks gradually intensified by the cross-linking reaction with EGDE. That means the emergency of the two peaks have a close relationship with the chemical reaction of keratin with the cross-linker.

The crystallinities of the three samples were calculated based on the X-ray diffraction curves. The crystalline and amorphous profiles could be obtained by curve decomposition using Gaussian function, as shown in Figure 8. The degree of crystallinity was determined based on the estimation ratio of the crystalline to amorphous material in the sample and listed in Table 3.

The results showed that the crystallinity of the keratin/PEO blend nanofiber mat increased from 13.14% for the uncross-linked sample to 21.54% and 35.15% for the first cross-linked and second cross-linked samples, respectively. The reason might be attributed to a new crystalline structure from the chemical reaction between cyclic ether bond of EGDE and the hydroxyl group of the keratin. In addition, the increased crystallinity of the first cross-linked and second cross-linked nanofiber mats keeps well with their improved thermal stability by TG test.

Table 3: Crystallinity of the keratin/PEO blend mats.

Sample	Crystallinity
Uncross-linked	13.14
First cross-linked	21.54
Secondary cross-linked	35.15

4. Conclusions

Keratin was extracted from human hair, and blended with PEO in aqueous solutions. The EGDE, as cross-linker, was firstly added to the high-content keratin/PEO (90/10) aqueous solutions for preparing nanofibers with negligible bead defects. EGDE vapor were then employed to cross-link keratin/PEO (90/10) nanofibers. The results showed that the use of cross-linker is capable of improving electrospinnability of keratin and could produce high-content keratin/PEO nanofibers mat. The secondary cross-linking through EGDE vapor could increase the hydrophobic property and the crystallinity of keratin/PEO (90/10) nanofibers mat. This study opens an effective way to fabricate the high-content keratin nanofibrous mats for cells growth or tissue engineering.

Conflict of Interests

There is no conflict of interests regarding the publication of this paper.

Acknowledgments

The present work is supported by National Natural Science Foundation of China under Grant (no. 51003073), Foundation for the Author of National Excellent Doctoral Dissertation of PR China (no. 201255), Program for New Century Excellent Talents in University (NCET-12-1063), Tianjin Natural Science Foundation (14JCYBJC17600), Ningbo Natural Science Foundation (2013A610016), and China Postdoctoral Science Foundation Grants nos. 2012M521122 and 2013T60559.

References

[1] L. Michaelis, "A study of keratin," *Journal of the American Leather Chemists Association*, vol. 30, no. 11, pp. 557–568, 1935.

[2] K. Yamauchi, A. Yamauchi, T. Kusunoki, A. Kohda, and Y. Konishi, "Preparation of stable aqueous solution of keratins, and physiochemical and biodegradational properties of films," *Journal of Biomedical Materials Research*, vol. 31, no. 4, pp. 439–444, 1996.

[3] K. Yamauchi and A. Khoda, "Novel proteinous microcapsules from wool keratins," *Colloids and Surfaces B*, vol. 9, pp. 117–119, 1997.

[4] A. Tachibana, Y. Furuta, H. Takeshima, T. Tanabe, and K. Yamauchi, "Fabrication of wool keratin sponge scaffolds for long-term cell cultivation," *Journal of Biotechnology*, vol. 93, no. 2, pp. 165–170, 2002.

[5] T. Tanabe, N. Okitsu, A. Tachibana, and K. Yamauchi, "Preparation and characterization of keratin-chitosan composite film," *Biomaterials*, vol. 23, no. 3, pp. 817–825, 2002.

[6] K. Katoh, M. Shibayama, T. Tanabe, and K. Yamauchi, "Preparation and physicochemical properties of compression-molded keratin films," *Biomaterials*, vol. 25, no. 12, pp. 2265–2272, 2004.

[7] K. Katoh, T. Tanabe, and K. Yamauchi, "Novel approach to fabricate keratin sponge scaffolds with controlled pore size and porosity," *Biomaterials*, vol. 25, no. 18, pp. 4255–4262, 2004.

[8] W. T. Sow, Y. S. Lui, and K. W. Ng, "Electrospun human keratin matrices as templates for tissue regeneration," *Nanomedicine*, vol. 8, no. 4, pp. 531–541, 2013.

[9] D. B. Khadka and D. T. Haynie, "Protein- and peptide-based electrospun nanofibers in medical biomaterials," *Nanomedicine: Nanotechnology, Biology, and Medicine*, vol. 8, no. 8, pp. 1242–1262, 2012.

[10] Y. Liu, J. Li, Y. Tian, J. Liu, and J. Fan, "Multi-physics coupled fem method to simulate the formation of crater-like taylor cone in electrospinning of nanofibers," *Journal of Nano Research*, vol. 27, pp. 153–162, 2014.

[11] Y. Liu, J. Li, Y. Tian, X. Yu, J. Liu, and B.-M. Zhou, "CLSVOF method to study the formation process of Taylor cone in crater-like electrospinning of nanofibers," *Journal of Nanomaterials*, vol. 2014, Article ID 635609, 12 pages, 2014.

[12] J.-H. He, Y. Liu, L.-F. Mo, Y.-Q. Wan, and L. Xu, *Electrospun Nanofibres and Their Applications*, Smithers Rapra Technology, Shropshire, UK, 2008.

[13] A. Aluigi, C. Vineis, A. Varesano, G. Mazzuchetti, F. Ferrero, and C. Tonin, "Structure and properties of keratin/PEO blend nanofibres," *European Polymer Journal*, vol. 44, no. 8, pp. 2465–2475, 2008.

[14] J. Li, Y. Li, L. Li, A. F. T. Mak, F. Ko, and L. Qin, "Preparation and biodegradation of electrospun PLLA/keratin nonwoven fibrous membrane," *Polymer Degradation and Stability*, vol. 94, no. 10, pp. 1800–1807, 2009.

[15] H. Thomas, E. Heine, R. Wollseifen, C. Cimpeanu, and M. Möller, "Nanofibers from natural and inorganic polymers via electrospinning," *International Nonwovens*, vol. 14, no. 3, pp. 12–18, 2005.

[16] J. Choi, G. Panthi, Y. Liu et al., "Keratin/poly (vinyl alcohol) blended nanofibers with high optical transmittance," *Polymer*, vol. 58, pp. 146–152, 2015.

[17] J. G. Rouse and M. E. van Dyke, "A review of keratin-based biomaterials for biomedical applications," *Materials*, vol. 3, no. 2, pp. 999–1014, 2010.

[18] A. Varesano, A. Aluigi, C. Vineis, and C. Tonin, "Study on the shear viscosity behavior of keratin/PEO blends for nanofibre electrospinning," *Journal of Polymer Science. Part B: Polymer Physics*, vol. 46, no. 12, pp. 1193–1201, 2008.

[19] Z.-C. Xin, J. Yuan, W.-P. Chae, and I.-K. Kang, "Keratin nanofibers as a biomaterial," in *2010 International Conference on Nanotechnology and Biosensors*, vol. 2, pp. 120–124, IACSIT Press, Singapore, 2011.

[20] A. Aluigi, A. Varesano, A. Montarsolo et al., "Electrospinning of keratin/poly(ethylene oxide) blend nanofibers," *Journal of Applied Polymer Science*, vol. 104, no. 2, pp. 863–870, 2007.

[21] X. Li and S. L. Hsu, "An analysis of the crystallization behavior of poly(ethylene oxide)/poly(methyl methacrylate) blends by spectroscopic and calorimetric techniques," *Journal of Polymer Science: Polymer Physics Edition*, vol. 22, no. 7, pp. 1331–1342, 1984.

[22] C. Tonin, A. Aluigi, C. Vineis, A. Varesano, A. Montarsolo, and F. Ferrero, "Thermal and structural characterization of poly(ethylene-oxide)/keratin blend films," *Journal of Thermal Analysis and Calorimetry*, vol. 89, no. 2, pp. 601–608, 2007.

[23] D. Huang, Z. Peng, Z. Hu et al., "A new consolidation system for aged silk fabrics: effect of reactive epoxide-ethylene glycol diglycidyl ether," *Reactive and Functional Polymers*, vol. 73, no. 1, pp. 168–174, 2013.

[24] Z. Éhen, C. Novák, J. Sztatisz, and O. Bene, "Thermal characterization of hair using TG-MS combined thermoanalytical technique," *Journal of Thermal Analysis and Calorimetry*, vol. 78, no. 2, pp. 427–440, 2004.

[25] N. Eslahi, F. Dadashian, and N. H. Nejad, "Optimization of enzymatic hydrolysis of wool fibers for nanoparticles production using response surface methodology," *Advanced Powder Technology*, vol. 24, no. 1, pp. 416–426, 2013.

[26] J. Cao, "Melting study of the α-form crystallites in human hair keratin by DSC," *Thermochimica Acta*, vol. 335, no. 1-2, pp. 5–9, 1999.

[27] J. Cao and C. A. Billows, "Crystallinity determination of native and stretched wool by X-ray diffraction," *Polymer International*, vol. 48, no. 10, pp. 1027–1033, 1999.

Hindawi Publishing Corporation
Journal of Nanomaterials
Volume 2015, Article ID 750726, 10 pages
http://dx.doi.org/10.1155/2015/750726

Research Article

Fabrication, Characterization, and Antibacterial Properties of Electrospun Membrane Composed of Gum Karaya, Polyvinyl Alcohol, and Silver Nanoparticles

Vinod Vellora Thekkae Padil, Nhung H. A. Nguyen, Alena Ševců, and Miroslav Černík

Institute for Nanomaterials, Advanced Technologies and Innovation, Technical University of Liberec, Studentská 1402/2, Czech Republic

Correspondence should be addressed to Miroslav Černík; miroslav.cernik@tul.cz

Received 30 July 2014; Accepted 13 October 2014

Academic Editor: Naeem Faraz

Gum karaya (GK), a natural hydrocolloid, was mixed with polyvinyl alcohol (PVA) at different weight ratios and electrospun to produce PVA/GK nanofibers. An 80 : 20 PVA/GK ratio produced the most suitable nanofiber for further testing. Silver nanoparticles (Ag-NPs) were synthesised through chemical reduction of $AgNO_3$ (at different concentrations) in the PVA/GK solution, the GK hydroxyl groups being oxidised to carbonyl groups, and Ag^+ cations reduced to metallic Ag-NPs. These PVA/GK/Ag solutions were then electrospun to produce nanofiber membranes containing Ag-NPs (Ag-MEMs). Membrane morphology and other characteristics were analysed using scanning electron microscopy coupled with energy dispersive X-ray analysis, transmission electron microscopy, and UV-Vis and ATR-FTIR spectroscopy. The antibacterial activity of the Ag-NP solution and Ag-MEM was then investigated against Gram-negative *Escherichia coli* and *Pseudomonas aeruginosa* and Gram-positive *Staphylococcus aureus*. Our results show that electrospun nanofiber membranes based on natural hydrocolloid, synthetic polymer, and Ag-NPs have many potential uses in medical applications, food packaging, and water treatment.

1. Introduction

Natural gums derived from plants have many potentially valuable uses as food additives and pharmaceutical ingredients as well as stabilising, suspending, gelling, emulsifying, thickening, binding, and coating agents [1]. In recent years, much research has been undertaken on the application and physicochemical, morphological, and structural properties of exudate gums, such as gum arabic, gum tragacanth, gum karaya, and gum kondagogu [2–5]. Natural biopolymers based on plant exudates have already been used in the preparation of nanoparticles, with gum arabic, for example, having been assessed as a nontoxic phytochemical scaffold for the production of biocompatible gold nanoparticles, which have diagnosis and therapeutic applications [6]. Natural tree-based hydrocolloids serve as both an environmentally benign medium and as a chemical reductant, as they have extensive numbers of hydroxyl, carbonyl, and carboxylic groups. These groups facilitate the formation of metal nanoparticles through the reduction of metal ions and the biopolymer can act as a stabilising agent to prevent nanoparticle agglomeration [7, 8]. Furthermore, the complex polysaccharide and protein structures of such gums can effectively lock metal nanoparticles to produce nontoxic nanoparticulate products that have a wide range of applications (e.g., in nanomedicine) and are stable under *in vivo* conditions [9]. Gum karaya (GK), defined by JECFA (Joint Expert Committee for Food Additives) as dried exudates from the stems and branches of *Sterculia urens* Roxburgh and other species of *Sterculia* (family: Sterculiaceae), is a partially acetylated polysaccharide with a branched structure and a high molecular mass of ~16×10^6 Da [1, 10]. This gum contains about 60% neutral sugars (rhamnose and galactose) and 40% acidic sugars (glucuronic and galacturonic acids) [11]. Due to its high viscosity and suspension properties, GK is widely used as a food stabiliser, meat binder, bulk laxative, denture powder, and textile size [1].

Electrospinning, an environmentally friendly process capable of producing polymer nanofibers with high porosity and large surface area, allows for the use of a variety of polymers and polymer mixtures together with additives and fillers such as gums [12, 13]. Nanofibers produced by electrospinning can be further supplemented with a variety of nanoparticles in order to fabricate composites with unique, tailor-made properties for different applications [14]. The "spinnability" and mechanical integrity of natural polymers, such as chitin, chitosan, GK, or ulvan polysaccharide, can be improved by blending with synthetic biodegradable polymers such as polyvinyl alcohol (PVA), polyethylene oxide (PEO), and polyvinylpyrrolidone (PVP) [15–18]. The nature and morphology of the nanofibers produced will be affected by many factors, including the physicochemical properties of the polymer and various parameters of the electrospinning process, including solution viscosity and mixture conductivity [19]. Nanofibers have recently been successfully electrospun using ulvan polysaccharide extracted from an *Ulva* sp. seaweed blended with PVA [16]. As PVA is a water soluble and biocompatible polymer, it is one of the best materials for preparation of a wide range of potential biomedical materials [20, 21].

The properties of silver nanoparticles (Ag-NPs) make them particularly useful as antimicrobial materials, biosensors, composite fibres, cryogenic superconducting materials, cosmetic products, antibacterial medical textiles, wound dressing materials, and electronic components [22–24]. Silver (Ag), especially in nanoparticulate form, is widely recognised as an efficient disinfectant against a wide spectrum of bacteria and viruses and, as such, Ag-NPs (usually between 10 and 20 nm) have been used as additives in both natural and synthetic biomedical gels, films, and fibers to improve the antibacterial capability of these materials [25–27]. To date, Ag-NPs have been incorporated into a wide variety of natural or synthetic electrospun nanofibers, including carboxymethyl/chitosan, chitosan/PVA, PVA/gum arabic, PVA/carboxyl methyl/chitosan, PVA/tetraethyl orthosilicate, carboxymethyl chitosan/polyethylene oxide, and curcumin/chitosan-PVA [28–33]. As an advanced process for generating nanostructures, coaxial electrospinning was also reported to prepare Ag NPs loaded polyacrylonitrile nanofibers [34, 35].

In this study, we describe a method for producing a new nanofiber membrane and film composed of PVA/GK coated with Ag-NPs. We assess the material's morphology using various microscopy and spectroscopy techniques and assess its antibacterial activity using Gram-positive and Gram-negative bacteria. The results are discussed in the light of their potential usefulness in the medical, food packaging, and water treatment industries.

2. Experimental Section

2.1. Materials. Commercial gum karaya (partially deacetylated) with molecular weight (Mw: 1.827×10^6 g/mole), PVA (Mw 88,000, 88% deacetylated), silver nitrate ($AgNO_3$), and glutaraldehyde solution (Grade 1, 50% in water) were purchased from Sigma-Aldrich, USA. All other reagents used in the experiment were of analytical grade. Deionised water was used throughout.

2.2. Preparation of PVA, GK, and Electrospinning Solutions (PVA/GK). A 10 wt% aqueous PVA solution and 1 wt% GA were prepared in deionised water. A range of PVA/GK electrospinning solutions were produced by mixing PVA (10 wt%) solution with GK (1.0 wt%) at different weight ratios (i.e., 100 : 0, 90 : 10, 80 : 20, 60 : 40, and 50 : 50) in order to identify that, giving the best spinnability and most uniform nanofiber size distribution. The mixtures were kept on a magnetic stirrer at 70°C for 5 h to ensure complete dissolution. The solutions were centrifuged to remove any suspended particles prior to electrospinning.

2.3. Preparation of Ag-NP (PVA/GK/Ag Solution). Based on the results of electrospinning different weight ratios of PVA/GK, the most suitable combination was found to be an 80 : 20 weight ratio mix. This was mixed with aqueous $AgNO_3$ solutions of 1, 2, 4, 5, and 10 mmol L^{-1} and the resultant solutions stirred at room temperature for 12 h to obtain homogeneous solutions. Sufficient Ag-NP formation was indicated by a dark yellowish colour, whereupon the PVA/GK/Ag solution was deemed ready for electrospinning and testing for antibacterial activity.

2.4. Preparation of Ag-MEMs. The PVA/GK and PVA/GK/Ag solutionswere electrospun in order to produce nanofiber membranes. All electrospinning was carried out with a Nanospider electrospinning machine (NS IWS500U, Elmarco, Czech Republic) under the following parameters: spinning electrode width = 500 mm, effective nanofiber layer width = 200–500 mm; spinning distance = 130–280 mm, substrate speed = 0.015–1.95 m/min, process air flow = 20–150 m^3/h, and voltage 0–50 kV. The PVA/GK and PVA/GK/Ag (Ag-MEM) membranes were then cross-linked through exposure to glutaraldehyde vapour in desiccators for 12 h. Both the membranes were then heated in an oven for 12 h at 110°C to complete the cross-linking process. Any excess of glutaraldehyde was removed by keeping membranes under vacuum for 24 h.

2.5. Characterization. Formation of Ag-NPs was confirmed through UV-Vis spectroscopy (UV-1601, Shimadzu, Japan) and transmission electron microscopy (TEM; Tecnai F30, Japan; acceleration voltage 15 kV) was used to analyse Ag-NP size distribution. The morphology of the PVA/GK nanofibers (different weight ratios) and the Ag-MEM was assessed using scanning electron microscopy with energy dispersive X-ray spectroscopy (SEM-EDXA; Zeiss, Ultra/Plus, Germany). Attenuated total reflectance-fourier transform infrared spectroscopy (ATR-FTIR; NICOLET IZ10, Thermo Scientific, USA) was used to characterise the functional groups of PVA, GK, PVA/GK, and Ag-MEM. Conductivity and viscosity of the electrospinning solutions were recorded using a Toledo FG3 electric conductivity meter (Mettler, USA) and a rotational viscometer (Brookfield Engineering Laboratories,

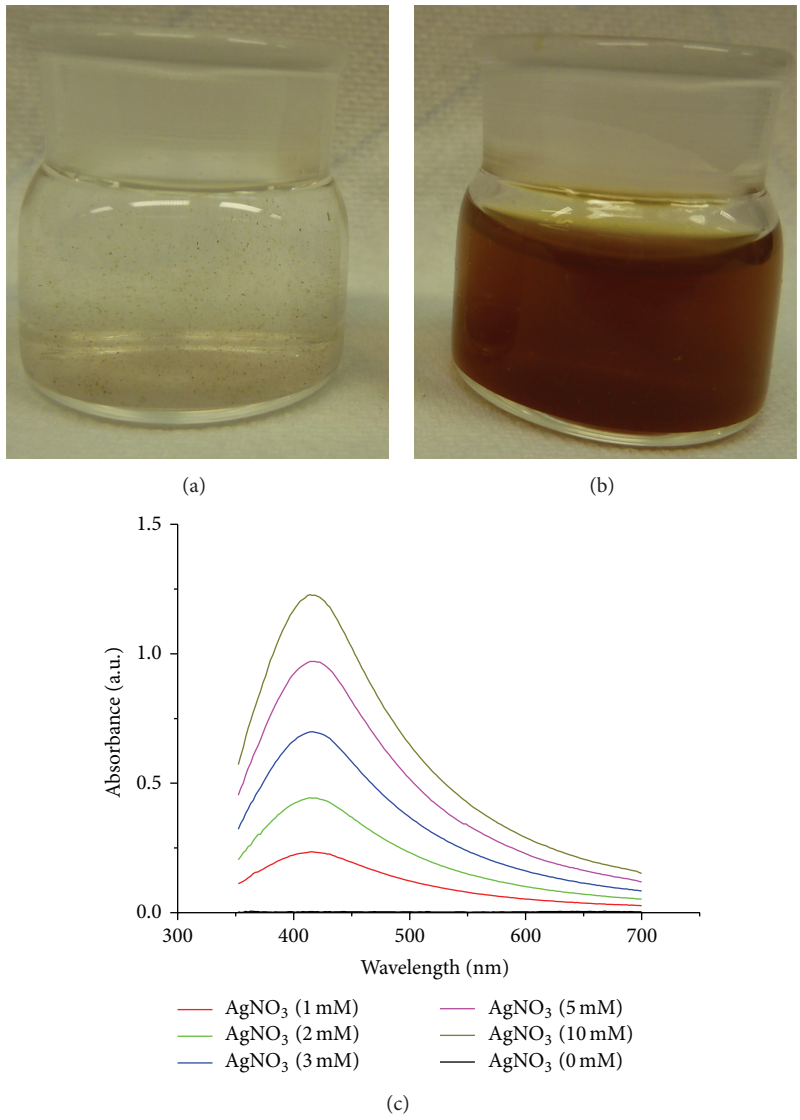

Figure 1: PVA/GK solution (a) before formation of Ag NPs and (b) after Ag NPS formation; and (c) UV-vis spectra of PVA/GK aqueous solution containing Ag-NP prepared at various concentrations of $AgNO_3$ (0, 1, 2, 4, 5, and 10 mM).

USA). The concentration of Ag NPs in PVA/GK/Ag solution and Ag-MEM was established by ICP-AES.

2.6. Antibacterial Activity Tests

2.6.1. Bacterial Strains and Culture Media. The bacterial strains of Gram-negative *Escherichia coli* (CCM 3954) and *Pseudomonas aeruginosa* (CCM 3955) and Gram-positive *Staphylococcus aureus* (CCM 3953) used in this study were obtained from the Czech Collection of Microorganisms, Masaryk University Brno, Czech Republic. Bacterial suspensions were always prepared fresh by growing a single colony overnight at 37°C in a nutrient broth. The sample turbidity was adjusted to an optical density of 0.1 at 600 (OD 600) before performing the antibacterial experiments. All agar plates were freshly prepared before the antibacterial tests. A sterilised cotton swab was dipped into the culture suspension and the cells spread homogeneously over the agar plates. These plates were immediately used for the antibacterial activity tests.

2.6.2. Determining Zone of Inhibition. We determined the antibacterial activity of four PVA/GK/Ag solutions (1, 2, 4, 5, and 10 mM) and samples of Ag-MEM (each containing the equivalent of 1 mM of $AgNO_3$). The PVA/GK/Ag solutions were pipetted onto a sterilised membrane filter and placed onto an inoculated agar plate, while 6 mm diameter circles of Ag-MEM were placed directly onto inoculated agar plates. Similarly sized samples of PVA/GK solution (10 mg/mL) and samples of nanofiber membrane without Ag-NP were used as controls. The samples and inoculated agar plates were then incubated for 24 h at 37°C. The zone of inhibition (ZOI) was determined as the total diameter (mm) of PVA/GK/Ag-filter paper or Ag-MEM sample plus the halo zone where bacterial

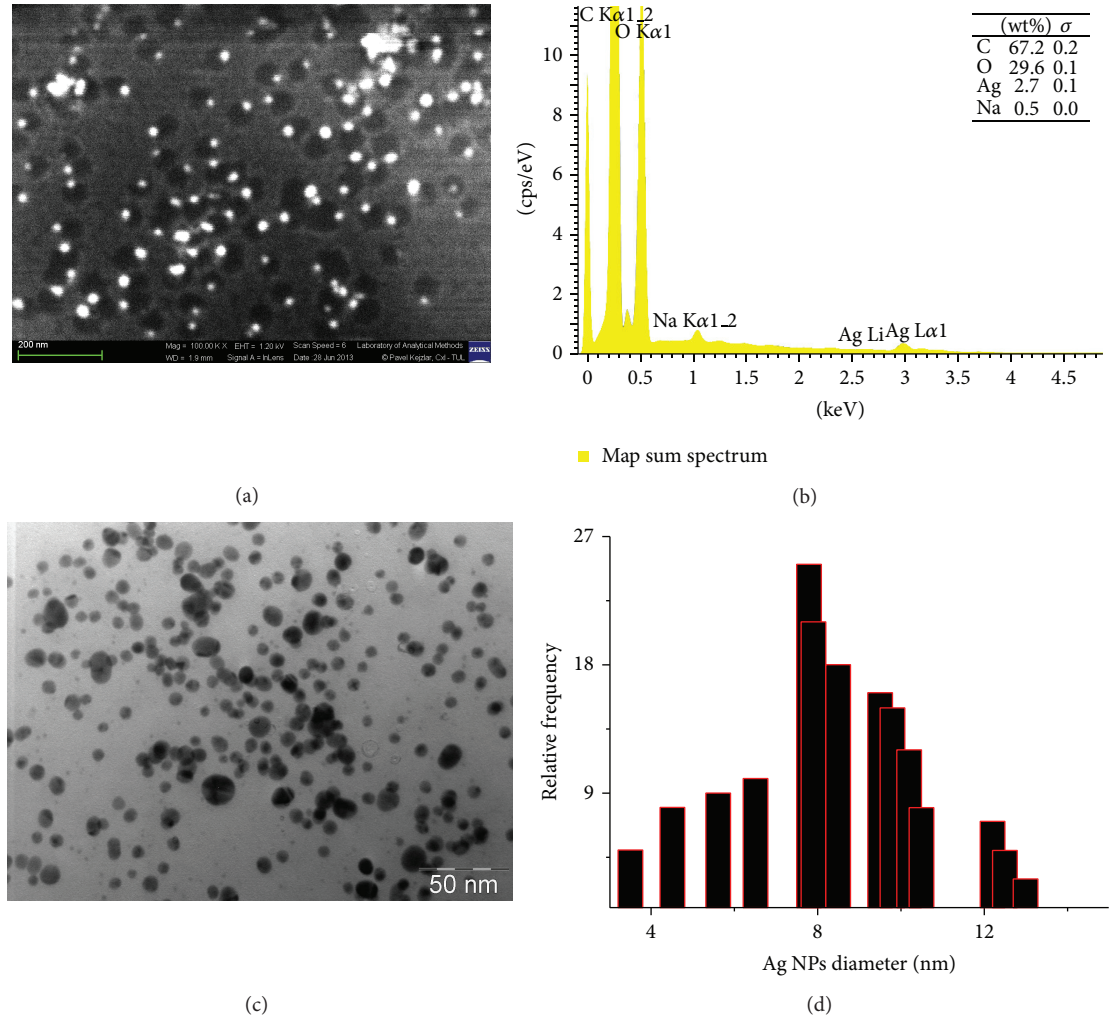

Figure 2: SEM image of (a) Ag-NP prepared using PVA/GK; (b) EDS of Ag-NP, showing the presence of Ag; and (c) TEM image of Ag-NP prepared using PVA/GK and 10 mM $AgNO_3$; and (d) particles diameter distribution of Ag NPs (7–10 nm).

growth was inhibited. All measurements were performed in triplicate for the PVA/GK/Ag solutions and repeated three times (once for each bacterial strain, i.e., nine runs) for the Ag-MEM.

2.7. Statistical Analysis. One-way ANOVA and the Mann-Whitney test (GraphPad Prism Software, CA, USA) were used to compare differences among the mean ZOIs for the PVA/GK/Ag solutions and Ag-MEM on *E. coli*, *P. aeruginosa,* and *S. aureus*.

3. Results and Discussion

3.1. Preparation of Ag-NP and PVA/GK. The colour change of the PVA/GK solution with a ratio of 80 : 20 to dark yellow following formation of Ag-NPs is shown in Figures 1(a) and 1(b). The 420 nm maximum absorption band seen in the PVA/GK UV-Vis spectra (Figure 1(c)) is a typical plasmon absorption of Ag-NP formation [33].

GK comprises around 60% neutral sugars and 40% acidic sugars and a range of hydroxyl, carbonyl, carboxyl, and acetyl functional groups [36]. Following addition of $AgNO_3$, the GK hydroxyl groups are oxidised to carbonyl groups and Ag^+ cations are reduced to metallic Ag-NPs. PVA acts as a good stabilising agent for these Ag-NPs due to a free electron pair on the hydroxyl oxygen [31]. Similar observations have been reported for synthesis of Ag-NPs using PVA/carboxymethyl-chitosan and chitosan/PVA polymer blends and gum arabic/PVA hydrogel [28, 29, 31].

Presence of Ag-NPs in the PVA/GK/Ag solution was confirmed by SEM imaging of freshly formed Ag-NP (Figure 2(a)) and its corresponding EDXA analysis (Figure 2(b)). TEM imaging and a particle-size histogram indicate that the majority of the Ag-NPs formed were within a range of 7–10 nm (Figures 2(c) and 2(d)).

3.2. Electrospinning of PVA/GK and PVA/GK/Ag. We prepared a range of PVA/GK weight ratio mixtures (100 : 0,

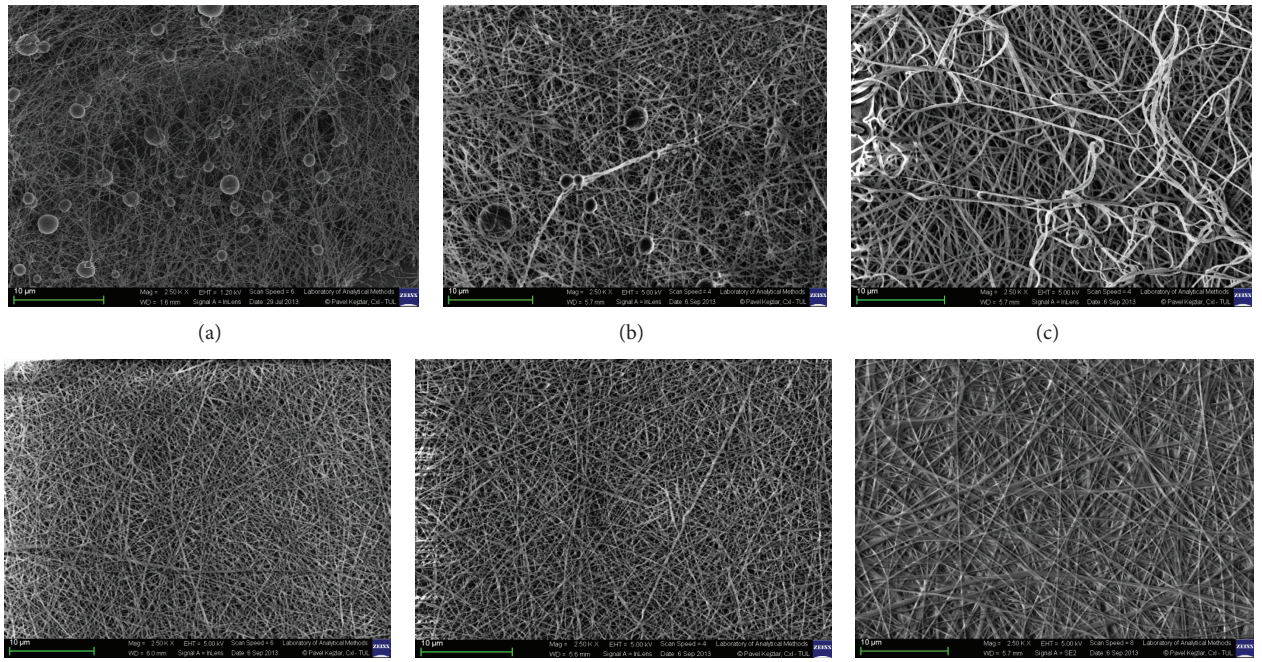

(a) (b) (c)

(d) (e) (f)

Figure 3: SEM images of electrospun PVA/GK mixed with different weight ratios: (a) PVA/GK (50/50); (b) PVA/GK (60/40); (c) PVA/GK (70/30); (d) PVA/GK (80/20); (e) PVA/GK (90/10); and (f) neat PVA (100/0) 10 μm.

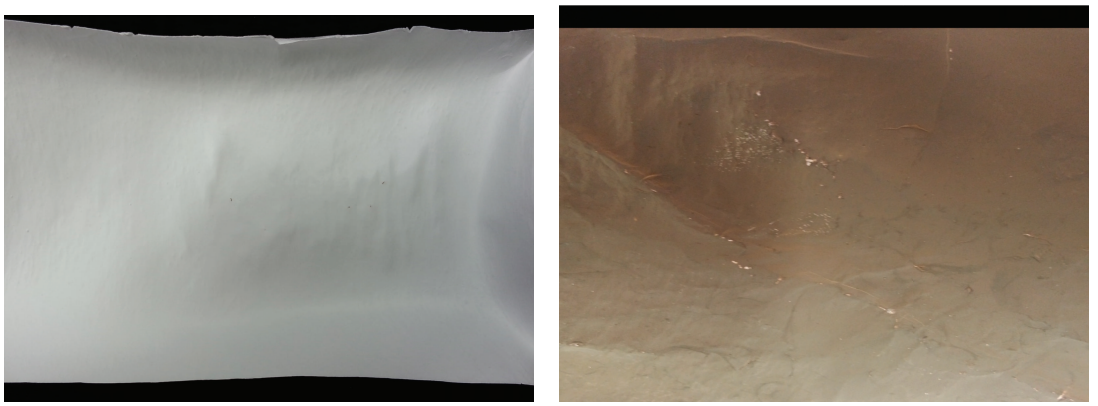

(a) (b)

Figure 4: Digital image of (a) PVA/GK membrane and (b) Ag-MEM prepared by electrospinning of PVA/GK and PVA/GK/Ag NP solution, respectively.

90 : 10, 80 : 20, 60 : 40, and 50 : 50) in order to optimise the electrospinning solution, that is, to obtain optimal spinnability and uniform nanofiber size. SEM images of the resultant nanofibers (Figures 3(a)–3(f)) indicate that, while nanofibers of pure PVA were uniformly distributed (Figure 3(f)), pure GK fibres could not be electrospun at all due to repulsion from the various highly charged polyanions resulting in chain entanglement.

Further, the pure GK solution proved too viscous for electrospinning as GK is an acidic polymer with high viscosity and molecular weight [8]. Indeed, the PVA/GK blend ratio proved critical in obtaining uniform nanofibers, with evenly formed nanofibers only obtained at PVA/GK weight ratios of 80 : 20 and 90 : 10 (Figures 3(d) and 3(e)). Uniform nanofiber diameters of 200 nm were only produced at a PVA/GK weight ratio 80 : 20, however; hence, this ratio was selected for all further experiments. Overall, higher PVA/GK ratios enhanced fibre size homogeneity by improving the solubility of the mixed polymers and by decreasing polymer chain aggregation.

Not only were the nature and morphology of the nanofibers affected by polymer solution viscosity and conductivity (both affected by the PVA/GK weight ratio used), but we also found that the viscosity of the PVA/GK/Ag

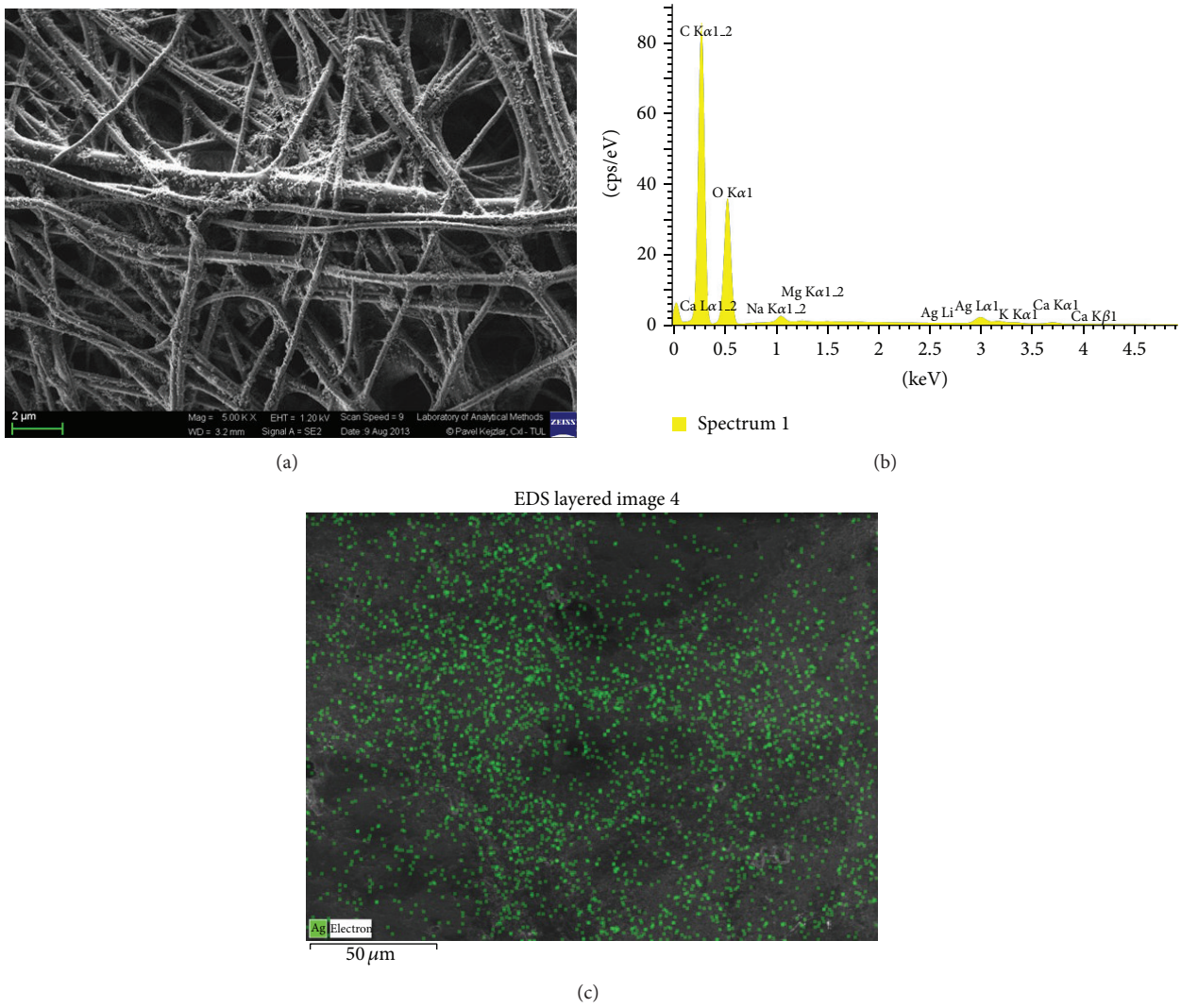

Figure 5: SEM micrograph of (a) Ag-MEM showing the presence of Ag NPs on the surface membrane; (b) EDXA analysis of Ag-NP on Ag-MEM; (c) EDXA layered image indicating the presence of Ag-NP on the surface of Ag-MEM.

electrospinning solution increased from 300 to 500 mPa·s and its conductivity from 2500 to 3200 mS·cm^{-1}, with increasing $AgNO_3$ concentration (1, 2, 4, 5, and 10 mmol L^{-1}). The levels at 1 mM, however, were within acceptable limits for electrospinning using the 80 : 20 PVA/GK weight ratios and provided reasonable Ag-NP coverage in the final Ag-MEM (Figure 4(b)) products. The digital photographs of electrospun PVA/GK nanofiber and Ag-MEM are presented in Figures 4(a) and 4(b), respectively.

SEM micrographs of the final electrospun Ag-MEM (Figure 5(a)) clearly show Ag-NPs on the PVA/GK nanofiber surface, and Ag and Ag-NP presence was also confirmed by EDXA analysis (Figure 5(b)) and an EDXA layered image (Figure 5(c)).

3.3. ATR-FTIR Characterisation of Ag-MEM. In examining the bonding between Ag-NPs and the Ag-MEM (also GK, PVA, and PVA/GK) using ATR-FTIR, we noted a broad absorption peak centred around 3318–3350 cm^{-1} for all samples, attributable to O–H stretching vibration in the hydrogen bonded hydroxyl groups (Figure 6).

The peaks at 1430 cm^{-1} and 1326 cm^{-1} are characteristic of O–H groups and C–H deformation vibration in PVA, respectively, while the peak at 1000–1100 cm^{-1} can be assigned to C–O stretching and O–H bending vibrations arising from the PVA chain. The appearance of a new peak at 1561 cm^{-1} in the PVA/GK blend represents O–H group deformation vibration with the H bond, suggesting the formation of an H bond between PVA and GK when forming the PVA/GK blend. Structurally, GK has abundant hydroxyl groups; hence, H bonding interactions between GK and PVA occur readily on blending with PVA. The O–H bond absorption band at 3300–3500 cm^{-1} indicates that the O–H bond was involved in bonding with the Ag-NPs. Carboxylate group stretching vibration at 1419 cm^{-1} was considerably reduced in the PVA/GK/Ag-MEM spectrum, demonstrating binding of Ag^+

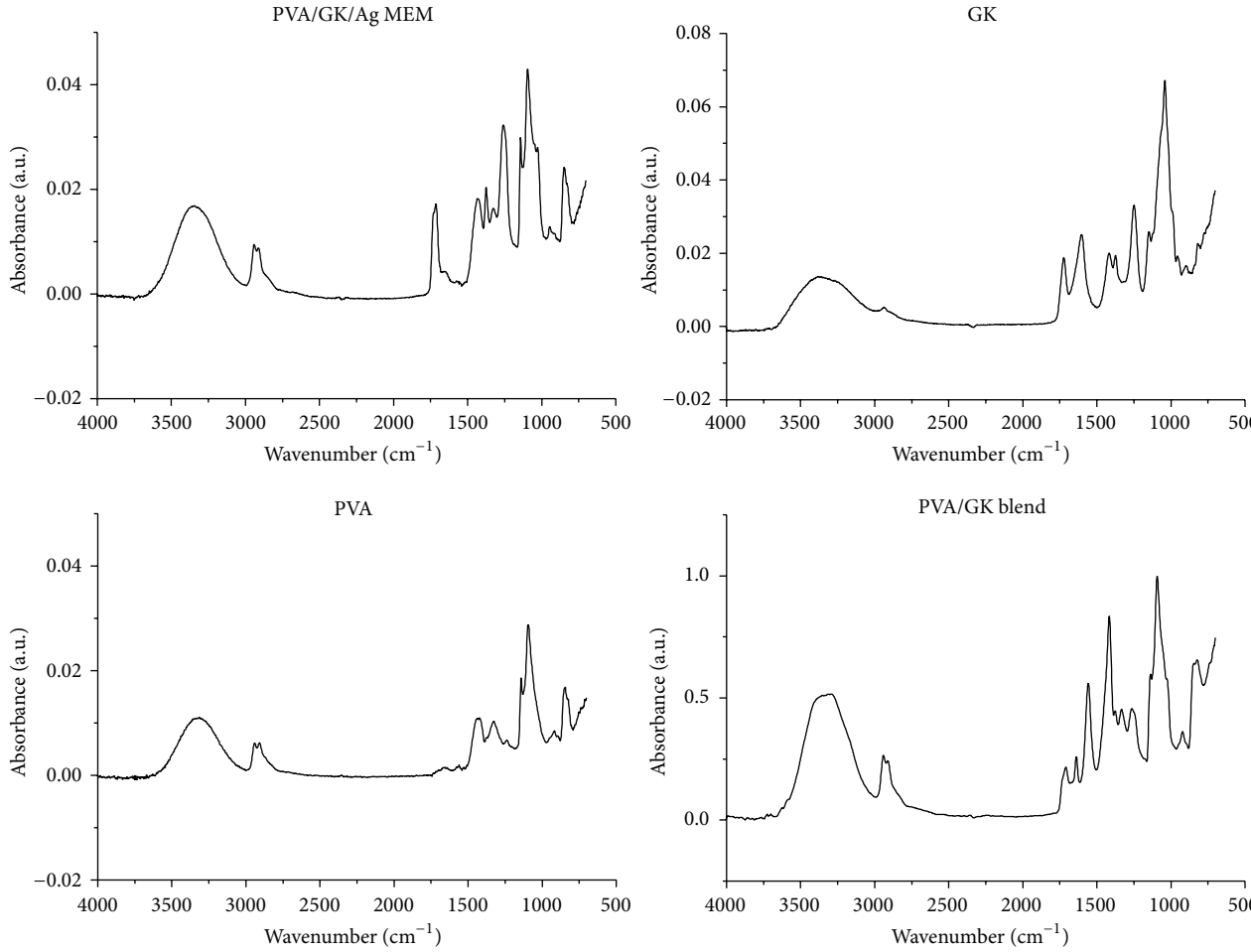

Figure 6: ATR-FTIR spectra of PVA, GK, PVA/GK blend, and Ag-MEM.

Table 1: Diameter (mm) of zone of inhibition (ZOI) for PVA/GK/Ag solutions produced with different concentrations of $AgNO_3$ (1, 2, 4, 5, and 10 mM) and Ag-MEM (1 mM $AgNO_3$). Means were calculated from in triplicate tests on the PVA/GK/Ag solution and nine replicates for the Ag-MEM (±SD).

	PVA/GK/Ag solution					Ag-MEM
$AgNO_3$ (mM)	1	2	4	5	10	1
E. coli	8.0 ± 0.7	9.0 ± 0.5	10.0 ± 0.8	11.0 ± 0.5	14.0 ± 0.7	7.9 ± 0.8
P. aeruginosa	8.0 ± 0.8	10.5 ± 0.8	11.5 ± 0.7	12.5 ± 0.7	14.5 ± 0.7	8.0 ± 0.7
S. aureus	8.1 ± 0.8	10.5 ± 0.7	11.5 ± 0.6	12.5 ± 0.6	14.5 ± 0.8	8.0 ± 0.8

ions with the PVA/GK nanofibres. These results are in agreement with earlier reported studies on the binding of Ag-NPs with other natural gums [7, 11].

3.4. Antibacterial Properties. We tested the antibacterial activity of the PVA/GK/Ag and Ag-MEM composites synthesised in this study against Gram-negative *E. coli* and *P. aeruginosa* and Gram-positive *S. aureus*. The results indicate that PVA/GK and Ag-MEM without Ag-NPs show no antibacterial activity.

For the PVA/GK/Ag solution, zone of inhibitions (ZOIs) for Gram-negative *E. coli* and *P. aeruginosa* shows similar antibacterial trends. The ZOI of *E. coli* increased from 8 to 14 mm with increasing Ag NPs concentration. Similarly, the ZOI of *P. aeruginosa* increased from 8 to 14.5 mm with increasing Ag NPs concentration (Table 1).

The ZOI of Gram-positive *S. aureus* increased from 8.5 to 14.5 mm with increasing Ag NPs concentration (Table 1). Interestingly, growth of both Gram-negative (*E. coli* and *P. aeruginosa)* and Gram-positive bacteria (*S. aureus*) was inhibited by the Ag-MEM (ZOI ~ 8), with no significant difference ($P > 0.05$) between the bacterial strains (Table 1 and Figure 7). The concentration of the Ag NPs was observed to be 157.2 mgL^{-1} in both Ag solution and Ag-MEM (prepared from 1 mM each concentration of $AgNO_3$) as determined using ICP-AES, respectively. These results were in

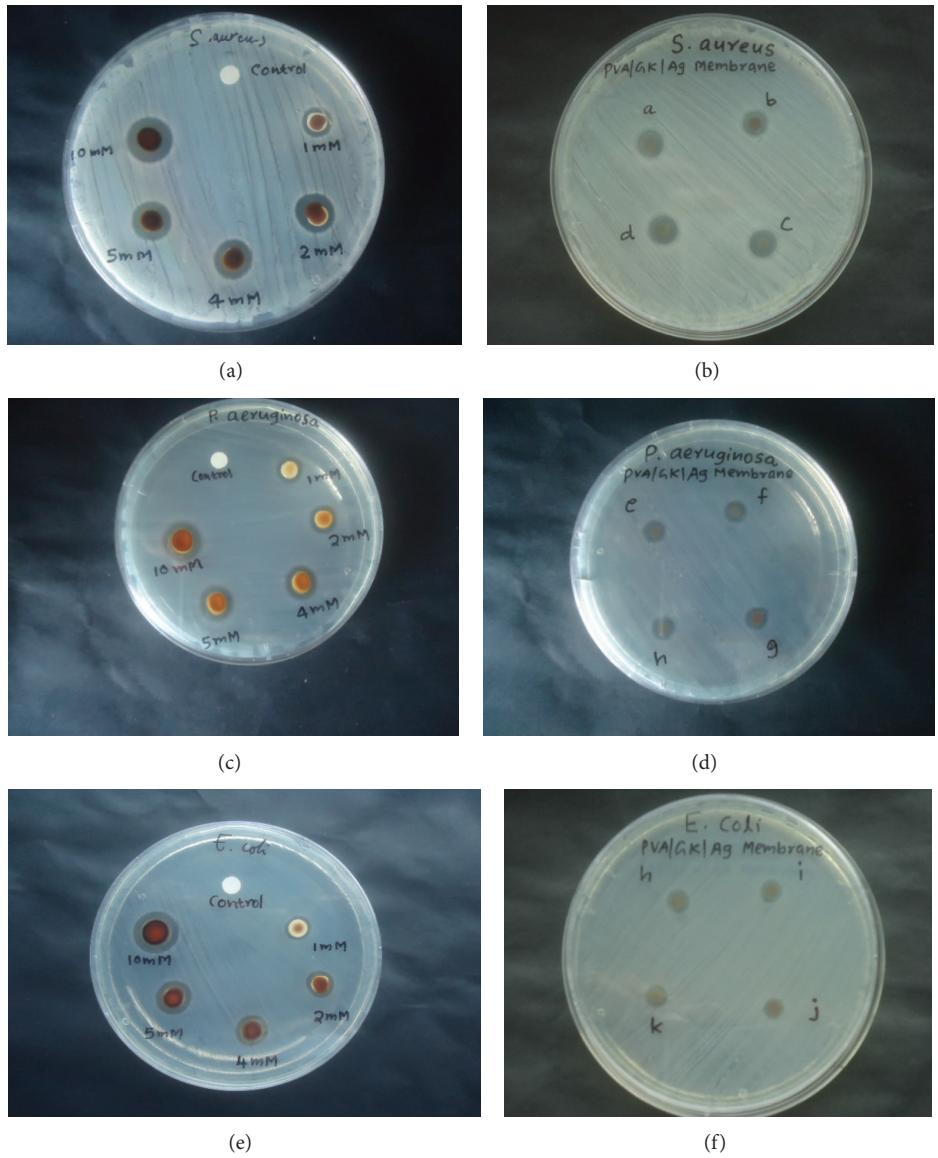

Figure 7: The bacterial growth inhibition zones of *S. aureus* (a, b), *P. aeruginosa* (c, d), and *E. coli* (e, f); left panels represent the antibacterial effect of PVA/GK/Ag NP solution (0, 1, 2, 4, 5 and 10 mM concentration of $AgNO_3$) and right panels of Ag-MEM (quadruplicates represent the zone of inhibition of 1mM concentration of $AgNO_3$), respectively.

a good agreement with earlier reported investigation onto antibacterial properties of PVA/Ag NPS/TEOS films and PVA/carboxymethyl-chitosan/AgNanofibers [27, 31].

While the mechanism for Ag-NP action is still not fully understood, it has been documented that Ag-NPs cause structural changes when they interact with the outer membrane of bacteria [37]. Such changes may lead to an increase in membrane permeability and leakage of intracellular constituents and cause severe damage, ultimately resulting in cell death. Differences in bacterial susceptibility may be due to structural and compositional differences in the cell membrane of Gram-positive and Gram-negative bacteria [38, 39]. Gram-negative *E. coli* cell walls, for example, have dynamic lipopolysaccharide O-side chains that are not present in Gram-positive cell walls. Rapidly moving side chains may disable the formation of a metal-ion salt bridge and prevent an antibiotic effect when Ag-NPs are not present in sufficient concentration [40]. The present investigation showed that Ag-MEM and Ag solution with Ag NP concentration ($157.2\ mgL^{-1}$) indicate almost similar zone of inhibition (~8) against both Gram-negative (*E. coli* and *P. aeruginosa*) and Gram-positive bacteria (*S. aureus*). The PVK/GK/Ag solution and Ag-MEM show high potential as environmentally friendly antibacterial materials for a variety of applications, such as medical wound dressings and cosmetics.

4. Conclusions

In this study, we produced an electrospun nanofiber membrane from GK, a natural hydrocolloid, blended with PVA.

Uniform PVA/GK nanofibers were obtained at a PVA/GK weight ratio of 80 : 20. The 80 : 20 PVA/GK was blended with various concentrations of $AgNO_3$ solution to produce a PVA/GK/Ag NP solution. PVA/GK/Ag NP solution was then used to produce nanofibers containing AG-NPs, from which an antibacterial nanofiber membrane (Ag-MEM) was fabricated. The PVA/GK/Ag solution and Ag-MEM showed clear antibacterial activity toward Gram-negative *E. coli* and *P. aeruginosa* and Gram-positive *S. aureus*. As all bacterial species showed similar susceptibility to Ag-MEM, they show bactericidal action toward a wide range of potentially pathogenic bacteria. These newly synthesised Ag NP solutions and Ag-MEM show great potential for the development of environmentally friendly antibacterial materials for medical devices, food packaging, and water purification purposes.

Conflict of Interests

The authors declare no conflict of interests.

Acknowledgments

The research reported in this paper was supported in part by Project LO1201, the financial support of the Ministry of Education, Youth and Sports in the framework of the targeted support of the "National Programme for Sustainability I," the OPR & DI Project and OP VaVpI of the Centre for Nanomaterials, Advanced Technologies and Innovation, CZ.1.05/2.1.00/01.0005, the "Project Development of Research Teams for R & D Projects" at the Technical university of Liberec, CZ.1.07/2.3.00/30.0024, and a Grant from the Competence Centre, TE01020218.

References

[1] D. Verbeken, S. Dierckx, and K. Dewettinck, "Exudate gums: occurrence, production, and applications," *Applied Microbiology and Biotechnology*, vol. 63, no. 1, pp. 10–21, 2003.

[2] D. M. W. Anderson and W. Weiping, "Gum arabic (*Acacia senegal*) from Uganda: characterization, NMR spectra, amino acid composite and gum/soil cationic relationship," *International Tree Crops Journal*, vol. 7, pp. 167–179, 1992.

[3] G. O. Aspinall, L. Khondo, and B. A. Williams, "The hex-5-enose degradation: cleavage of glycosiduronic acid linkages in modified methylated *Sterculia* gums," *Canadian Journal of Chemistry*, vol. 65, no. 9, pp. 2069–2076, 1986.

[4] M. A. Mohammadifar, S. M. Musavi, A. Kiumarsi, and P. A. Williams, "Solution properties of targacanthin (water-soluble part of gum tragacanth exudate from *Astragalus gossypinus*)," *International Journal of Biological Macromolecules*, vol. 38, no. 1, pp. 31–39, 2006.

[5] V. T. P. Vinod, R. B. Sashidhar, K. I. Suresh, B. R. Rao, U. V. R. V. Saradhi, and T. O. Rao, "Morphological, physico-chemical and structural characterization of gum kondagogu (*Cochlospermum gossypium*): a tree gum from India," *Food Hydrocolloids*, vol. 22, no. 5, pp. 899–915, 2008.

[6] V. Kattumuri, K. Katti, S. Bhaskaran et al., "Gum arabic as a phytochemical construct for the stabilization of gold nanoparticles: in vivo pharmacokinetics and X-ray-contrast-imaging studies," *Small*, vol. 3, no. 2, pp. 333–341, 2007.

[7] V. T. P. Vinod, P. Saravanan, B. Sreedhar, D. K. Devi, and R. B. Sashidhar, "A facile synthesis and characterization of Ag, Au and Pt nanoparticles using a natural hydrocolloid gum kondagogu (*Cochlospermum gossypium*)," *Colloids and Surfaces B: Biointerfaces*, vol. 83, no. 2, pp. 291–298, 2011.

[8] V. V. T. Padil and M. Černík, "Green synthesis of copper oxide nanoparticles using gum karaya as a biotemplate and their antibacterial application," *International Journal of Nanomedicine*, vol. 8, pp. 889–898, 2013.

[9] R. Arvizo, R. Bhattacharya, and P. Mukherjee, "Gold nanoparticles: opportunities and challenges in nanomedicine," *Expert Opinion on Drug Delivery*, vol. 7, no. 6, pp. 753–763, 2010.

[10] A. M. Stephen and C. S. C. A. M. Stephen, Eds., *Gums and Mucilages*, Marcel Dekker, New York, NY, USA, 1995.

[11] D. A. Silva, A. C. F. Brito, R. C. M. de Paula, J. P. A. Feitosa, and H. C. B. Paula, "Effect of mono and divalent salts on gelation of native, Na and deacetylated *Sterculia striata* and *Sterculia urens* polysaccharide gels," *Carbohydrate Polymers*, vol. 54, no. 2, pp. 229–236, 2003.

[12] T. J. Sill and H. A. von Recum, "Electrospinning: applications in drug delivery and tissue engineering," *Biomaterials*, vol. 29, no. 13, pp. 1989–2006, 2008.

[13] P. Schexnailder and G. Schmidt, "Nanocomposite polymer hydrogels," *Colloid and Polymer Science*, vol. 287, no. 1, pp. 1–11, 2009.

[14] V. Thavasi, G. Singh, and S. Ramakrishna, "Electrospun nanofibers in energy and environmental applications," *Energy and Environmental Science*, vol. 1, no. 2, pp. 205–221, 2008.

[15] M. Z. Elsabee, H. F. Naguib, and R. E. Morsi, "Chitosan based nanofibers, a review," *Materials Science and Engineering C*, vol. 32, no. 7, pp. 1711–1726, 2012.

[16] G. Toskas, R.-D. Hund, E. Laourine, C. Cherif, V. Smyrniotopoulos, and V. Roussis, "Nanofibers based on polysaccharides from the green seaweed *Ulva Rigida*," *Carbohydrate Polymers*, vol. 84, no. 3, pp. 1093–1102, 2011.

[17] M. Ignatova, K. Starbova, N. Markova, N. Manolova, and I. Rashkov, "Electrospun nano-fibre mats with antibacterial properties from quaternised chitosan and poly(vinyl alcohol)," *Carbohydrate Research*, vol. 341, no. 12, pp. 2098–2107, 2006.

[18] M. Pakravan, M. C. Heuzey, and A. Ajji, "A fundamental study of chitosan/PEO electrospinning," *Polymer*, vol. 52, no. 21, pp. 4813–4824, 2011.

[19] C. Zhang, X. Yuan, L. Wu, Y. Han, and J. Sheng, "Study on morphology of electrospun poly(vinyl alcohol) mats," *European Polymer Journal*, vol. 41, no. 3, pp. 423–432, 2005.

[20] E. Yang, X. Qin, and S. Wang, "Electrospun crosslinked polyvinyl alcohol membrane," *Materials Letters*, vol. 62, no. 20, pp. 3555–3557, 2008.

[21] A. Ravindran, P. Chandran, and S. S. Khan, "Bio-functionalized silver nanoparticles: advances and prospects," *Colloids and Surfaces B: Biointerfaces*, vol. 105, pp. 342–352, 2013.

[22] O. D. Choi, "The inhibitory effects of silver nanoparticles, silver ions, and silver chloride colloids on microbial growth," *Water Research*, vol. 42, no. 12, pp. 3066–3074, 2008.

[23] S. Porel, D. Ramakrishna, E. Hariprasad, A. D. Gupta, and T. P. Radhakrishnan, "Polymer thin film with in situ synthesized silver nanoparticles as a potent reusable bactericide," *Current Science*, vol. 101, no. 7, pp. 927–934, 2011.

[24] P.-O. Rujitanaroj, N. Pimpha, and P. Supaphol, "Wound-dressing materials with antibacterial activity from electrospun gelatin fiber mats containing silver nanoparticles," *Polymer*, vol. 49, no. 21, pp. 4723–4732, 2008.

[25] X. Zhuang, B. Cheng, W. Kang, and X. Xu, "Electrospun chitosan/gelatin nanofibers containing silver nanoparticles," *Carbohydrate Polymers*, vol. 82, no. 2, pp. 524–527, 2010.

[26] M. S. Peresin, Y. Habibi, J. O. Zoppe, J. J. Pawlak, and O. J. Rojas, "Nanofiber composites of polyvinyl alcohol and cellulose nanocrystals: manufacture and characterization," *Biomacromolecules*, vol. 11, no. 3, pp. 674–681, 2010.

[27] R. Bryaskova, D. Pencheva, G. M. Kale, U. Lad, and T. Kantardjiev, "Synthesis, characterisation and antibacterial activity of PVA/TEOS/Ag-Np hybrid thin films," *Journal of Colloid and Interface Science*, vol. 349, no. 1, pp. 77–85, 2010.

[28] K. A. Juby, C. Dwivedi, M. Kumar, S. Kota, H. S. Misra, and P. N. Bajaj, "Silver nanoparticle-loaded PVA/gum acacia hydrogel: synthesis, characterization and antibacterial study," *Carbohydrate Polymers*, vol. 89, no. 3, pp. 906–913, 2012.

[29] C. W. Li, R. Q. Fu, C. P. Yu et al., "Silver nanoparticle/chitosan oligosaccharide/poly(vinyl alcohol) nanofibers as wound dressings: a preclinical study," *International Journal of Nanomedicine*, vol. 8, pp. 4131–4145, 2013.

[30] C. Marambio-Jones and E. M. V. Hoek, "A review of the antibacterial effects of silver nanomaterials and potential implications for human health and the environment," *Journal of Nanoparticle Research*, vol. 12, no. 5, pp. 1531–1551, 2010.

[31] Y. Zhao, Y. Zhou, X. Wu, L. Wang, L. Xu, and S. Wei, "A facile method for electrospinning of Ag nanoparticles/poly (vinyl alcohol)/carboxymethyl-chitosan nanofibers," *Applied Surface Science*, vol. 258, no. 22, pp. 8867–8873, 2012.

[32] K. Vimala, Y. M. Mohan, K. Varaprasad et al., "Fabrication of curcumin encapsulated chitosan-PVA silver nanocomposite films for improved antimicrobial activity," *Journal of Biomaterials and Nanobiotechnology*, vol. 2, pp. 55–64, 2011.

[33] H. H. Huang, X. P. Ni, G. L. Loy et al., "Photochemical formation of silver nanoparticles in poly(N-vinylpyrrolidone)," *Langmuir*, vol. 12, no. 4, pp. 909–912, 1996.

[34] D.-G. Yu, G. R. Williams, X. Wang, X.-K. Liu, H.-L. Li, and S. W. A. Bligh, "Dual drug release nanocomposites prepared using a combination of electrospraying and electrospinning," *RSC Advances*, vol. 3, no. 14, pp. 4652–4658, 2013.

[35] D.-G. Yu, J. Zhou, N. P. Chatterton, Y. Li, J. Huang, and X. Wang, "Polyacrylonitrile nanofibers coated with silver nanoparticles using a modified coaxial electrospinning process," *International Journal of Nanomedicine*, vol. 7, pp. 5725–5732, 2012.

[36] V. T. P. Vinod, R. B. Sashidhar, V. U. M. Sarma, and S. S. Raju, "Comparative amino acid and fatty acid compositions of edible gums kondagogu (*Cochlospermum gossypium*) and karaya (*Sterculia urens*)," *Food Chemistry*, vol. 123, no. 1, pp. 57–62, 2010.

[37] I. Sondi and B. Salopek-Sondi, "Silver nanoparticles as antimicrobial agent: a case study on *E. coli* as a model for Gram-negative bacteria," *Journal of Colloid and Interface Science*, vol. 275, no. 1, pp. 177–182, 2004.

[38] T. J. Beveridge, "Structures of gram-negative cell walls and their derived membrane vesicles," *Journal of Bacteriology*, vol. 181, no. 16, pp. 4725–4733, 1999.

[39] V. Vadillo-Rodriguez, S. R. Schooling, and J. R. Dutcher, "*In situ* characterization of differences in the viscoelastic response of individual gram-negative and gram-positive bacterial cells," *Journal of Bacteriology*, vol. 191, no. 17, pp. 5518–5525, 2009.

[40] S. Langley and T. J. Beveridge, "Effect of O-side-chain-lipopolysaccharide chemistry on metal binding," *Applied and Environmental Microbiology*, vol. 65, no. 2, pp. 489–498, 1999.

Hindawi Publishing Corporation
Journal of Nanomaterials
Volume 2015, Article ID 747420, 11 pages
http://dx.doi.org/10.1155/2015/747420

Research Article

Effects of Chitosan Concentration on the Protein Release Behaviour of Electrospun Poly(ε-caprolactone)/Chitosan Nanofibers

Fatemeh Roozbahani,[1] Naznin Sultana,[1] Davood Almasi,[2] and Farnaz Naghizadeh[1]

[1]*Faculty of Biosciences and Medical Engineering, Universiti Teknologi Malaysia, UTM Skudai, 81310 Johor Bahru, Johor, Malaysia*
[2]*Department of Manufacturing and Industrial Engineering, Faculty of Mechanical Engineering, Universiti Teknologi Malaysia, 81310 Johor Bahru, Johor, Malaysia*

Correspondence should be addressed to Naznin Sultana; naznin@biomedical.utm.my

Received 15 October 2014; Accepted 6 December 2014

Academic Editor: Naeem Faraz

Poly(ε-caprolactone)/chitosan (PCL/chitosan) blend nanofibers with different ratios of chitosan were electrospun from a formic acid/acetic acid (FA/AA) solvent system. Bovine serum albumin (BSA) was used as a model protein to incorporate biochemical cues into the nanofibrous scaffolds. The morphological characteristics of PCL/chitosan and PCL/chitosan/BSA Nanofibers were investigated by scanning electron microscopy (SEM). Fourier transform infrared spectroscopy (FTIR) was used to detect the presence of polymeric ingredients and BSA in the Nanofibers. The effects of the polymer blend ratio and BSA concentration on the morphological characteristics and consequently on the BSA release pattern were evaluated. The average fiber diameter and pore size were greater in Nanofibers containing BSA. The chitosan ratio played a significant role in the BSA release profile from the PCL/chitosan/BSA blend. Nanofibrous scaffolds with higher chitosan ratios exhibited less intense bursts in the BSA release profile.

1. Introduction

Tissue engineering scaffolds in the form of electrospun nanofibers provide support for cells to adhere, grow, and propagate by mimicking the natural extracellular matrix (ECM) structure [1]. Nanofibers have the following several advantages as tissue engineering scaffolds: (i) a high surface area for the delivery of drugs, nutrients, and biochemical materials through the seeded cells; (ii) a structure comprised of a network of interconnected pores; (iii) high porosity for cells to migrate and nutrients and metabolic waste to flow in vivo.

In addition to architecture, biomolecules are another vital element for cell attachment, proliferation, and differentiation and should be released in a constant and controlled manner, maintaining their bioactivity. Therefore, the aforementioned morphological characteristics coupled with controlled biomolecule delivery provide both morphological and biomedical applications for tissue regeneration. Nonetheless, research in this area is still quite limited [2–12], although the release pattern of pharmaceutical drugs with nanofibrous scaffolds has already been considered by a number of authors [13–19].

Blend [3], emulsion [5, 10, 20], and coaxial [3, 9, 12] electrospinning are three conventional electrospinning techniques for the incorporation of biomolecules into fibers. Researchers have reported burst release as a disadvantage of blend electrospinning comparing with coaxial electrospinning, which requires a special apparatus and careful selection of materials. Emulsion electrospinning has attracted increasing attention in recent years due to its simplicity [7]. Nevertheless, the effects of emulsifiers as an additive in electrospinning are still unknown. Generally, the compatibility of the polymer, drug, and other ingredients affects the release profile [21].

Chitosan is a partially deacetylated derivative of chitin, the second most abundant polysaccharide in nature [22]. It has several unique characteristics that are beneficial for

biomedical applications, such as its biodegradable, biocompatible, nontoxic, and antibacterial properties. The electrospinning of pure chitosan and its blends with synthetic polymers, proteins, and inorganic nanoparticles has been studied [23, 24]. Chitosan is soluble in most organic acids. The electrospinning of chitosan is relatively complicated due to its high molecular weight, high viscosity, and high density of positive charges in acidic solution [25–28]. The electrospinning of chitosan in a blend with a second polymer with a flexible structure and lower molecular weight is a potential solution to this problem. In further attempts to minimise the limitation of molecular weight on the electrospinning process, even in blends with a second polymer, reducing the molecular weight of chitosan through alkali treatment has been investigated [29, 30].

Poly ε-caprolactone (PCL) has been used for scaffold fabrication and the controlled release of drugs and biomolecules [31–33], but it has several drawbacks, such as its hydrophobicity, initial burst release, and extremely long degradation period. To overcome the abovementioned drawbacks, blends of PCL and other natural or synthetic polymers, such as gelatin and chitosan, have been used [31, 33–35]. Studies related to nanofibrous scaffolds composed of PCL/chitosan blends are very rare due to their lack of common solvent systems.

In 2012 [36] introduced a solution system consisting of formic acid/acetic acid (FA/AA) as a substitute for previous expensive and toxic solvents [32, 33, 37]. This new solvent system opens the door for further feasibility studies for PCL/chitosan scaffolds as means to simulate the basic requirements of ECM. Bovine serum albumin (BSA) as a model protein was added to the solvent system to generate biochemical signals in fabricated scaffolds.

The aim of this study was to fabricate PCL/chitosan nanofibrous scaffolds with BSA from FA/AA solution via blend electrospinning. Nanofibers with different PCL/chitosan/BSA ratios have been fabricated and investigated in terms of fiber diameter, pore size, and BSA release behaviour. The main objective was to show that the BSA release profile could be finely tailored by modulation of the morphology, porosity, and composition of the nanofibers. The results illustrated that the morphological characteristics play a fundamental rule in explaining the release pattern of nanofibers.

2. Materials and Methods

2.1. Materials. Medium-molecular-weight chitosan, poly(ε-caprolactone) (PCL), bovine serum albumin (BSA), and phosphate-buffered saline (PBS) all were obtained from Sigma-Aldrich for use in the protein release studies. The solvents, including formic acid (FA; 98%) and acetic acid (AA; 99.8%), were supplied by Merck.

2.2. Electrospinning. The electrospinning solutions were prepared by simultaneously adding certain amounts of PCL and chitosan to a mixed solvent system and stirring for 3 h. The solvent system was composed of formic acid/acetic acid (FA/AA) in a ratio of 70/30 [36, 38].

The PCL and chitosan concentrations were expressed in wt.% relative to the solution, while the BSA concentration was presented as the wt.% relative to the total polymeric material (PCL and chitosan).

To prepare electrospun nanofibers, approximately 2 mL of the prepared solution was placed in a 5 mL syringe. A 23-gauge needle was used for the spinning process. The distance from the needle to the collector was fixed at 12.5 cm, and the voltage range of stable electrospinning was generally in the range of 18 to 25 kV depending on the stability of the Taylor cone during the process. Electrospinning was carried out at room temperature (22 ± 2°C) and a relative humidity of 65 ± 5%. The flow rate was set at 0.5 mL h^{-1}.

2.3. Protein Loading in the Electrospun Scaffolds. Protein was loaded on the nanofibers using the blend electrospinning technique. First, solutions of 8 wt.% PCL and different concentrations of chitosan (0.2, 0.4, 0.6, 0.8, and 1 wt.%) were prepared. Next, 5, 10, 15, and 20% BSA were added to the solution systems to determine the optimum BSA concentration in terms of fiber morphology and protein release behaviour. Lastly, the experiments for preliminary solvents were repeated with the optimum amount of BSA.

2.4. Characterisation of Electrospun Scaffolds

2.4.1. Scanning Electron Microscopy (SEM). To evaluate the morphology of the electrospun scaffolds, electrospun nanofibrous samples were cut into small pieces, sputter-coated with gold, and imaged using a Hitachi TM-3000 SEM apparatus. The fiber diameters and pore sizes of the scaffolds were analysed using image visualisation software (ImageJ, National Institute of Health, Bethesda, MD; http://rsb.info.nih.gov/ij/). Approximately 100 counts per image were used to calculate the fiber diameter.

2.4.2. Pore Size. As a morphological characteristic of nanofibrous matrices, the pore size of the electrospun PCL/chitosan was measured. To this end, nanofibers were electrospun for 5 min for each blend. The surface porosity of the electrospun web was calculated by processing the SEM images and measuring the free space between nanofibers, which corresponds to the dark area in the SEM images.

2.4.3. FTIR. FTIR spectroscopy was used to identify the components in the blend and the changes to the blend composition after adding BSA. Samples of the same dimensions were mixed with potassium bromide to form pellets. FTIR spectra in transmission mode were recorded using an FTIR spectrometer (Perkin Elmer, USA) connected to a PC, and the data were analysed using IR Solution software.

2.5. In Vitro Protein Release Study. For the in vitro release studies, all nanofibrous membranes were cut into small squares (1 × 1 cm^2) and then immersed in 2 mL microtubes containing PBS (pH = 7.4) at 37°C. After predetermined intervals of time, the release buffer was completely replaced with fresh PBS and placed in a water bath to continue

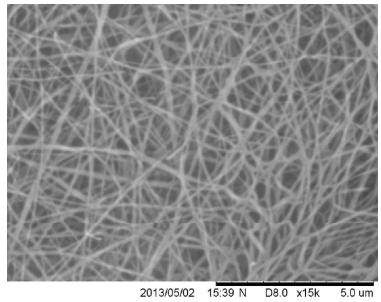

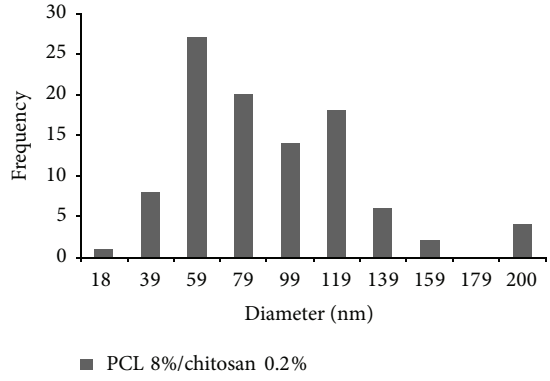

(a)

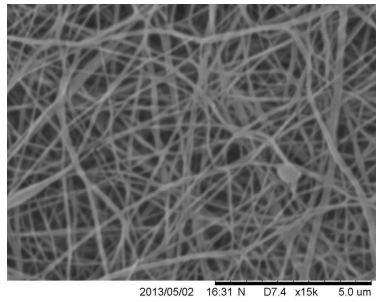

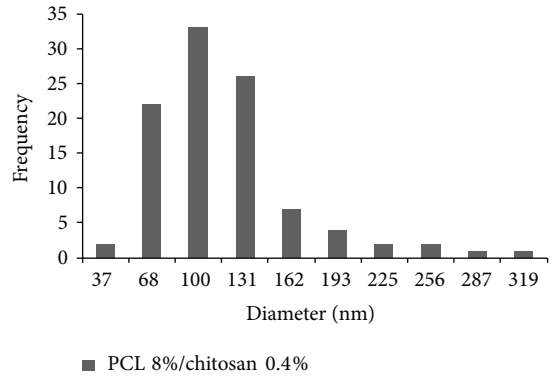

(b)

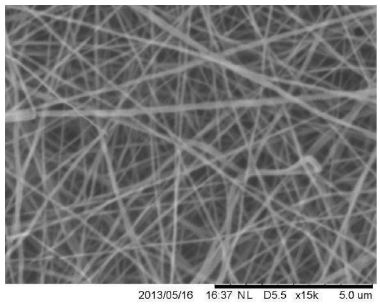

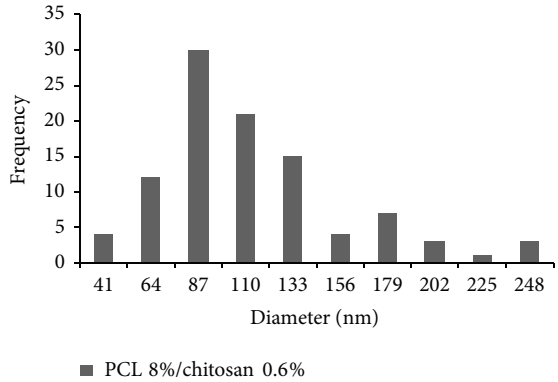

(c)

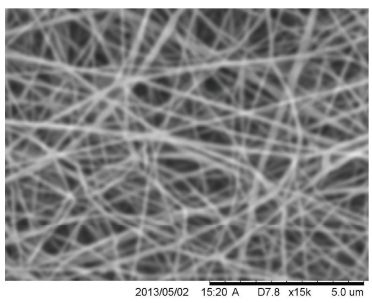

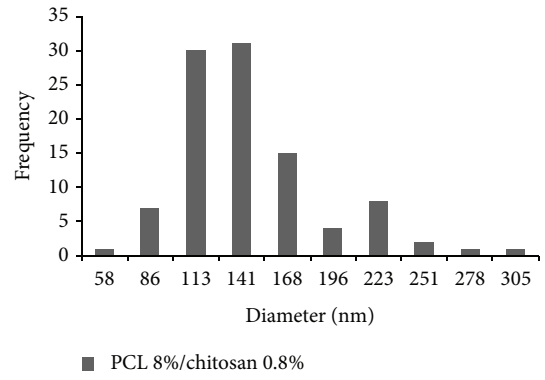

(d)

Figure 1: Continued.

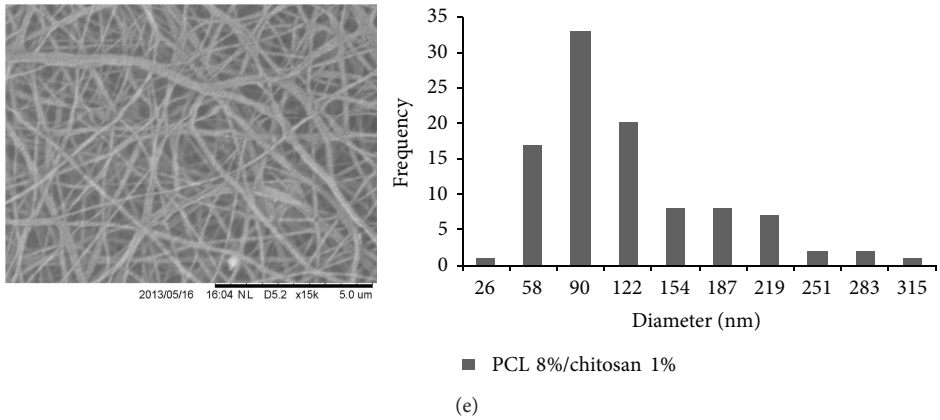

Figure 1: SEM images of PCL/chitosan nanofibers with wt.% ratio of (a) 8/0.2, (b) 8/0.4, (c) 8/0.6, (d) 8/0.8, and (e) 8/1 with fiber diameter frequency diagrams.

the release study. The concentration of each retrieved BSA solution was then determined by measuring the absorbance at 280 nm using a UV-Vis spectrophotometer (Hitachi Corp., Tokyo, Japan). The concentrations were calculated using the Beer-Lambert law:

$$A = \varepsilon bc, \tag{1}$$

where A is the absorbance, b is the path length of the sample, that is, the path length (cm) of the cuvette in which the sample is contained, ε is the molar absorptivity with units of L mol^{-1} cm^{-1}, and c is the concentration of the compound in solution, expressed in mol L^{-1}.

The results were demonstrated in terms of cumulative amount released (%):

$$\text{Cumulative release } \% = \left(\frac{M_t}{M_\infty}\right) \times 100, \tag{2}$$

where M_t is the amount of BSA at time t and M_∞ is the total amount of BSA in the nanofibrous membrane.

After completing the release study, the samples were dried using tissue paper, and each sample was dissolved in 3 mL of methylene chloride. The amount of protein extracted was assayed in a similar manner as described above.

3. Results and Discussion

3.1. Morphology. Figure 1 shows the SEM micrographs of the PCL/chitosan fibrous material made with 8 wt.% PCL and chitosan concentrations ranging from 0.2 to 1 wt.% without protein encapsulation, which was fabricated under the conditions described in Section 2.2. The fiber diameter distribution was presented for all samples. The mean diameter of the PCL/chitosan fibers increased gradually from 82.39 to 131.85 nm with the chitosan ratio in the blend (Table 1(a)), except for the last chitosan ratio, which produced a narrower fiber with a ribbon-like structure. For lower chitosan ratios (Figures 1(a) and 1(b)), the nanofibrous structure displayed beads alongside the nanofibers.

The stable electrospinning of pure PCL in FA/AA as a solvent system was only possible at relatively high concentrations, starting from 12 wt.% [38]. Below this concentration, the electrospun nanofibers most resembled a string of beads, and the process condition was not stable regarding the formation of the Taylor cone. Chitosan, even when added in smaller quantities, increased the solution viscosity sufficiently for the spinning process to be possible with a mix of PCL/chitosan at a lower wt.% of PCL [36, 38].

The pore size increased with increasing chitosan concentration, except for the highest concentration, at which the pore size decreased from 421.61 nm for 0.8 wt.% chitosan to 335.61 nm for 1 wt.% chitosan (Table 1(b)). Increasing the solid material content produced a more viscous solution, which, along with aggregation of the positive charges of chitosan in the acidic solvent in the needle, affected the morphological properties of the polymer in the distance between the syringe and the collector such that a higher repulsive force on the polymer string was required to leave the needle. Thus, a smaller fiber diameter and larger pore size resulted.

The impact of the BSA concentration on the PCL/chitosan nanofiber morphology is illustrated in Figure 2. To study the effects of BSA concentration on electrospun nanofibers, different amounts of BSA (5%, 10%, 15%, and 20%) were added to 8% PCL and 0.6% chitosan. The polymer jet containing BSA carries extra charges, which induce a more effective elongation and finer fibers at the same applied voltage. Nevertheless, as the BSA concentration increased, the average fiber diameter increased due to the presence of more solid material in the solvent system [7]. The results showed no significant changes in the mean fiber diameter, except for an increase at 10% BSA, which was approximately 10 nm and was negligible under these criteria. The fiber diameter fluctuated slightly from 122.4 nm for 5% BSA to 109.95 nm for 20% BSA, whereas the pore size increased from 387.19 to 490.24 nm (Table 2). The fiber diameter initially increased gradually due to the naturalisation effect of the functional groups of BSA molecules on the positive charges of chitosan.

Table 1: (a) Fiber diameter and (b) pore size calculated for PCL/chitosan nanofibers comparing PCL/chitosan/BSA nanofibers.

(a)

PCL/chitosan wt.% ratio	Average fiber diameter (nm)	Coefficient of deviation (%)	Average fiber diameter (nm)	Coefficient of deviation (%)
	Without BSA		With 20 wt.% BSA	
8/0.2	82.39	3.73	108.68	5.72
8/0.4	101.69	4.93	123.58	5.37
8/0.6	101.66	4.51	121.54	5.48
8/0.8	131.85	4.45	132.73	5.17
8/1.0	109.01	6.24	159.12	7.66

(b)

PCL/chitosan wt.% ratio	Average pore size (nm)	Coefficient of deviation (%)	Average pore size (nm)	Coefficient of deviation (%)
	Without BSA		With 20% BSA	
8/0.2	233.62	11.63	462.89	24.97
8/0.4	322.96	12.64	437.28	18.57
8/0.6	423.56	21.42	554.14	34.06
8/0.8	421.61	22.05	621.52	35.79
8/1.0	335.61	19.02	783.77	41.85

Table 2: Applied voltage and average nanofibers diameter and pore size in electrospinning PCL/chitosan nanofibers with different BSA%.

BSA wt.%	Voltage (KV)	Average fiber diameter (nm)	Coefficient of deviation (%)	Average pore size (nm)	Coefficient of deviation (%)
5	18	122.4	5.60	387.19	21.25
10	21	133.47	5.60	429.45	24.88
15	20	117.39	6.74	418.43	22.71
20	21	109.95	5.09	490.24	25.10

When the BSA concentration was increased to 15% and 20%, the extra charges produced a finer fiber. The increase in pore size is also attributed to greater repellence between the polymer jet after leaving the needle tip and before grounding. The assessment of the effect of the BSA ratio on the nanofibers release property will be considered in Section 3.3.

Adding 20% BSA to all formulations of the PCL/chitosan blend necessitated a 2-3 kV higher voltage for all samples (Figure 2(a)) to achieve the stable conditions for electrospinning.

The SEM images of different formulations of PCL/chitosan with 20% BSA are shown in Figures 3(a)–3(e). The PCL/chitosan nanofibers diameters increased steadily by approximately 23 ± 4 nm in all cases as a result of the addition of BSA. Alternatively, the pore sizes increased by 50% compared to the samples without BSA. This may be related to the repelling effects of the same charges of the BSA molecules, which moved to the surface of the nanofibers during the bending and splaying before collecting on the collector [39].

Comparing Figures 1(a) and 1(b), no beads were formed during the electrospinning. This effect is related to the compensation of the low viscosity by adding BSA to the system. In Figure 3(e), although the solid material was the same as the sample in Figure 1(e) except for the presence of BSA, fine nanofibers were formed, and no ribbon shape was observed. This result can be ascribed to the modifying effect of BSA for chitosan positive charges in the needle and the reduction of the repelling force applied to the polymer during the spinning process.

Figure 4(a) shows the applied voltages for each group of PCL/chitosan with or without BSA. The voltage was adjusted based on the stable Taylor cone during the process. As expected, higher chitosan concentrations required higher voltages for electrospinning, which is related to the higher viscosity of the solution resulting from the increased chitosan concentration.

All of the data related to the mean fiber diameter, average pore size, and coefficient of deviation are summarised in Tables 1(a) and 1(b). Figures 4(b) and 4(c) compare the characteristics of the PCL/chitosan blend nanofibers after inserting BSA. The figures also show that BSA increased the fiber diameter and pore size in all PCL/chitosan blend formulations.

3.2. FTIR. FTIR spectroscopy was performed to detect the polymeric ingredients and BSA in the fabricated nanofibers. The main features of the FTIR spectrum of chitosan powder included the carboxylate band in the range of 1400 to 1790 cm^{-1}, with a maximum at 1675 cm^{-1}, and a N–H band

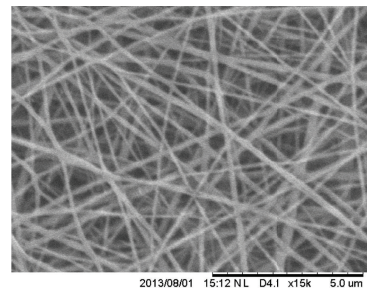

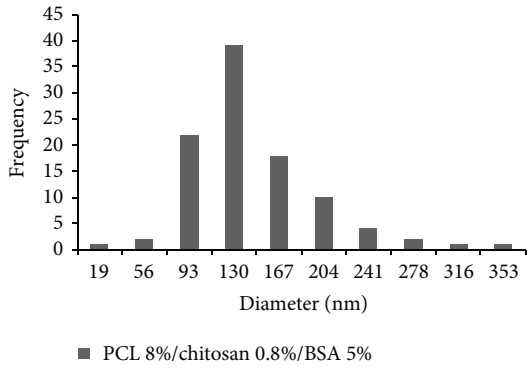

(a)

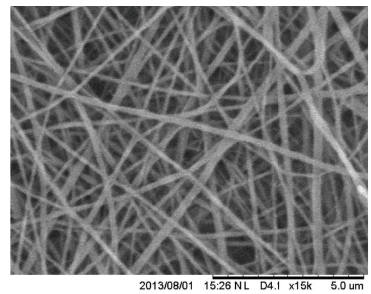

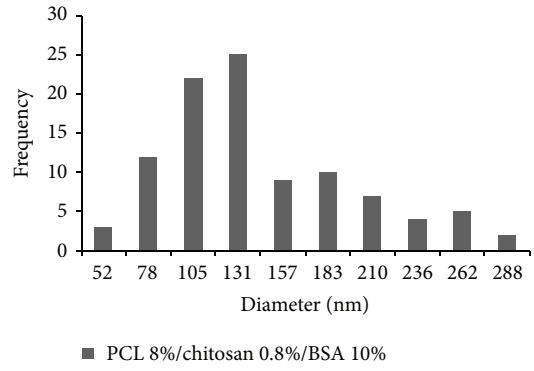

(b)

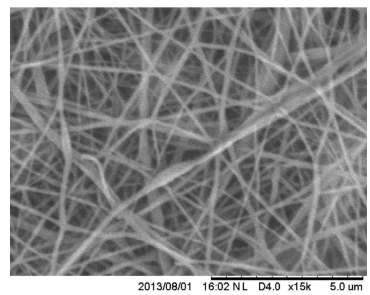

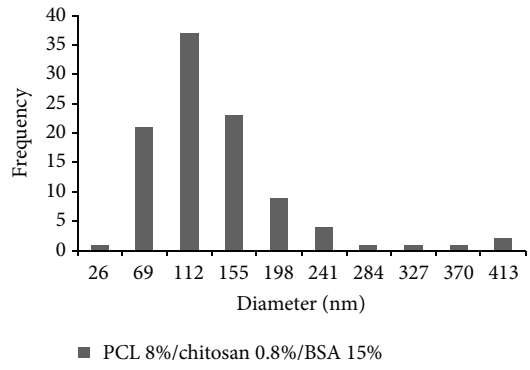

(c)

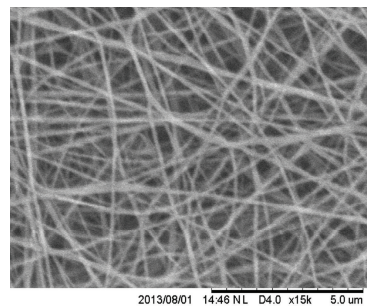

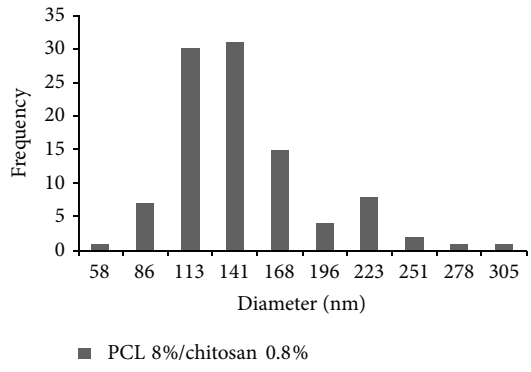

(d)

Figure 2: SEM images of PCL/chitosan/BSA nanofibers with BSA different concentration of (a) 5%, (b) 10%, (c) 15%, and (d) 20% with fiber diameter frequency diagrams.

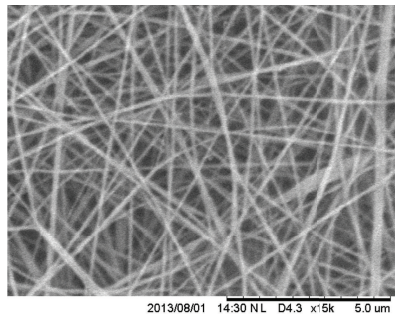

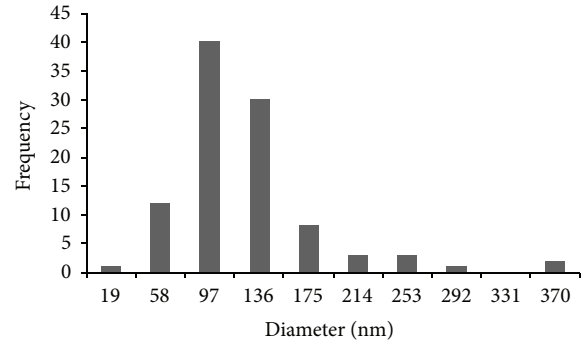

(a)

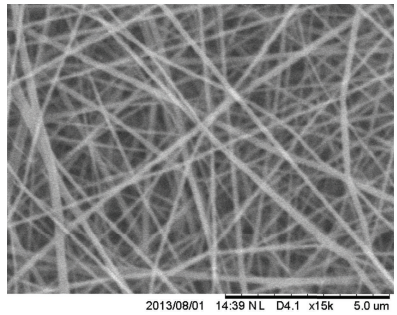

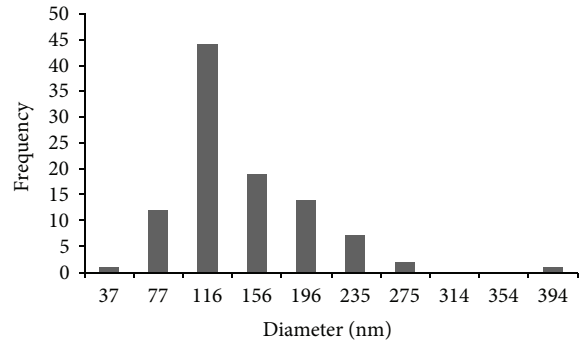

(b)

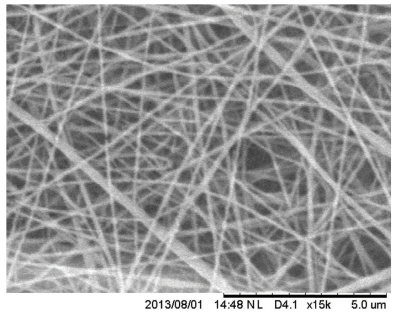

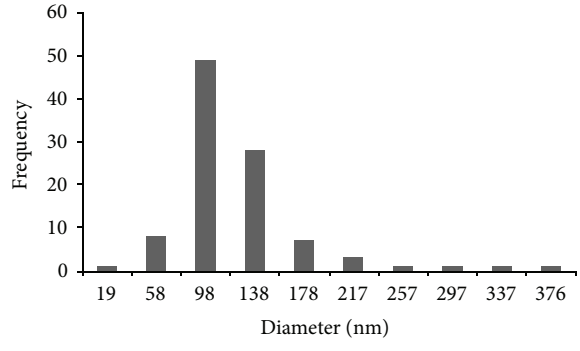

(c)

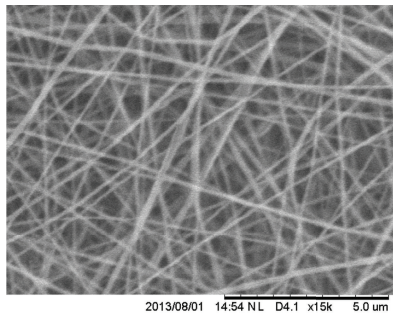

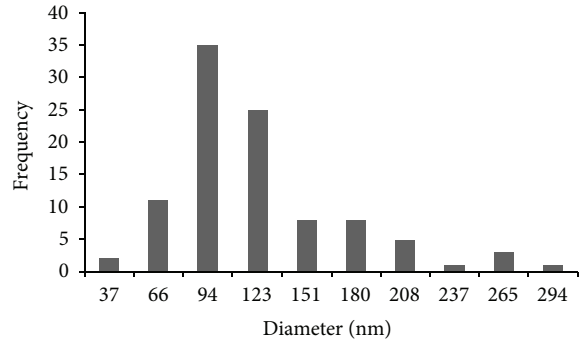

(d)

Figure 3: Continued.

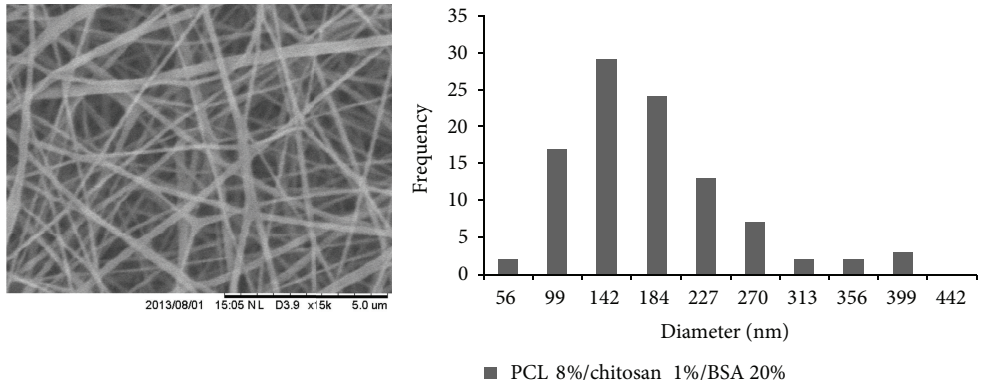

(e)

Figure 3: SEM images of PCL/chitosan/BSA nanofibers with 20% BSA and different PCL/chitosan wt.% ratio of (a) 8/0.2, (b) 8/0.4, (c) 8/0.6, (d) 8/0.8, and (e) 8/1 with fiber diameter frequency diagrams.

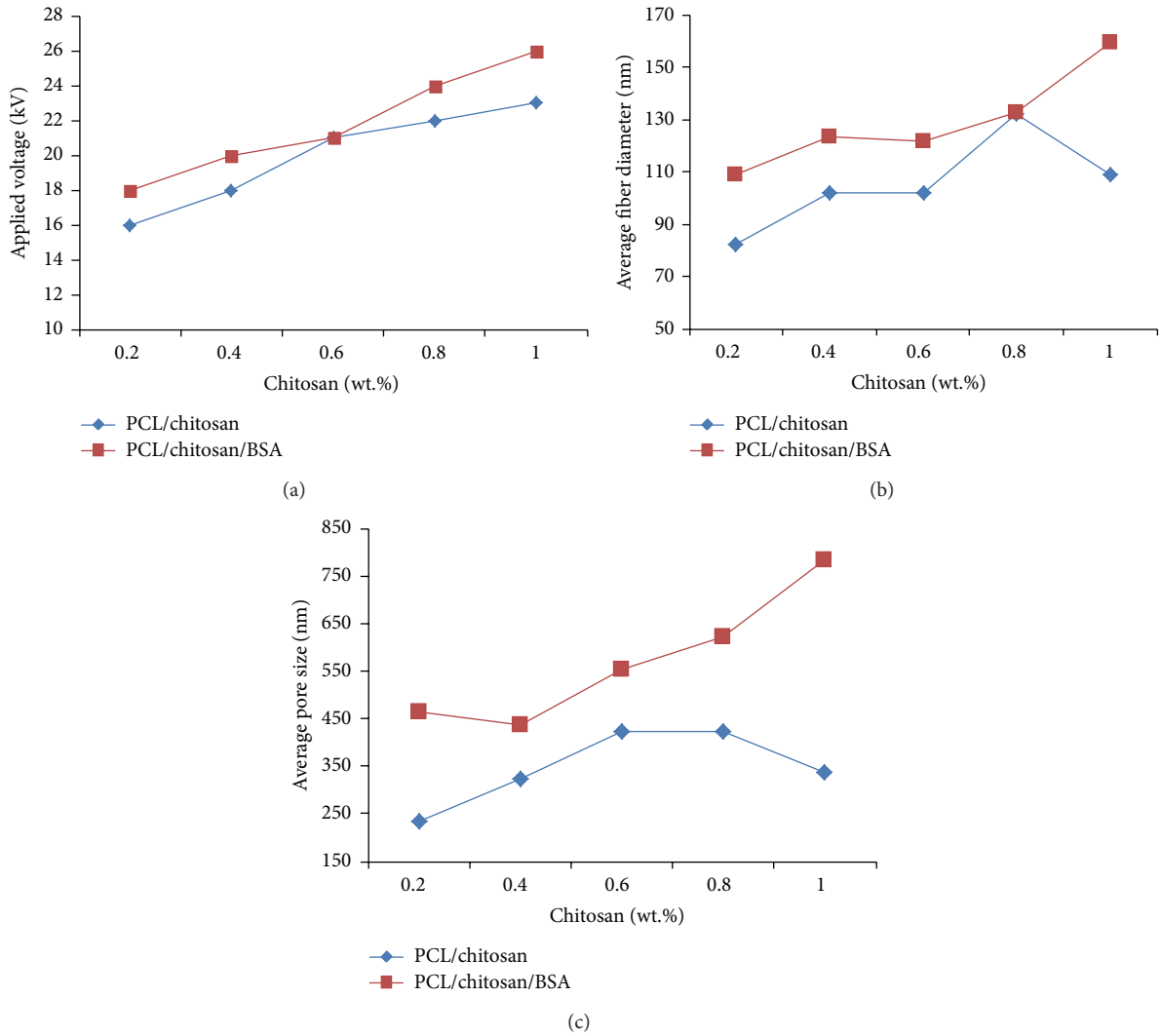

Figure 4: (a) Applied voltage, (b) average nanofibers diameters, and (c) average pore size of PCL/chitosan versus PCL/chitosan BSA nanofibers.

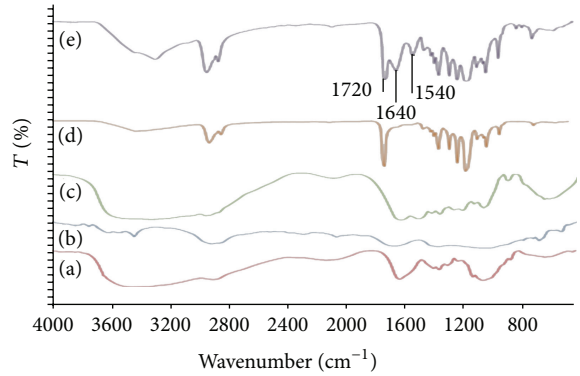

Figure 5: FTIR graph: (a) chitosan powder, (b) PCL granule, (c) BSA powder, (d) PCL/chitosan nanofibers, and (e) PCL/chitosan/BSA nanofibers.

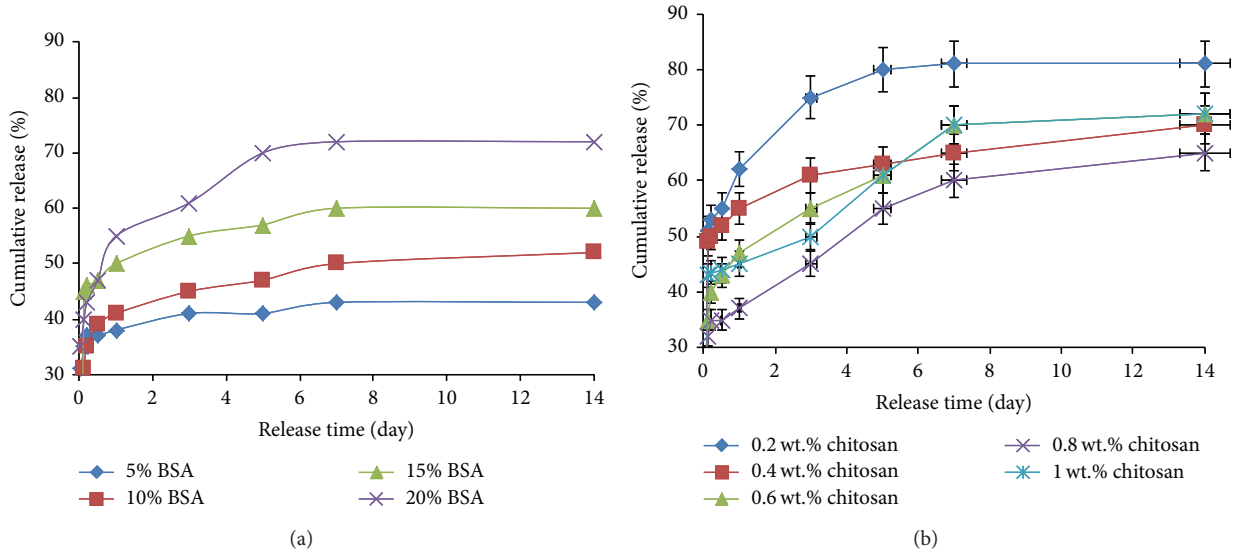

Figure 6: Release profile of BSA from PCL/chitosan/BSA blend nanofibers (a) with different BSA and (b) with different PCL/chitosan ratio.

at approximately 3350 cm^{-1} (Figure 5(a)). PCL exhibited a strong absorption at 1720 cm^{-1} corresponding to its carbonyl group (Figure 5(b)). The FTIR spectra in Figure 6(d) included contributions from the carboxylate and amine groups of chitosan and the carbonyl group of PCL. No additional peaks were observed, indicating that the chitosan was embedded physically within the nanofibers.

Figure 5(c) depicts the FTIR spectrum of BSA powder. The main absorption bands of BSA were located at 1640 and 1540 cm^{-1}, which correspond to the protein-related amide I and II absorptions. The spectrum of the PCL/chitosan nanofibers containing BSA (Figure 5(e)) showed both peaks for BSA as well as the characteristic peaks for PCL and chitosan, which confirmed the presence of BSA in the blend nanofibers.

3.3. Release Kinetics. The release profiles of PCL/chitosan/BSA blend nanofibers with different proportions of BSA are shown in Figure 6(a). The release kinetics can be described as consisting of two phases: an initial burst at approximately 30–40% of the total BSA during the first hours of the release study and a gradual release until 14 days, at which point the 80% of the release had been accomplished [40].

During the release experiments, the BSA existing on the surface leaves the nanofibers to enter the release solution. In the case of nanofibers that were electrospun from a mixture of drugs, biomolecules, and polymer, the drugs and/or biomolecules are likely to conglomerate on the surface. Consequently, a poor burst release of the dissolved drug is generally observed in the early phase.

Nanofibers with higher BSA concentration exhibited a more robust burst in the first stage and a longer delay of the second stage than those with lower BSA concentrations. As described in Section 3.1, for equivalent PCL/chitosan, a higher amount of BSA decreased the nanofibers diameter and increased the pore size. Although the changes in the nanofibers diameter were negligible due to the complexity of the interaction between the chitosan and BSA charges, the overall movement of BSA molecules from the nanofibers surface to the release medium was easier for nanofibrous matrices with higher surface areas and larger pore sizes. Additionally, a higher BSA concentration led to greater

uptake on the nanofibers surface and a stronger diffusion force encouraging the molecules to enter the release medium. As shown in Figure 6(a), a higher amount of BSA led to a more intense sustained release stage: 75% for 20% BSA compared to 42% for 5% BSA for blend nanofibers. It was clear that the release was not completed, and the rest of the BSA may continue to release over a longer time period.

The release pattern in PCL/chitosan/BSA nanofibers as a function of chitosan ratio is shown in Figure 6(b). Nanofibers with higher amounts of chitosan demonstrated less intense bursts and more sustained behaviour in the second stage of release. Nanofibers with 0.2 wt.% chitosan had 51% burst in the first hour of the release study, compared to 43% for 1 wt.% chitosan and 35% and 32% for 0.6 and 0.8 wt.% chitosan, respectively. Nanofibrous matrices with 0.8 wt.% chitosan exhibited a release pattern similar to the sustained release kinetics. The deviation of 1 wt.% chitosan from this trend was strongly related to the BSA saturation of its surface.

Based on the morphological studies, nanofibers with higher chitosan content exhibited a higher fiber diameter and pore size. Thus, similar to the aforementioned discussion for nanofibers with different BSA contents, the determined amount of nanofibrous scaffold with higher surface area and larger pore size is correlated with stronger burst release for nanofibers with less chitosan. However, BSA contains more charged groups (such as $-NH_2$ and $-COOH$) than PCL. Therefore, BSA was forced to move onto the fiber surface by the electric forces during electrospinning and was thereby in strong competition with chitosan. Consequently, chitosan limits BSA transfer to the surface of nanofibers and ultimately decreases the release amount of BSA in release graphs for PCL/chitosan/BSA with higher chitosan contents.

4. Conclusion

BSA as a model protein was successfully embedded in PCL/chitosan blend nanofibers using FA/AA as solvent system through a blending electrospinning technique. Compared to PCL/chitosan nanofibers, PCL/chitosan/BSA nanofibers had higher fiber diameter and larger pore size. Some electrospinning defects, such as beads at lower chitosan concentrations and ribbon-like nanofibers, were observed because of the accumulation of chitosan positive charges in the needle during electrospinning. This phenomenon was reduced by adding BSA. PCL/chitosan/BSA nanofibers with higher chitosan concentrations exhibited less intense bursts in the first hour of BSA release, which was related to the higher diameter and consequently lower surface area of the nanofibers exposed to the release medium.

Conflict of Interests

The authors declare that there is no conflict of interests regarding the publication of this paper.

Acknowledgments

The authors would like to thank Universiti Teknologi Malaysia for the International Doctoral Fellowship. The authors also acknowledge MOHE, GUP Tier 1 grants (Vot: 03H13, Vot: 05H07), FRGS (Vot: 4F126), MOHE, UTM, and RMC for financial support. The lab facilities of FBME are also acknowledged.

References

[1] R. Langer and J. P. Vacanti, "Tissue engineering," *Science*, vol. 260, no. 5110, pp. 920–926, 1993.

[2] S. Y. Chew, J. Wen, E. K. F. Yim, and K. W. Leong, "Sustained release of proteins from electrospun biodegradable fibers," *Biomacromolecules*, vol. 6, no. 4, pp. 2017–2024, 2005.

[3] W. Ji, F. Yang, J. J. J. P. Van Den Beucken et al., "Fibrous scaffolds loaded with protein prepared by blend or coaxial electrospinning," *Acta Biomaterialia*, vol. 6, no. 11, pp. 4199–4207, 2010.

[4] H. Jiang, Y. Hu, Y. Li, P. Zhao, K. Zhu, and W. Chen, "A facile technique to prepare biodegradable coaxial electrospun nanofibers for controlled release of bioactive agents," *Journal of Controlled Release*, vol. 108, no. 2-3, pp. 237–243, 2005.

[5] X. Li, Y. Su, S. Liu, L. Tan, X. Mo, and S. Ramakrishna, "Encapsulation of proteins in poly(L-lactide-co-caprolactone) fibers by emulsion electrospinning," *Colloids and Surfaces B: Biointerfaces*, vol. 75, no. 2, pp. 418–424, 2010.

[6] S. Maretschek, A. Greiner, and T. Kissel, "Electrospun biodegradable nanofiber nonwovens for controlled release of proteins," *Journal of Controlled Release*, vol. 127, no. 2, pp. 180–187, 2008.

[7] M. Norouzi, M. Soleimani, I. Shabani, F. Atyabi, H. H. Ahvaz, and A. Rashidi, "Protein encapsulated in electrospun nanofibrous scaffolds for tissue engineering applications," *Polymer International*, vol. 62, no. 8, pp. 1250–1256, 2013.

[8] C. M. Valmikinathan, S. Defroda, and X. Yu, "Polycaprolactone and bovine serum albumin based nanofibers for controlled release of nerve growth factor," *Biomacromolecules*, vol. 10, no. 5, pp. 1084–1089, 2009.

[9] L. Xiaoqiang, S. Yan, C. Rui et al., "Fabrication and properties of core-shell structure P(LLA-CL) nanofibers by coaxial electrospinning," *Journal of Applied Polymer Science*, vol. 111, no. 3, pp. 1564–1570, 2009.

[10] X. Xu, L. Yang, X. Xu et al., "Ultrafine medicated fibers electrospun from W/O emulsions," *Journal of Controlled Release*, vol. 108, no. 1, pp. 33–42, 2005.

[11] S. Yan, L. Xiaoqiang, T. Lianjiang, H. Chen, and M. Xiumei, "Poly(l-lactide-co-ε-caprolactone) electrospun nanofibers for encapsulating and sustained releasing proteins," *Polymer*, vol. 50, no. 17, pp. 4212–4219, 2009.

[12] Y. Z. Zhang, X. Wang, Y. Feng, J. Li, C. T. Lim, and S. Ramakrishna, "Coaxial electrospinning of (fluorescein isothiocyanate-conjugated bovine serum albumin)-encapsulated poly(ε-caprolactone) nanofibers for sustained release," *Biomacromolecules*, vol. 7, no. 4, pp. 1049–1057, 2006.

[13] E.-R. Kenawy, G. L. Bowlin, K. Mansfield et al., "Release of tetracycline hydrochloride from electrospun poly(ethylene-co-vinylacetate), poly(lactic acid), and a blend," *Journal of Controlled Release*, vol. 81, no. 1-2, pp. 57–64, 2002.

[14] G. Verreck, I. Chun, J. Rosenblatt et al., "Incorporation of drugs in an amorphous state into electrospun nanofibers composed of a water-insoluble, nonbiodegradable polymer," *Journal of Controlled Release*, vol. 92, no. 3, pp. 349–360, 2003.

[15] X. Zong, K. Kim, D. Fang, S. Ran, B. S. Hsiao, and B. Chu, "Structure and process relationship of electrospun bioabsorbable nanofiber membranes," *Polymer*, vol. 43, no. 16, pp. 4403–4412, 2002.

[16] H. Wang, Y. Feng, H. Zhao et al., "Controlled heparin release from electrospun gelatin fibers," *Journal of Controlled Release*, vol. 152, supplement 1, pp. e28–e29, 2011.

[17] Y. Su and X. Mo, "Dual drug release from coaxial electrospun nanofibers," *Journal of Controlled Release*, vol. 152, supplement 1, pp. e82–e84, 2011.

[18] E. Luong-Van, L. Grøndahl, K. N. Chua, K. W. Leong, V. Nurcombe, and S. M. Cool, "Controlled release of heparin from poly(ε-caprolactone) electrospun fibers," *Biomaterials*, vol. 27, no. 9, pp. 2042–2050, 2006.

[19] K. Kim, Y. K. Luu, C. Chang et al., "Incorporation and controlled release of a hydrophilic antibiotic using poly(lactide-co-glycolide)-based electrospun nanofibrous scaffolds," *Journal of Controlled Release*, vol. 98, no. 1, pp. 47–56, 2004.

[20] J. K. Tessmar and A. M. Göpferich, "Matrices and scaffolds for protein delivery in tissue engineering," *Advanced Drug Delivery Reviews*, vol. 59, no. 4-5, pp. 274–291, 2007.

[21] J. Zeng, L. Yang, Q. Liang et al., "Influence of the drug compatibility with polymer solution on the release kinetics of electrospun fiber formulation," *Journal of Controlled Release*, vol. 105, no. 1-2, pp. 43–51, 2005.

[22] C. K. S. Pillai, W. Paul, and C. P. Sharma, "Chitin and chitosan polymers: chemistry, solubility and fiber formation," *Progress in Polymer Science*, vol. 34, no. 7, pp. 641–678, 2009.

[23] M. Z. Elsabee, H. F. Naguib, and R. E. Morsi, "Chitosan based nanofibers, review," *Materials Science and Engineering C*, vol. 32, no. 7, pp. 1711–1726, 2012.

[24] K. Sun and Z. H. Li, "Preparations, properties and applications of chitosan based nanofibers fabricated by electrospinning," *Express Polymer Letters*, vol. 5, no. 4, pp. 342–361, 2011.

[25] X. Geng, O.-H. Kwon, and J. Jang, "Electrospinning of chitosan dissolved in concentrated acetic acid solution," *Biomaterials*, vol. 26, no. 27, pp. 5427–5432, 2005.

[26] K. Ohkawa, D. Cha, H. Kim, A. Nishida, and H. Yamamoto, "Electrospinning of chitosan," *Macromolecular Rapid Communications*, vol. 25, no. 18, pp. 1600–1605, 2004.

[27] H. Homayoni, S. A. H. Ravandi, and M. Valizadeh, "Electrospinning of chitosan nanofibers: processing optimization," *Carbohydrate Polymers*, vol. 77, no. 3, pp. 656–661, 2009.

[28] J. D. Schiffman and C. L. Schauer, "Cross-linking chitosan nanofibers," *Biomacromolecules*, vol. 8, no. 2, pp. 594–601, 2007.

[29] H. Homayoni, S. A. H. Ravandi, and M. Valizadeh, "Influence of the molecular weight of chitosan on the spinnability of chitosan/poly(vinyl alcohol) blend nanofibers," *Journal of Applied Polymer Science*, vol. 113, no. 4, pp. 2507–2513, 2009.

[30] F. Roozbahani, N. Sultana, A. Fauzi Ismail, and H. Nouparvar, "Effects of chitosan alkali pretreatment on the preparation of electrospun PCL/chitosan blend nanofibrous scaffolds for tissue engineering application," *Journal of Nanomaterials*, vol. 2013, Article ID 641502, 6 pages, 2013.

[31] K. T. Shalumon, K. H. Anulekha, K. P. Chennazhi, H. Tamura, S. V. Nair, and R. Jayakumar, "Fabrication of chitosan/poly(caprolactone) nanofibrous scaffold for bone and skin tissue engineering," *International Journal of Biological Macromolecules*, vol. 48, no. 4, pp. 571–576, 2011.

[32] S. Hong and G. Kim, "Fabrication of electrospun polycaprolactone biocomposites reinforced with chitosan for the proliferation of mesenchymal stem cells," *Carbohydrate Polymers*, vol. 83, no. 2, pp. 940–946, 2011.

[33] A. Cooper, N. Bhattarai, and M. Zhang, "Fabrication and cellular compatibility of aligned chitosan-PCL fibers for nerve tissue regeneration," *Carbohydrate Polymers*, vol. 85, no. 1, pp. 149–156, 2011.

[34] Y. Zhang, H. Ouyang, T. L. Chwee, S. Ramakrishna, and Z.-M. Huang, "Electrospinning of gelatin fibers and gelatin/PCL composite fibrous scaffolds," *Journal of Biomedical Materials Research Part B: Applied Biomaterials*, vol. 72, no. 1, pp. 156–165, 2005.

[35] E. J. Chong, T. T. Phan, I. J. Lim et al., "Evaluation of electrospun PCL/gelatin nanofibrous scaffold for wound healing and layered dermal reconstitution," *Acta Biomaterialia*, vol. 3, no. 3, pp. 321–330, 2007.

[36] L. van der Schueren, I. Steyaert, B. de Schoenmaker, and K. de Clerck, "Polycaprolactone/chitosan blend nanofibres electrospun from an acetic acid/formic acid solvent system," *Carbohydrate Polymers*, vol. 88, no. 4, pp. 1221–1226, 2012.

[37] X. Yang, X. Chen, and H. Wang, "Acceleration of osteogenic differentiation of preosteoblastic cells by chitosan containing nanofibrous scaffolds," *Biomacromolecules*, vol. 10, no. 10, pp. 2772–2778, 2009.

[38] L. van der Schueren, B. de Schoenmaker, Ö. I. Kalaoglu, and K. de Clerck, "An alternative solvent system for the steady state electrospinning of polycaprolactone," *European Polymer Journal*, vol. 47, no. 6, pp. 1256–1263, 2011.

[39] D. H. Reneker and A. L. Yarin, "Electrospinning jets and polymer nanofibers," *Polymer*, vol. 49, no. 10, pp. 2387–2425, 2008.

[40] H. Qi, P. Hu, J. Xu, and A. Wang, "Encapsulation of drug reservoirs in fibers by emulsion electrospinning: morphology characterization and preliminary release assessment," *Biomacromolecules*, vol. 7, no. 8, pp. 2327–2330, 2006.

Hindawi Publishing Corporation
Journal of Nanomaterials
Volume 2015, Article ID 514501, 9 pages
http://dx.doi.org/10.1155/2015/514501

Research Article

Measuring the Electrical Properties of MWNT-PA6 Reinforced Nanocomposites

Monica Alina Călin,[1] Liliana Rozemarie Manea,[1] Laurence Schacher,[2] Dominique Adolphe,[2] Ana Lăcrămioara Leon,[1] Georgeta Lidia Potop,[1] and Maricel Agop[3]

[1]*Faculty of Textile-Leather Engineering and Industrial Management, Technical "Gheorghe Asachi" University of Iași, Bulevardul D. Mangeron No. 67, 700050 Iași, Romania*
[2]*Laboratoire de Physique et Mécanique Textiles EAC 7189 CNRS/UHA, ENSISA, 11 rue Alfred Werner, 68093 Mulhouse Cedex, France*
[3]*Department of Physics, Technical "Gheorghe Asachi" University of Iași, Bulevardul D. Mangeron No. 63, 700050 Iași, Romania*

Correspondence should be addressed to Monica Alina Călin; ma.calin@yahoo.com

Received 17 October 2014; Accepted 25 December 2014

Academic Editor: Davood D. Ganji

The paper studies the electrical properties of polyamide 6- (PA6-) carbon nanotubes (CNTs) nanowebs, obtained through electrospinning. Three different treatments (chemical, mechanical, and mixed) were applied to the CNT in order to prepare the electrospinning solutions. For each treatment, the CNT content was different: 0.5%, 1%, 1.5%, and 2%. The electrical volume and surface conductivity of the obtained samples were studied by measuring their electrical volume and surface resistance. Homemade plate electrodes were used. The samples were also analyzed using a scanning electron microscope (SEM) and an atomic force microscope (AFM). Defects were found on the extremities: solvent traces, flat fibers, and beads. The mixed treatment seems too aggressive and it is not recommended. The AFM analysis gave values for roughness and profile height (Ra and Rz): extreme values were obtained for the chemically and mechanically treated samples. Next, a pristine PA6 sample was used to compare the influence of the CNT content on the electric behavior of the samples. By increasing the pressure on the specimens, the volume resistivity decreased exponentially, while the surface resistivity showed no significant changes, independently of the CNT content. The obtained behavior proves a great potential of the MWNT-PA6 reinforced nanocomposites for sensor applications.

1. Introduction

Fullerene, which is a third allotropy form of carbon, was discovered in 1985, after the other known forms of carbon: graphite and diamond (which are hybridized sp2 and sp3, resp.). The most famous of all carbon forms in the fields of nanoscience are carbon nanotubes (CNTs). They were observed for the first time in 1991 by Sumio Iijima, a Japanese scientist, who used a high resolution transmission electron microscope (HRTEM). Carbon nanotubes can be found in two structures: single- or multiwalled (SWNT/MWNT) [1]. CNTs possess magnificent thermal, electrical, mechanical, and electrical properties which make them excellent candidates for a lot of applications. It is well known that CNTs can carry a current density of 10^9 A/cm^2, which is the highest of any known materials [2, 3].

In order for CNT to be used effectively for obtaining polymer nanocomposites, an appropriate interfacial adhesion between the CNTs and the polymer matrix must be guaranteed [4–6]. There are usually two distinct techniques: mechanical and chemical. The mechanical approach consists of procedures such as ultrasonication, high shear mixing, and ball milling, while the chemical approach uses surface functionalization of CNTs, in order to improve their chemical compatibility to the polymer matrix and reduce their tendency to agglomerate. In the case of the chemical treatment, boiling acids are used (H_2SO_4 + HNO_3) under ultrasonication, followed by boiling [4].

In this study, three distinct techniques were applied to the CNTs: chemical, mechanical, and mixed treatments. The last is a combination of the chemical and the mechanical treatments.

2. Experimental

2.1. Materials. The materials used for this experiment are *polyamide 6* (*PA6*), presented as pellets of 3 mm in diameter, bought from Sigma-Aldrich (France), with a molecular weight M_w = 150000 g·mol^{-1}; *nitric acid* (HNO_3), purchased from Fisher Scientific (France); *sulphuric acid* (H_2SO_4), 50% purity, also purchased from Fischer Scientific (France); *93% purity multiwalled carbon nanotubes*, with an external diameter of 11 nm and 3.2 ± 1 nm thickness, purchased from Arkema (France). The sulphuric acid is a highly corrosive strong mineral acid, colourless to slightly yellow, viscous, and soluble in water at all concentrations. The nitric acid is also a highly corrosive acid, colourless, with a usual concentration of 68%. Both acids are very toxic.

2.2. Protocol of Work. Firstly, three different types of treatments were applied to the MWNTs: chemical, mechanical, and mixed. The MWNT content was different as follows: 0.5%, 1%, 1.5%, and 2%. The three treatments are described below.

2.2.1. Chemical Treatment. A mixture of 65% HNO_3 and 50% H_2SO_4 (v/v = 1 : 3) was prepared in an Erlenmeyer glass and then 4 g of MWNTs was added. The solution was sonicated at 50°C for 4 hours. Then the MWNTs were separated from the mixture of acids and purified with oxygenated water until the pH value reached 7. Then the MWNTs were left for 48 hours into an oven at 130°C, for drying. After the drying process, the MWNTs were weighted and there were 2.8 g left. The rest of 1.2 g was wasted during the washing procedure. Next, the acidic MWNTs were split into 4 different concentrations, 0.5%, 1%, 1.5%, and 2%, and dispersed into 27.77 mL of 90% CH_2O_2 (which is the equivalent of 25 mL of pure CH_2O_2) together with the PA6 pellets. The quantity of PA6 for each solution was calculated so that the final solutions should have a 20% PA6 content. The solutions were left for 72 hours at 70°C on a magnetic stirrer in order to ease the dissolving process of the PA6 and homogenize the solution.

Four chemically treated solutions resulted. They were left to reach room temperature.

2.2.2. Mechanical Treatment. The first stage of the mechanical treatment was the separation of 0.1919 g, 0.3861 g, 0.5828 g, and 0.7821 g of MWNT corresponding to the 0.5%, 1%, 1.5%, and 2% MWNT concentrations, into 4 different bottles. 27.77 mL of 90% CH_2O_2 each was added and left for 1 hour for sonication at 50°C. The process was followed by high mixing using the Ika T25 digital Ultra Turrax, at 18.000 rpm for 30 minutes. The final step was adding the PA6 pellets quantity so that the final solution should have a 20% PA6 content and then they were left for 72 hours at 70°C on a magnetic stirrer. The 4 mechanically treated solutions which resulted were left to reach room temperature.

2.2.3. Mixed Treatment. The same mixture of 65% HNO_3 and 50% H_2SO_4 (v/v = 1 : 3) which was used for the chemical treatment was prepared in an Erlenmeyer glass and 4 g of MWNTs was added. It was left for sonication at 50°C for 4 hours and then mixed with Ultra Turrax at 18.000 rpm for 30 minutes. Then the MWNTs were separated from the mixture of acids and washed with oxygenated water until the pH value reached 7. Next, the MWNTs were put into an oven at 130°C, for 48 hours, for drying. Similar to the previous two procedures, the mixed treated MWNTs were split into 4 different concentrations, 0.5%, 1%, 1.5%, and 2%, and then dispersed into 27.77 mL of 90% CH_2O_2 together with the PA6 pellets. The solutions were left for 72 hours at 70°C on a magnetic stirrer. Four mixed treated solutions resulted. They were left to reach room temperature.

2.2.4. Electrospinning Conditions. For the electrospinning procedure, an experimental device, built in the "Laboratoire de Physique et Mécanique Textiles," ENSISA, Mulhouse (France), was used [7]. The 12 obtained solutions were electrospun for 15 minutes at 30 kV voltage, room conditions of 30% humidity, and 20°C. A 0.7 × 30 mm needle was used, with a 15 cm distance from the needle to the collecting area and a 0.283 mL feed rate was applied.

2.2.5. Structural Analysis of the Samples. The obtained samples have been characterized using the scanning electron microscopy (SEM, Hitachi S-2360N) and the atomic force microscopy (AFM, NTEGRA Spectra NT-MDT). Table 1 shows the SEM results, for each CNT concentration. In these pictures, 100 different fibers of each sample were measured in order to evaluate their diameters.

Table 3 shows the AFM results for each CNT concentration. The surface roughness for 100 nanofibers per sample was calculated using the Gwyddion free software. Average values of the roughness (Ra) and the average profile height (Rz) were obtained (Table 2).

The extreme Ra and Rz values were obtained for the chemically and mechanically treated samples:

(i) min: 0.5% CNT content, chemical treatment: Ra = 2 nm; Rz = 9 nm;

(ii) max: 0.5% CNT content, mechanical treatment: Ra = 11.2 nm; Rz = 57.8 nm.

2.2.6. Preparing the Samples for the Resistance Measurements. In order to measure the volume resistance, three specimens of 1 × 1 cm were cut from each of the obtained samples, while for the surface resistance the cut dimension was 1 × 3 cm. Both the surface and the volume resistance were measured up to the American Standard ASTM D 257-61, using homemade plate electrodes. The electrodes were made from copper and they were previously metallized with a gold layer. Before the measuring procedure, the samples were left for 24 hours in the room where they were to be tested, in atmospheric conditions of 20 ± 2°C and 60 ± 2% humidity. The device used was the Knick Terra Ohm Meter (LPMT, ENSISA, Mulhouse, France).

An assembly of loads with the purpose of studying the effect of compression on resistivity was also used (Figure 1).

Table 4 contains the parameters of the electrical resistance measurements.

Table 1: SEM results.

	Chemical treatment	Mechanical treatment	Mixed treatment
0.5% CNT	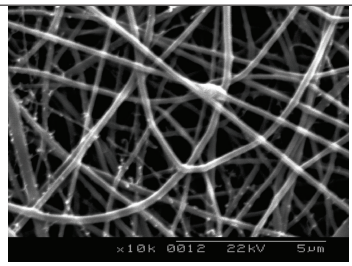	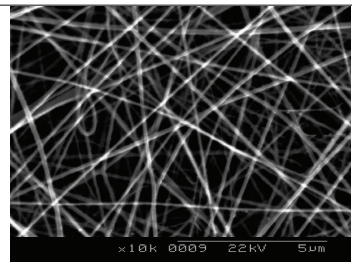	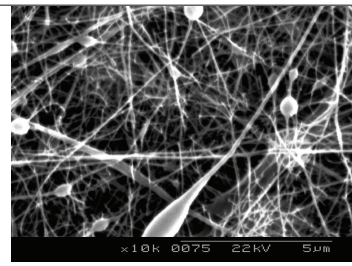
1% CNT	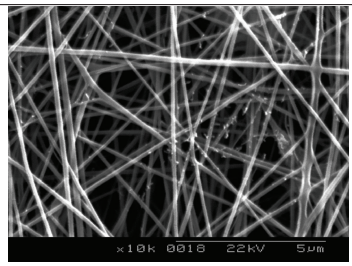	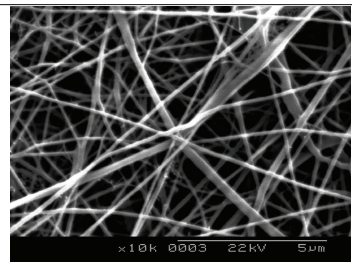	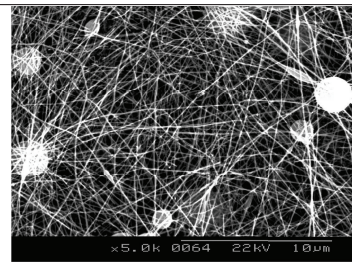
1.5% CNT	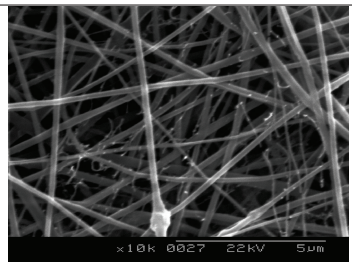	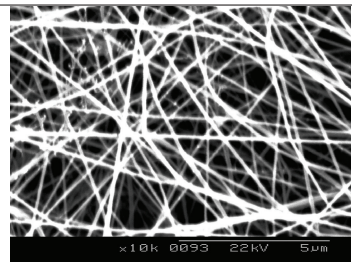	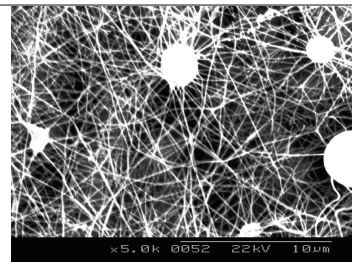
2% CNT	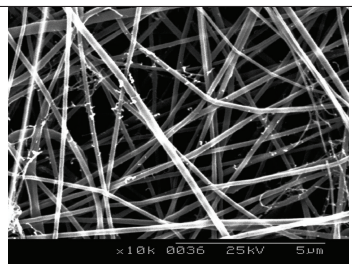	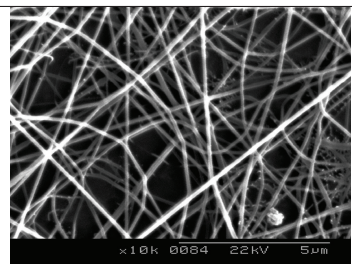	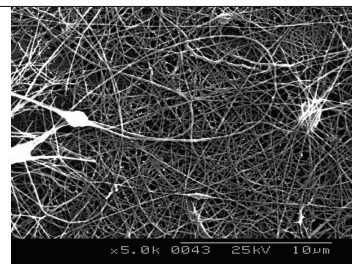

Table 2: Average values of the roughness (Ra) and profile height (Rz) for the electrospun nanofibers.

	Chemical treatment				Mechanical treatment				Mixed treatment			
	0.5%	1%	1.5%	2%	0.5%	1%	1.5%	2%	0.5%	1%	1.5%	2%
Ra (nm)	2	3.8	7	6.4	11.2	2.42	2.24	3.2	9	4.5	4.68	5.2
Rz (nm)	9	20.2	32.6	27.2	57.8	10.36	13.4	14.2	23	19.56	17.44	20.2

3. Results and Discussions

3.1. The Influence of the CNT Content on the Morphology of the Nanofibers. For the SEM analysis, for each sample, specimens from 3 different areas were taken: two extremities and the center. The diameters of the nanofibers varied from 43.37 nm corresponding to the 0.5% CNT mixed treated sample to 304.71 nm corresponding to the 0.5% CNT chemically treated sample. Analysing the values of the obtained diameters, the obtained nanofibers show a high level of homogeneity. As far as defects are concerned, the chemically treated samples exhibit solvent traces on the extremity specimens, which caused that the nanofibers stick to each other. At the same time, the nanofibers from the extremities are not uniform and are flat. However, the nanofibers analysed from the center specimens have a uniform aspect with a homogenous structure. Occasionally, few beads are also present [8].

In the case of mechanically treated samples, the traces of solvent are significantly reduced if compared to

Table 3: AFM results.

	Chemical treatment	Mechanical treatment	Mixed treatment
0.5% CNT	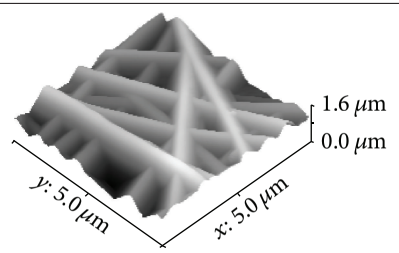	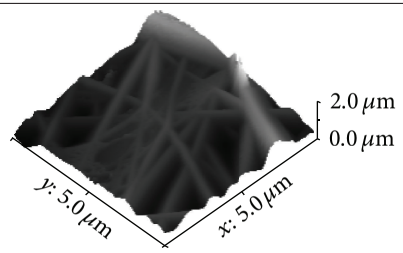	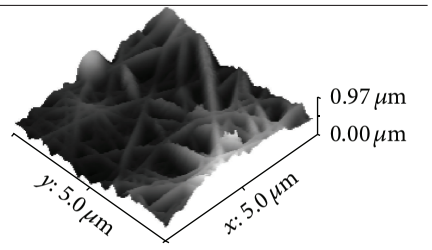
1% CNT	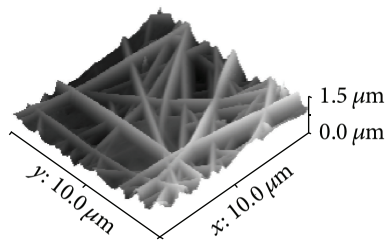	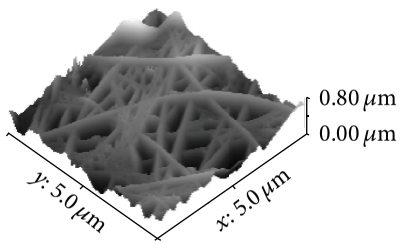	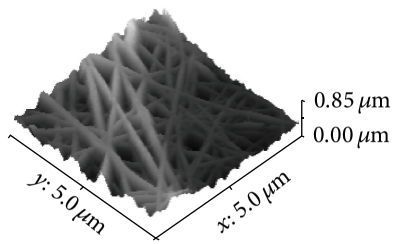
1.5% CNT	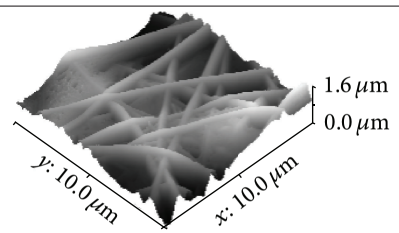	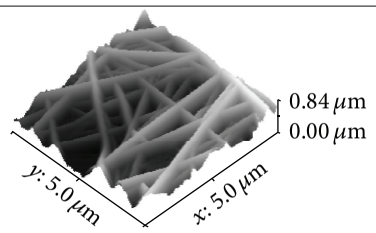	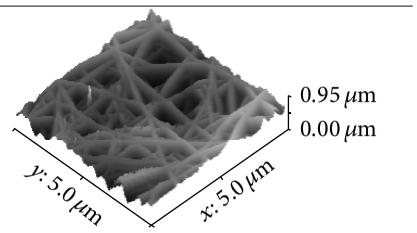
2% CNT	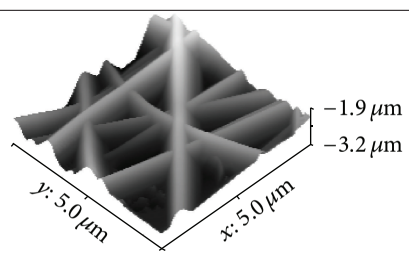	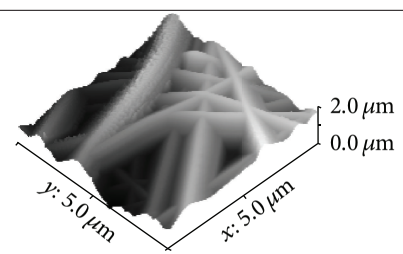	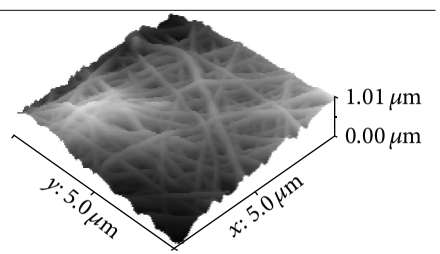

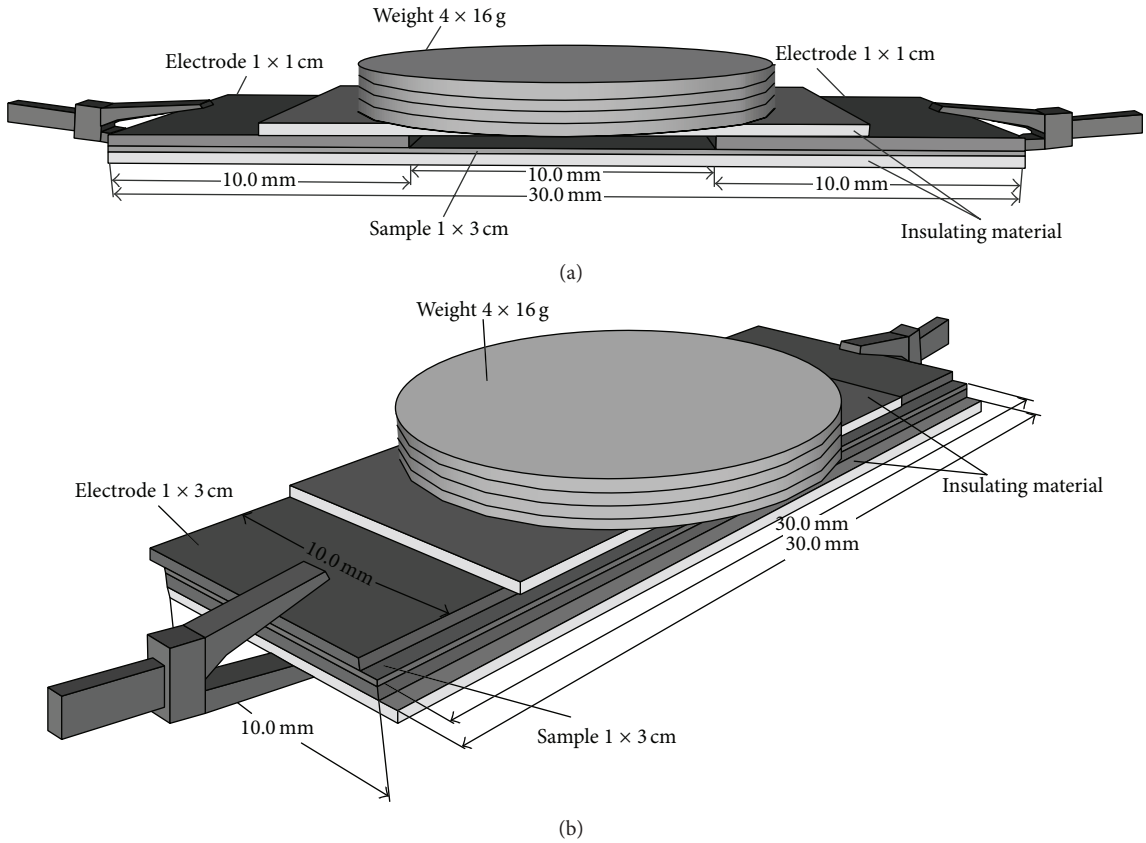

Figure 1: Surface resistance setup versus volume resistance setup.

Table 4: Parameters of the electrical resistance measurements.

Resistance type	Surface	Volume
Dimension of the specimens	1 × 1 cm	1 × 3 cm
Conditioning of the specimen	(i) No cleaning (ii) No predrying (iii) 24 h of conditioning	
Atmospheric testing conditions	20 ± 2°C 60 ± 2% RH	
Applied voltage	500 V	100 V
Time of electrification	2 min	

the chemically treated ones. Instead, the number of beads is higher. Another important aspect is that the electrospinning jet was not continuous, as droplets of solution are present on the surface of the nanofibers.

The mixed treatment led to the following results: very high number of beads on the surface of the nanofibers and flat fibers. This is caused by the fact that the CNT structure was influenced by two important factors: chemical and mechanical treatments. It can be concluded that both treatments combined proved to be too aggressive for the CNT structure.

Next we will analyse the percolation threshold of the nanocomposites and the influence of the CNT on the volume resistivity of the chemically treated nanofibers.

3.2. Percolation Threshold of the Reinforced Nanocomposites and the Influence of the CNT Content on the Volume Resistivity of the Nanocomposites. Figure 2 shows the behaviour of the electrical volume conductivity in S/m of the pristine PA6 sample, compared to the reinforced PA6, at different CNT content, for each of the 3 applied treatments. The obtained results have shown that the percolation threshold is below the 0.5% concentration. Increasing the CNT, conductivity also increases, which proves that the electrical status of the nanocomposite changes from an insulative into static dissipative material (where the conductivity is between 1×10^{-4} S and 1×10^{-11}) [9–11].

One can also notice that the values of the volume resistivity of the samples decrease together with the applied load (Figure 3). This shows the fact that the nanocomposites can be used as pressure sensors and be integrated in smart textiles [12].

3.3. The Influence of the CNT Content on the Surface Resistivity of Nanocomposites. Due to the fact that the dimension of the analysed specimens was 1 × 3 cm and the dimension of the electrodes was 1 × 1 cm, the distance between the electrodes equals the dimension of the contact surface (1 × 1 cm).

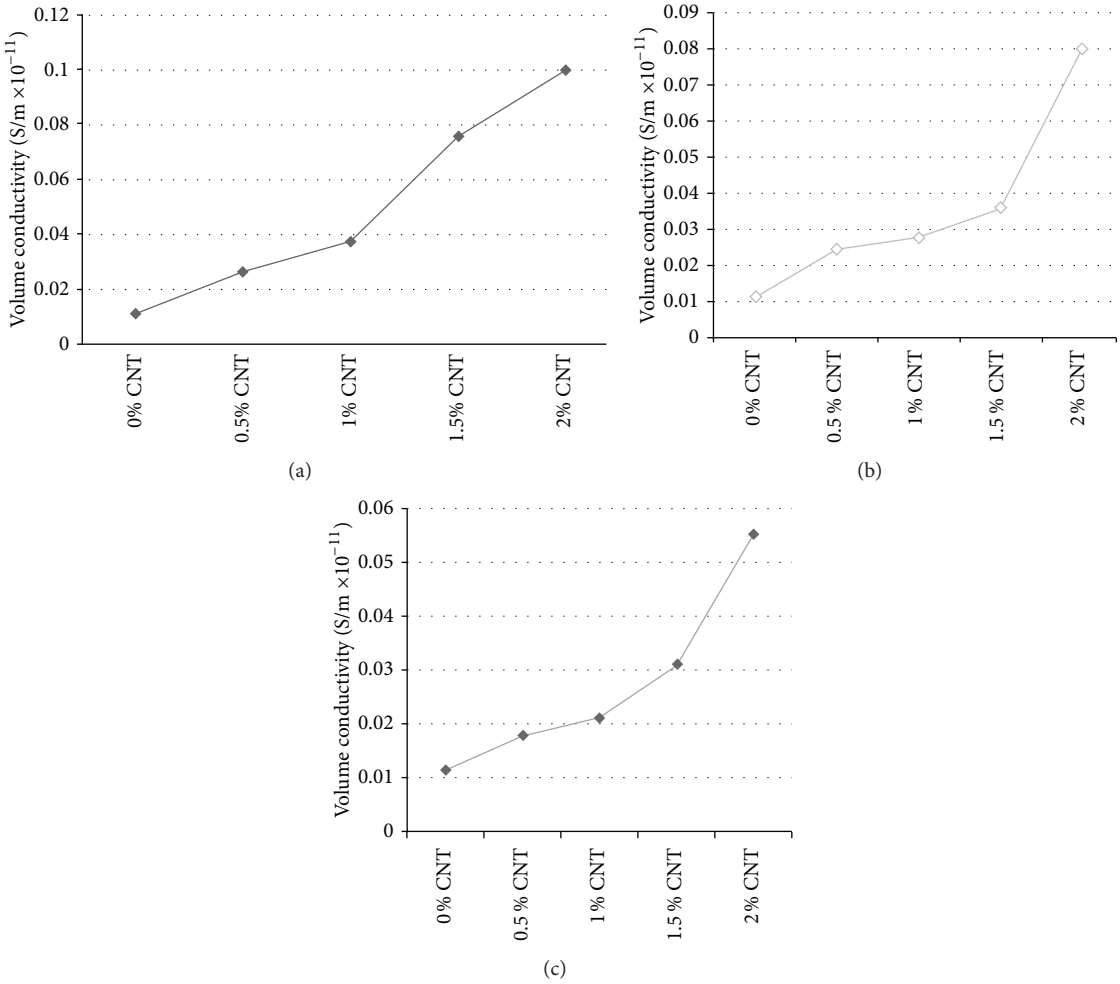

Figure 2: Volume conductivity of the 20% CNT PA6 composite with different CNT content: (a) chemical treatment; (b) mechanical treatment; (c) mixed treatment.

The CNTs are present both inside and on the surface of the nanofibers [13]. This means that the values of the surface resistivity are the same with those of the surface electrical resistance.

Figure 4 shows the evolution of the surface electrical resistivity for the obtained samples. There were no significant changes for the surface resistivity of the samples. Neither the CNT content nor the applied treatment has shown a significant change in the surface resistivity in relation to the applied load.

We note that the electrical behaviour of the PA6-CNT nanocomposites analysed in the current paper (volume resistivity and conductivity, surface resistivity and conductivity) can be theoretically approached using the two nanocomposite models, (the Tanaka or the Tsagaropoulos model) [14, 15]. In such a context, different dependencies of the above mentioned electrical parameters can be accepted (temperature dependency, etc.) so that the dynamics analysis can become more complex but complete. We consider that this study requires a separate analysis which will be done in a future paper.

4. Conclusions

The main conclusions of the present paper are as follows:

(i) as far as defects are concerned, the chemically treated solutions gave the most uniform nanofibers;

(ii) the biggest number of defects found on the nanofibers resulted from the mixed treatment;

(iii) the percolation threshold could not be reached; it is below 0.5% concentration;

(iv) increasing the CNT, the volume conductivity also increases;

(v) the values of the volume resistivity of the samples decrease together with the applied load;

(vi) for surface resistivity, no significant changes were observed; neither the CNT content nor the applied treatment has shown a significant change in the surface resistivity in relation to the applied load.

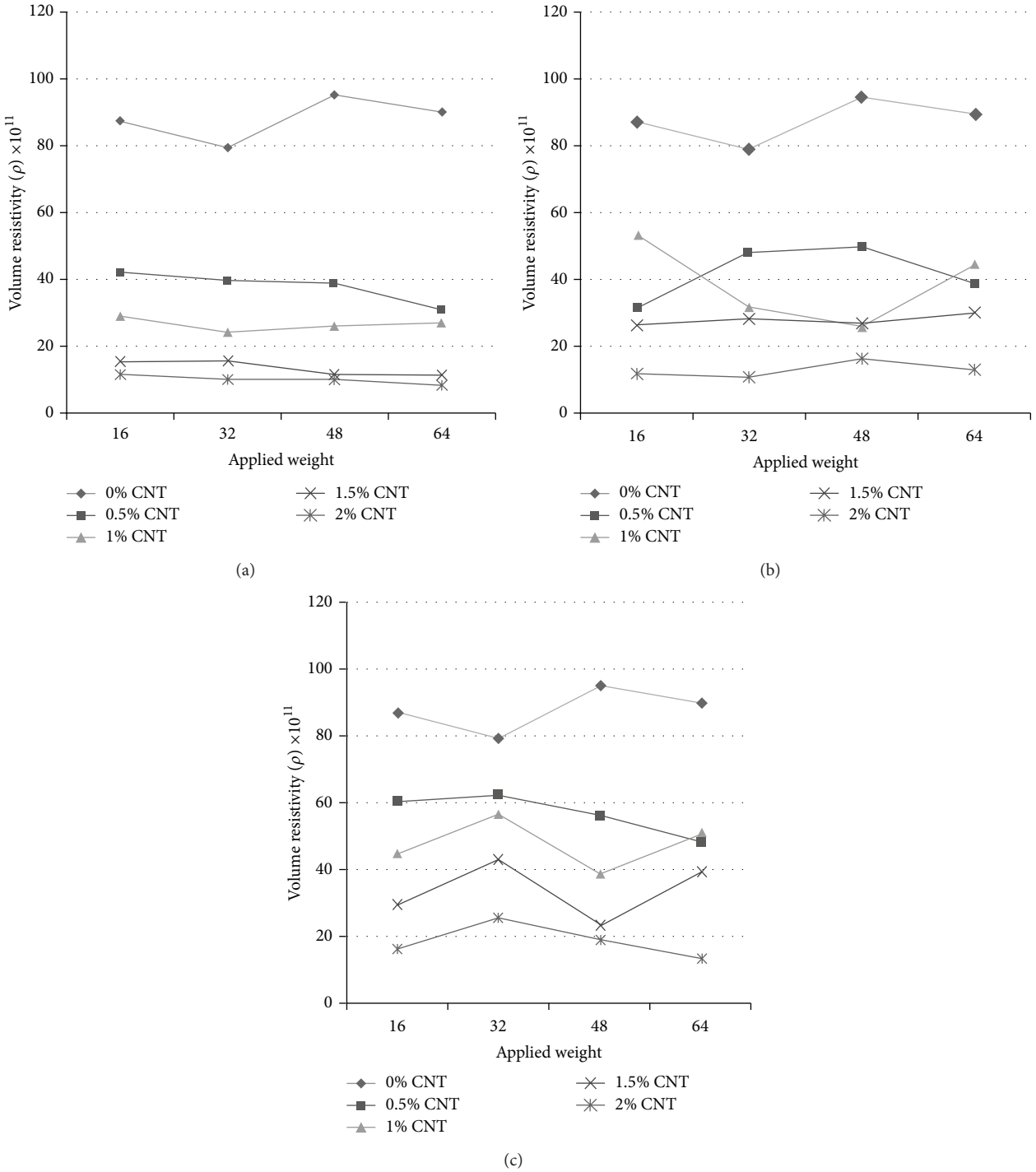

Figure 3: Volume resistivity of the 20% CNT PA6 composite with different CNT content: (a) chemical treatment; (b) mechanical treatment; (c) mixed treatment.

Conflict of Interests

The authors declare that there is no conflict of interests.

Authors' Contribution

M. A. Călin created the experimental solutions; electrospun the solutions; was responsible for SEM analysis of the nanofibers, AFM analysis of the nanofibers, analysis of the volume behavior of the nanofibers, analysis of the surface resistivity behavior of the nanofibers, and interpretation of the results; and has written the paper. L. R. Manea has helped with the interpretation of the electrospinning parameters. L. Schacher has provided support and assistance for the measurements and has provided the equipment required for the experimental research. D. Adolphe has provided support

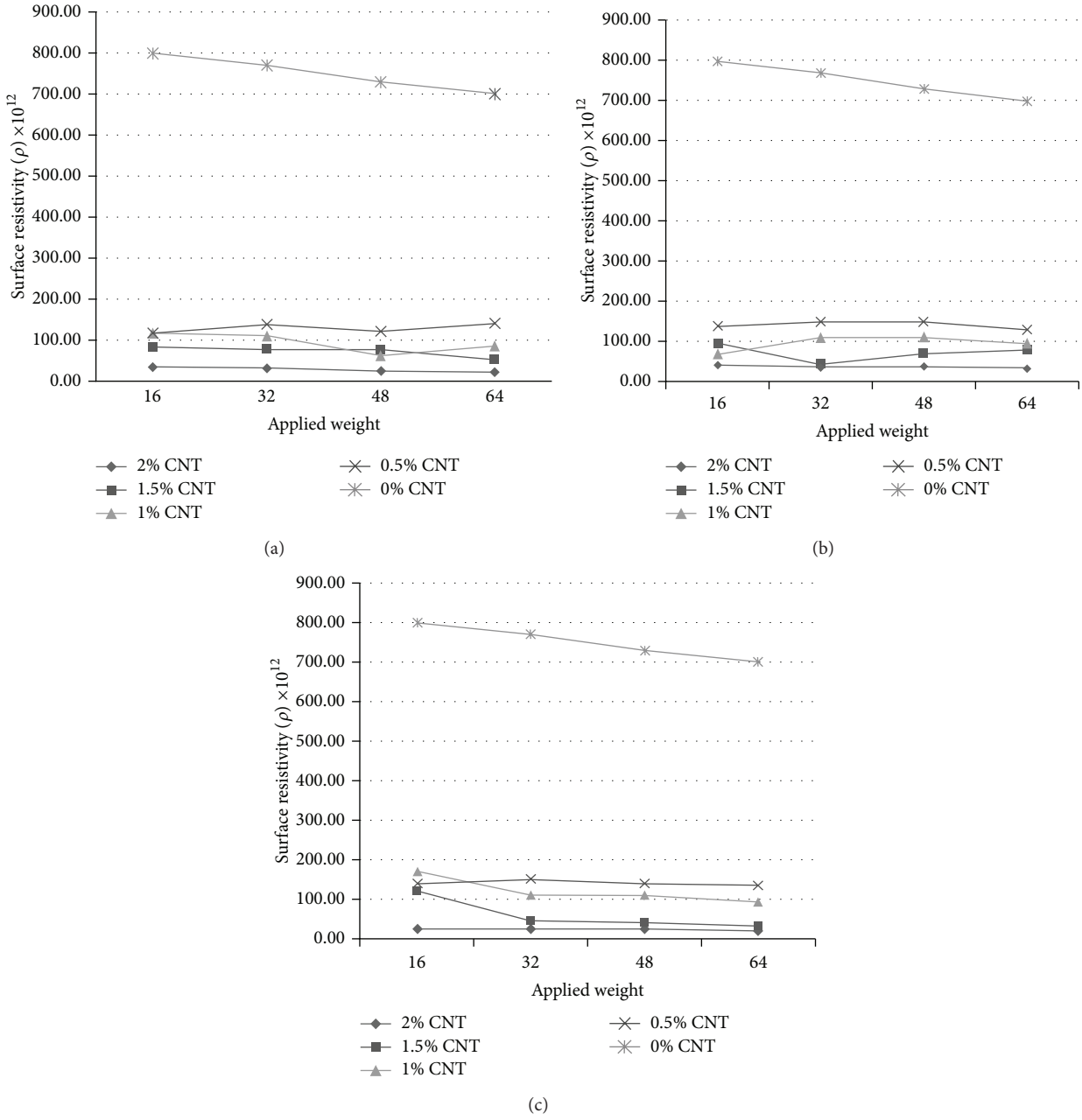

Figure 4: Surface resistivity of the 20% CNT PA6 composite with different CNT content: (a) chemical treatment; (b) mechanical treatment; (c) mixed treatment.

and assistance for the measurements and has provided the equipment required for the experimental research. A. L. Leon has helped with the interpretation of the electrospinning parameters. G. L. Potop has helped with the interpretation of the electrospinning parameters. M. Agop coordinated the interpretation and analysis of the electrical results.

References

[1] M. A. Călin, S. Almuhamed, N. Khenoussi et al., "Characterization of MWNT-reinforced PA6 nanocomposites (produced by electrospinning)," in *Proceedings of the 12th World Conference Autex*, Zadar, Croatia, June 2012.

[2] B. Q. Wei, R. Vajtai, and P. M. Ajayan, "Reliability and current carrying capacity of carbon nanotubes," *Applied Physics Letters*, vol. 79, no. 8, pp. 1172–1174, 2001.

[3] A. P. S. Sawhney, B. Condon, K. V. Singh, S. S. Pang, G. Li, and D. Hui, "Modern applications of nanotechnology in textiles," *Textile Research Journal*, vol. 78, no. 8, pp. 731–739, 2008.

[4] P.-C. Ma, N. A. Siddiqui, G. Marom, and J.-K. Kim, "Dispersion and functionalization of carbon nanotubes for polymer-based nanocomposites: a review," *Composites Part A: Applied Science and Manufacturing*, vol. 41, no. 10, pp. 1345–1367, 2010.

[5] X. L. Xie, Y.-W. Mai, and X.-P. Zhou, "Dispersion and alignment of carbon nanotubes in polymer matrix: a review," *Materials Science and Engineering R: Reports*, vol. 49, no. 4, pp. 89–112, 2005.

[6] B. Fiedler, F. H. Gojny, M. H. G. Wichmann, M. C. M. Nolte, and K. Schulte, "Fundamental aspects of nano-reinforced composites," *Composites Science and Technology*, vol. 66, no. 16, pp. 3115–3125, 2006.

[7] N. Khenoussi, L. Schacher, and D. C. Adolphe, "Nanofiber production: study and development of electrospinning device," *Experimental Techniques*, vol. 36, no. 2, pp. 32–39, 2012.

[8] Y. Liu, J.-H. He, J.-Y. Yu, and H.-M. Zeng, "Controlling numbers and sizes of beads in electrospun nanofibers," *Polymer International*, vol. 57, no. 4, pp. 632–636, 2008.

[9] S. Almuhamed, N. Khenoussi, L. Schacher, D. Adolphe, and H. Balard, "Measuring of electrical properties of MWNT-reinforced PAN nanocomposites," *Journal of Nanomaterials*, vol. 2012, Article ID 750698, 7 pages, 2012.

[10] S. Pfeifer, S.-H. Park, and P. R. Bandaru, "Analysis of electrical percolation thresholds in carbon nanotube networks using the Weibull probability distribution," *Journal of Applied Physics*, vol. 108, no. 2, Article ID 024305, 2010.

[11] J. Li, P. C. Ma, C. W. Sze, T. C. Kai, B. Z. Tang, and J.-K. Kim, "Percolation threshold of polymer nanocomposites containing graphite nanoplatelets and carbon nanotubes," in *Proceedings of the 16th International Conference on Composite Materials (ICCM '07)*, July 2007.

[12] ESDA, *ESD Association Advisory for Electrostatic Discharge Terminology*, ESD Association, 2009.

[13] J. M. Deitzel, J. Kleinmeyer, D. Harris, and N. C. B. Tan, "The effect of processing variables on the morphology of electrospun nanofibers and textiles," *Polymer*, vol. 42, no. 1, pp. 261–272, 2001.

[14] M. G. Danikas, "On two nanocomposite models: differences, similarities and interpretational possibilities regarding Tsagaropoulos' model and Tanaka's model," *Journal of Electrical Engineering*, vol. 61, no. 4, pp. 241–246, 2010.

[15] M. G. Danikas, A. Bairaktari, R. Sarathi, and A. Basri Bin Abd Ghani, "A review of two nanocomposite insulating materials models: Lewis' contribution in the development of the models, their differences, their similarities and future challenges," *Engineering, Technology & Applied Science Research*, vol. 4, no. 3, pp. 636–643, 2014.

Hindawi Publishing Corporation
Journal of Nanomaterials
Volume 2015, Article ID 275230, 8 pages
http://dx.doi.org/10.1155/2015/275230

Research Article

Fabrication and Characterization of Cellulose Acetate/Montmorillonite Composite Nanofibers by Electrospinning

Se Wook Kim,[1] Seong Ok Han,[1] I Na Sim,[1] Ja Young Cheon,[2] and Won Ho Park[2]

[1]*Energy Materials and Convergence Research Department, Korea Institute of Energy Research, 71-2 Jang-dong, Yuseong-gu, Daejeon 305-343, Republic of Korea*
[2]*Department of Advanced Organic Materials and Textile System Engineering, Chungnam National University, 220 Gung-dong, Yuseong-gu, Daejeon 305-764, Republic of Korea*

Correspondence should be addressed to Seong Ok Han; sohan@kier.re.kr and Won Ho Park; parkwh@cnu.ac.kr

Received 3 September 2014; Accepted 11 February 2015

Academic Editor: Lan Xu

Nanofibers composed of cellulose acetate (CA) and montmorillonite (MMT) were prepared by electrospinning method. MMT was first dispersed in water and mixed with an acetic acid solution of CA. The viscosity and conductivity of the CA/MMT solutions with different MMT contents were measured to compare with those of the CA solution. The CA/MMT solutions were electrospun to fabricate the CA/MMT composite nanofibers. The morphology, thermal stability, and crystalline and mechanical properties of the composite nanofibers were characterized by scanning electron microscopy (SEM), transmission electron microscopy (TEM), energy dispersive X-ray spectroscopy (EDX), thermogravimetric analysis (TGA), X-ray diffraction (XRD), and tensile test. The average diameters of the CA/MMT composite nanofibers obtained by electrospinning 18 wt% CA/MMT solutions in a mixed acetic acid/water (75/25, w/w) solvent ranged from 150~350 nm. The nanofiber diameter decreased with increasing MMT content. TEM indicated the coexistence of CA nanofibers. The CA/MMT composite nanofibers showed improved tensile strength compared to the CA nanofiber due to the physical protective barriers of the silicate clay layers. MMT could be incorporated into the CA nanofibers resulting in about 400% improvement in tensile strength for the CA sample containing 5 wt% MMT.

1. Introduction

Electrospinning is a unique technique for producing nonwoven fabrics of nanofibers, which exhibit high specific surface area and porosity on account of their potential applications, such as sensors [1, 2], filtration [3–5], membranes, tissue engineering, and drug delivery [6–9]. In addition, electrospinning is a good and effective method for fabricating micro- to nanoscale fibers from a variety of polymers, such as cellulose acetate [10], polystyrene [11], polybutadiene [12], and polycaprolactone [13]. In electrospinning, a high voltage (ca. 10–30 kV) that is sufficient to overcome the surface tension of a pendant drop of polymer solution is applied to a capillary containing polymer solution to induce the ejection of fine charged jets toward a target. These jets are stretched and elongated before they reach the target and are then dried and collected as an interconnected web of small fibers [14].

Cellulose is the most abundant natural polymeric material with a polyfunctional macromolecular structure and environmentally benign nature. Despite being characterized by its extensive linearity, good flexibility, excellent durability, biodegradability, chemical resistance, mechanical strength, nontoxicity, and low cost, cellulose suffers from a lack of solubility in most organic solvents due to its supramolecular architecture. However, one of its organic soluble derivatives, cellulose acetate (CA), carries all of the aforementioned remarkable features as well as good solubility in organic solvents, making it an excellent material for electrospinning [15]. The electrospinning of CA has been studied using various solvents [10, 16].

Functional nanomaterials, such as metal nanoparticles, carbon nanotubes, and nanoclays, can be incorporated into the electrospun CA nanofibers. The incorporation of functional nanomaterials into a CA nanofibrous structure is an attractive hybridization method, because nanomaterials distributed evenly in the CA nanofibrous structure can be used for novel specific applications. The CA nanocomposites reinforced with nanoclay (montmorillonite, MMT) can be quite promising due to the remarkable improvement in the material properties of polymer composites with only a low percentage of MMT added. The main advantages of these nanocomposites are the improvements in mechanical properties, reduced flammability, and superior barrier properties compared to polymers or conventional micro- and macrocomposites. Nanocomposites of CA and MMT have been prepared into film- or paper-shaped composite structures by conventional compounding methods, such as solution casting [16], melt processing [17], and dispersion method [18], and mechanical properties of CA/MMT composites have been further improved by the addition of compatibilizer or plasticizer [19, 20]. On the contrary, nanofiber-nanoclay composites of CA and MMT have unique advantages compared to conventional CA/MMT nanocomposites, because of higher surface area and biodegradability. However, there is no report on the electrospinning of CA nanofiber incorporated with MMT.

In this study, CA/MMT composite nanofibers were prepared by facile compounding and electrospinning. The morphological, thermal, structural, and mechanical properties of CA/MMT nanofibers were analyzed by scanning electron microscopy (SEM), transmission electron microscopy (TEM), thermogravimetric analysis (TGA), X-ray diffraction (XRD), and tensile test. In addition, the effect of electrospinning parameters on the distribution of MMT in the CA nanofibers was described.

2. Materials and Methods

2.1. Materials. Cellulose acetate (CA, acetyl content 39.8%, MW = 30,000 g/mol) was purchased from Aldrich Co., USA. Acetic acid (>99%) was purchased from DC chemical Pure Chemical Co., Korea. The clay (montmorillonite, MMT cloisite 93A) was supplied by Southern Clay Products Co., USA. Acetic acid and water were mixed to a weight ratio of 75 : 25. The resulting solution is abbreviated to acetic acid/water (75/25).

2.2. Preparation of CA/MMT Solution for Electrospinning. The CA and CA/MMT solutions were prepared using an ultrasonic treatment. MMT powders were dried at 80°C for 24 h under vacuum prior to use. For the CA solution, CA at a concentration of 18 wt% was dissolved in acetic acid/water (75/25) between 65°C and 75°C for 5 h. For the CA/MMT solutions, a predetermined amount of MMT was dispersed in water with constant stirring for one day after ultrasonication for 2 h. The CA/MMT solutions were compounded with a 1, 3, 5, 7, or 9 wt% of MMT and CA solution. The CA/MMT composites electrospun from these solutions are referred to as CA/MMT-1, CA/MMT-3, CA/MMT-5, CA/MMT-7, and CA/MMT-9, respectively.

2.3. Electrospinning of CA/MMT Nanofibers. Electrospinning was performed using a single syringe attached to a needle (ID = 0.84 mm), a ground electrode (d = 21.5 cm, aluminum sheet on a drum with a variable rotation speed), and high voltage supply (ChungPa EMT Co., Korea). Each solution was fed at a rate of 2 mL/h using a syringe pump and electrospun at a positive voltage of 27 kV. The tip-to-collector distance was 10 cm and all electrospinning procedures were carried out at 19°C.

2.4. Characterization of CA/MMT Solutions and Nanofibers. The viscosity and conductivity of the CA and CA/MMT solutions were determined using a Brookfield digital viscometer (Model-DV-prime) and a conductivity meter (Isteck model 455C) at 19°C, respectively. The thermal properties of the electrospun nanofibers were characterized by TGA (TGA Q 500, TA Instruments) at a heating rate of 10°C/min with purging nitrogen gas at 100 mL/min. The derivative thermogravimetric (DTG) curves were also recorded. The crystallinity of the CA and CA/MMT nanofibers was investigated by XRD (D/MAX-2500 diffractometer, Rich. Rigaku Co., Japan) with Cu-Kα radiation (100 mA, 40 kV). The tensile strength of the electrospun nanofibers was examined under tensile loading conditions using an Instron tensile testing machine (model 4467, Instron Co., USA) according to the ASTM D-638 method. The crosshead speed was 5 mm/min. At least twenty measurements were taken for each sample, and the results were averaged to obtain a mean value. The surface morphology of the CA and the CA/MMT nanofibers was characterized by SEM (S-4700, Hitachi, Japan) at an acceleration voltage of 15–25 kV. Prior to the measurement, the specimens were coated with Au to prevent surface charging. Field emission TEM (FE-TEM, FEI, Tecnai F30 Super-twin operated at an accelerating voltage of 200~300 kV with a Gatan imaging filter (GIF) model 2002) was performed to confirm existence of the MMT layers within the nanofibers that were directly electrospun onto carbon-coated TEM grid with a 300 mesh. The composition of the nanofibers was confirmed from the energy dispersive X-ray spectroscopy (EDAX, Genesis) spectrum and mapping images.

3. Results and Discussion

3.1. Characterization of CA Solution. Han et al. reported that CA nanofibers could be electrospun continuously using a mixed acetic acid/water solvent and the optimum concentration of CA for long uniform nanofibers was 17 wt% [10]. In this study, the viscosities of CA and CA/MMT-5 solutions were measured to determine the optimum concentration of CA solution and the effect of MMT addition on the CA solution for electrospinning. Figure 1 shows the viscosity of the CA and CA/MMT solutions with various CA concentrations in the range of 13~23 wt% in the acetic acid/water (75/25) solvent system. The viscosities of the CA and CA/MMT solutions were similar and the addition of 5 wt% MMT to CA solutions had little effect on the viscosity at CA solution concentrations < 18 wt%. The viscosity of CA and CA/MMT-5 increased relatively rapidly at CA concentrations > 18 wt%.

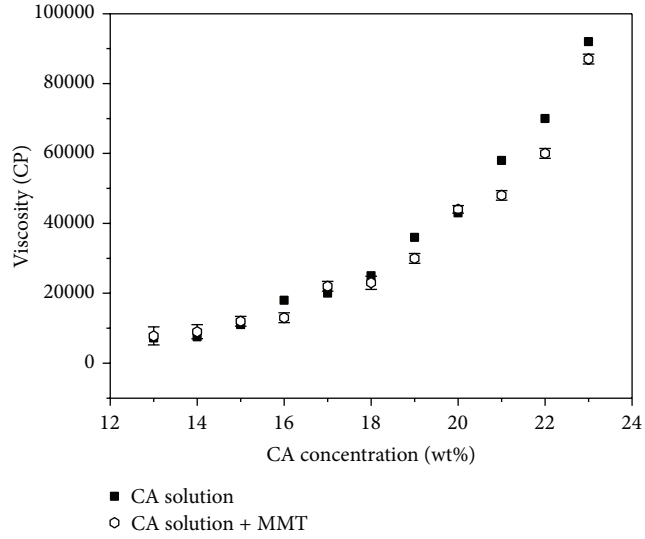

Figure 1: Changes in the viscosities according to the CA concentration.

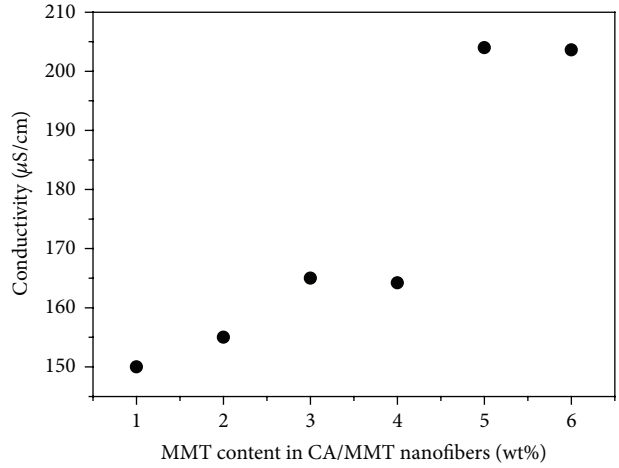

Figure 2: Changes in the conductivities with the MMT weight (1: pure CA, 2: CA/MMT1 wt%, 3: CA/MMT3 wt%, 4: CA/MMT5 wt%, 5: CA/MMT7 wt%, and 6: CA/MMT9 wt%).

The 18 wt% CA and CA/MMT-5 solutions were quite stable during the electrospinning process and could be electrospun continuously in a mixed acetic acid/water (75/25) solvent. Therefore, the CA nanofiber electrospun at 18 wt% was assigned as a standard nanofiber to examine the effect of MMT addition. CA and CA/MMT nanofibers with 18 wt% CA could be electrospun continuously using a mixed acetic acid/water (75/25) solvent.

Figure 2 shows the conductivity of the CA/MMT solutions with different MMT concentrations of 1, 3, 5, 7, and 9 wt% in the 18 wt% CA solution. The conductivity was relatively constant over the range of 1–5 wt% MMT but increased dramatically at MMT concentrations > 7 wt%. MMT addition at lower concentrations enhanced the mobility, but MMT concentrations > 7 wt% caused an increase in repulsion in the CA/MMT solution due to the charge of excess MMT. Some MMT did not interact with CA molecules and separately located in the solution at higher concentrations > 7 wt%, because there was lack of miscibility in those concentrations. The high conductivity due to excess MMT seemed to induce the formation of smaller nanofibers with some beads, as shown in Figures 3(e) and 3(f).

3.2. Morphology of CA and CA/MMT Nanofibers. Figure 3 shows the SEM images of the electrospun CA fiber and CA/MMT composite fibers with different MMT loadings prepared from 18 wt% CA in the acetic acid/water (75/25) solvent system. CA nanofibers were well electrospun and formed a fibrous web with diameters ranging from 150 to 350 nm. The diameter of the nanofibers was reduced by adding MMT. In case of CA/MMT-5, a relatively uniform nanoweb was obtained through the continuous electrospinning from the solution to the charged target wrapped with aluminum sheet. However, the diameters of the nanofibers electrospun

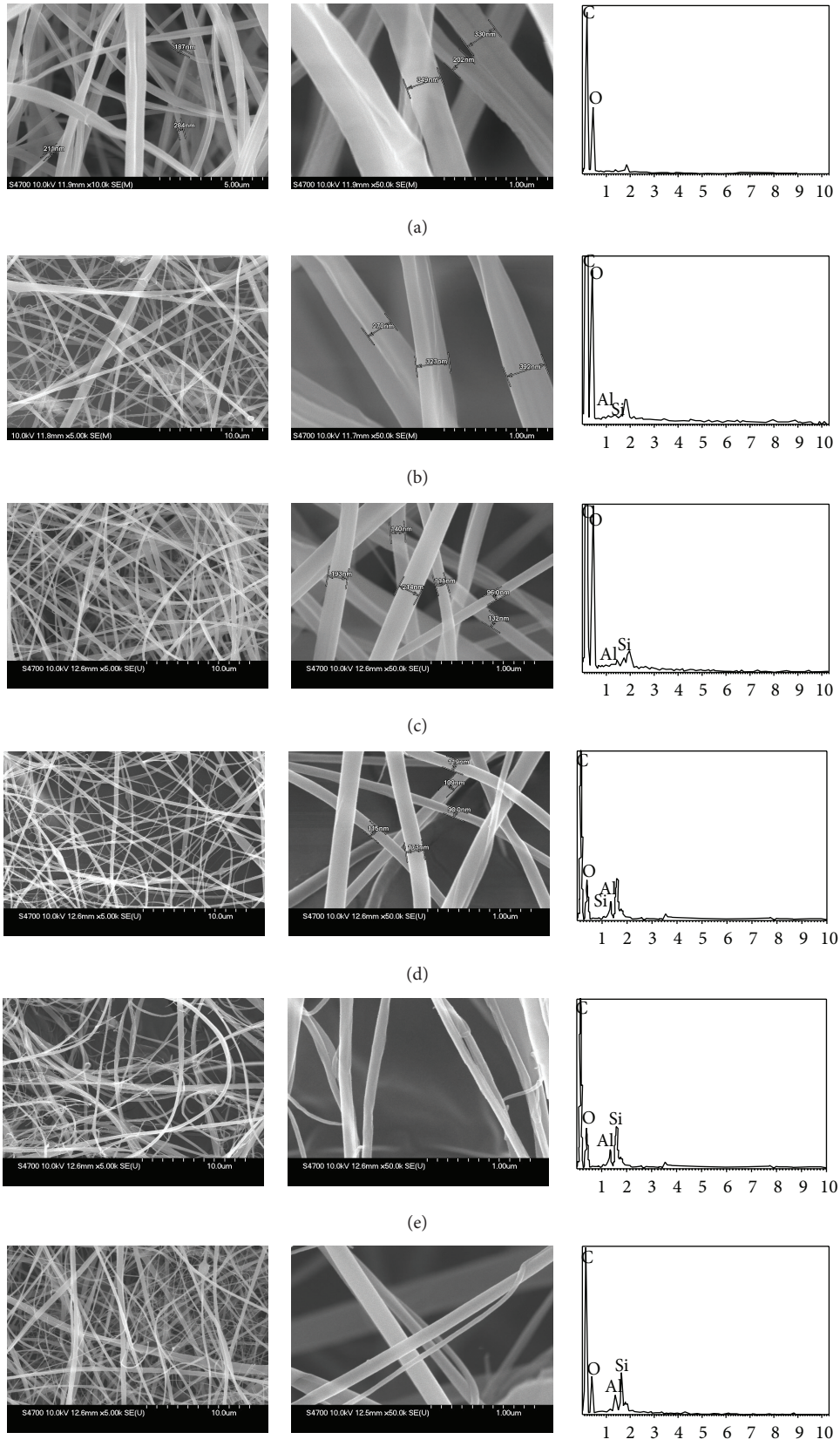

Figure 3: SEM images of (a) CA, (b) CA/MMT1 wt%, (c) CA/MMT3 wt%, (d) CA/MMT5 wt%, (e) CA/MMT7 wt%, and (f) CA/MMT9 wt%.

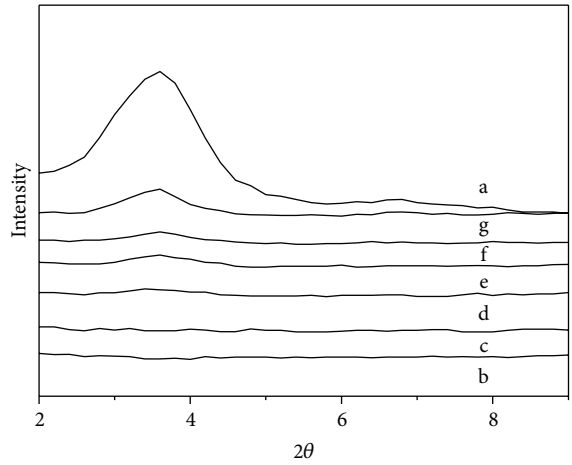

Figure 4: XRD patterns of CA nanofibers with various MMT contents (a, pure MMT; b, CA/MMT9 wt%; c, CA/MMT7 wt%; d, CA/MMT5 wt%; e, CA/MMT3 wt%; f, CA/MMT1 wt%; g, pure CA).

from higher MMT concentrations, such as CA/MMT-7 and CA/MMT-9, were decreased, but not uniform with increasing MMT concentration. An increase in the Si and Al peaks was observed with the addition of higher concentrations of MMT from the EDAX analysis of CA/MMT nanofibers. The addition of a quaternary ammonium salt of MMT increased the charge density in the ejected jets and imposed stronger elongation forces to the jets because of the self-repulsion of the excess charges under the electrostatic field, resulting in electrospun fibers with a substantially smaller diameter [19, 20]. As expected, the increase in the conductivity of CA/MMT with higher MMT concentrations caused a significant decrease in the diameter of the CA/MMT nanofibers.

The extent of MMT intercalation and dispersion can be usually obtained from the WAXS and TEM results [21]. Figure 4 shows the XRD patterns of MMT, CA, and CA/MMT nanofibers with different MMT contents. The patterns revealed changes in the interlayer distances. The CA nanofibers did not show any XRD, but MMT showed a (001) diffraction peak at 3.8° 2θ. This diffraction peak was not observed in the CA/MMT-1 and CA/MMT-3 samples, indicating that most of the MMT had been exfoliated and well-dispersed in the CA matrix. However, the CA/MMT-5, CA/MMT-7, and CA/MMT-9 samples showed a broad weak diffraction peak at 3.5° 2θ due to a small amount of intercalated MMT layers. This peak was shifted towards lower 2θ values (by 0.3 2θ), indicating that the polymer chains had diffused into the clay galleries, expanding the clay structure [22].

Figure 5 shows the TEM and EDX results of CA/MMT-5 that support MMT incorporation into CA fibers. The TEM image showed that the exfoliated MMT layers were distributed within the CA/MMT composite nanofibers. The EDX spectra recorded at two points identified C, Al, Si, and O in the CA/MMT composite nanofibers (right insets of (a)). A detail observation in scanning TEM (STEM) mode clearly showed that the MMT layers appeared to be incorporated into the CA/MMT composite nanofibers. The mapping data of the STEM image revealed that C element is a primary component of the CA/MMT composite nanofibers, and MMT layers composed of Al, Si, and O elements were evenly distributed in the CA nanofibers. These results were well consistent with previous reports [20].

Table 1: The residue and decomposition temperature at onset and 20% rate of pure MMT and nanofibers (pure CA, CA/MMT-1, CA/MMT-3, CA/MMT-5, CA/MMT-7, and CA/MMT-9).

Materials	T_d onset (°C)	T_d 20% (°C)	Residue at 500°C (%)
Pure CA	280	340	13
Pure MMT	280	380	65
CA/MMT-1	275	330	13
CA/MMT-3	275	325	14
CA/MMT-5	270	315	15
CA/MMT-7	270	310	17
CA/MMT-9	270	310	18

3.3. Thermal and Mechanical Properties of CA and CA/MMT Nanofibers. The thermal stability of the electrospun fibers was evaluated using TGA in a nitrogen atmosphere. Figure 6 shows the TGA curves of MMT, pure CA nanofiber, and CA/MMT composite nanofibers with different MMT loadings. Both the MMT and the CA nanofibers began to decompose at 280°C. However, they have single maximum decomposition temperatures of 390°C and 350°C, respectively (Samples a and b). In addition, the residues of MMT and CA nanofibers after thermal decomposition at 500°C were 65% and 13%, respectively (Table 1). However, the decomposition peaks for the CA/MMT composite nanofibers were divided into two peaks, at approximately 300°C and 350°C, as clearly seen from DTG curves. A higher concentration of MMT in the CA nanofiber induced a lower onset temperature of decomposition for CA/MMT composite nanofibers (Table 1). This is because the alkylammonium cations of MMT were thermally unstable and decomposed at lower temperatures. These aspects would reduce the thermal stability of CA nanofibers with the addition of MMT. However, the silicate clay layers could act as a superior insulator and mass-transport barrier and mitigate the escape of volatile products generated during thermal decomposition [23, 24].

Figure 7 shows the tensile strength of the CA/MMT nanofibers with different MMT concentrations. The tensile strength of the CA nanofibers increased with increasing MMT concentration reaching the highest tensile strength of 3.2 MPa (about 400% increase) at 5 wt% MMT. At higher MMT concentration (7 wt%), the tensile strength decreased abruptly to 1.5 MPa. The improvement in tensile strength was mainly due to reinforcing effect of MMT layers originated from the good dispersion of MMT layers in the CA fibrous matrix. However, some excess MMT seemed to be phase-separated and poorly dispersed in CA/MMT nanofibers at higher MMT concentration (7 wt%), whereas the exfoliated MMT layers were well-dispersed within CA/MMT nanofibers at 5 wt% MMT. The tensile strength of CA/MMT composite nanofibers was consistent with the results of XRD and EDX.

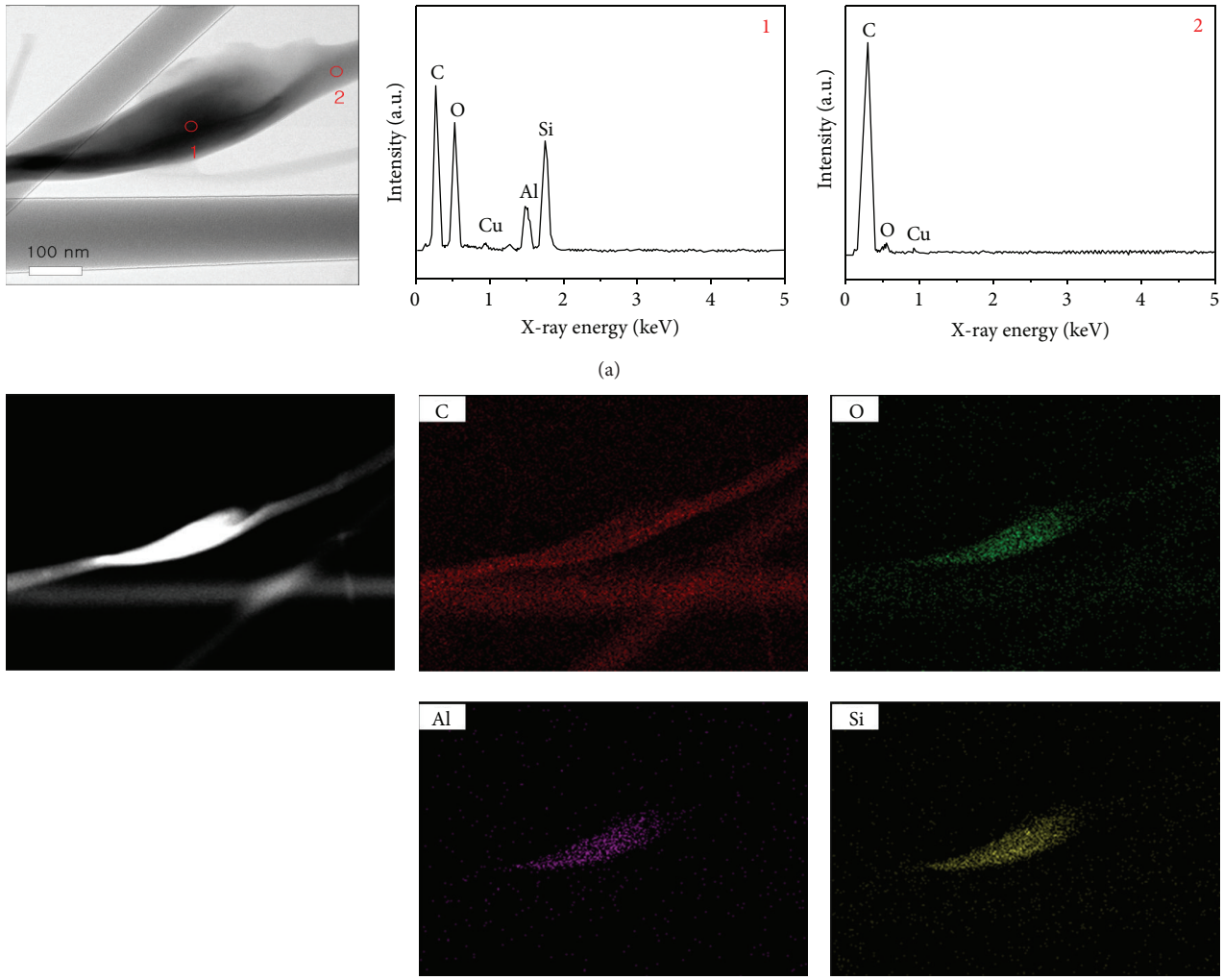

Figure 5: (a) TEM image and EDX spectra (right insets) of the CA/MMT nanofibers. (b) STEM image and mapping images clearly showed the existence of a MMT layer, composed of Al, Si, and O, within the CA/MMT nanofibers.

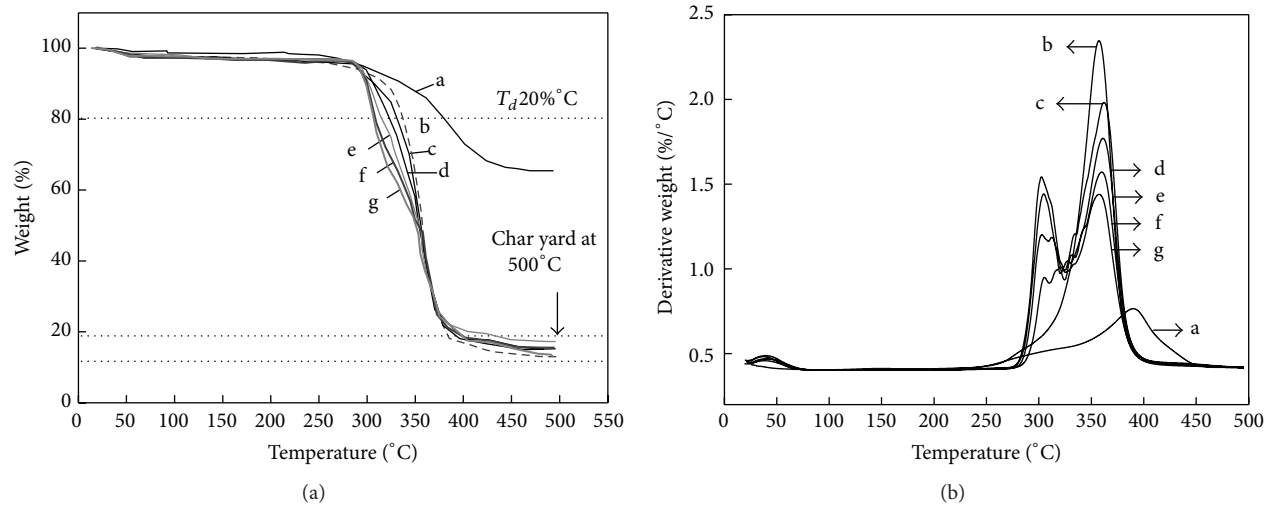

Figure 6: (a) TGA and (b) DTG thermograms showing the thermal stability of electrospun CA nanofiber and CA/MMT nanofiber (a, pure MMT; b, CA/MMT9 wt%; c, CA/MMT7 wt%; d, CA/MMT5 wt%; e, CA/MMT3 wt%; f, CA/MMT1 wt%; g, pure CA).

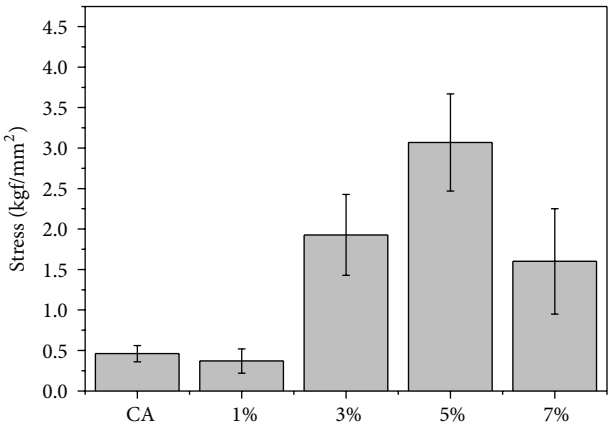

Figure 7: Tensile strength of CA, CA/MMT1 wt%, CA/MMT3 wt%, CA/MMT5 wt%, and CA/MMT7 wt% nanofibers.

4. Conclusions

The CA/MMT composite nanofibers were prepared using a facile compounding and electrospinning technique. The structures, thermal stability, and crystalline properties of the electrospun composite nanofibers were investigated. The average diameters of the CA/MMT nanofibers obtained by electrospinning 18 wt% CA/MMT solutions in a mixed acetic acid/water (75/25, w/w) solvent ranged from 150~350 nm. The nanofiber diameter decreased with increasing MMT content. TEM indicated the coexistence of CA nanofibers and MMT layers. The CA/MMT composite nanofibers showed improved tensile strength compared to the CA nanofiber due to the physical protective barriers of the silicate clay layers.

Conflict of Interests

The authors declare that there is no conflict of interests regarding the publication of this paper.

Acknowledgments

This study was supported financially by the Carbon Dioxide Reduction and Sequestration (CDRS) R&D Center (the 21st Century Frontier R&D Program) and by the Basic Science Research Program through the National Research Foundation of Korea (NRF), funded by the Ministry of Science, ICT & Future Planning (2012R1A1A2008761).

References

[1] Y. Xia, T. Fei, Y. He, R. Wang, F. Jiang, and T. Zhang, "Preparation and humidity sensing properties of $Ba_{0.8}Sr_{0.2}TiO_3$ nanofibers via electrospinning," *Materials Letters*, vol. 66, no. 1, pp. 19–21, 2012.

[2] S.-H. Choi, S.-J. Choi, B. K. Min, W. Y. Lee, J. S. Park, and I.-D. Kim, "Facile synthesis of p-type perovskite $SrTi_{0.65}Fe_{0.35}O_{3-\delta}$ nanofibers prepared by electrospinning and their oxygen-sensing properties," *Macromolecular Materials and Engineering*, vol. 298, no. 5, pp. 521–527, 2013.

[3] A. F. Lubambo, R. A. de Freitas, M.-R. Sierakowski et al., "Electrospinning of commercial guar-gum: effects of purification and filtration," *Carbohydrate Polymers*, vol. 93, no. 2, pp. 484–491, 2013.

[4] M. J. A. Shirazi, S. Bazgir, M. M. A. Shirazi, and S. Ramakrishna, "Coalescing filtration of oily wastewaters: characterization and application of thermal treated, electrospun polystyrene filters," *Desalination and Water Treatment*, vol. 51, no. 31–33, pp. 5974–5986, 2013.

[5] S. Adibzadeh, S. Bazgir, and A. A. Katbab, "Fabrication and characterization of chitosan/poly(vinyl alcohol) electrospun nanofibrous membranes containing silver nanoparticles for antibacterial water filtration," *Iranian Polymer Journal*, vol. 23, no. 8, pp. 645–654, 2014.

[6] H. Zhang, X. Jia, F. Han et al., "Dual-delivery of VEGF and PDGF by double-layered electrospun membranes for blood vessel regeneration," *Biomaterials*, vol. 34, no. 9, pp. 2202–2212, 2013.

[7] J. Jiang, J. Xie, B. Ma, D. E. Bartlett, A. Xu, and C. H. Wang, "Mussel-inspired protein-mediated surface functionalization of electrospun nanofibers for pH-responsive drug delivery," *Acta Biomaterialia*, vol. 10, no. 3, pp. 1324–1332, 2014.

[8] N. G. Rim, C. S. Shin, and H. Shin, "Current approaches to electrospun nanofibers for tissue engineering," *Biomedical Materials*, vol. 8, no. 1, Article ID 014102, 2013.

[9] S. Huang, X. Kang, Z. Cheng, P. Ma, Y. Jia, and J. Lin, "Electrospinning preparation and drug delivery properties of Eu^{3+}/Tb^{3+} doped mesoporous bioactive glass nanofibers," *Journal of Colloid and Interface Science*, vol. 387, no. 1, pp. 285–291, 2012.

[10] S. O. Han, J. H. Youk, K. D. Min, Y. O. Kang, and W. H. Park, "Electrospinning of cellulose acetate nanofibers using a mixed solvent of acetic acid/water: effects of solvent composition on the fiber diameter," *Materials Letters*, vol. 62, no. 4-5, pp. 759–762, 2008.

[11] J. Lin, B. Ding, Y. Jianyong, and Y. Hsieh, "Direct fabrication of highly nanoporous polystyrene fibers via electrospinning," *ACS Applied Materials and Interfaces*, vol. 2, no. 2, pp. 521–528, 2010.

[12] M. Tian, Q. Hu, H. Wu, L. Zhang, H. Fong, and L. Zhang, "Formation and morphological stability of polybutadiene rubber fibers prepared through combination of electrospinning and in-situ photo-crosslinking," *Materials Letters*, vol. 65, no. 19-20, pp. 3076–3079, 2011.

[13] J. Johnson, A. Niehaus, S. Nichols et al., "Electrospun PCL in vitro: a microstructural basis for mechanical property changes," *Journal of Biomaterials Science*, vol. 20, no. 4, pp. 467–481, 2009.

[14] G. E. Wnek, M. E. Carr, D. G. Simpson, and G. L. Bowlin, "Electrospinning of nanofiber fibrinogen structures," *Nano Letters*, vol. 3, no. 2, pp. 213–216, 2003.

[15] Y. Nishio, "Material functionalization of cellulose and related polysaccharides via diverse microcompositions," *Advances in Polymer Science*, vol. 205, no. 1, pp. 97–151, 2006.

[16] R. Konwarh, N. Karak, and M. Misra, "Electrospun cellulose acetate nanofibers: the present status and gamut of biotechnological applications," *Biotechnology Advances*, vol. 31, no. 4, pp. 421–437, 2013.

[17] H. M. Park, X. Liang, A. K. Mohanty, M. Misra, and L. T. Drzal, "Effect of compatibilizer on nanostructure of the biodegradable cellulose acetate/organoclay nanocomposites," *Macromolecules*, vol. 37, no. 24, pp. 9076–9082, 2004.

[18] H.-M. Park, M. Misra, L. T. Drzal, and A. K. Mohanty, "'Green' nanocomposites from cellulose acetate bioplastic and clay: effect of eco-friendly triethyl citrate plasticizer," *Biomacromolecules*, vol. 5, no. 6, pp. 2281–2288, 2004.

[19] Y. Cai, F. Huang, Q. Wei et al., "Structure, morphology, thermal stability and carbonization mechanism studies of electrospun PA6/Fe-OMT nanocomposite fibers," *Polymer Degradation and Stability*, vol. 93, no. 12, pp. 2180–2185, 2008.

[20] M. Manitiu, S. Horsch, E. Gulari, and R. M. Kannan, "Role of polymer-clay interactions and nano-clay dispersion on the viscoelastic response of supercritical CO_2 dispersed polyvinylmethylether (PVME)-Clay nanocomposites," *Polymer*, vol. 50, no. 15, pp. 3786–3796, 2009.

[21] M. Hassan-Nejad, J. Ganster, A. Bohn, M. Pinnow, and B. Volkert, "Bio-based nanocomposites of cellulose acetate and nano-clay with superior mechanical properties," *Macromolecular Symposia*, vol. 280, no. 1, pp. 123–129, 2009.

[22] Y. Ji, B. Li, S. Ge, J. C. Sokolov, and M. H. Rafailovich, "Structure and nanomechanical characterization of electrospun PS/clay nanocomposite fibers," *Langmuir*, vol. 22, no. 3, pp. 1321–1328, 2006.

[23] J. Zhang and C. A. Wilkie, "Fire retardancy of polyethylene-alumina trihydrate containing clay as a synergist," *Polymers for Advanced Technologies*, vol. 16, no. 7, pp. 549–553, 2005.

[24] J. Zhu, A. B. Morgan, F. J. Lamelas, and C. A. Wilkie, "Fire properties of polystyrene-clay nanocomposites," *Chemistry of Materials*, vol. 13, no. 10, pp. 3774–3780, 2001.

Hindawi Publishing Corporation
Journal of Nanomaterials
Volume 2015, Article ID 134251, 12 pages
http://dx.doi.org/10.1155/2015/134251

Research Article

Influence of Salts on Electrospinning of Aqueous and Nonaqueous Polymer Solutions

Fatma Yalcinkaya, Baturalp Yalcinkaya, and Oldrich Jirsak

Department of Nonwovens and Nanofibrous Materials, Faculty of Textile Engineering, Technical University of Liberec, Studentska 1402/2, 46117 Liberec, Czech Republic

Correspondence should be addressed to Fatma Yalcinkaya; yenertex@hotmail.com

Received 7 October 2014; Revised 21 December 2014; Accepted 8 January 2015

Academic Editor: Yuqin Wan

A roller electrospinning system was used to produce nanofibres by using different solution systems. Although the process of electrospinning has been known for over half a century, knowledge about spinning behaviour is still lacking. In this work, we investigated the effects of salt for two solution systems on spinning performance, fibre diameter, and web structure. Polyurethane (PU) and polyethylene oxide (PEO) were used as polymer, and tetraethylammonium bromide and lithium chloride were used as salt. Both polymer and salt concentrations had a noteworthy influence on the spinning performance, morphology, and diameter of the nanofibres. Results indicated that adding salt increased the spinnability of PU. Salt created complex bonding with dimethylformamide solvent and PU polymer. Salt added to PEO solution decreased the spinning performance of fibres while creating thin nanofibres, as explained by the leaky dielectric model.

1. Introduction

Polymer nanofibres have attracted increasing attention in previous decades because of their high surface to mass ratio, small pore size, and special characteristics attractive in advanced applications. They have potential application in tissue engineering scaffolds, filters, wound dressings, drug delivery materials, biomimetic materials, electronics, and composite reinforcement, among others [1–6].

Techniques to produce nanofibres have been developed for many years. Electrospinning is one of the versatile methods to produce nanofibres. Various worldwide researchers have started to develop alternative methods to produce nanofibres to improve production rates and quality. The most common methods are melt-blown, phase separation, self-assembly, template synthesis, bicomponent, centrifugal, and drawing methods, among others [7–13].

An effective electrospinning method was recently investigated by Jirsak et al. [14]. The principle of this method is based on free surface spinning. This method involves an electrode rotating roller that is immersed in a solution bath. The role of the roller is to feed the solution to the surface of the roller to continue spinning. Fibres form between the roller surface and the collector. By changing the spinning parameters, having hundreds of Taylor cones on the surface of the roller at the same time is possible. Therefore, a highly dense nanoweb can be achieved by using this method. In general, the diameter of fibres changes from 50 nm to 800 nm depending on the solution properties and spinning parameters.

This paper aims to evaluate the influence of salt on the spinning performance of both aqueous and nonaqueous solution systems by using the roller electrospinning system. To date, many researchers have studied the salt effect on nanofibre morphology, but only a few have focused on spinning performance. For instance, Cengiz and Jirsak [15] examined the effect of salt on polyurethane nanofibre and spinning performance. They found that adding salt increases the number of Taylor cones on the roller surface, thus increasing spinning performance. By contrast, Dao and Jirsak showed that adding salt to polyvinyl alcohol (PVA) solution decreases the number of jets and spinning performance [16].

To the best of our knowledge, no study has been made to explain the opposite effect of salt on spinning performance with different solution systems. To achieve this aim, we used

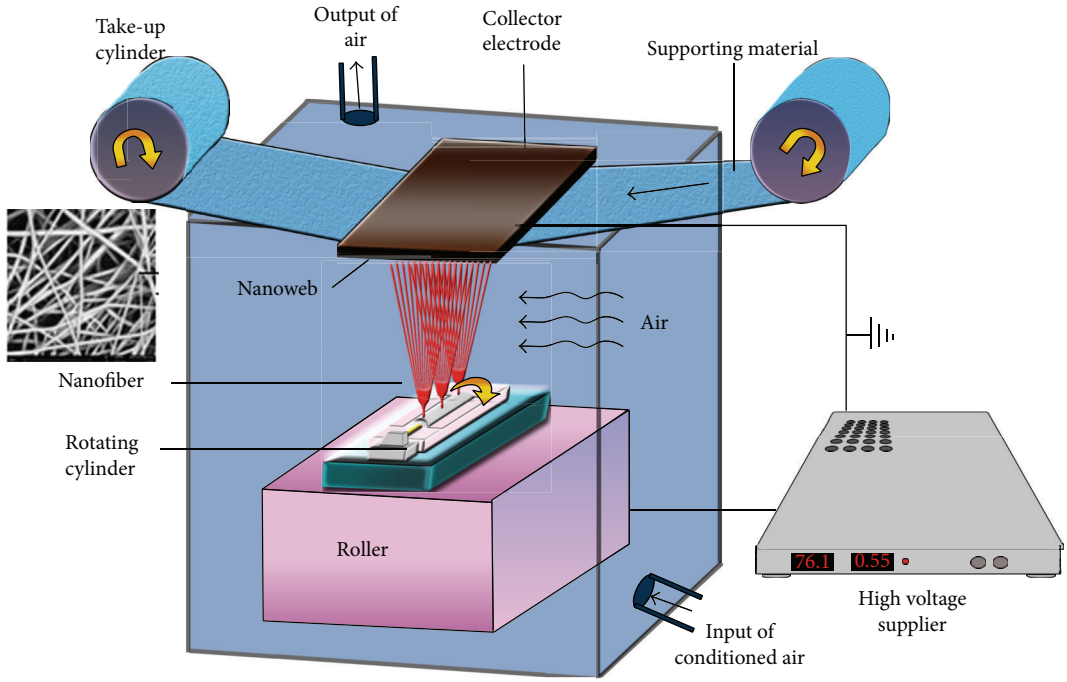

Figure 1: Diagram of the roller electrospinning system.

polyurethane (PU) and polyethylene oxide (PEO) polymers with various concentrations of tetraethylammonium bromide (TEAB) and lithium chloride (LiCl) salts. We chose PU in this work for two reasons. First, the PU used in this study is pure and industrially produced. Second, much information on this polymer is available from previous studies, including information on optimum spinning conditions.

In the current work, PEO was used with both TEAB and LiCl salts. In case of PEO, adding salt decreases its spinning performance, similar to PVA solutions. Moreover, PEO is produced in better purity than PVA. One of the aims of this study is to determine the different spinning behaviours of both water-soluble and -insoluble polymers. Using PVA, which is mostly used in electrospinning, is possible. Although PVA has been studied by many researchers, PEO was chosen in this work for its more stable quality and better purity. The possible salt-polymer, salt-solvent, and solvent-polymer relations are explained in the following section.

2. Experimental

2.1. Materials. Polyurethane Larithane LS 1086 (Novotex, Italy), which is an aliphatic elastomer composed of 2000 g/mol linear polycarbonate diol and isophorone diisocyanate and extended by isophorone diamine, was chosen as the second polymer.

Most PUs are block polymers prepared with a diisocyanate, which is a short diol such as 1,4-butanediol or 1,6-hexanediol, a diamine (the chain extender), and a diol, with a molecular weight of 500 to 4000 based on a polyether, polyester, or polycarbonate. Preparation is usually performed in two steps: the reaction of the longer polyol with isocyanate in the first stage and that with the chain extender in the second stage [17]. PU has excellent damping properties, good mechanical and physical properties even at low temperatures, high combustion resistance, and low thermal conductivity [18]. DMF (Fluka, Switzerland) was used as the solvent.

Water-soluble PEO with molecular weight of 400 kDa was purchased from Scientific Polymers, Inc., USA. Distilled water was used as the solvent. PEO is a water-soluble and non-ionic polymer. PEOs are also commonly studied in electrospinning. They are available in a large range of molecular weights. PEOs can be applied in areas such as textile applications, cosmetics, antifoaming agents, and food industry, among others. PEOs are produced by the polymerization of ethylene oxide, and they have a structural polyether unit of $-CH_2-CH_2-O-$. They are a good candidate for an electrospinning system because of their high spinnability and water solubility.

Tetraethylammonium bromide was purchased from Fluka (Switzerland) and LiCl from Lach-Ner s.r.o. (Czech Republic). Based on previous works, 6% PEO and 17.5% PU were chosen as the constant polymer concentrations. Various amounts of salt were used according to the molar ratio of salt. The nomenclature of solutions is tabulated as shown in Nomenclature and Symbols of Solutions according to salt content. We used a small amount of LiCl salt content for the PEO solution because the fibre diameter increases with increased amount of salt.

2.2. Methods

2.2.1. Spinning Conditions. The solutions were spun using a spinning device, as shown in Figure 1. All the measured

Table 1: Spinning conditions of PEO solutions in the roller electrospinning system.

Sample	Voltage (kV)	Distance (mm)	Roller speed (rpm)	RH (%)	Temperature (°C)	Roller length (mm)	Roller diameter (mm)
6% PEO + salt series	42	150	1	28.5 ± 2	23 ± 1	145	20

Table 2: Spinning conditions of PU solutions in the roller electrospinning system.

Sample	Voltage (kV)	Distance (mm)	Roller speed (rpm)	RH (%)	Temperature (°C)	Roller length (mm)	Roller diameter (mm)
17.5% PU + salt series	62	130	1.5	24.5 ± 2	16 ± 1	145	20

results in the figure have an error bar at 95% confidence intervals. The spinning conditions of PEO and PU are shown in Tables 1 and 2.

(i) Measurement of surface tension: measurement was carried out using a KRÜSS tensiometer at 25°C and LabDesk software by using plate method.

(ii) Measurement of viscosity: the zero-shear viscosities of solutions were measured by Haake RotoVisco1 at 23°C.

(iii) Measurement of conductivity: the conductivities of polymer solutions were measured at 23°C by a Radelkis OK-102/1 conductivity meter.

(iv) Measurement of jets and spinning area: a Sony Full HD NEX-VG10E Handycam E 18–200 mm lens camera was used in the experiments. By using camera, the number of jets was recorded. Spinning area and number of jets were determined by taking an image from the camera and using NIS-Elements software. 10 images per second were taken. A number of jets were counted by using images.

(v) Measurement of spinning performance and performance per jet: $10 \times 10\,\text{cm}^2$ nanofibre webs were prepared and measured on a balance. The calculations were made according to (1)-(2).

(vi) Measurement of fibre diameter and diameter distribution: images of the microstructure of the nanofibre membrane were taken by scanning electron microscope (SEM; Feico). NIS-Elements software was used to determine the fibre diameter and diameter distribution.

(vii) Measurement of nonfibrous area: using SEM images and NIS-Elements software, nonfibrous areas were calculated.

2.2.2. Calculation of Spinning Performance. Spinning performance (SP) can be determined from the mass of nanofibres produced in a 1 m long roller spinning electrode in 1 min. Spinning performance is calculated from an area weight of the produced nanofibre layer as follows:

$$\text{SP} = \frac{G * v * L_f}{L_r}, \text{ g/min/m}, \quad (1)$$

where G is the area weight of the nanofibre membrane per area in g/m^2. v is the velocity of running of the collected fabric in m/min. L_f is the width of the nanofibre membrane on the collected fabric in m. L_r is the length of the spinning roller in m.

Spinning performance per one Taylor cone (SPC) can be calculated from the known values of spinning performance and an average total number of Taylor cones in the spinning electrode Nc using (2). SPC is an amount of polymer solution transported through one Taylor cone (or a jet):

$$\text{SPC} = \frac{\text{SP} * L_r * 60}{\text{Nc}}, \text{ g/h}. \quad (2)$$

SPC is one of the parameters to be measured in the experiments to determine whether spinning performance is realized through SPC or Nc.

3. Results and Discussions

3.1. Polymer Solution Properties. The basic properties of polymer solutions are given in Figures 2, 3, and 9.

Surface tension of the solutions corresponds to that of the used solvents and is not significantly dependent on the content of salts. Thus, surface tension is not an influencing independent parameter, such as spinning performance and fibre diameter, in the experiments.

Viscosity of the solutions, as a function of share rate, shows considerably different characteristics of both polymers. Effective viscosity of PEO strongly depends on share rate and that of PU shows only moderate dependence. Therefore, the macromolecules of PEO 400 kDa show a high degree of mechanical entanglement and a highly macromolecular characteristic. The strength of PEO jets as a necessary requirement for spinnability is satisfactorily high at a relatively low polymer concentration and corresponding viscosity. However, spinnability of PU requires a high polymer concentration and corresponding viscosity. Viscosity of PU solutions increases with salt content; this is not the case in PEO solutions.

The addition of LiCl to PU solution increases its viscosity. Erokhina et al. explained that this increase in viscosity could be due to the same coordination of lithium cation bonds in the solution with DMF molecules. They concluded that the partial recoordination of the lithium cation from the DMF carbonyl groups to the PU carbonyl groups in the ternary system probably caused the unfolding of macromolecular

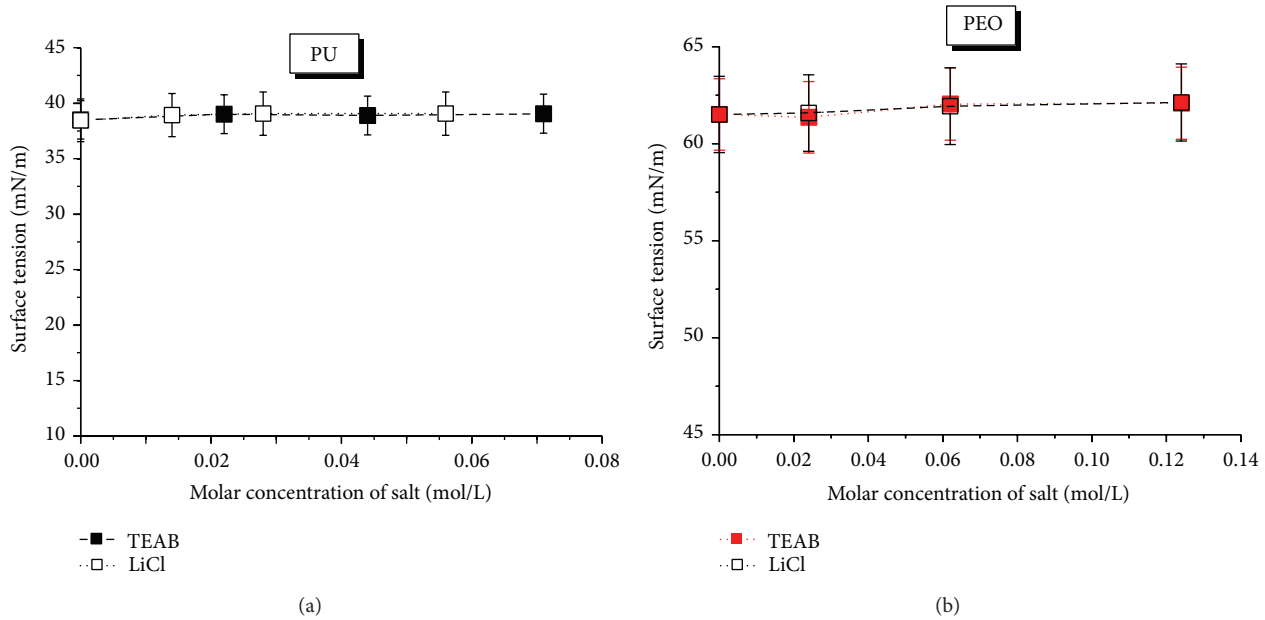

Figure 2: Surface tension of polymer solutions.

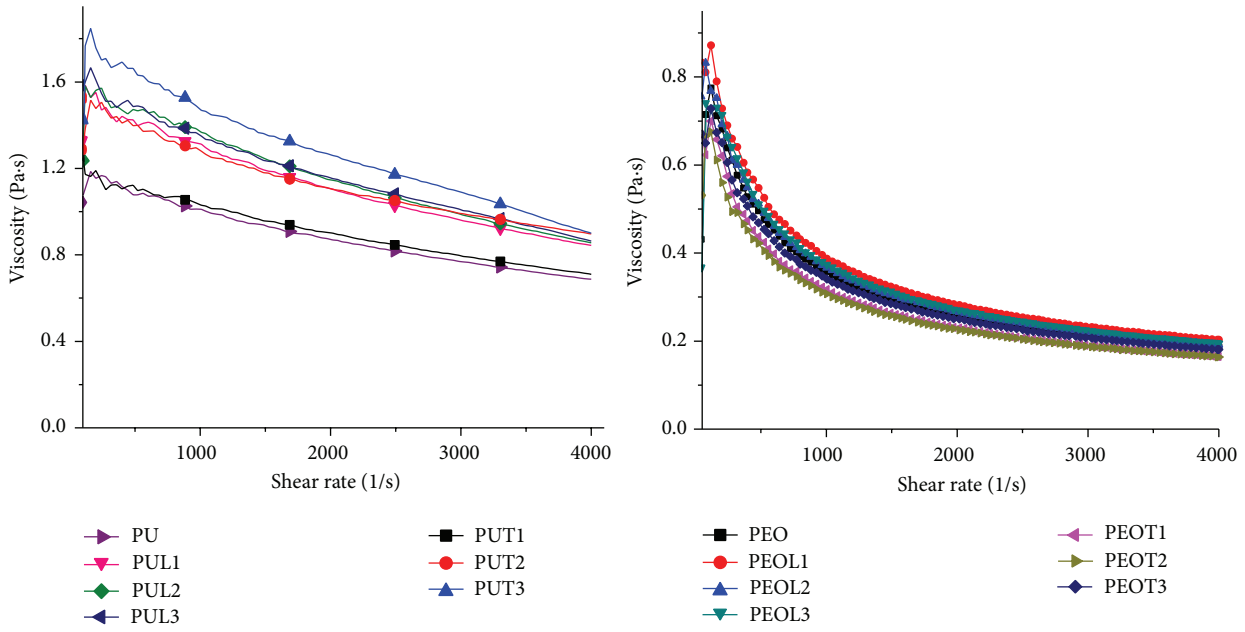

Figure 3: Viscosity of polymer solutions.

coils in PU with the formation of intermolecular crosslinks [20].

PU and LiCl salts have secondary bonds similar to the H-bridges between PU and LiCl ions (Figure 4). Intermolecular interactions are positively influenced by polar groups. Beside this, LiCl makes the functional groups of PU more polar.

The interactions between dimethylformamide (DMF) and TEAB [19] or between PU and salts [15, 21] are shown in Figures 5 and 6.

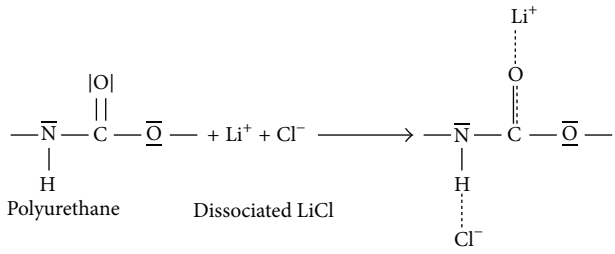

Figure 4: Chemical interaction between PU and LiCl.

Fry studied the interactions between polar organic solvents and salts [19]. The electrostatic interaction between the dipolar solvent and the individual ions of the salt is greater than the attraction of the ions of the salt for each other in the lattice. Salts dissolve in polar solvents, and this phenomenon is called as general solvation. Fry [19] found that, aside from general solvation, small or highly charged metal cations, such as Li^+ or Mg^{+2}, in water or other electron pair donor solvents could also attract a shell of tightly bound solvent molecules. This phenomenon, known as inner-sphere or specific solvation, provides added stability to the positive charge in the cation through its interaction with the negative end of the solvent dipoles. General solvation mainly depends on the dielectric constant (ε) of the solvent regardless of its chemical structure. Conversely, specific solvation depends on the chemical structures of both solute and solvent. Fry conducted a computational study demonstrating that smaller tetraalkylammonium ions (Me_4N^+ and Et_4N^+) are surrounded by a strong solvation shell in the strong donor DMF solvent. The four solvent molecules are distributed symmetrically around the tetrahedral cation, and no remaining space is sterically allotted for a fifth solvent molecule. The tetrahedral arrangement of solvent molecules is the same as the structure of $Et_4N^+/(H_2O)_4$, as established by molecular dynamics, and is similar to that of the $Li(THF)_4{}^+$ion, as established by X-ray crystallography [19].

Rastogi [22] studied the ion-dipole interaction energy of alkali metal cations (e.g., Li^+), anions (e.g., Cl^-), and symmetrical tetraalkylammonium ions in DMF and other solvents. He showed that the ion-dipole interaction energy decreases in increasing order of $Li^+ > Cl^- > Et_4N^+$ in DMF solvent. Moreover, the ion-dipole interaction energy of ions is generally higher than the dipolar interaction energy of solvents that cause secondary solvation in large ions (Cl^-, Br^-) and long-range polarization in small ions (Li^+).

In the case of PEO-water solutions, the addition of salt only affects conductivity and permittivity. Viscosity of solutions does not change when salt is added. Salt and polymer macromolecules do not seem to have a significant interaction.

The values of solution conductivities of LiCl and TEAB salts in the same molar concentration in DMF are illustrated in Figure 7. Dash lines indicate the connection points.

The conductivity of LiCl and TEAB in the same molar concentration in water is illustrated in Figure 8. Dotted lines indicate the connection points.

The conductivity of the solutions of both TEAB and LiCl in water and DMF is generally high, and all the values are surprisingly close to each other. TEAB shows the same conductivity in water as LiCl does despite its evidently larger ions. The values of conductivity in DMF are surprisingly close to those in water, thus indicating the high degree of dissociation of salt in DMF. Conversely, the conductivities of polymer solutions containing salt differ from each other to some extent. PEO solutions show higher conductivity than PU solutions because of their lower viscosity and corresponding greater movability of ions in a direct electric field. PU solutions containing LiCl are more conductive than those with TEAB because their ions are more movable in highly viscous liquid.

According to Karmakar and Ghosh, in PEO-lithium salt-based solid polymer, the macromolecule coils around Li^+ ions and the O-atom in PEO chain provide a coordination site for Li^+ ions through the Lewis acid-base interaction. Li^+ ions jump from one coordination site to another within the amorphous phase. Moreover, the chain mobility of the polymer host, which plays an important role in ion transport, makes the ion transport mechanism in polymer electrolytes complex [23].

Collins et al. [24] showed that, in the absence of an electric field, charged structures capable of supporting current could be produced by the general equilibrium as follows:

$$\text{Neutral molecule} \underset{k_2}{\overset{k_1}{\rightleftarrows}} \text{ion pair} \underset{k_f}{\overset{k_d}{\rightleftarrows}} \text{free ions} \tag{3}$$

The neutral molecule and the ion pair are not capable of supporting current, and the rate constants k_1 and k_2 are generally not known and are not important to the treatment of the problem of conduction in liquids. This step that produces free ions from ion pairs is critical to understanding the development of conduction in liquids. The rate constant k_d is related to the dissociation of the ion pair into the charged ions, and the rate constant k_f is related to the removal of free ions through the recombination into ion pairs. Moreover, with the application of a voltage with a positive polarity to the electrode that supports the solution, the mechanism of the charge carrier generation is called field enhanced dissociation. Negative charges are immobilized in the electrode, leaving mobile positive charges to respond to the electrostatic stresses imposed by the electric field. The unconstrained surface of the fluid enables multiple spinning sites to develop, as shown in Figure 10 [24].

In the case of PEO in water solution, the dissociation of the ion pair into the charged ions of the water molecules under electric field is expressed as follows:

$$2H_2O \longleftrightarrow H_3O^+ + OH^- \tag{4}$$

This creates a high number of ions. Negatively charged ions are immobilized in the positively charged spinning electrode, whereas positive charges move towards the collector electrode. Adding salt increases the conductivity of solution over the value required for the leaky dielectric model and leads to the decreased number of Taylor cones. In the case of PU solution, the molecules of DMF solvent do not dissociate. Therefore, field enhanced dissociation is also not present.

PEOs in water solution show extremely high spinning performance because of their high polarity and hygroscopicity. The PEO chains are used as a hygroscopic part of detergents because of these properties. Their high polarity, especially in water solutions, is characterized by a high value of the dielectric constant, $\varepsilon = 39$ [25, 26].

Other basic properties of the solutions were not measured. However, a number of differences between the two solutions may exist that may cause their different behaviours in the electrospinning process. For instance, the kind and

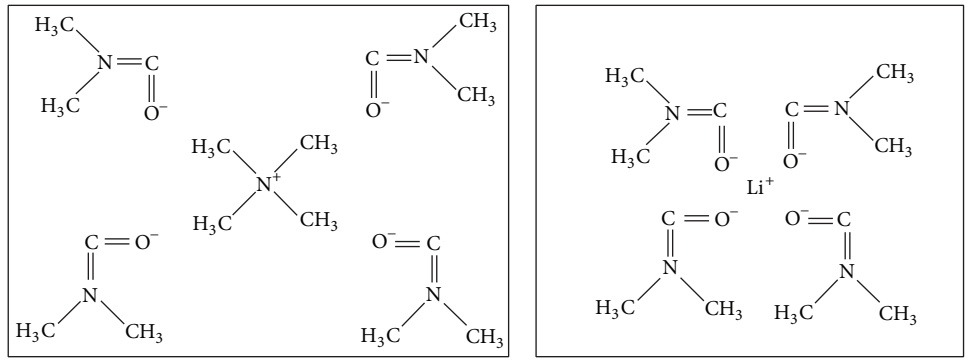

Figure 5: Computed structure of the tetramethylammonium ion and lithium ion complexed to four N,N-dimethylformamide molecules [19].

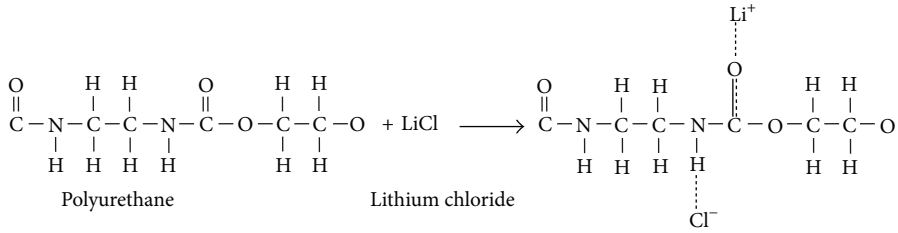

Figure 6: Chemical interaction between LiCl and PU.

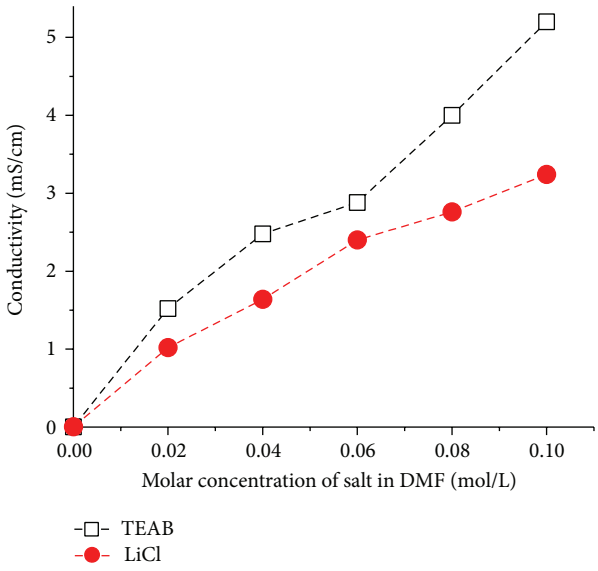

Figure 7: Conductivity of TEAB and LiCl solutions in DMF. Dash lines indicate the connection of points.

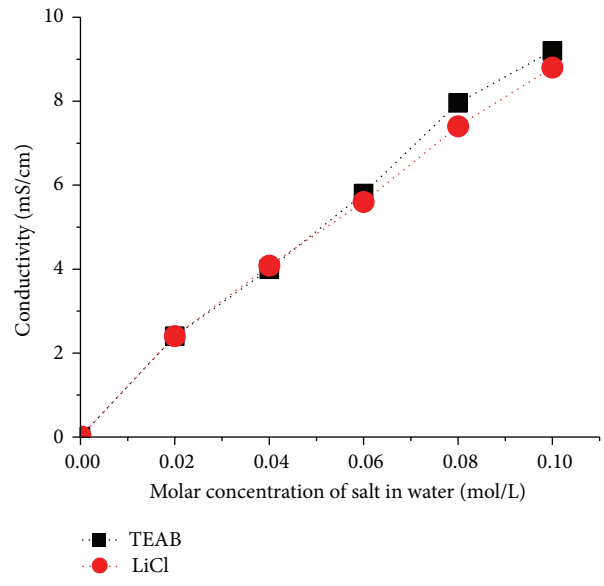

Figure 8: Dependence of water solution conductivity on the concentrations of LiCl and TEAB. Dash lines indicate the connection points.

concentration of polar groups in polymers, solvents, and polymer-solvent-salt systems are responsible for the interactions of the component solutions with the electric field. The characteristic and content of polar groups influence the dielectric constant of materials. Water, DMF, and PEO show high values of permittivity (80, 38, and 39, resp.) [25, 26]. The permittivity of PU is low (5–7), which may be the reason for its poor spinnability. Spinnability of PU considerably increases with the addition of salt [15]. This increase may be caused by the interactions between DMF and TEAB [19] or between PU and salt.

3.2. Number of Jets. In electrospinning, PU and PEO show important differences in their behaviour, such as the number of jets on the spinning roller, as shown in Figure 11.

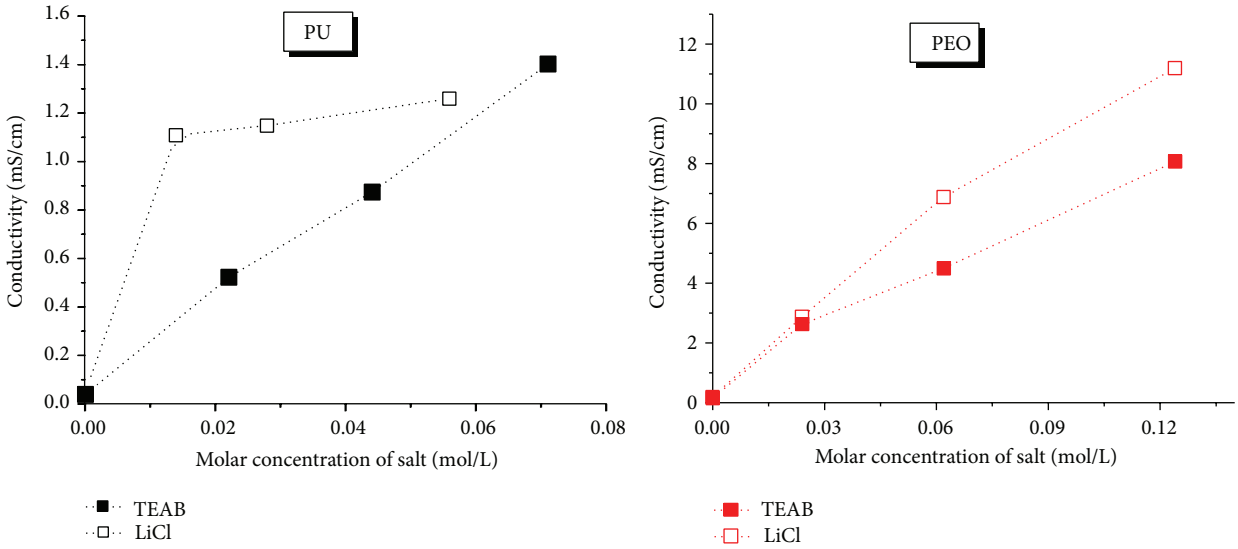

Figure 9: Conductivities of polymer solutions with salt content (dotted lines indicate the connection of points).

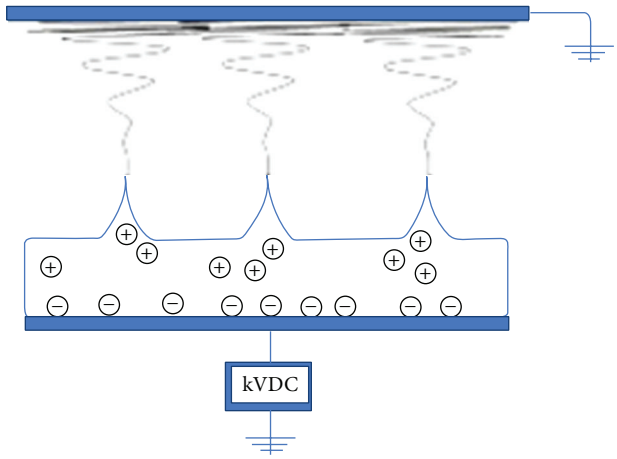

Figure 10: Multiple fluid jets using the plane-plane electrode configuration without capillaries.

First, the number of jets is considerably larger in PU than in PEO by adding salt. Two attempts have been made to explain this difference.

(1) The theory of shielding effect of conducting lightning rods was considered [27]. According to this theory, the electric field is screened out in conical space with a tip at the end of the conductor and a top angle of about 45°–60° [28–34].

(2) Lukáš et al. [35–37] calculated the distance between jets by calculating the inter-jet distance called the critical wavelength. This parameter enables the estimation of the relative productivity of the electrospinning process.

Second, the number of PU cones increases with the salt content of the solution. By contrast, the number of PEO cones decreases with the increase in salt concentration. These effects are difficult to explain as salt plays multiple roles.

(1) Salt (TEAB more than LiCl) creates complex structures (Figure 6) with PU, which leads to changes in the macromolecule-macromolecule and macromolecule-solvent interactions. Consequently, viscosity, related entanglement number, and stronger jets increase. The following are the effects of salt on a PU solution.

(i) Stronger jets result in longer average life of jets [20].

(ii) The jets are shorter because of higher content of ions and greater viscosity [38], and the number of jets increases.

These effects of salt do not occur in a PEO solution as salt does not create complex structures with PEO.

(2) Salt increases the conductivity of polymer solutions. Increase in conductivity changes the characteristic of the polymer solution from a semiconductor to a conductor. Therefore, the solution loses the characteristic of a leaky model, which leads to the loss of ability to create Taylor cones. The leaky dielectric model was first proposed by Melcher and Taylor [39]. According to Bahattacharjee and Rutledge [40], "a leaky dielectric differs from a perfect conductor or a dielectric material in that free charges accumulate on the surface of the material in the presence of an external electric field and modify the local field. Under these conditions, two components of the electrical field develop, one tangential to the interface and another normal to it. The presence of a tangential component on the surface prevents the interface from being in an equilibrium condition and provokes it to deform. By contrast, the electrical stress in perfect dielectrics and conductors is always perpendicular to the interface.

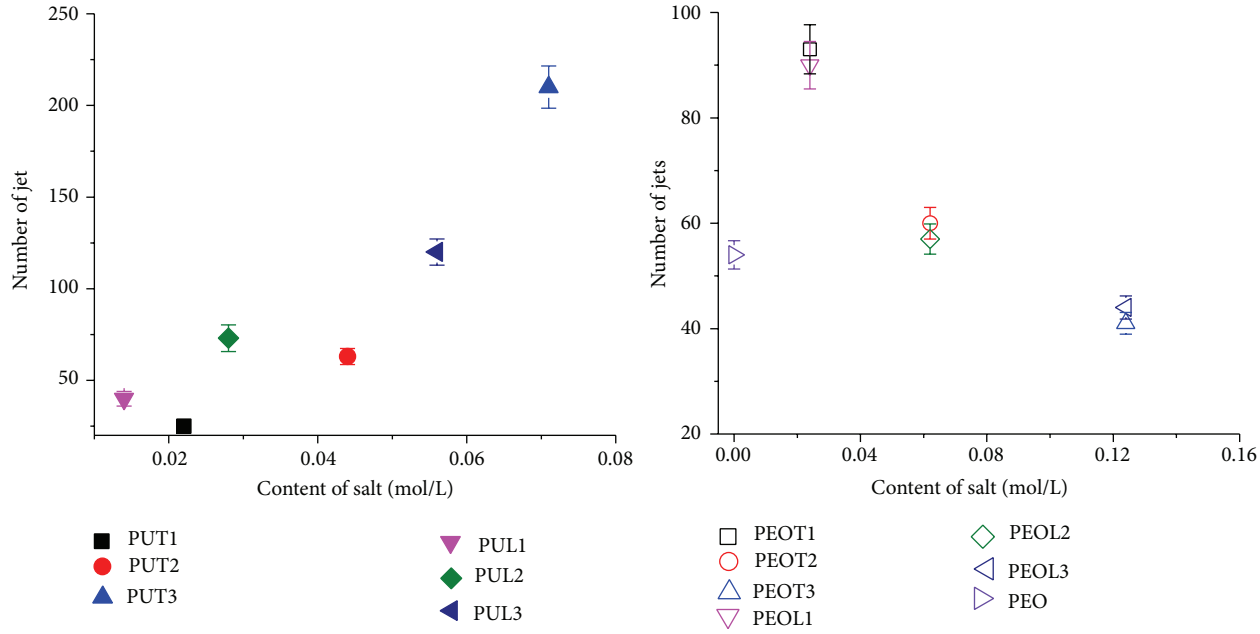

Figure 11: Number of jets on a roller.

> Electromechanical coupling occurs at the fluid-fluid interface alone; forces resulting from charges in the bulk are negligibly small. As the fluid accelerates, the tangential component of the electrical stress is largely balanced by the viscous, or viscoelastic, response of the fluid. Therefore, both the constitutive behaviour and the electrical properties of the fluid determine the condition of the process. If changes in the conductivity resulting from salt addition are large enough to alter the behaviour of the fluid from that of a leaky dielectric to that resembling a conductor, then the tangential component of the electrical stress that accelerates the fluid is likely to diminish and the flow process to be stopped. Through this limit, the electrical stress is balanced only by the alteration of the shape of the interface and surface tension only" [40].

Apparently, the effect of salt according to (2) works against that in (1). In the case of PU, the effects described in (1) predominate those in (2). In the case of PEO, only the effects according to (2) apply.

The differences between PU and PEO behaviours are also based on different polymer characteristics.

(1) PEO 400 kDa has a molecular weight high enough to create strong jets even at a low concentration and corresponding viscosity. This is not the case in PU as PU needs an increase in entanglement level using salt.

(2) PEO contains strong polar groups to obtain strong interactions with an electric field. This condition is expressed by a high value of dielectric constant. Again, this is not the case in PU as PU needs an increase in polarity by creating complexes with salt.

3.3. Spinning Performance and Spinning Performance per One Cone. Spinning performance and spinning performance per jet were measured and calculated for both solution systems. In case of PU without salt, spinning was not observed. However, in the case of PEO without salt, spinnability was high and only the polymer solution was transported to the surface of the collector without forming fibres. A possible consequence of this behaviour is the electrical conductivity variation.

PU polymer shows good spinnability when salt is added to it. Two kinds of salts (TEAB and LiCl) are used as additives; both increase the conductivity and viscosity of solutions. Cengiz and Jirsak [15] observed that TEAB increases the viscosity of PU solutions, which means more extensive interactions among macromolecules. A polymer network becomes more solid. It leads to higher spinning performance of solution [21].

PEO solution without salt is transported from the spinning electrode to the collector in the electrospinning device, but no fibres are formed; only the polymer solution moves towards the collector. Hundreds of jets can be observed. The addition of salt to the solution decreases its spinning performance, and nanofibres are formed.

In principle, the spinning performance (Figure 12) shows the same tendencies as the number of jets. Nevertheless, spinning performance per jet (Figure 13) is not an independent quantity. The amount of polymer solution flowing through one Taylor cone depends on the viscosity of solution, the thickness of a solution layer, and the drawing force of an electric field, which are dependent on the dielectric properties of the polymer or polymer solution.

3.4. Fibre Diameter and Nonfibrous Area. Quality of the produced nanofibres and nanofibre layers was tested in the

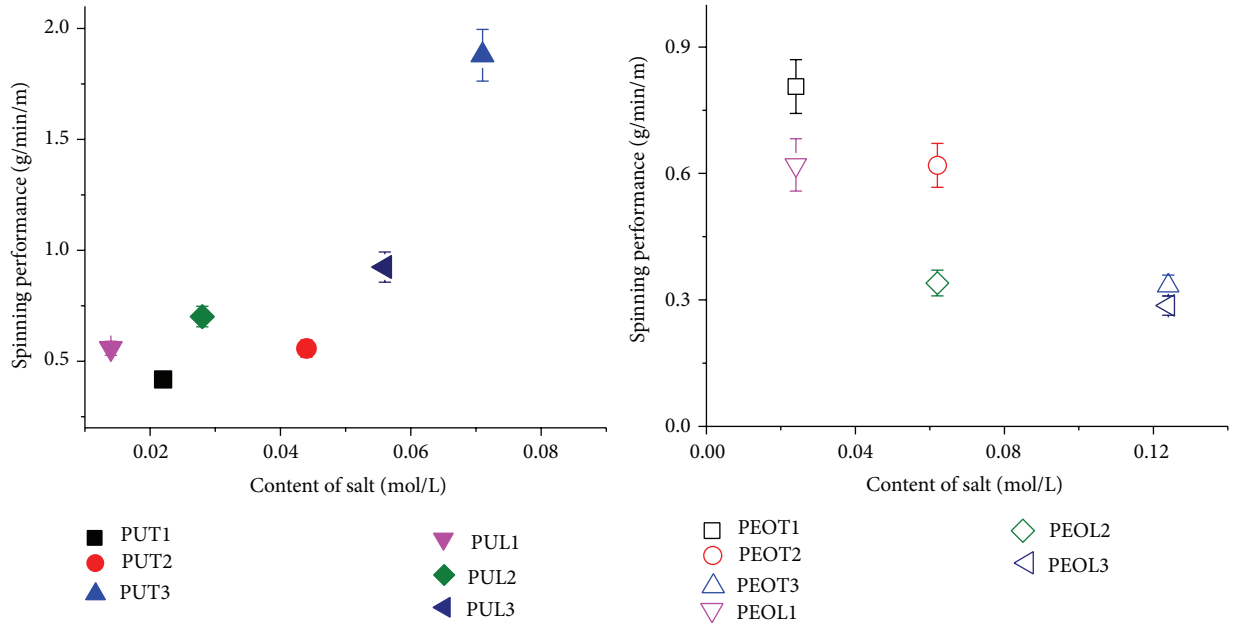

Figure 12: Spinning performance of PU and PEO nanofibres in various salt contents.

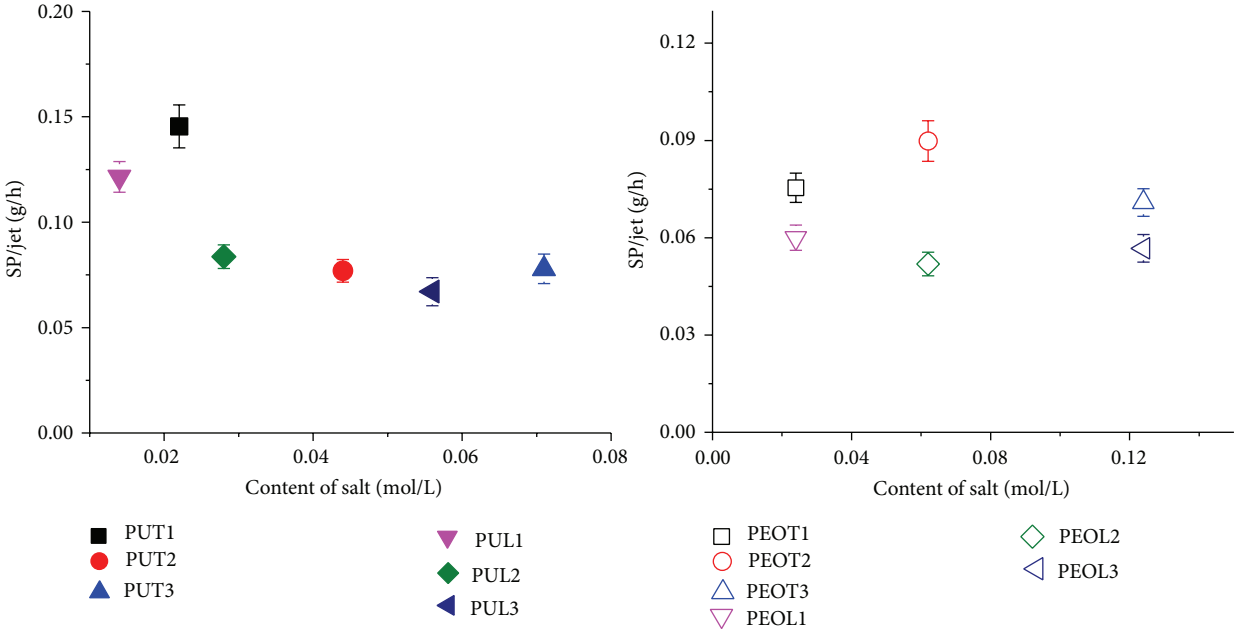

Figure 13: Spinning performance per jet of PU and PEO nanofibres in various salt contents.

experiments in terms of fibre diameter (Figure 14) and nonfibrous area (Figure 15). In the PU electrospinning, the highest salt content leads to an increase in viscosity and slightly changes fibre diameters. High salt content also leads to a low quality of PU nanofibre layers. By contrast, PEO nanofibre diameter and quality of nanofibre layers do not significantly depend on salt content above a certain limit.

4. Conclusion

The main results of the experiments are as follows.

(i) Salt may influence the entanglement number and polarity of macromolecules when creating complex bonds with them. It also increases the conductivity of

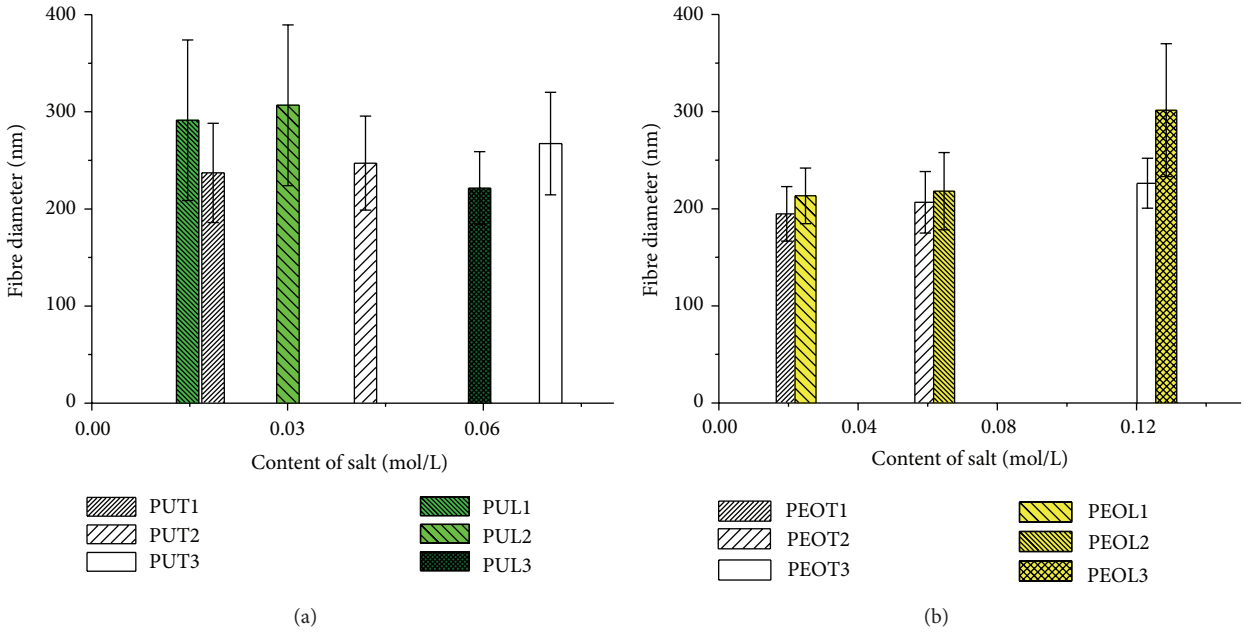

Figure 14: Fibre diameter versus salt content (a) PU with TEAB and LiCl salts, (b) PEO with TEAB and LiCl salts.

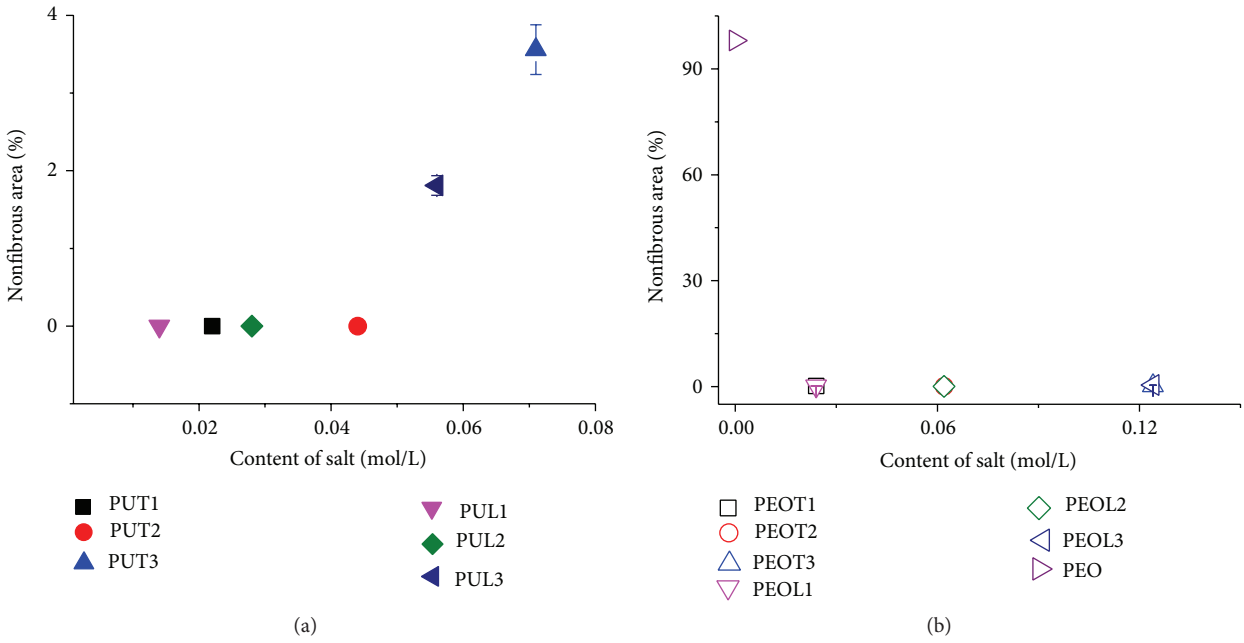

Figure 15: Nonfibrous area versus salt content (a) PU, (b) PEO nanofibres.

solutions that may cross the limit suggested in the leaky dielectric model.

(ii) PEO at 400 kDa, with its high polarity and high entanglement number (strength of jets), shows high spinning performance. This performance is reduced by the increase in conductivity.

(iii) In the case of PU, salt creates complex bonds with the polymer and increases the low polarity and entanglement number, consequently increasing the spinning performance. Further addition of salt may lead to reduced spinning performance. However, it cannot be proved because of the extreme increase in solution viscosity.

Future Works

The results of this work should be considered as initial findings on defining the parameters of needleless electrospinning, introducing new parameters and developing methods

to measure these new parameters for both aqueous and nonaqueous solution systems. In the future, the following topics should be focused on.

(i) Not enough studies have been conducted on the permittivity effect on electrospinning. Theoretical studies should present a full explanation and complete description of the electrospinning process involving the effects of permittivity on dependent parameters, such as length of jet, distance between jets, current on a jet, spinning performance, fibre diameter, lifetime of jets, and spinning area.

(ii) Studies should be made on dependent and independent parameters for both solution systems.

(iii) A full understanding of the relation between independent and dependent parameters should be presented.

Nomenclature and Symbols of Solutions

PEO Solutions in Water, Polymer Concentration 6 wt.%

PEO-▷: 0 concentration of salts
PEOT1-□: 0.024 mol/L TEAB
PEOT2-○: 0.062 mol/L TEAB
PEOT3-△: 0.124 mol/L TEAB
PEOL1-▽: 0.024 mol/L LiCl
PEOL2-◇: 0.062 mol/L
PEOL3-◁: 0.124 mol/L.

PU Solutions in DMF, Polymer Concentration 17.5 wt.%

PU-▶: 0 concentration of salts
PUT1-■: 0.022 mol/L TEAB
PUT2-●: 0.044 mol/L TEAB
PUT3-▲: 0.071 mol/L TEAB
PUL1-▼: 0.014 mol/L LiCl
PUL2-◆: 0.028 mol/L LiCl
PUL3-◀: 0.056 mol/L LiCl.

Conflict of Interests

The authors declare that there is no conflict of interests regarding the publication of this paper.

Acknowledgments

The authors would like to thank the Ministry of Education, Youth and Sports of the Czech Republic, Student's Grant Competition TUL in Specific University Research in 2013 (Project no. 48004) and in 2014 (Project no. 21041) for their financial support.

References

[1] T. Lin, H. Wang, and X. Wang, "Self-crimping bicomponent nanofibers electrospun from polyacrylonitrile and elastomeric polyurethane," *Advanced Materials*, vol. 17, no. 22, pp. 2699–2703, 2005.

[2] D. H. L. Bail, W. Schneider, K. Khalighi, and H. Seboldt, "Temporary wound covering with a silicon sheet for the soft tissue defect following open fasciotomy. Technical note," *Journal of Cardiovascular Surgery*, vol. 39, no. 5, pp. 587–591, 1998.

[3] P. Taepaiboon, U. Rungsardthong, and P. Supaphol, "Drug-loaded electrospun mats of poly(vinyl alcohol) fibres and their release characteristics of four model drugs," *Nanotechnology*, vol. 17, no. 9, pp. 2317–2329, 2006.

[4] K. Kosmider and J. Scott, "Polymeric nanofibre exhibit an enhanced air filtration performance," *Filtration and Separation*, vol. 39, no. 6, pp. 20–22, 2002.

[5] A. C. Patel, S. Li, J.-M. Yuan, and Y. Wei, "In situ encapsulation of horseradish peroxidase in electrospun porous silica fibers for potential biosensor applications," *Nano Letters*, vol. 6, no. 5, pp. 1042–1046, 2006.

[6] X. M. Mo, C. Y. Xu, M. Kotaki, and S. Ramakrishna, "Electrospun P(LLA-CL) nanofiber: a biomimetic extracellular matrix for smooth muscle cell and endothelial cell proliferation," *Biomaterials*, vol. 25, no. 10, pp. 1883–1890, 2004.

[7] P. X. Ma and R. Y. Zhang, "Synthetic nano-scale fibrous extracellular matrix," *Journal of Biomedical Materials Research*, vol. 46, no. 1, pp. 60–72, 1999.

[8] L. Torobin and R. C. Findlow, "Method and apparatus for producing high efficiency fibrous media incorporating discontinuous sub-micron diameter fibers, and web media formed thereby," Google Patents, 2001.

[9] T. J. Fabbricante, A. S. Fabbricante, and G. F. Ward, "Micro-denier nonwoven materials made using modular die units," US6114017 A, 2000.

[10] T. Huang, L. R. Marshall, J. E. Armantrout et al., "Production of nanofibers by melt spinning," Google Patents, 2012.

[11] T. Huang, "Centrifugal solution spun nanofiber process," Google Patents, 2010.

[12] R. D. Pike, "Superfine microfiber nonwoven web," Google Patents, 1999.

[13] A. S. Nain, J. C. Wong, C. Amon, and M. Sitti, "Drawing suspended polymer micro-/nanofibers using glass micropipettes," *Applied Physics Letters*, vol. 89, no. 18, p. 183105, 2006.

[14] O. Jirsak, F. Sanetrnik, D. Lukas, V. Kotek, L. Martinova, and J. Chaloupek, "Method of nanofibres production from a polymer solution using electrostatic spinning and a device for carrying out the method," Google Patents, 2009.

[15] F. Cengiz and O. Jirsak, "The effect of salt on the roller electrospinning of polyurethane nanofibers," *Fibers and Polymers*, vol. 10, no. 2, pp. 177–184, 2009.

[16] T. A. Dao and O. Jirsak, *The Role of Rheological Properties of Polymer Solutions in Needleless Electrostatic Spinning*, 2010.

[17] T. H. Meyer and J. Keurentjes, *Handbook of Polymer Reaction Engineering*, Wiley-VCH, Weinheim, Germany, 2005.

[18] J. E. Mark, *Polymer Data Handbook*, Oxford University Press, New York, NY, USA, 1999.

[19] A. J. Fry, "Tetraalkylammonium ions are surrounded by an inner solvation shell in strong electron pair donor solvents," *Electrochemistry Communications*, vol. 11, no. 2, pp. 309–312, 2009.

[20] O. V. Erokhina, A. V. Artemov, L. S. Gal'Braikh, G. A. Vikhoreva, and A. A. Polyutov, "State of lithium cation in a solution of polyurethane in deviethylformamide," *Fibre Chemistry*, vol. 38, no. 6, pp. 447–449, 2006.

[21] F. Cengiz-Çallioğlu, O. Jirsak, and M. Dayik, "Investigation into the relationships between independent and dependent parameters in roller electrospinning of polyurethane," *Textile Research Journal*, vol. 83, no. 7, pp. 718–729, 2013.

[22] P. P. Rastogi, "A study on ion-dipole interaction energy of some alkali metal cations, halide anions and symmetrical tetraalkylammonium ions in different solvents," *Zeitschrift für Physikalische Chemie*, vol. 75, no. 3-4, pp. 202–206, 1971.

[23] A. Karmakar and A. Ghosh, "Dielectric permittivity and electric modulus of polyethylene oxide (PEO)-$LiClO_4$ composite electrolytes," *Current Applied Physics*, vol. 12, no. 2, pp. 539–543, 2012.

[24] G. Collins, J. Federici, Y. Imura, and L. H. Catalani, "Charge generation, charge transport, and residual charge in the electrospinning of polymers: a review of issues and complications," *Journal of Applied Physics*, vol. 111, no. 4, Article ID 044701, 2012.

[25] H. Kliem, K. Schroeder, and W. Bauhofer, "High dielectric permittivity of polyethylene oxide in humid atmospheres," in *Proceedings of the Annual Conference on Electrical Insulation and Dielectric Phenomena*, pp. 12–15, October 1996.

[26] C. Fanggao, G. A. Saunders, E. F. Lambson et al., "Frequency dependence of the complex dielectric constant of poly(ethylene oxide) under hydrostatic pressure," *Il Nuovo Cimento D*, vol. 16, no. 7, pp. 855–864, 1994.

[27] M. W. Jernegan, "Benjamin Franklin's 'electrical kite' and lightning rod," *The New England Quarterly*, vol. 1, no. 2, pp. 180–196, 1928.

[28] V. Cooray, *Lightning Protection*, The Institution of Engineering and Technology, 2009.

[29] J. L. G. Lussac, *Instruction Sur Les Paratonnerres*, Kessinger Publishing, LLC, Paris, France, 1824.

[30] M. Nayel, "Investigation of lightning rod shielding angle," in *Proceedings of the IEEE Industry Applications Society Annual Meeting (IAS '10)*, pp. 1–4, IEEE, Houston, Tex, USA, October 2010.

[31] A. V. Rakov and M. A. Uman, *Lightning: Physics and Effects*, Cambridge University Press, Cambridge, UK, 2003.

[32] M. A. Uman, *All about Lightning*, Dover Publications, New York, NY, USA, 1987.

[33] C. F. Wagner, G. D. McCann, and G. L. MacLane, "Shielding of transmission lines," *Electrical Engineering*, vol. 60, pp. 313–328, 1941.

[34] X. Zhang, L. Dong, J. He, S. Chen, and R. Zeng, "Study on the effectiveness of single lightning rods by a fractal approach," *Journal of Lightning Research*, vol. 1, no. 1, pp. 1–8, 2009.

[35] D. Lukáš, A. Sarkar, L. Martinová et al., "Physical principles of electrospinning (electrospinning as a nano-scale technology of the twenty-first century)," *Textile Progress*, vol. 41, no. 2, pp. 59–140, 2009.

[36] D. Lukáš, A. Sarkar, and P. Pokorny, "Self-organization of jets in electrospinning from free liquid surface: a generalized approach," *Journal of Applied Physics*, vol. 103, no. 8, Article ID 084309, 2008.

[37] M. Komarek and L. Martinova, "Design and evaluation of melt electrospinning electrodes," in *Proceedings of the 2nd Nanocon International Conference*, Tanger, Ed., pp. 72–77, Olomouc, Czech Republic, October 2010.

[38] A. T. Dao, *The role of rheological properties of polymer solutions in needleless electrostatic spinning [Ph.D. thesis]*, Technical University of Liberec, Liberec, Czech Republic, 2010.

[39] J. R. Melcher and G. I. Taylor, "Electrohydrodynamics—a review of role of interfacial shear stresses," *Annual Review of Fluid Mechanics*, vol. 1, no. 1, pp. 111–146, 1969.

[40] P. K. Bahattacharjee and G. C. Rutledge, "Electrospinning and polymer nanofibers: process fundamentals," in *Comprehensive Biomaterials*, vol. 1, pp. 497–512, 2011.

Hindawi Publishing Corporation
Journal of Nanomaterials
Volume 2014, Article ID 964621, 7 pages
http://dx.doi.org/10.1155/2014/964621

Research Article

Fabrication and Characterization of Electrospun Polycaprolactone Blended with Chitosan-Gelatin Complex Nanofibrous Mats

Yongfang Qian, Zhen Zhang, Laijiu Zheng, Ruoyuan Song, and Yuping Zhao

School of Textile and Material Engineering, Dalian Polytechnic University, Dalian, Liaoning, 116021, China

Correspondence should be addressed to Yongfang Qian; qyfdhu@126.com

Received 10 July 2014; Revised 18 August 2014; Accepted 21 August 2014; Published 2 September 2014

Academic Editor: Lan Xu

Design and fabrication of nanofibrous scaffolds should mimic the native extracellular matrix. This study is aimed at investigating electrospinning of polycaprolactone (PCL) blended with chitosan-gelatin complex. The morphologies were observed from scanning electron microscope. As-spun blended mats had thinner fibers than pure PCL. X-ray diffraction was used to analyze the degree of crystallinity. The intensity at two peaks at 2θ of 21° and 23.5° gradually decreased with the percentage of chitosan-gelatin complex increasing. Moreover, incorporation of the complex could obviously improve the hydrophilicity of as-spun blended mats. Mechanical properties of as-spun nanofibrous mats were also tested. The elongation at break of fibrous mats increased with the PCL content increasing and the ultimate tensile strength varied with different weight ratios. The as-spun mats had higher tensile strength when the weight ratio of PCL to CS-Gel was 75/25 compared to pure PCL. Both as-spun PCL scaffolds and PCL/CS-Gel scaffolds supported the proliferation of porcine iliac endothelial cells, and PCL/CS-Gel had better cell viability than pure PCL. Therefore, electrospun PCL/Chitosan-gelatin nanofibrous mats with weight ratio of 75/25 have better hydrophilicity mechanical properties, and cell proliferation and thus would be a promising candidate for tissue engineering scaffolds.

1. Introduction

Tissue engineering scaffolds play a key role that provides an environment for cells activities in regeneration of new tissue. In natural tissues, cells are surrounded by extracellular matrix (ECM), which is a complex composed of nanosized proteins and glycosaminoglycans (GAGs) [1–3]. Electrospinning has been proven to be a relatively simple technique that utilizes high-voltage electrostatic field to drive the polymer solutions or melts to produce nanofibers with diameter in the range from micrometers down to tens of nanometers, which has been investigated as a polymer processing technique for tissue engineering application in recent years [4, 5]. Therefore, scaffolds fabricated by electrospinning could mimic the architecture of ECM.

Gelatin is a protein derived from partial hydrolysis of collagen, and chitosan from deacetylated chitin is a polysaccharide that has structure similar to GAGs in the ECM [6, 7]. Therefore, electrospun chitosan and gelatin complex could further mimic the composition of natural ECM. During our previous work, chitosan and gelatin complex, defined as CS/Gel below, was successfully electrospun into nanofibers [8]. However, the tensile strength and elongation of as-spun mats were still too weak even after modification by cross-linking, which would limit its application as nanofibrous scaffolds. Thus, incorporation of a synthetic polymer would be necessary to improve the mechanical properties for tissue engineering applications. Desired physical properties could be achieved through the development of hybrid materials consist of synthetic and natural materials. Poly(ε-caprolactone) (PCL) is a linear synthetic degradable polymer with high mechanical strength and biocompatibility [9] and is also a suitable candidate for fabricating fibrous scaffolds and has been approved by Food and Drug Administration (FDA) for various medical applications [10]. PCL has been blended with chitosan to improve the spinnability [11] and blended with collagen to fabricate aligned nanofibrous scaffolds to support the oriented growth of nerve axons [12]. However,

electrospun PCL nanofibrous mats had poor hydrophilicity that would lead to reduction in its ability of cell adhesion, proliferation, and differentiation [13]. Therefore, hybrids made of synthetic and natural polymers could combine the mechanical properties of synthetic polymers and the biocompatibility of natural polymers. In the present work, PCL was blended with CS-Gel complex and then electrospun into nanofibrous mats. The fibers morphology, crystallites, wettability, and mechanical properties of as-spun mats were investigated by SEM, XRD, water contact angle test, and tensile measurement. To evaluate the application in tissue engineering, cell morphology and proliferation were also studied.

2. Materials and Methods

2.1. Materials. Chitosan (Mη, about 10^6) with a degree of deacetylation (DD = 85%) was purchased from Haidebei Marine Bioengineering Co., Ltd. (Jinan, China). Gelatin (Type A, 300 bloom) and polycaprolactone (PCL) (Mw = 80000) were purchased from Sigma-Aldrich (St. Louis, Missouri, USA). 1,1,1,3,3,3-Hexafluoro-2-propanol (HFP) was from Daikin Industries Ltd. (Japan) and trifluoroacetic acid (TFA) was from Runjie Chemical Reagent Company (Shanghai, China). All products were received without further purification.

2.2. Preparation of the PCL Blended with CS-Gel Solutions and Electrospinning. Chitosan and gelatin complex (w/w = 50/50) solution was obtained by mixing the chitosan solution, in which chitosan was dissolved in HFP/TFA (V/V = 8/2), and gelatin solution, in which gelatin was dissolved in HFP at the same volume ratio, with concentration of 0.08 g/mL in the final mixed solution.

Polycaprolactone (PCL) was dissolved in pure HFP with concentration of 0.08 g/mL. PCL was blended with chitosan-gelatin complex at different weight ratios by mixing solutions at different volume ratios. Electrospinning was performed as previously described [8]. If brief, 1 mL plastic syringe containing the above mixed PCL/CS-Gel solutions was mounted in an accurate syringe pump (789100C, Cole-Parmer, USA). The mass flow rate was set to 1.0 mL/h. A voltage of 15 KV between the syringe tip and the target, generated by high-voltage power supply (BGG DC high-voltage generator), purchased from the BMEI Co., Ltd. (Beijing, China), was applied to the tip of a syringe needle. The as-spun nanofibers were collected on a grounded metal plate, which was covered with aluminum foil (or had medical grade plastic cover-slides onside) and placed 13 cm from the tip of the syringe needle. The electrospinning process was conducted under the ambient conditions.

2.3. Characterization

2.3.1. Scanning Electron Microscopy. The morphologies of the as-spun nanofibrous mats were observed by scanning electron microscope (SEM, JSM-5600LV, Japan) and the diameter distributions were conducted by image visualization software Image J (National Institutes of Health, USA).

2.3.2. Contact Angle Measurements. Surface wettability of the electrospun scaffolds was characterized by water contact angle measurement. The images of the droplet on the membrane were visualized through the image analyzer (OCA 40, Dataphysics, Germany) and the angles between the water droplet and the surface were measured. The measurement used distilled water as the reference liquid and it was automatically dropped on the electrospun scaffolds. To confirm the uniform distribution of blend nanofibrous scaffolds, the contact angle was measured three times from different positions and an average value was calculated by statistical method.

2.3.3. Mechanical Properties Test. The mechanical properties of the as-spun PCL/CS-Gel nanofibrous mats were tested using universal materials tester (H5K-S, Hounsfield, UK). All the samples (50 mm × 10 mm) were prepared and tested in ambient temperature of 20°C and humidity of 65%. The gauge length was 30 mm and the strain rate was set at 10 mm/min. Micrometer with precision of 0.01 mm was used to measure the thicknesses of the samples. The tensile stress-strain curves of the specimens were obtained from machine-recorded data.

2.4. Cell Viability and Proliferation. Porcine iliac endothelial cells (PIECs) were cultured in DMEM medium containing 10% fetal bovine serum, 100 units/mL penicillin, and 100 units/mL streptomycin. Cells were placed in an incubator set to 37°C and 5% carbon dioxide (CO_2). The medium was changed every 3 days. Electrospun scaffolds were prepared on circular cover slips (14 mm in diameter). The cover slips were placed in 24-well plates and then secured with stainless O-ring, sterilized with 75% alcohol solution which was replaced with phosphate-buffered saline solution (PBS) for washing after two hours.

To evaluate the morphology and proliferation of cells growing on the scaffolds, PIECs were seeded onto fibrous scaffolds and control glass cover slips. For the morphology study, PIECs were seeded carefully in the center of each well at a density of 1.0×10^5 cells/cm^2. After culturing for 24 hours, the cells on the mats were rinsed with PBS and then fixed in 4% glutaraldehyde water solution for 45 min at 4°C temperature. Thereafter, the samples were dehydrated in alcohol solutions with concentrations of 50%, 75%, and 100% in turn and then dried under vacuum overnight. The dry cellular constructs were coated with gold sputter and observed under the SEM at a voltage of 10 KV. For cell proliferation tests, PIECs were seeded onto the as-spun mats at a density of 2.5×10^4 cells/cm^2. Cell proliferation was continually monitored on days 1, 3, 5, and 7 after cell seeding. At the time points stated above, the cells and electrospun mats were incubated with 5 mg/mL 3-[4,5-dimethyl-2-thiazolyl]-2,5-diphenyl-2H-tetrazolium bromide (MTT) for 4 h and then the culture medium was extracted and 400 μL dimethyl sulfoxide (DMSO) was added and stayed for 20 min. Finally, aliquots were pipetted into the wells of a 96-well plate and

tested by an enzyme-labeled instrument (MK3, Thermo) and the absorbance at 492 nm for each well was measured.

3. Results and Discussion

3.1. Fiber Morphologies. Figure 1 shows SEM micrographs of electrospun mats prepared from PCL blended with CS-Gel complex at different weight ratios. From Figure 1(a), the as-spun pure PCL fibers lost their basic morphology of ultrathin fiber structure and interconnected between fibers. When the weight ratio of PCL to CS-Gel complex was 75/25, the morphology of as-spun fibers became smooth and the nanofibers diameter decreased significantly from 893 nm to 114 nm, as shown in Figure 1(b). The reason could be that the conductivity of the blended solutions was increased. Chitosan and gelatin have many polar groups, such as $-NH_2$ and –COOH, that could carry positive or negative charges and form polyanion-polycation complex. The ejected jet would be subjected to greater elongation forces due to higher charge density on the surface [14, 15]. Moreover, the jet bending instability could be enhanced because of the increasing of charge density and thus result in smaller fiber diameter [16, 17]. However, when the weight ratio of PCL to CS-Gel complex was 50/50, the average diameter slightly increased to 154 nm. The reason of increasing could be the diameters distributed at larger range from 40 nm to 388 nm, while the diameters ranged from 57 nm to 221 nm when PCL content was 75%. When estimating the size of as-spun diameters, at least 60 fibers randomly observed on the SEM images were calculated to get the average diameter. The proportions of fibers with diameters less than 100 nm, ranging from 100 nm to 200 nm, and more than 200 nm were 46.2%, 49.2%, and 4.6%, respectively, at PCL percentage of 75%, while 40.3%, 25.4%, and 34.3%, respectively, at PCL content 50%. It could also be illustrated from Figure 1(c) that the fibers exhibit less uniform at PCL content of 50% than fibers at PCL content of 25%. For the CS-Gel complex, the average diameter was 231 nm and the diameters ranged from 63 nm to 707 nm.

3.2. X-Ray Diffraction (XRD). Figure 2 shows X-ray patterns of electrospun PCL blended with CS-Gel complex at different weight ratios. PCL showed a sharp peak at 2θ of 21° and a relatively low intensity peak at 23.5°, showing the crystalline nature of PCL nanofibrous mats. With the percentage of CS-Gel complex increasing, the intensity of peak at 2θ of 21° and 23.5° gradually decreased and became amorphous broad peak for CS-Gel nanofibrous mats. The decreased intensity of blended nanofibrous mats indicates reduction in the degree of crystallinity and the as-spun CS-Gel mats have an amorphous structure.

3.3. Water Contact Angle Analysis. The surface wettability of biomaterials plays an important role for the attachment and proliferation of different cells [13, 18]. To investigate the surface properties of fibrous mats, water contact angles were measured and shown in Figure 3. The pure PCL nanofibrous mats showed an angle around 128° indicating that PCL nanofibrous scaffolds were hydrophobic. The reason could be the presence of CH_2 groups in the main chain of PCL that leads to the hydrophobic property. The contact angles of blended nanofibrous mats decreased to 69°, 60°, and 28°, respectively, when the percentages of CS-Gel were 25%, 50%, and 75%, implying that the blended nanofibrous mats transformed to be hydrophilic. The reason is that CS-Gel complex has many hydrophilic groups, such as amine and carboxyl. Hydrophilic surfaces exhibit better affinity for cells than hydrophobic surfaces [19]. However, when the CS-Gel content was more than 50%, the membrane partly dissolved during the water contact angle test, and CS-Gel membrane dissolved completely.

Table 1: Mechanical properties of PCL blended with CS-Gel complex at different weight ratios ($n = 3$).

PCL/CS-Gel	Elongation at break (%)	Tensile strength (MPa)	Thickness (mm)
100/0	127.2 ± 12.22	5.52 ± 0.07	0.119 ± 0.015
75/25	85.87 ± 2.41	17.6 ± 0.51	0.096 ± 0.005
50/50	34.93 ± 5.88	3.67 ± 0.26	0.111 ± 0.014
25/75	19.47 ± 2.34	2.24 ± 0.35	0.201 ± 0.017
0/100	2.71 ± 0.16	2.07 ± 0.18	0.106 ± 0.005

3.4. Mechanical Properties of Electrospun PCL Blended with Chitosan-Gelatin Complex. The mechanical properties of as-spun mats have an important effect on successful application in tissue engineering. The typical tensile stress-strain curves of PCL blended with CS-Gel complex nanofibrous mats were shown in Figure 4. The average elongation at break and average ultimate tensile strength, as determined by the stress at break normalized to the cross-sectional area of as-spun mats, were summarized in Table 1. Figure 4 and Table 1 showed that the elongation at break of nanofibrous mats increased with the PCL content increasing, while the ultimate tensile strength varied with different weight ratios. The failure process of nanofibrous mats involved slippage and break of fibers. The unit of PCL molecule has five methylenes that lead to the good flexibility. When the percentage of CS-Gel complex was more than 50%, as-spun nanofibrous mats exhibit typical brittle fracture. With increasing the PCL percentage to 75%, nanofibrous mats transformed from brittle to flexible. However, it is interesting to find that pure PCL mats had lower tensile strength than PCL/CS-Gel (75/25). Lee et al. [2] studied the effect of gelatin incorporation into PLCL and also found that gelatin incorporation of 10–30 wt% had an enhanced tensile strength. The reason could be the reduction of fibers diameter when incorporating chitosan and gelatin complex. Fibers with thinner diameter would have better tensile strength. Thus, the mechanical properties of PCL/CS-Gel at weight ratio 75/25 were better compared with both PCL and CS-Gel complex.

3.5. Morphology and Proliferation of PIECs on PCL and PCL/CS-Gel Scaffolds. When the weight ratio of PCL to

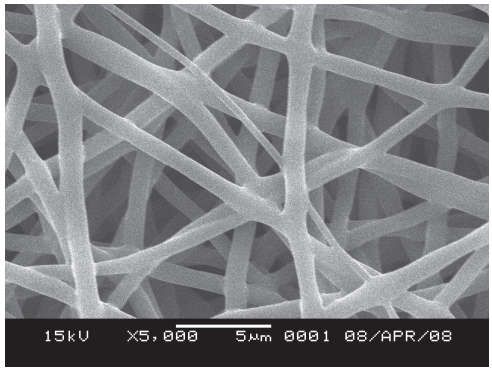

(a)

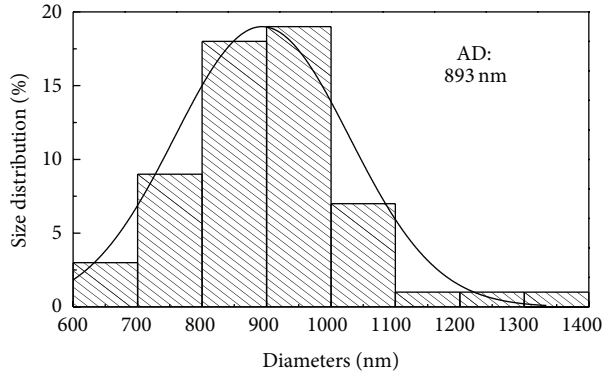

(a′)

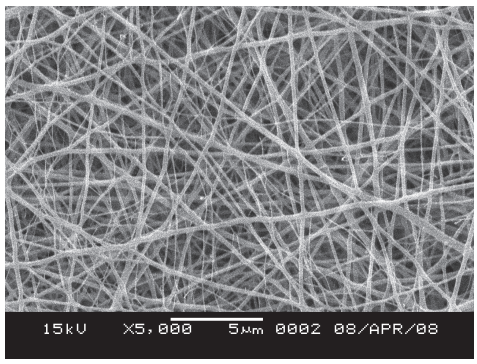

(b)

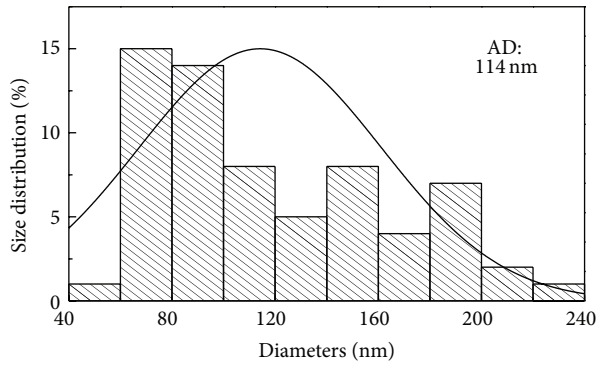

(b′)

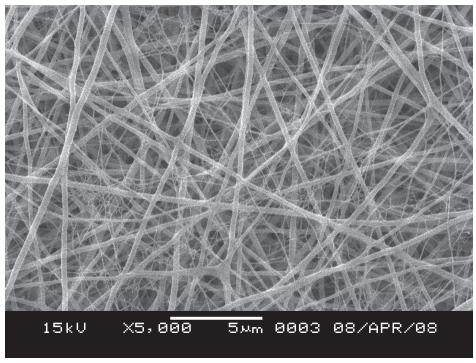

(c)

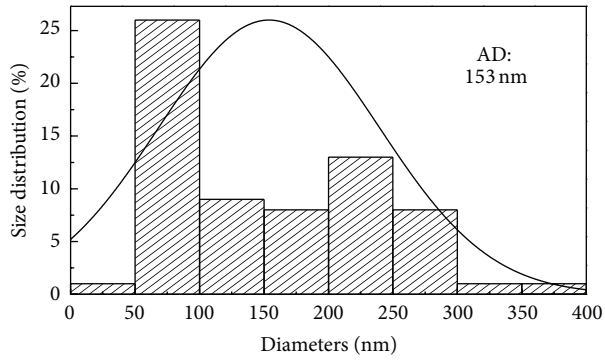

(c′)

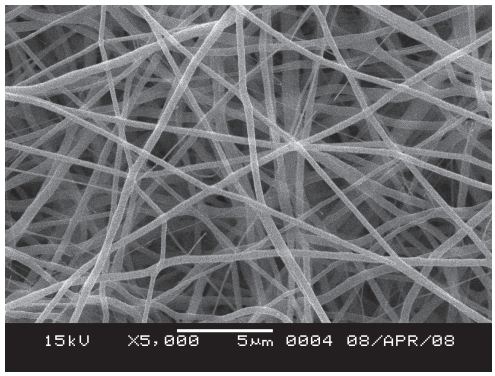

(d)

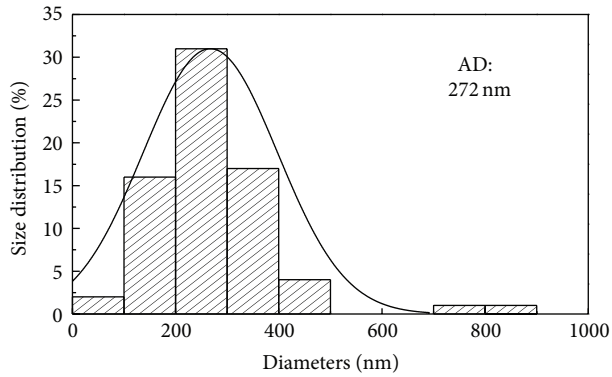

(d′)

Figure 1: Continued.

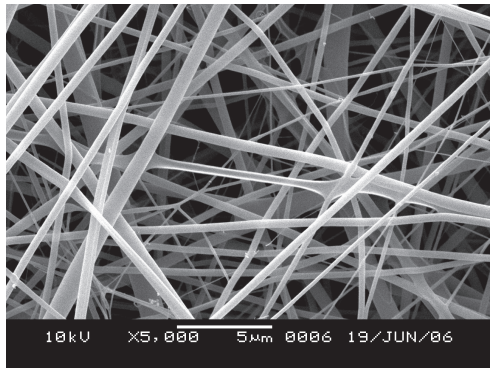

(e)

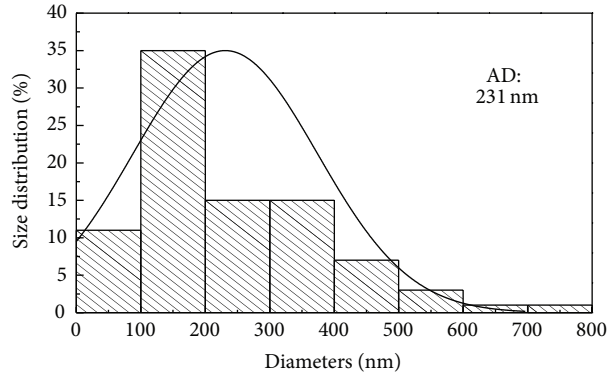

(e′)

Figure 1: SEM micrographs and diameter distributions of as-spun PCL blended with CS-Gel complex at different weight ratios, PCL to CS-Gel complex: (a) 100/0; (b) 75/25; (c) 50/50; (d) 25/75; (e) 0/100.

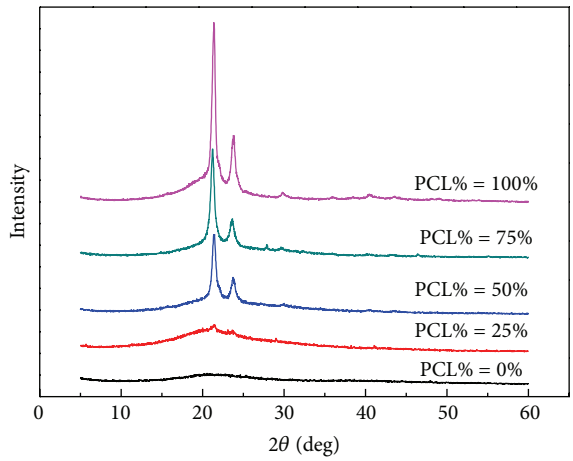

Figure 2: XRD pattern of as-spun PCL blended with CS-Gel complex nanofibrous mats with different percentages of PCL.

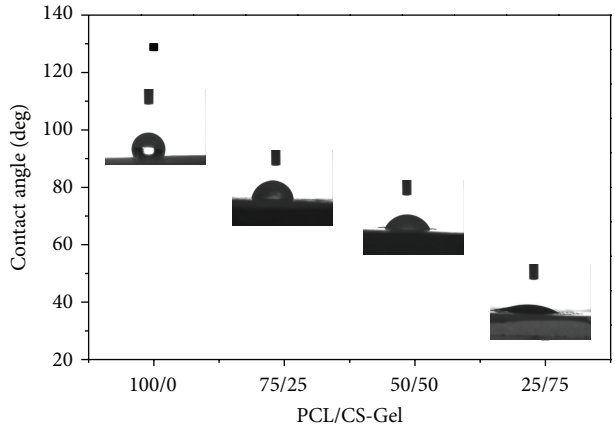

Figure 3: Water contact angle of electrospun PCL blended with gelatin and chitosan complex at different weight ratios (Inset of this figure shows the variation shapes of contact angle on different mats).

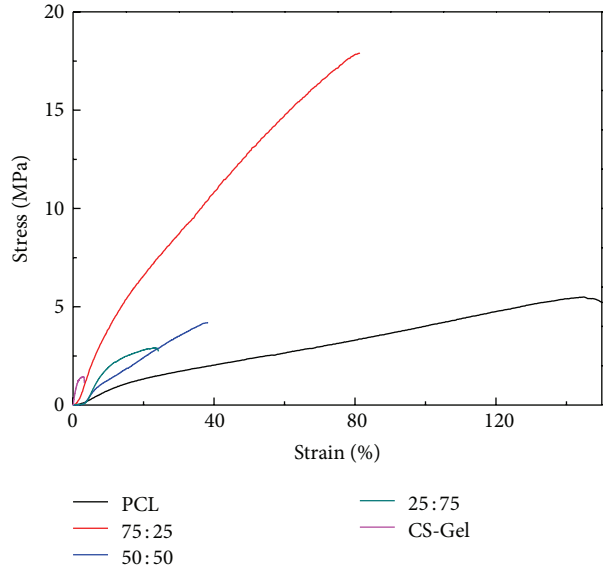

Figure 4: Mechanical properties of electrospun PCL blended with chitosan and gelatin complex at different weight ratios.

CS-Gel was 75/25, defined as PCL/CS-Gel below, the as-spun mats had better mechanical properties and hydrophilic surfaces. The morphology of the cells cultured on PCL and PCL/CS-Gel scaffolds was evaluated by SEM. Figure 5 shows the cell morphology on PCL, PCL/CS-Gel scaffolds, and cover slips (control) at 24 h after seeding. PIECs extended well on the surface of the above two scaffolds with polygonal shape, and nanofibrous scaffolds had better cell viability in comparison with cover slips. Moreover, cells spread more easily to form endothelial layer on PCL/CS-Gel scaffold than pure PCL, implying that incorporation of CS-Gel into PCL could improve the biocompatibility. The incorporation of functional groups such as NH_2, COOH, and OH could introduce cell recognition sites to promote cell-material interactions [20].

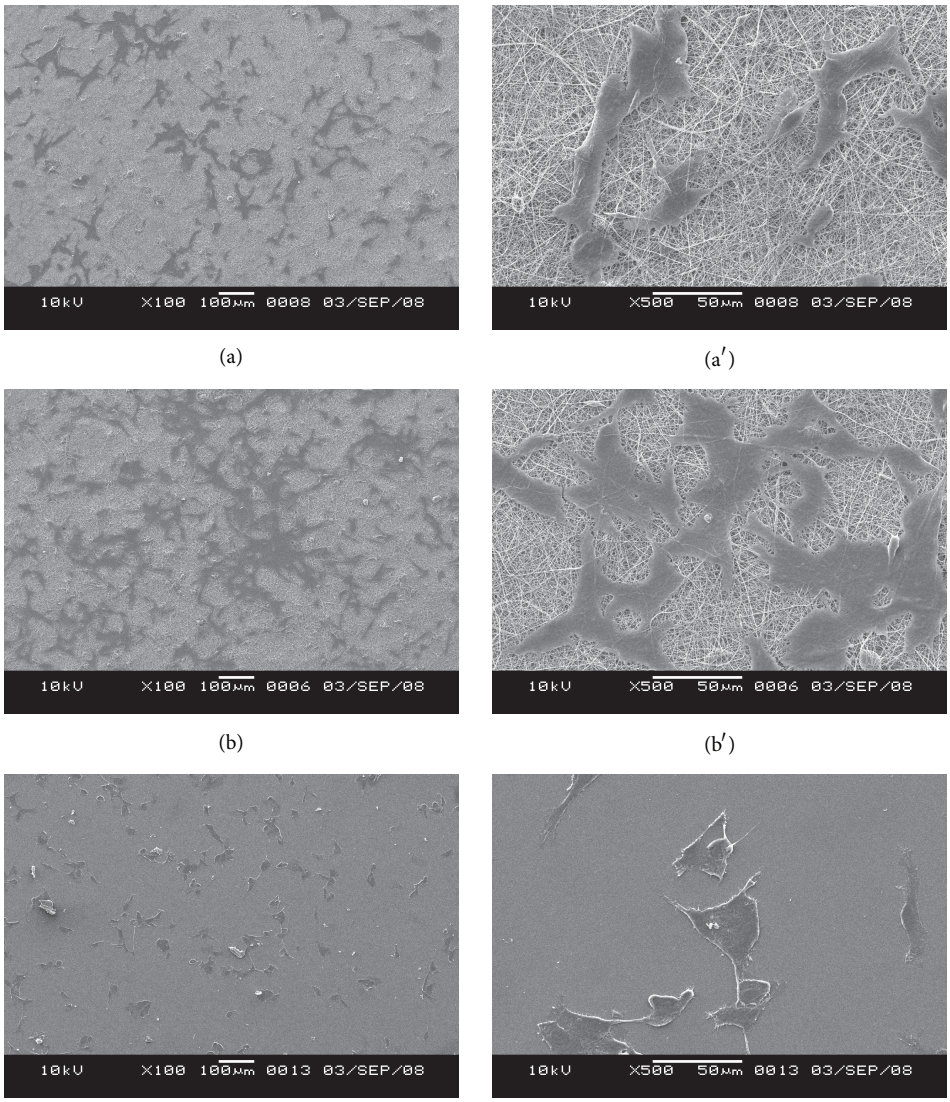

Figure 5: Morphology of PIECs cultured on PCL, PCL/CS-Gel, and cover slips (control): (a) PCL, (b) PCL/CS-Gel, and (c) cover slips.

The proliferation of PIECs cultured on PCL, PCL/CS-Gel, cover slips, and tissue culture plates (TCPs) on days 1, 3, 5, and 7 after seeding was shown in Figure 6. During being cultured for 7 days, cells grew well and exhibited increasing trend. On day 7, cells on PCL/CS-Gel appeared more increasing than PCL and cover slips. Thus, PCL/CS-Gel scaffolds would be potential candidate in tissue engineering.

4. Conclusion

In this work, we developed PCL blended with CS-Gel complex nanofibrous mats. PCL blended with CS-Gel complex at different weight ratios was successfully electrospun and subsequently characterized by SEM, XRD, and water contact angle test. SEM analysis indicates that blended mats have thinner fibers than pure PCL, and the average diameter was the smallest when PCL to CS-Gel (w/w) ratio was 75/25. From XRD analysis, the degree of crystallinity decreased with the percentage of CS-Gel complex increasing. Incorporation of chitosan-gelatin complex could obviously improve the hydrophilicity of as-spun mats from water contact angle test. However, the nanofibrous mats became partly dissolved when CS-Gel complex content was more than 50%. From mechanical properties test, the elongation at break increased with the PCL content increasing. PCL/CS-Gel (w/w = 75/25) exhibited higher tensile strength. Finally, cell morphology and proliferation were studied. PCL/CS-Gel scaffolds have better proliferation than pure PCL. Based on these results, PCL/CS-Gel nanofibrous scaffolds with weight ratio of 75/25 have better hydrophilic property, mechanical properties, and cell proliferation, which would be a promising candidate for tissue engineering scaffolds.

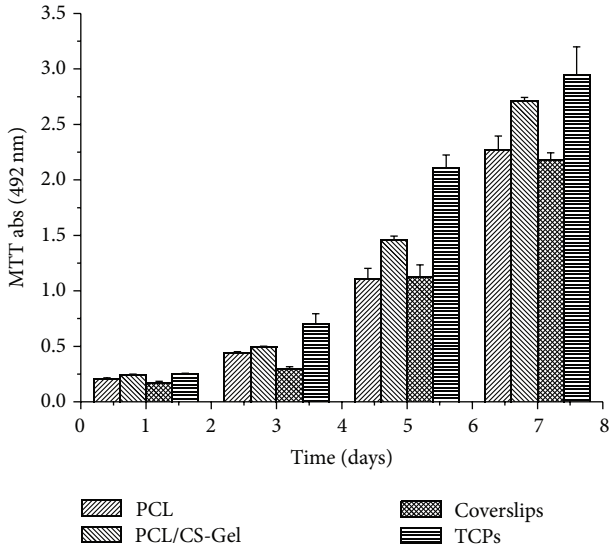

Figure 6: Proliferation of PIECs cultured on PCL, PCL/CS-Gel, cover slips, and TCPs.

Conflict of Interests

The authors declare that there is no conflict of interests.

Acknowledgment

This research was supported by a grant from The Education Department of Liaoning Province (Project no. 2012191).

References

[1] C. Xu, R. Inai, M. Kotaki, and S. Ramakrishna, "Electrospun nanofiber fabrication as synthetic extracellular matrix and its potential for vascular tissue engineering," *Tissue Engineering*, vol. 10, no. 7-8, pp. 1160–1168, 2004.

[2] J. Lee, G. Tae, Y. H. Kim, I. S. Park, S.-H. Kim, and S. H. Kim, "The effect of gelatin incorporation into electrospun poly(*L*-lactide-*co*-ε-caprolactone) fibers on mechanical properties and cytocompatibility," *Biomaterials*, vol. 29, no. 12, pp. 1872–1879, 2008.

[3] S. F. Badylak, "The extracellular matrix as a scaffold for tissue reconstruction," *Seminars in Cell and Developmental Biology*, vol. 13, no. 5, pp. 377–383, 2002.

[4] L. M. Bellan and H. G. Craighead, "Control of an electrospinning jet using electric focusing and jet-steering fields," *Journal of Vacuum Science and Technology B*, vol. 24, no. 6, pp. 3179–3183, 2006.

[5] H. M. Liou, L. R. Rau, C. C. Huang, M. R. Lu, and F. Y. Hsu, "Electrospun Hyaluronan-Gelatin nanofibrous matrix for nerve tissue engineering," *Journal of Nanomaterials*, vol. 2013, Article ID 613638, 9 pages, 2013.

[6] Z.-M. Huang, Y. Z. Zhang, S. Ramakrishna, and C. T. Lim, "Electrospinning and mechanical characterization of gelatin nanofibers," *Polymer*, vol. 45, no. 15, pp. 5361–5368, 2004.

[7] Y. Z. Zhang, B. Su, S. Ramakrishna, and C. T. Lim, "Chitosan nanofibers from an easily electrospinnable UHMWPEO-doped chitosan solution system," *Biomacromolecules*, vol. 9, no. 1, pp. 136–141, 2008.

[8] Y.-F. Qian, K.-H. Zhang, F. Chen, Q.-F. Ke, and X.-M. Mo, "Cross-linking of gelatin and chitosan complex nanofibers for tissue-engineering scaffolds," *Journal of Biomaterials Science, Polymer Edition*, vol. 22, no. 8, pp. 1099–1113, 2011.

[9] S. Gautam, A. K. Dinda, and N. C. Mishra, "Fabrication and characterization of PCL/gelatin composite nanofibrous scaffold for tissue engineering applications by electrospinning method," *Materials Science and Engineering C*, vol. 33, no. 3, pp. 1228–1235, 2013.

[10] M. I. Hassan, T. Sun, and N. Sultana, "Fabrication of nanohydroxyapatite/poly(caprolactone) composite microfibers using electrospinning technique for tissue engineering applications," *Journal of Nanomaterials*, vol. 2014, Article ID 209049, 7 pages, 2014.

[11] F. Roozbahani, N. Sultana, A. F. Ismail, and H. Noupavar, "Effect of chitosan alkali pretreatment on the preparation of electrospun PCL/Chitosan blend nanofibrous scaffolds for tissue engineering application," *Journal of Nanomaterials*, vol. 2013, Article ID 641502, 6 pages, 2013.

[12] E. Schnell, K. Klinkhammer, S. Balzer et al., "Guidance of glial cell migration and axonal growth on electrospun nanofibers of poly-ε-caprolactone and a collagen/poly-ε-caprolactone blend," *Biomaterials*, vol. 28, no. 19, pp. 3012–3025, 2007.

[13] C. H. Kim, M. S. Khil, H. Y. Kim, H. U. Lee, and K. Y. Jahng, "An improved hydrophilicity via electrospinning for enhanced cell attachment and proliferation," *Journal of Biomedical Materials Research B Applied Biomaterials*, vol. 78, no. 2, pp. 283–290, 2006.

[14] X. Zong, K. Kim, D. Fang, S. Ran, B. S. Hsiao, and B. Chu, "Structure and process relationship of electrospun bioabsorbable nanofiber membranes," *Polymer*, vol. 43, no. 16, pp. 4403–4412, 2002.

[15] C. X. Zhang, X. Y. Yuan, L. L. Wu, Y. Han, and J. Sheng, "Study on morphology of electrospun poly(vinyl alcohol) mats," *European Polymer Journal*, vol. 41, no. 3, pp. 423–432, 2005.

[16] J. S. Choi, S. W. Lee, L. Jeong et al., "Effect of organosoluble salts on the nanofibrous structure of electrospun poly(3-hydroxybutyrate-co-3-hydroxyvalerate)," *International Journal of Biological Macromolecules*, vol. 34, no. 4, pp. 249–256, 2004.

[17] T. Subbiah, G. S. Bhat, R. W. Tock, S. Parameswaran, and S. S. Ramkumar, "Electrospinning of nanofibers," *Journal of Applied Polymer Science*, vol. 96, no. 2, pp. 557–569, 2005.

[18] L. De Bartolo, S. Morelli, A. Bader, and E. Drioli, "The influence of polymeric membrane surface free energy on cell metabolic functions," *Journal of Materials Science: Materials in Medicine*, vol. 12, no. 10–12, pp. 959–963, 2001.

[19] K. E. Park, H. K. Kang, S. J. Lee, B.-M. Min, and W. H. Park, "Biomimetic nanofibrous scaffolds: preparation and characterization of PGA/chitin blend nanofibers," *Biomacromolecules*, vol. 7, no. 2, pp. 635–643, 2006.

[20] K. Zhang, H. Wang, C. Huang, Y. Su, X. Mo, and Y. Ikada, "Fabrication of silk fibroin blended P(LLA-CL) nanofibrous scaffolds for tissue engineering," *Journal of Biomedical Materials Research A*, vol. 93, no. 3, pp. 984–993, 2010.